QUANTUM LIQUIDS AND QUANTUM CRYSTALS

Effective mass of atom and the excitation spectrum in liquid helium-4 at $T=0$ K

A. A. Rovenchak*

Department of Theoretical Physics, Ivan Franko National University of Lviv, 12 Drahomanov St., Lviv 79005, Ukraine

(Submitted April 22, 2002; revised August 20, 2002)
Fiz. Nizk. Temp. **29**, 145–148 (February 2003)

A self-consistent approach is applied for calculations within the two-time temperature Green function formalism in the random phase approximation for superfluid ^{4}He. The effective mass of the ^{4}He atom is computed as $m^*=1.58m$. The excitation spectrum is found to be in satisfactory agreement with experiment. The sound velocity is calculated as 230 m/s. The Bose-condensation temperature with the effective mass taken into consideration is estimated as 1.99 K. © *2003 American Institute of Physics.* [DOI: 10.1063/1.1542407]

1. INTRODUCTION

The idea of the effective mass of the helium atom in superfluid phase was suggested by Feynman in 1953.[1] He stated that one should insert the effective mass (slightly larger than the mass m of a ''pure'' atom) in the expressions for the density matrix.

Isihara and Samulski[2] used the effective mass $m^*=1.71m$ in order to obtain good agreement of the sound branch of the excitation spectrum with the experimental data on the sound velocity.

While in both these cases the effective mass was introduced phenomenologically, it turned out to be possible to obtain the value of this quantity on the basis of experimental data for the structure factor of liquid helium-4,[3] and a result of $1.70m$ was calculated there by Vakarchuk.

The main idea of the present paper is to give a way of obtaining the ^{4}He atom effective mass by means of a self-consistent equation. The expressions are written within the collective variables formalism as described by Bogoliubov and Zubarev.[4] Two-time temperature Green functions[5] are utilized for the calculation of the thermodynamic averages.

We also intend to show the possibility of an essentially simple approach to the problem of the many-boson system with strong interaction, such as liquid helium-4. The method applied does not require much computational effort. This advantage allows for the development of further approximations.

In addition, if one accepts the assumption that the phenomena in liquid ^{4}He are at least partly due to the Bose condensation being ''spoiled'' by the interatomic interaction, it turns out to be possible to estimate the lambda transition temperature as the critical temperature of the ideal Bose gas. We show that such an approach leads to very good agreement with experiment: if the effective mass is about 50% larger than the pure one, the Bose condensation temperature decreases to a value of $\simeq 2$ K.

The Green function technique also provides a possibility of obtaining the excitation spectrum of the system. As a result of the mass renormalization, the excitation spectrum is found to be in better agreement with experiment than the Bogoliubov or Feynman spectrum, while the expressions are the same (the latter two spectra suffer from the well-known problem of the so-called ''roton'' minimum overestimation if one considers the pure mass).

A self-consistent approach was recently applied for the calculation of the ^{4}He excitation spectrum by Pashitskii *et al.*[6] The results of that paper are in excellent agreement with experiment. The authors used the ''semitransparent spheres'' potential for the calculation, with some adjustable parameters.

A new interpretation of the roton region of the helium excitation spectrum was given by Kruglov and Collett.[7] They considered the so-called roton cluster as a bound state of 13 atoms and solved the nonlinear Schrödinger equation for this system surrounded by the condensate. This approach reflects the experimental data for the roton branch of the excitation curve very well.

In our work, we utilize the potential of Ref. 8 as input information for the computations. This potential was obtained on the basis of the quantum-mechanical equations with the static structure factor as the only experimental datum. Since this quantity is quite easily measured directly in the scattering experiments, we consider this a good approach. Unfortunately, a direct calculation of the potential for the many-body problem cannot be carried out at the present time.

The paper is organized as follows. The calculation procedure is given in Sec. 2. The Hamiltonian is written and the equations of motion for the Green functions are solved in the random phase approximation (RPA), providing a self-consistent equation for the effective mass extraction. The numerical results are adduced and discussed in Sec. 3.

2. CALCULATION PROCEDURE

The Hamiltonian of the Bose system in the collective variables representation reads:[4]

$$\hat{\mathcal{H}}=\sum_{\mathbf{k}\neq 0}\left\{\varepsilon_k[\rho_{\mathbf{k}}\partial_{-\mathbf{k}}-\partial_{\mathbf{k}}\partial_{-\mathbf{k}}]+\frac{N}{2V}\nu_k[\rho_{\mathbf{k}}\rho_{-\mathbf{k}}-1]\right\}$$
$$+\frac{1}{\sqrt{N}}\sum_{k\neq 0}\sum_{\substack{\mathbf{q}\neq 0\\ \mathbf{k}+\mathbf{q}\neq 0}}\frac{\hbar^2}{2m}\mathbf{k}\cdot\mathbf{q}\rho_{\mathbf{k}+\mathbf{q}}\partial_{-\mathbf{k}}\partial_{-\mathbf{q}}, \quad (1)$$

where the operator $\partial_{\mathbf{k}}=\partial/\partial\rho_{-\mathbf{k}}$. Here ε_k is the energy spectrum of a free particle, $\varepsilon_k=\hbar^2k^2/2m$, N is the total number of particles in the system, V is the system volume, ν_k is the Fourier transform of the interatomic potential in the thermodynamic limit, and $N/V=\wp=\text{const}$. The item with one summation over the wave vector $\mathbf{k}$ in Eq. (1) corresponds to the random phase approximation, and the second one is the correction. Let us assume that our system is described exactly by the RPA Hamiltonian $\hat{\mathcal{H}}^{(*)}$, i.e.,

$$\hat{\mathcal{H}}^{(*)}=\sum_{\mathbf{k}\neq 0}\left\{\varepsilon^*_{\mathbf{k}}[\rho_{\mathbf{k}}\partial_{-\mathbf{k}}-\partial_{\mathbf{k}}\partial_{-\mathbf{k}}]+\frac{N}{2V}\nu_k[\rho_{\mathbf{k}}\rho_{-\mathbf{k}}-1]\right\}, \quad (2)$$

where $\varepsilon^*_{\mathbf{k}}=\hbar^2k^2/2m^*$, and m^* is the effective mass of the ^{4}He atom. It is the only quantity suitable for the ''effective'' role, since we wish to preserve the interatomic potential as the initial information.

Such a definition of the effective mass means that we partly transfer the interaction and the higher-order correction onto the kinetic term in the energy. This approach correlates with that of Feynman.[1] As was also shown by Vakarchuk,[9] the mass renormalization obtained in a similar fashion leads to the expression obtained for the effective mass of ^{3}He impurity in ^{4}He but with the ''pure'' mass of the ^{3}He atom replaced by that of the ^{4}He atom.

We define m^* by demanding that the effective Hamiltonian (2) leads to the same ground-state energy as the initial Hamiltonian (1), $\langle\hat{\mathcal{H}}^{(*)}\rangle=\langle\hat{\mathcal{H}}\rangle$:

$$\sum_{\mathbf{k}\neq 0}\left\{\varepsilon^*_k[\langle\rho_{\mathbf{k}}\partial_{-\mathbf{k}}\rangle^{(*)}-\langle\partial_{\mathbf{k}}\partial_{-\mathbf{k}}\rangle^{(*)}]\right.$$
$$\left.+\frac{N}{2V}\nu_{\mathbf{k}}[\langle\rho_{\mathbf{k}}\rho_{-\mathbf{k}}\rangle^{(*)}-1]\right\}=\sum_{\mathbf{k}\neq 0}\left\{\varepsilon_k[\langle\rho_{\mathbf{k}}\partial_{-\mathbf{k}}\rangle-\langle\partial_{\mathbf{k}}\partial_{-\mathbf{k}}\rangle]\right.$$
$$\left.+\frac{N}{2V}\nu_k[\langle\rho_{\mathbf{k}}\rho_{-\mathbf{k}}\rangle-1]\right\}$$
$$+\frac{1}{\sqrt{N}}\sum_{k\neq 0}\sum_{\substack{\mathbf{q}\neq 0\\ \mathbf{k}+\mathbf{q}\neq 0}}\frac{\hbar^2}{2m}\mathbf{kq}\langle\rho_{\mathbf{k}+\mathbf{q}}\partial_{-\mathbf{k}}\partial_{-\mathbf{q}}\rangle, \quad (3)$$

where the superscript (*) near the angle brackets is introduced for convenience.

One can find the operator product average by utilizing two-time temperature Green functions defined as follows:[5]

$$\langle\langle A(t)|B(t')\rangle\rangle=i\,\theta(t-t')\langle[A(t),B(t')]\rangle, \quad (4)$$

with the operators given in the Heisenberg representation; θ is the Heaviside step function.

$$\langle AB\rangle=\hat{\mathcal{A}}G_{BA}(\hbar\omega)$$
$$=\frac{i}{\hbar}\int_{-\infty}^{+\infty}d\hbar\omega\,\frac{G_{BA}(\hbar\omega-i\varepsilon)-G_{BA}(\hbar\omega-i\varepsilon)}{e^{\beta\hbar\omega}-1}\Bigg|_{\varepsilon\to+0}, \quad (5)$$

where G_{BA} stands for $\langle\langle B|A\rangle\rangle$ and the operator $\hat{\mathcal{A}}$ is introduced for convenience. We set the time arguments in the operators $A(t)$, $B(t')$ to coincide: $t-t'=0$. This will provide the static properties of the system under consideration. In the above expression, β is the inverse temperature, $\beta=1/T$.

Now we proceed to the equations of motion for the Green functions $G_{\rho\rho}(\mathbf{k})\equiv\langle\langle\rho_{\mathbf{k}}|\rho_{-\mathbf{k}}\rangle\rangle$, $G_{\rho\partial}(\mathbf{k})=\langle\langle\rho_{\mathbf{k}}|\partial_{-\mathbf{k}}\rangle\rangle$, etc. It is easy to obtain the following set of equations in the RPA:

$$(\hbar\omega-\varepsilon_k)G_{\rho\rho}(\mathbf{k})=2\varepsilon_kG_{\partial\rho}(\mathbf{k}),$$
$$(\hbar\omega-\varepsilon_k)G_{\partial\rho}(\mathbf{k})=\wp\,\nu_kG_{\rho\rho}(\mathbf{k})+\frac{1}{2\pi},$$
$$(\hbar\omega+\varepsilon_k)G_{\rho\partial}(\mathbf{k})=2\varepsilon_kG_{\partial\partial}(\mathbf{k})-\frac{1}{2\pi},$$
$$(\hbar\omega-\varepsilon_k)G_{\partial\partial}(\mathbf{k})=\wp\,\nu_kG_{\rho\partial}(\mathbf{k}). \quad (6)$$

Here $\wp$ is equilibrium density.

Next, let us consider the triple product average $\langle ABC\rangle$. One can obtain it utilizing either the Green function $G_{C;AB}\equiv\langle\langle C|AB\rangle\rangle$ or $G_{BC;A}\equiv\langle\langle BC|A\rangle\rangle$. We suggest the first possibility to fulfill

$$\langle ABC\rangle=\hat{\mathcal{A}}G_{C;AB}\equiv\langle\langle C|AB\rangle\rangle. \quad (7)$$

In other words, we neglect the functions of the type $G_{BC;A}\equiv\langle\langle BC|A\rangle\rangle$ for the sake of simplicity (when applying this to Eq. (6) it means that only the RPA term of the Hamiltonian (1) is taken into consideration when constructing the equations of motion). Having performed a similar procedure with the function $G_{\partial;\rho\partial}(\mathbf{k}_1,\mathbf{k}_2,\mathbf{k}_3)\equiv\langle\langle\partial_{\mathbf{k}_1}|\rho_{\mathbf{k}_2}\partial_{\mathbf{k}_3}\rangle\rangle$, we obtain in the RPA the following set of equations:

$$(\hbar\omega-\varepsilon_{k_2})G_{\partial;\rho\partial}(-\mathbf{k}_2,\mathbf{k}_1+\mathbf{k}_2,-\mathbf{k}_1)$$
$$=\wp\,\nu_{k_2}G_{\rho;\rho\partial}(-\mathbf{k}_2,\mathbf{k}_1+\mathbf{k}_2,-\mathbf{k}_1)-g_{\partial\rho\partial}(\omega),$$
$$(\hbar\omega+\varepsilon_{k_2})G_{\rho;\rho\partial}(-\mathbf{k}_2,\mathbf{k}_1+\mathbf{k}_2,-\mathbf{k}_1)$$
$$=2\varepsilon_{k_2}G_{\partial;\rho\partial}(-\mathbf{k}_2,\mathbf{k}_1+\mathbf{k}_2,-\mathbf{k}_1)-g_{\rho\rho\partial}(\omega), \quad (8)$$

where the quadruple Green functions were decoupled in such a way as to provide the inhomogeneous set of equations:

$$\langle\langle AB|CD\rangle\rangle=\langle BD\rangle\langle\langle A|C\rangle\rangle+\langle CA\rangle\langle\langle B|D\rangle\rangle+\langle AD\rangle\langle\langle B|C\rangle\rangle$$
$$+\langle CB\rangle\langle\langle A|D\rangle\rangle. \quad (9)$$

The inhomogeneous terms in Eq. (8) read:

$$g_{\rho\rho\partial}(\omega)=\frac{\hbar^2}{2m}[\mathbf{k}_1\cdot\mathbf{k}_2 2D_{k_1}G_{\rho\rho}(\mathbf{k}_1+\mathbf{k}_2)+\mathbf{k}_1$$
$$\cdot\mathbf{k}_2S_{|\mathbf{k}_1+\mathbf{k}_2|}G_{\partial\partial}(\mathbf{k}_1)+\mathbf{k}_2\cdot(\mathbf{k}_1+\mathbf{k}_2)D''_{k_1}G_{\partial\rho}(\mathbf{k}_1$$
$$+\mathbf{k}_2)+\mathbf{k}_2\cdot(\mathbf{k}_1+\mathbf{k}_2)D''_{|\mathbf{k}_1+\mathbf{k}_2|}G_{\rho\partial}(\mathbf{k}_1)],$$
$$g_{\partial\rho\partial}(\omega)=\frac{\hbar^2}{m}[\mathbf{k}_1\cdot(\mathbf{k}_1+\mathbf{k}_2)D_{k_1}G_{\partial\rho}(\mathbf{k}_1+\mathbf{k}_2)+\mathbf{k}_1\cdot(\mathbf{k}_1$$
$$+\mathbf{k}_2)D''_{|\mathbf{k}_1+\mathbf{k}_2|}G_{\partial\partial}(\mathbf{k}_1)]. \quad (10)$$

The notations for the averages of pair products are listed below:

$$\langle \rho_{-\mathbf{k}}\rho_{\mathbf{k}}\rangle \equiv S_k = \frac{1}{\alpha_k}\coth\frac{\varepsilon_k\alpha_k}{2T},$$

$$\langle \rho_{-\mathbf{k}}\partial_{\mathbf{k}}\rangle \equiv D_k'' = \frac{1}{2}\left(\frac{1}{\alpha_k}\coth\frac{\varepsilon_k\alpha_k}{2T}-1\right)=\frac{1}{2}(S_k-1),$$

$$\langle \partial_{-\mathbf{k}}\partial_{\mathbf{k}}\rangle \equiv D_k = \frac{1-\alpha_k^2}{4\alpha_k}\coth\frac{\varepsilon_k\alpha_k}{2T} = -\frac{\wp\nu_k}{2\varepsilon_k}S_k. \tag{11}$$

The quantity α_k is defined as follows:

$$\alpha_k = \left(1+2\frac{\wp\nu_k}{\varepsilon_k}\right)^{1/2}. \tag{12}$$

Now, if we turn back to correlation (3), the meaning of the asterisk as a superscript becomes clear: one should replace m by m^* in the left-hand side of this equation.

In the ground state ($T=0$ K), the hyperbolic cotangents in Eq. (11) are equal to unity. Therefore, a self-consistent equation for the extraction of m^* becomes as follows:

$$-\frac{1}{N}\sum_{k\neq 0}\frac{\varepsilon_k^*}{4}(\alpha_k^*-1)^2$$

$$=-\frac{1}{N}\sum_{\mathbf{k}\neq 0}\frac{\varepsilon_k}{4}(\alpha_k-1)^2-\frac{1}{N^2}\sum_{\mathbf{k}\neq 0}\sum_{\substack{\mathbf{q}\neq 0\\ \mathbf{k}+\mathbf{q}\neq 0}}\left(\frac{\hbar^2}{2m}\right)^2\frac{\mathbf{k}\cdot\mathbf{q}}{\alpha_{\mathbf{k}}\alpha_q\alpha_p}$$

$$\times\left[\mathbf{k}\cdot\mathbf{p}\frac{\wp\nu_k}{2\varepsilon_k}\left(\frac{-\alpha_p}{\varepsilon_k\alpha_k+\varepsilon_q\alpha_q}+\frac{\alpha_q\alpha_p}{\varepsilon_q\alpha_q+\varepsilon_p\alpha_p}\right)\right.$$

$$-\mathbf{q}\cdot\mathbf{p}\frac{\wp\nu_q}{2\varepsilon_q}\left(\frac{\alpha_p}{\varepsilon_k\alpha_k+\varepsilon_q\alpha_q}+\frac{\alpha_k}{\varepsilon_q\alpha_q+\varepsilon_p\alpha_p}\right)$$

$$+\left(\frac{1}{\varepsilon_k\alpha_k+\varepsilon_q\alpha_q}+\frac{1}{\varepsilon_q\alpha_q-\varepsilon_p\alpha_p}\right)$$

$$\left.\times\left(\mathbf{k}\cdot\mathbf{q}\frac{\wp\nu_k\wp\nu_q}{\varepsilon_k\varepsilon_q}+\mathbf{k}\cdot\mathbf{p}\frac{\wp\nu_k}{2\varepsilon_k}+\mathbf{q}\cdot\mathbf{p}\frac{\wp\nu_q}{2\varepsilon_q}\right)\right], \tag{13}$$

where $\mathbf{p}=\mathbf{k}+\mathbf{q}$. We also consider the specific energy instead of the total energy by introducing the factor of $1/N$. One should notice that for the noninteracting system, when $\nu_k=0$, the above equation is satisfied trivially ($\alpha_k=\alpha_k^*=1$ in this case). In particular, the triple product average $\langle\rho_{\mathbf{k}+\mathbf{q}}\partial_{-\mathbf{k}}\partial_{-\mathbf{q}}\rangle$ in (3) equals zero, providing a well-known expression for the ideal Bose-gas (IBG) energy:

$$E_{IBG}=\sum_{\mathbf{k}\neq 0}\frac{\varepsilon_k}{2}\left[\coth\frac{\varepsilon_k}{2T}-1\right]=\sum_{\mathbf{k}\neq 0}\frac{\varepsilon_k}{e^{\varepsilon_k/T}-1}.$$

3. NUMERICAL RESULTS AND DISCUSSION

We use the previously obtained results[8] for the Fourier transform ν_k of the interatomic potential. The value of the equilibrium density is $\wp=0.02185$ Å^{-3}. The mass of the helium-4 atom is $m=4.0026$ a.m.u. We pass from the summation over the wave vector to integration in the usual way: $\Sigma_{\mathbf{k}}\to V\int d\mathbf{k}/(2\pi)^3$. The value of the upper cutoff for the integration over the wave vector is 16.0 Å^{-1}.

The solution of Eq. (13) under the above-listed conditions is

$$m^*=1.58m. \tag{14}$$

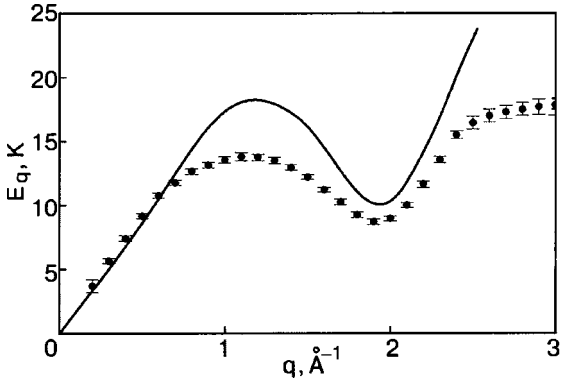

FIG. 1. Excitation spectrum of liquid helium-4. Filled circles-experimental data;[10] solid line-calculated energy.

One can also obtain the excitation spectrum using Green functions. The solutions of set (6) are proportional to $1/(\hbar^2\omega^2-\varepsilon_k^2\alpha_k^2)$, providing the spectrum $E_k=\pm\varepsilon_k\alpha_k$, which is a very well known result.[4] If one inserts the effective mass into the definitions of ε_k and α_k, the resulting curve fits the experimental one in a quite satisfactory manner (see Fig. 1).

The phonon branch is reflected quite well, providing a sound velocity of approximately 230 m/s versus the experimental one 238 m/s at $T=0.8$ K[11] or 240 m/s at $T=0.1$ K.[12] The so-called ''roton'' minimum also has a value close to the experimental one.

In addition, the value obtained for the effective mass shifts the temperature of the Bose condensation from $T_c=3.14$ K for the pure mass to $T_c=1.99$ K, versus the experimental temperature of the lambda transition $T_\lambda=2.17$ K. We consider the results discussed above to be quite good for such a rough approximation as random phases.

The author is grateful to Prof. I. Vakarchuk for valuable discussions on the problem considered in this work.

*E-mail: andrij@ktf.franko.lviv.ua

[1] R. P. Feynman, Phys. Rev. **91**, 1291 (1953).
[2] A. Isihara and T. Samulski, Phys. Rev. B **16**, 1969 (1977).
[3] I. O. Vakarchuk, Visn. Lviv. Univer. Ser. Fiz. **26**, 29 (1993) (in Ukrainian).
[4] N. N. Bogoliubov and D. N. Zubarev, Zhurn. Éksp. Teor. Fiz. **28**, 129, (1955)[Sov. Phys. JETP **1**, 83 (1955)].
[5] D. N. Zubarev, *Neravnovesnaia Statisticheskaia Termodinamika*, Nauka, Moscow (1971) (in Russian); D. N. Zubarev, *Nonequilibrium Statistical Thermodynamics*, Consultants Bureau, New York (1974).
[6] E. A. Pashitskii, S. I. Vilchinskyy, and S. V. Mashkevich, Fiz. Nizk. Temp. **28**, 115 (2002) [Low Temp. Phys. **28**, 79 (2002)].
[7] V. I. Kruglov and M. J. Collett, Phys. Rev. Lett. **87**, 185302 (2001).
[8] I. O. Vakarchuk, V. V. Babin, and A. A. Rovenchak, J. Phys. Stud. (Lviv) **4**, 16 (2000).
[9] I. O. Vakarchuk, J. Phys. Stud. (Lviv) **1**, 25 (1996); **1**, 156 (1997) (in Ukrainian).
[10] R. A. Cowley and A. D. B. Woods, Can. J. Phys. **49**, 177 (1971).
[11] V. D. Arp, R. D. McCarty, and D. G. Friend, Natl. Inst. Stand. Technol. (U.S.) Tech. Note **1334**, (1998) (revised).
[12] R. D. McCarty, Natl. Bur. Stand. (U.S.) Tech. Note **1029**, (1980).

This article was published in English in the original Russian journal. Reproduced here with stylistic changes by AIP.

SUPERCONDUCTIVITY, INCLUDING HIGH-TEMPERATURE SUPERCONDUCTIVITY

ab-plane tunneling and Andreev spectroscopy of the superconducting gap and pseudogap in $(Bi,Pb)_2Sr_2Ca_2Cu_3O_{10+\delta}$ and $Bi_2Sr_2CaCu_2O_{8+\delta}$

A. I. D'yachenko and V. Yu. Tarenkov

A. Galkin Donetsk Physical and Technical Institute of the National Academy of Sciences of Ukraine, 72 R. Luxemburg St., Donetsk 83114, Ukraine

R. Szymczak, H. Szymczak, A. V. Abal'oshev,* and S. J. Lewandowski

Institute of Physics, Polish Academy of Sciences, 32/46 Al. Lotnikow, 02-668 Warsaw, Poland

L. Leonyuk†

Moscow State University, Moscow, 118899 Russia

(Submitted May 7, 2002; revised July 29, 2002)
Fiz. Nizk. Temp. **29**, 149–155 (February 2003)

We have measured the temperature dependence of gap features revealed by Andreev reflection (Δ_s) and by tunneling (Δ) in the *ab* plane of optimally and slightly overdoped microcrystals of $(BiPb)_2Sr_2Ca_2Cu_3O_{10+\delta}$ (Bi2223) with critical temperature $T_c = 110-115$ K, and $Bi_2Sr_2CaCu_2O_{8+\delta}$ (Bi2212) with $T_c = 80-84$ K. The tunneling conductance of a Bi2223-insulator-Bi2223 junction shows peaks at the 2Δ gap voltage, as well as dips and broad humps at other voltages. In Bi2223, similarly to the well-known Bi2212 spectra, the energies corresponding to 2Δ, to the dip, and to the hump structure are in the ratio 2:3:4. This confirms that the dip and hump features are generic to the high-temperature superconductors, irrespective of the number of CuO_2 layers or the BiO superstructure. On the other hand, in both compounds the $\Delta(T)$ and $\Delta_s(T)$ dependences are completely different, and we conclude that the two entities are of different natures. [DOI: 10.1063/1.1542408]

1. INTRODUCTION

Along with the usual coherence gap Δ_s, in the spectrum of quasiparticle excitations in high-T_c superconductors there appears a gap Δ_p (pseudogap), which persists above the superconducting transition temperature T_c (Refs. 1 and 2). The pseudogap has the same *d* symmetry as Δ_s, but disappears (more accurately: becomes indistinct) at some temperature $T^* > T_c$ (Ref. 3). The relationship between the pseudogap and superconductivity is far from clear.[1,2] One of the reasons appears to be that the most popular methods of investigating the excitation spectrum in cuprates, like tunneling and angle-resolved photoemission (ARPES), cannot distinguish between Δ_p and Δ_s without recourse to various theoretical models. However, it is known that in the process of Andreev reflection of an electron from a normal metal-superconductor (N–S) interface, a Cooper pair is created in the superconductor.[4] This occurs only in the presence of a nonzero energy gap Δ_s in the superconductor. In other words, the process of Andreev transformation of an electron-hole pair into a Cooper pair is possible only for a reflection from the superconducting order parameter Δ_s. In marked contrast, the tunneling effect is sensitive to any singularity in the quasiparticle excitation spectrum.[5] Therefore, the tunneling characteristics at $T < T_c$ in general depend on joint contributions of the energy gap and pseudogap.

d-wave symmetry of the energy gap introduces some additional complications. The dominant contribution to the junction conductivity in classical (Giaever) tunneling comes from electrons with wave vectors forming a narrow cone only a few degrees wide.[5] Accordingly, tunnel junctions yield information on the gap anisotropy $\Delta(\mathbf{k})$, and the gap revealed in tunneling experiments can be expressed as $\Delta(\mathbf{k}) = [\Delta_s^2(\mathbf{k}) + \Delta_p^2(\mathbf{k})]^{1/2}$ (Ref. 6). In the case of Andreev reflection from a clean N-S interface, the situation is different. The incident electron is not scattered, but reflected back along the same trajectory. This is true for any angle of incidence. It can be said that all incident electrons participate in Andreev reflection on an equal footing. Therefore, measurement of a single Andreev N–S junction is in principle sufficient to determine the maximal value of the superconducting gap $\Delta_s(\mathbf{k})$.

In this paper we employ the above discussed characteristic features of tunneling and Andreev spectroscopy to investigate the temperature dependence of the energy gaps Δ and Δ_s in $Bi_2Sr_2CaCu_2O_{8+\delta}$ (Bi2212) and $(Bi,Pb)_2Sr_2Ca_2Cu_3O_{10+\delta}$ [(BiPb)2223] cuprates. The well-studied Bi2212 has two CuO_2 layers per unit cell and strong incommensurate modulation in the BiO layer,[7] which complicates the interpretation of tunneling and ARPES data. The substitution of Bi by Pb in the (BiPb)2223 compound completely erases the superstructure in the BiO layers.

Tunneling measurements were carried out on "break

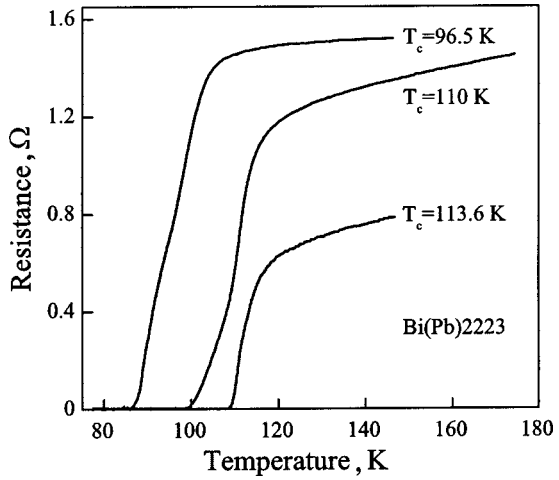

FIG. 1. Temperature dependence of the *ab*-plane resistance of (BiPb)2223 samples with different oxygen doping.

junctions'' with the barrier surface practically normal to the crystallographic axes in the base *ab* plane of the material. In the *c* direction, the influence of the BiO layer on the tunneling spectra is much more pronounced. Andreev experiments were performed on S–N–S junctions. In both cases we retained only the samples showing pure tunneling or Andreev characteristics. The temperature dependences of the energy gaps obtained in the two types of experiments are completely different and attest to fundamental differences between the ''superconducting'' gap Δ_s and the *a*,*b*-axis quasiparticle gap Δ.

2. SAMPLE PREPARATION

The tunnel junctions were elaborated from Bi2223 and Bi2212 single crystals. Textured $(Bi_{1.6}Pb_{0.4})Sr_2Ca_2Cu_3O_{10+\delta}$ and $Bi_2Sr_2CaCu_2O_8$ samples in the form of $10\times1\times0.1$ mm rectangular bars were prepared[8–10] by compacting powdered (BiPb)2223 and Bi2212 compounds, respectively, at 30–40 kbar between two steel anvils. The powder was contained between two thin copper wires, whose deformation provided a uniform pressure distribution in the sample volume. In this manner the powder was compacted into dense plane-parallel bars about 0.1 mm thick. The bars were then pre-annealed at $T=845\,^\circ$C for 16 h, compressed again, and finally annealed at $T=830\,^\circ$C for 14 h, producing a well-pronounced texture. Usually the Bi2212 samples were slightly overdoped and exhibited a critical temperature $T_c=80-84$ K. The doping level of the oxygen content was controlled by annealing optimally doped samples in flowing gas adjusted for different partial pressures of oxygen. The samples emerging from this procedure were highly textured, composed of tightly packed microcrystals aligned in one direction. Sample quality was controlled by transport measurements. We used for further processing only those samples which were showing a critical current density $J_c(T=4.2\text{ K})>4\cdot10^4$ A/cm^2. The superconducting transition temperature T_c was determined from the midpoint of the resistive $R(T)$ transition (see Fig. 1).

The S–I–S and S–N–S junctions were made by breaking specially prepared Bi2212 and Bi2223 samples. Each sample was hermetically sealed by insulating resin and glued to an elastic steel plate, which was then bent until a crack occurred, running across the sample width and detected by monitoring the sample resistance. The hermetic seal remained unbroken in this process. After the external load was relieved, the sample returned to its initial position with the crack closed and the microcrystals once again tightly pressed to each other along the line of the fracture. The best alignment is expected in the sample region in which the shear deformation was minimal. This is apparently one of the reasons why such a procedure results in the realization of one effective junction of the microcrystal-microcrystal type. The selection of a single junction with minimal tunneling resistance from among the competing junctions is further assisted by the nature of the tunneling effect, which decreases exponentially with the barrier thickness. A small sample thickness (<100 μm) and a relatively large size of the microcrystals (>10 μm) are also important factors enhancing junction quality. Such break junctions on microcrystals were found to be particularly effective in the investigation of high-T_c superconductors.[9] The typical normal-state resistance of junctions used in the present study was between a few ohms and a few tens of ohms, and was remarkably stable.

The surface of our Bi2212 and (BiPb)2223 break junctions was perpendicular to the CuO_2 plane, and the direction of tunneling formed only a very small angle α with one of the crystallographic axes (*a* or *b*) in this plane, as is attested to by the presence of Andreev bound states, seen in the tunneling S–I–S characteristics as a characteristic peak of the conductivity at zero bias (cf. Fig. 2). Numerical calculations based on a simplified theoretical model[9,11] and taking into account the *d*-wave mechanism of pairing show that the appearance of such a narrow zero-bias peak in the tunneling conductance occurs at $\alpha\leqslant6°$. In high-quality break junctions the zero-bias conductance peak (ZBCP) has been reported to coexist with the Josephson effect,[12] but we have to rule out this possibility because of the wrong signature: the ZBCP was insensitive to magnetic field and did not reflect on the *I*-*V* characteristics. The spectra $\sigma(V)=dI/dV$ show the quasiparticle peaks at 2Δ, where Δ is defined as a quarter of the peak-to-peak separation (Fig. 2). We use this Δ value as

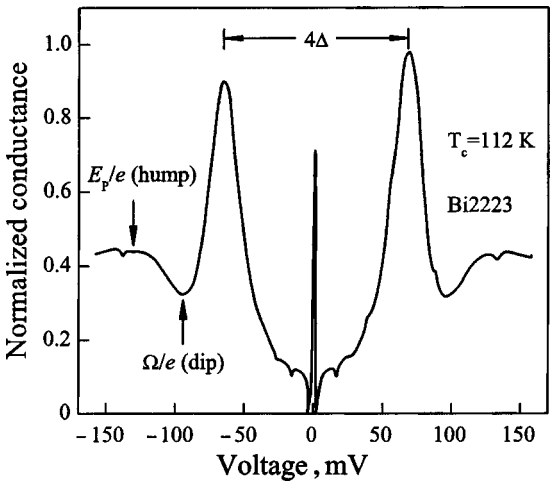

FIG. 2. Tunneling conductance of a Bi2223–I–Bi2223 junction at $T=77.4$ K. The zero-bias peak is due to the Andreev bound state. The spectra clearly show dip and hump structures. Arrows indicate the 3Δ and 4Δ positions.

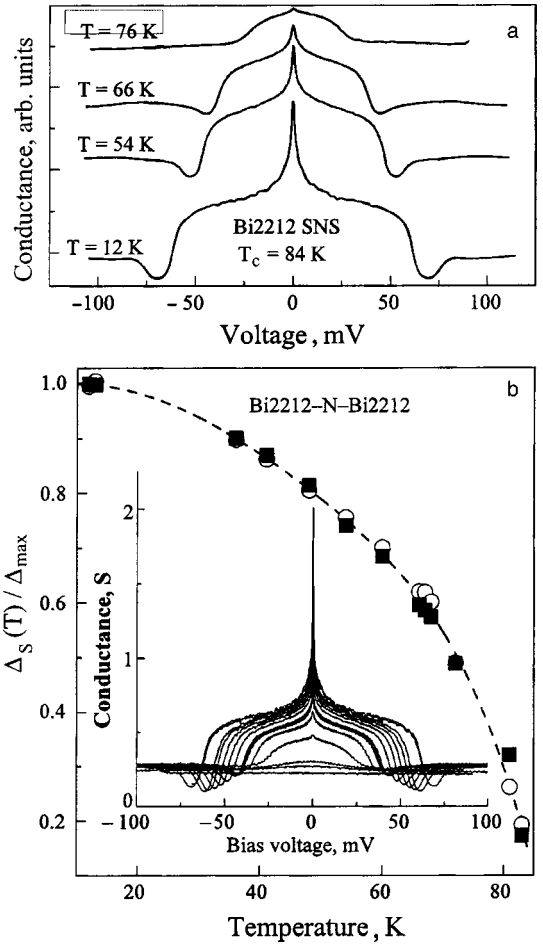

FIG. 3. Conductance σ of an S–N–S (Andreev) Bi2212–N–Bi2212 break junction. a—Temperature dependence of σ. The individual plots are shifted vertically for clarity. b—Temperature dependence of the energy gap Δ_s. The inset shows the σ plots in their original position.

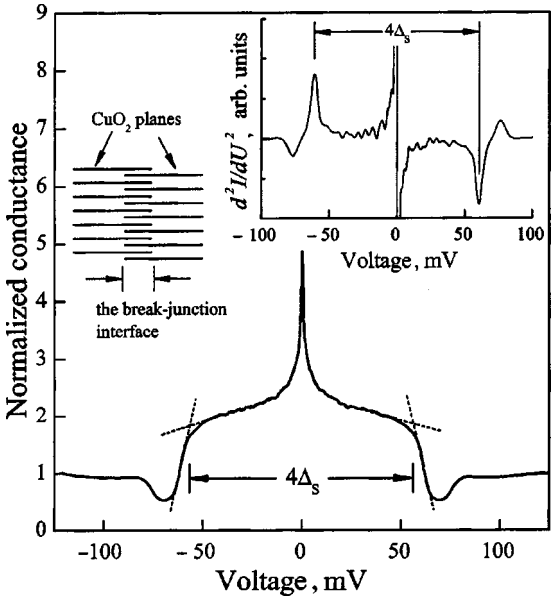

FIG. 4. Geometrical construction for the determination of Δ_s from Andreev measurements. The top inset shows the corresponding $d\sigma/dV$ plot. The left inset shows the hypothetical inner structure of the Andreev break junction.

a measure of the gap, since there is no exact method of extracting the energy gap from the tunneling spectra, given that the exact functional form of the density of states for high-T_c superconductors is not known.

In general, the type of the junction was determined *ex post facto* from their conductance spectra $\sigma(V)$. We retained for further investigation only the junctions conforming to either S–I–S or S–N–S types. For example, the $\sigma(V)$ curve in Fig. 2 reveals all the characteristic features of a superconducting tunnel S–I–S junction: an almost flat region around zero bias followed by a sharp increase in the tunneling current, peaking around ± 60 meV (2Δ); at still higher bias voltages V the conductance depends parabolically on V. The junction shown in Fig. 3, on the other hand, behaves as a typical Andreev S–N–S junction. First, there is a low-resistance region at low bias voltages, seen as a broad pedestal spanning the coordinate origin. The next indication is the excess current, which was observed in all S–N–S junctions included in this study. Finally, the differential conductivity of the junction at $eV > 2\Delta_s$ coincides with the normal-state conductivity at $T > T_c$ [see inset in Fig. 3b], i.e., for $T > T_c$ practically all of the bias voltage is applied directly to the junction.

One may inquire about the mechanism which might produce in an apparently random manner either S-I-S or S-N-S junctions. The insulating layer in S–I–S junctions is most probably caused by oxygen depletion. As to the normal barrier, we speculate that the CuO_2 planes are harder to fracture than the buffer layers. After the sample is broken, they penetrate slightly into the buffer layers (see left inset in Fig. 4). In this manner, the coupling between the CuO_2 planes belonging to the separated sample parts would be stronger than the normal coupling across the buffer layers, and it could assist in creating a constriction, which would act as a normal 3D metal. This hypothesis is in agreement with the scanning microscope study of the fracture surfaces of Bi2212 single-crystal break junctions, which revealed rough, but stratified fracture surfaces.[13]

3. EXPERIMENTAL RESULTS

The temperature dependence of the energy gap $\Delta_s(T)$ obtained from Andreev S–N–S measurements for Bi2212 exhibited a BCS-like form (see Fig. 3). We used two methods to determine Δ_s for Andreev junctions. The first one is shown in Fig. 4 and relies on measuring the distance between the points of maximal slope changes of the $\sigma(V)$ plot, which is taken as the measure of $4\Delta_s$. The details of the second one are shown in the top inset in Fig. 4. The rationale for both methods is found in recent calculations[14] based on the Klapwijk, Blonder, and Tinkham[15] treatment of multiple Andreev reflections between two superconductors, which indicate that $2\Delta_s$ is determined by the separation of the extrema in $d\sigma/dV$. The results obtained by both methods are plotted together in Fig. 3b. It is seen that these results differ slightly, but both outline essentially the same $\Delta_s(T)$ dependence.

The $\Delta(T)$ gap dependence determined from tunneling measurements performed on the same compounds diverged considerably from the BCS relation (Fig. 5). In fact, $\Delta(T)$ depends on temperature very weakly for $T \geqslant T_c$. According to an ARPES investigation,[16] such behavior of $\Delta(T)$ in Bi2212 near optimal doping is expected for the *a* (or *b*)

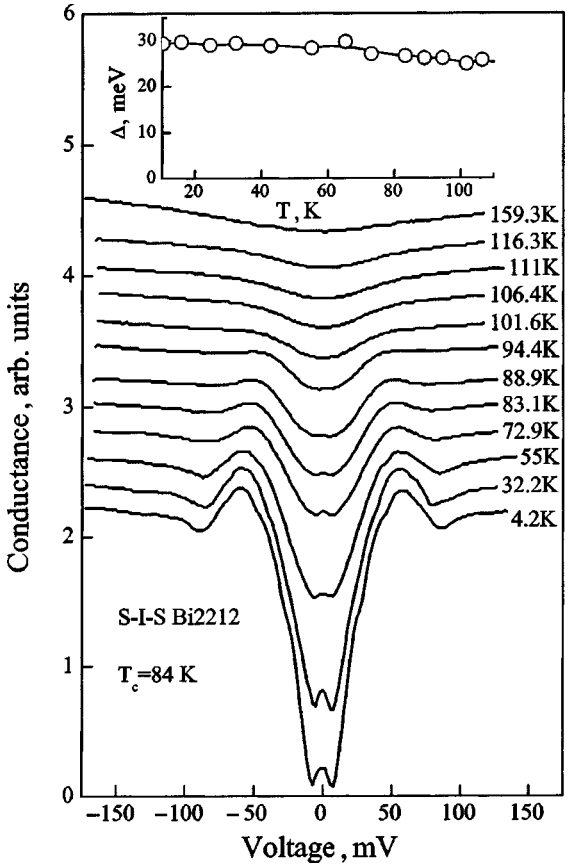

FIG. 5. Conductance of an S–I–S (tunneling) Bi2223–I–Bi2223 break junction. The inset shows the temperature dependence of the tunneling gap $\Delta(T)$. Some structural details of the spectra have been blurred by the speed of recording needed to overcome temperature instabilities of the experimental setup.

direction in the CuO_2 plane. This result agrees with our assumption about the direction of tunneling in our Bi2212-I-Bi2212 junctions. As we mentioned above, further confirmation is provided by the presence of an Andreev bound state, seen in the spectra of S–N–S and S–I–S junctions as a characteristic peak of the conductivity at zero bias (cf. Fig. 3 and Fig. 5). According to the ARPES data,[16] near optimal doping the $\Delta(T)$ gap becomes temperature dependent only when α is of the order of 15°. For technological reasons, the formation of break junctions with the crystal broken at such an angle is improbable. As a result, the tunneling characteristics at $T>T_c$ relate to the gap in (100) or (010) direction.

In full agreement with the ARPES results,[16] with increasing temperature the gap Δ of Bi2212 becomes filled with quasiparticle excitations, and the conductance peaks at 2Δ become less distinct. The distance between the still-discernible conductance peaks does not decrease, and the $\Delta(T)$ gap is seen to persist into the region $T>T_c$. Similar behavior is also observed for the (BiPb)2223 compound.

The temperature dependence of the proper coherent gap $\Delta_s(T)$ behaves in a completely different manner (Fig. 3). The gap narrows with increasing temperature, and at $T=T_c$ it closes completely. The high curvature of the Andreev conductance dip at $eV\approx 2\Delta_s$ is evidence both of the good quality of the investigated junctions and of the long lifetime of quasiparticles in the gap region. This was confirmed by an analysis of the spectra of normal-metal–constriction–superconductor (N–c–S) junctions.[9] For Bi2212 Andreev N–c–S junctions, the Blonder–Tinkham–Klapwijk[17] parameter Z used to obtain the theoretical fit was small, $Z\simeq 0.5$, a value characteristic for very clean N-S contacts.

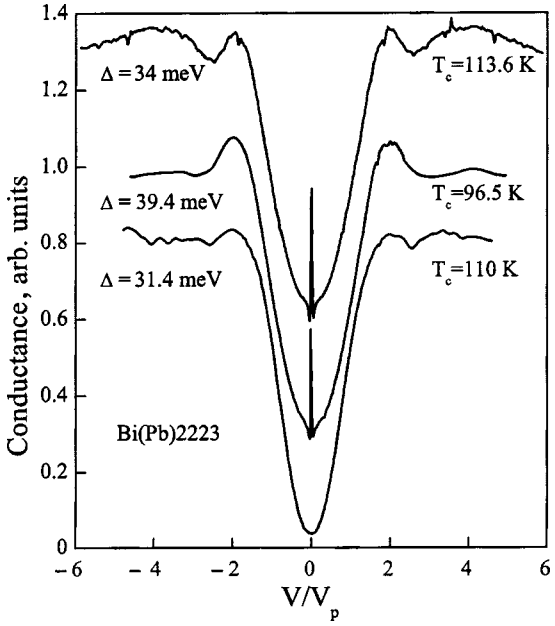

FIG. 6. S–I–S tunneling conductance in the *ab* plane for the Bi2223 samples of Fig. 1 at $T=77.4$ K. The voltage axis has been rescaled in units of Δ. Each curve has been rescaled and shifted for clarity.

For energies beyond the gap Δ value, tunneling in the *ab* plane of (BiPb)2223 S–I–S junctions revealed the so-called dip and hump structures, as shown in Fig. 2 and Fig. 6. In Fig. 6, the voltage axis is normalized to the voltage $eV_p=\Delta$, and the conductance axis is normalized to the background; the spectra are shifted vertically for clarity. The dip and hump features roughly scale with the gap Δ for different oxygen doping levels (see Fig. 7). There is, however, a slight deviation of the data from a straight line.

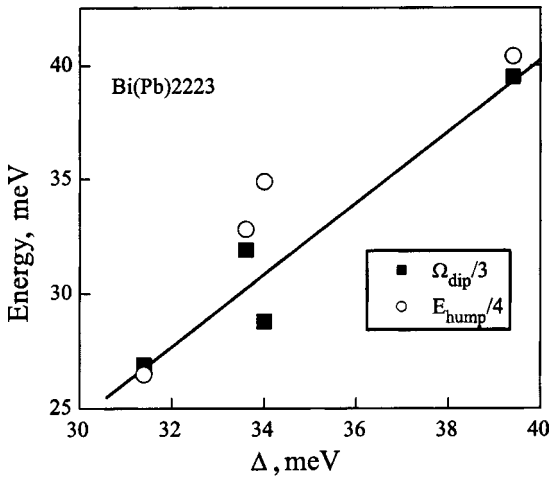

FIG. 7. Ω (dip) and E_p (hump) positions as a function of energy gap Δ, determined from the tunneling data of Figs. 2 and 6.

4. THEORETICAL IMPLICATIONS

The considerable interest in pseudogap investigation is stimulated to a great extent by the theoretical models of high-T_c superconductivity, in which a pseudogap appears as a precursor of the superconducting gap,[18,19] e.g., the bipolaron model.[20] In another group of models, the appearance of pseudogap is related to some sort of magnetic pairing.[21] However, the domains of applicability of these models are not very strictly defined, and it is quite possible that the pseudogap (like high-temperature superconductivity) is caused by several mechanisms acting simultaneously.

For example, in the Emerson–Kilverson–Zachar (EKZ) theory[19] the crucial role in the formation of high temperature superconductivity is ascribed to the separation of spin and charge, arising as a result of partitioning of the CuO_2 planes into narrow conducting and dielectric stripes. ''Pairing'' at $T^*>T_c$ in the EKZ model means the formation of a spin gap. A wide spin gap (or pseudogap Δ_p) is indeed formed in a spatially limited hole-free region, such as the region between the conducting stripes. A phase-coherent (i.e., actually superconducting) state is created only at $T<T_c$. The model explains well the smooth transition of the pseudogap into the tunneling gap Δ when the temperature decreases below T_c. However, the observed temperature dependence of the order parameter gap $\Delta(T)$ at $T<T_c$ is fundamentally different from that of the gap $\Delta_s(T)$, as is seen in Figs. 3 and 5. It is not clear how the BCS-like $\Delta_s(T)$ dependence arises in the phase-fluctuation picture. Such a situation would be possible, e.g., in the generation of charge (and spin) density waves, with the superconducting gap and pseudogap competing for the same region of the Brillouin zone.[22] Then the transition to the superconducting state could occur in the presence of a pseudogap in normal excitations, opening, e.g., in the electron-hole channel (i.e., a pseudogap, which would not transform directly into the superconducting gap, as in the Emery—Kivelson model).

There are numerous experiments[23–25] that confirm the essentially different nature of the superconducting gap Δ_s and the gap (pseudogap) Δ. The most convincing are intrinsic *c*-axis tunneling experiments (in stacked layers).[26] However, they yield different results from the point contact, scanning tunneling spectroscopy (STM), and break junction experiments: the hump was observed at an energy of 2Δ instead of 4Δ. The authors note a similarity between the observed *c*-axis pseudogap and Coulomb pseudogap for tunneling into a two-dimensional electron system. In our case, the tunneling and Andreev reflection were realized in the *ab* plane, and together with the $\Delta(T)$ dependence (Fig. 4), we clearly observed the peak–dip–hump structure (Figs. 2 and 3). The position of the dip and hump for S–I–S junctions was at 3Δ and 4Δ (Fig. 2). This suggests that the observed dip-hump structure may originate from short-range magnetic correlations in the *ab* plane.[27] Then the gap Δ would be the fermionic excitation gap and Δ_s-the mean-field order parameter. It should be emphasized, finally, that the observed $\Delta_s(T)$ dependence exhibits non-BCS behavior at $T\to 0$ (Fig. 3).

In summary, our *ab*-plane tunneling and Andreev spectroscopy studies of normal and slightly overdoped (BiPb)2223 and Bi2212 compounds show the presence of both a superconducting energy gap Δ_s, corresponding to *d*-wave Cooper pairing, and a dip-hump structure at 3Δ and 4Δ (for the S–I–S junction). This suggests that the high-energy pseudogap, which is associated with the dip and hump, could be magnetic in origin. The gap Δ is nearly temperature independent and becomes blurred above T_c, being continuously transformed with increasing temperature into the pseudogap. In contrast, the order parameter gap $\Delta_s(T)$ has a strong temperature dependence and for $T\to 0$ reveals a non-BCS mean field behavior. Our findings are in general agreement with those of Deutscher,[25] although it must be emphasized again that we have considered the slightly overdoped case.

This work was supported by Polish Government (KBN) Grant No. PBZ-KBN-013/T08/19.

*E-mail: abala@ifpan.edu.pl
†Deceased.

[1] T. Timusk and B. Statt, Rep. Prog. Phys. **62**, 61 (1999).
[2] T. Tohoyama and S. Maekawa, Supercond. Sci. Technol. **13**, R17 (2000).
[3] Ch. Renner, B. Revaz, J.-Y. Genoud, K. Kadowaki, and Ø. Fischer, Phys. Rev. Lett. **80**, 149 (1998).
[4] A. F. Andreev, Sov. Phys. JETP **19**, 1228 (1964).
[5] E. L. Wolf, *Principles of Electron Tunneling Spectroscopy*, Oxford University Press, New York (1985).
[6] J. L. Tallon and G. V. M. Williams, Phys. Rev. Lett. **82**, 3725 (1999).
[7] M. A. Subramanian, C. C. Torardi, J. C. Calabrese, J. Gopalakrishnan, K. J. Morrissey, T. R. Askew, R. B. Flippen, U. Chowdhry, and A. W. Sleight, Science **239**, 1015 (1988).
[8] A. I. Akimenko, T. Kita, J. Yamasaki, and V. A. Gudimenko, J. Low Temp. Phys. **107**, 511 (1997).
[9] A. I. D'yachenko, V. Yu. Tarenkov, R. Szymczak, A. V. Abal'oshev, I. S. Abal'osheva, S. J. Lewandowski, and L. Leonyuk, Phys. Rev. B **61**, 1500 (2000).
[10] V. M. Svistunov, V. Yu. Tarenkov, A. I. Dyachenko, and R. Aoki, Physica C **314**, 205 (1999).
[11] Y. Tanaka and S. Kashiwaya, Phys. Rev. Lett. **74**, 3451 (1995).
[12] A. M. Cucolo, A. I. Akimenko, F. Bobba, and F. Giubileo, Physica C **341–348**, 1589 (2000).
[13] A. I. Akimenko, R. Aoki, H. Murakami, and V. A. Gudimenko, Physica C **319**, 59 (1999).
[14] A. I. D'yachenko, *private communication* (2002).
[15] T. M. Klapwijk, G. E. Blonder, and M. Tinkham, Physica B **109–110**, 1657 (1982).
[16] M. R. Norman, H. Ding, M. Randeria, J. C. Campuzano, T. Yokoya, T. Takeuchi, T. Takahashi, T. Mochiku, K. Kadowaki, P. Guptasarma, and D. G. Hinks, Nature (London) **392**, 157 (1998).
[17] G. E. Blonder, M. Tinkham, and T. M. Klapwijk, Phys. Rev. B **25**, 4515 (1982).
[18] V. J. Emery and S. A. Kivelson, Phys. Rev. Lett. **74**, 3253 (1995); Nature (London) **374**, 434 (1995).
[19] V. J. Emery, S. A. Kivelson, and O. Zachar, Phys. Rev. B **56**, 6120 (1997).
[20] A. S. Alexandrov, Philos. Trans. R. Soc. London, Ser. A **356**, 197 (1998) (and references therein).
[21] P. W. Anderson, *The Theory of Superconductivity in the High-T_c Cuprate Superconductors*, Princeton University Press, Princeton (1997).
[22] R. S. Markiewicz, C. Kusko, and V. Kidambi, Phys. Rev. B **60**, 627 (1999).
[23] Q. Chen, K. Levin, and I. Kosztin, Phys. Rev. B **63**, 184519 (2001).
[24] V. V. Kabanov, J. Demsar, B. Podobnik, and D. Mihailovic, Phys. Rev. B **59**, 1497 (1999).
[25] G. Deutscher, Nature (London) **397**, 410 (1999).
[26] V. M. Krasnov, A. Yurgens, D. Winkler, P. Delsing, and T. Claeson, Phys. Rev. Lett. **84**, 5860 (2000).
[27] N. Miyakawa, J. F. Zasadzinski, L. Ozyuzer, P. Guptasarma, D. G. Hinks, C. Kendziora, and K. E. Gray, Phys. Rev. Lett. **83**, 1018 (1999).

This article was published in English in the original Russian journal. Reproduced here with stylistic changes by AIP.

Temperature dependence of the critical current of YBCO–STO–LCMO heterostructures near T_c

V. A. Khokhlov, A. Yu. Prokhorov,* V. F. Drobotko, and G. G. Levchenko

A. A. Galkin Donetsk Physicotechnical Institute, ul. R. Lyuksemburg 72, 83114 Donetsk, Ukraine

P. N. Mikheenko, R. Chakalov, and C. Muirhead

Department of Physics, The University of Birmingham, Birmingham B15 2TT

(Submitted May 27, 2002; revised September 5, 2002)
Fiz. Nizk. Temp. **29**, 156–160 (February 2003)

The complex differential susceptibility of a YBCO film and YBCO–STO–LCMO structures with different thicknesses of the STO layer (0, 2, and 7 nm) is investigated. It is shown that for a YBCO–LCMO structure the temperature of the superconducting transition T_{onset} and the critical current density j_c are observed to decrease in comparison with a pure YBCO film. In a YBCO–STO–LCMO structure, on the contrary, T_{onset} increases, while j_c increases for the structure with the 2 nm thickness of STO and decreases for that with 7 nm of STO. It is conjectured that there is a change of the vortex pinning mechanism as the temperature is lowered. © *2003 American Institute of Physics.* [DOI: 10.1063/1.1542409]

This paper is devoted to an experimental study of ferromagnet–insulator–superconductor ($F-I-S$) heterostructures with a YBCO film, which can have several factors that influence the superconducting properties of the latter:

1. In the case of direct $F-S$ contact, the strong exchange field in the ferromagnet suppresses the order parameter of the superconductor on account of the proximity effect. The attraction between electrons creates singlet pairs in the superconductor, and the exchange interaction, which leads to ferromagnetism, tends to align the electron spins parallel to each other. Therefore, when the Zeeman energy of an electron pair in the superconductor in the exchange field J exceeds the binding energy of the pair, a measure of which is the superconducting gap Δ, the superconductivity is destroyed. Because of the proximity effect, a superconducting order parameter (SOP) can arise in the F layer of an $F-S$ layered system. Here the term ''proximity effect'' is taken to mean the partial transfer of superconducting properties to a normal metal F brought into contact with a superconductor.[1] This effect has its roots in the large spatial extent of the wave function of the Cooper pairs, which penetrates from the S layer into the F layer (or a layer of nonferromagnetic metal) a certain distance, depending on the transparency of the interface. Because of this there occurs a ''collectivization'' of the electron–electron interactions responsible for the superconducting transition in the $F-S$ system. As a result, in this system the transition temperature T_c of the superconductor becomes lower than the temperature T_{cs} of the superconductor without the F layer. This is discussed in more detail in several reviews.[2,3]

2. In $F-I-S$ heterostructures a self-injection of quasiparticles from the superconductor into the ferromagnet has been noted.[4] The prevailing pair symmetry $d_{x^2-y^2}$ in YBCO[5] admits low-energy excitations, and an appreciable number of quasiparticles always exist in the YBCO. Because of the large extent of the wave function of the Cooper pairs, even in the presence of a thin insulating layer one should observe a decrease of T_c in comparison with T_{cs} and a decrease of the critical current j_c. Furthermore, in such structures there is an impedance mismatch for heat transfer and electrotransport at the boundary between the different kinds of materials, so that a chemical potential difference $\delta\mu$ exists between the F and S layers, promoting the diffusion of quasiparticles from S into F.[4]

3. A thin ferromagnetic film deposited on a superconductor breaks up into domains. The fringe fields of the domain structure in the ferromagnetic film can: a) destroy the superconductivity in a region of the order of the width of a domain wall if the magnetization in the ferromagnetic wall is large and lies in its plane and the domain wall is of the Néel type (e.g., yttrium–iron garnet); b) create regions in the superconducting film which not only can be sites of localization of pre-existing vortices owing to the electromagnetic interaction with the fringe fields but can also be sources of nucleation of vortex–antivortex pairs beneath domains of opposite magnetization.[6]

To elucidate the influence of the above-mentioned factors on the superconducting properties of YBCO films we carried out dynamic response measurements. Heterostructures are usually investigated in the temperature region $T/T_c<0.95$, by measuring the magnetization or the current–voltage (I–V) characteristics. Here, however, we investigated the heterostructures near T_c ($T/T_c\geqslant 0.98$) by measuring the complex susceptibility. Here $T_c=T_{\text{onset}}$ is the temperature at which the dynamic response appears, which is equal to the temperature at which the resistance of the superconductor becomes practically zero (the criterion used is $I=1$ mA, $U=1$ μV). In this range of temperatures the pinning potential due to the dislocation structure of the sample is small, and the ferromagnetic layer above the film should have a significant influence on j_c.

Four YBCO films were deposited simultaneously by laser ablation on a substrate of $SrTiO_3$ (STO). One of the YBCO samples was kept as a control, and the others had

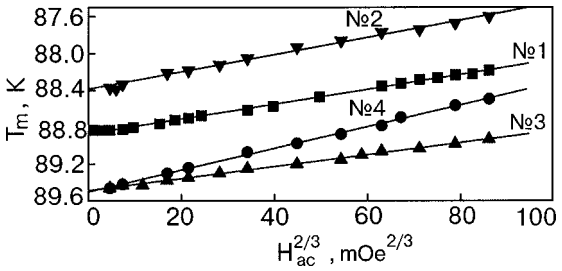

FIG. 1. Dependence of the temperature of the diamagnetic susceptibility peak on the exciting field for the four structures studied.

TABLE I. Values of the critical current and temperature of the onset of the diamagnetic response for the four heterostructures.

№ пленки	$J_c(0)$, 10^7 A/см^2	$J_c(77\,\mathrm{K})$, 10^6 A/см^2	T_{onset}, K
1	9,7	4,7	89,20
2	8,1	3,7	88,75
3	15,8	8,2	89,62
4	5,6	2,8	89,70

layers of $La_{0.7}Ca_{0.3}MnO_3$ (LCMO) and STO deposited on them: film No. 1—YBCO (100 nm); No. 2—YBCO (100 nm)–LCMO (100 nm); No. 3—YBCO (100 nm)–STO (2 nm)—LCMO (100 nm); No. 4—YBCO (100 nm)–STO (7 nm)–LCMO (100 nm).

Only quasiparticles having spin parallel to the majority of spins in the ferromagnet can tunnel from *S* into *F* through the barrier, leaving behind a spin-polarized quasiparticle. Tunneling of this kind makes it possible for further breaking of Cooper pairs to occur and lowers j_c. We therefore chose as the ferromagnet the manganite $La_{0.7}Ca_{0.3}MnO_3$, which has nearly 100% spin polarization (in comparison, Fe, Co, Ni, and Permalloy have spin polarizations of 44, 43, 11, and 40%, respectively).[7,8]

In the present study we have measured the differential complex magnetic susceptibility $\chi=\chi'-i\chi''$ in the Earth's magnetic field at exciting fields $H_{ac}=5\times10^{-3}-0.8$ Oe.

The dependence $T_m(H_{ac}^{2/3})$ [T_m is the temperature of the maximum on the $\chi''(T)$ curve] for all four samples is plotted in Fig. 1. At a fixed amplitude of the exciting field H_{ac} and at the temperature T_m of the maximum on the $\chi''(T)$ curve, one can determine the critical current density according to the theory of the critical state, using the formula[9]

$$j_c(T_m)=\frac{6.4\ H_{ac}}{\pi 2.474 d}. \tag{1}$$

Here H_{ac} is in oersteds, d is the film thickness in centimeters, and j_c is in A/cm^2. Since the dependence of T_m on H_{ac} is linear in the coordinates $T_m(H_{ac}^{2/3})$, the temperature dependence of $j_c(T)$ should be of the form

$$j_c(T)=j_c(0)\left(1-\frac{T}{T_c}\right)^{3/2}, \tag{2}$$

where T_c is the temperature to which the function $T_m(H_{ac}^{2/3})$ tends for $H_{ac}=0$. In the temperature range investigated there is significant flux creep. Unfortunately, there are no formulas relating the function $j_c(T)$ to T_m and H_{ac} with the flux creep taken into account, and we have therefore used the formulas given above. Because of this, the absolute values of $j_c(0)$ and $j_c(77\,\mathrm{K})$ obtained by the dynamic complex-susceptibility method will differ from the data of static measurements of the current–voltage characteristics or magnetic moment **m** by a coefficient proportional to the frequency of the exciting field. However, these differences do not reflect on the trends noted in the experiment.

The values of $j_c(0)$, $j_c(77\,\mathrm{K})$, and T_{onset} are presented in Table I.

We note the following trends:

1. Compared to the pure YBCO film, T_{onset} is almost 0.5 K lower for film No. 2 (YBCO–LSMO) and about the same amount higher for films Nos. 3 and 4.

2. For films Nos. 2 and 4 the values of $j_c(0)$ and $j_c(77\,\mathrm{K})$ are lower than for the pure YBCO film, while for film No. 3, with a 2-nm thick STO spacer layer between the YBCO and LCMO, they are significantly higher. These results disagree with those of Ref. 4, in which a decrease of j_c in comparison with a pure YBCO film was observed at an STO spacer thickness of 2 nm.

Before discussing the values of $j_c(0)$ and $j_c(77\,\mathrm{K})$, let us estimate the sizes of the vortices and of the potential wells acting as vortex pinning centers in the temperature range of this study. It is customarily assumed that the large values of $j_c(77\,\mathrm{K})$ ($\sim10^6$ A/cm^2) in YBCO films grown by laser ablation are due to the fact that they have a high density of edge and screw dislocations, which act as vortex pinning centers. According to Ref. 10, the elastic strains created in an anisotropic crystal by edge dislocations or a dislocation ensemble (e.g., a wall of dislocations) extend a distance **r** of around 2 nm from the dislocation core.[11] This strain field around a dislocation will decrease the order parameter in that region and acts as a potential well for a vortex. An estimate of the size L of the potential well according to the formulas of Ref. 10 gives a value ~40 nm in our temperature range, and the potential well is much less steep than at low temperatures.[12] The size of the vortex, which is given by $d=2\xi=2\xi_0/(1-T/T_c)^{1/2}$, where ($\xi_0\approx1.2$ nm), is ≈20 nm. A potential well can readily pin a vortex if its size is comparable to that of a vortex. From the above estimates for L and d we can see that at high temperatures the potential wells created by dislocations are no longer effective pinning centers for vortices. At a dislocation density of the order of 10^{11} lines/cm^2 in YBCO films,[13] the surface of the film probably presents a strain field ''speckled'' with mutually interfering and not very steep edges of the potential wells. Such a field does not pin vortices effectively. There must be some other reasons for the higher critical currents at high temperatures for film No. 3 and the slight drop in j_c in sample No. 2 in comparison with the pure YBCO film.

Roughness of the film surface can cause substantial vortex pinning, especially at high temperatures. The superconductor in all four samples is a thin YBCO film (100 nm thick). As we know,[14] the vortex pinning in superconducting films is made up of surface, interfacial, and bulk pinning. The thinner the film, the greater the role of surface pinning. Preliminary investigations for a large number of YBCO films

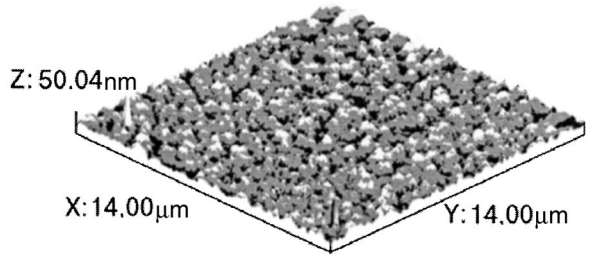

FIG. 2. AFM image of the pure YBCO film (sample No. 1).

showed that there is a correlation between the critical current density and the surface roughness of the film. Figure 2 shows an atomic force microscope (AFM) image of a clean YBCO film. It is seen that the islands have a height of around 20 nm, i.e., ~20% of the thickness of the film. The distance between islands is of the same order. Since the energy of a vortex is proportional to its length, a vortex prefers to be found in a ''valley,'' especially since dislocations arise at the spiral growth boundaries of the islands.[15] The size of the ''valleys'' is close to that of the vortices at high temperatures, and they can be good pinning centers.

Another cause of localization and nucleation of new vortex–antivortex pairs, as we pointed out in the Introduction, can be the fringe field of the domain structure of the LCMO. However, the LCMO domain structure observed in Ref. 16 consisted of large domains (several microns) with magnetic moments normal to or inclined from the normal to the film, and the domain walls between them are of the same order of magnitude. In such a case the fringe fields of the domains are too small to be efficient pinning centers.

Let us discuss the results.

1. While the decrease of T_{onset} in structure No. 2 in comparison with the pure YBCO film (see Table I) can be explained by the circumstance that the superconducting correlations induced by the YBCO film are destroyed by the exchange field of LSMO, the increase in T_{onset} for films Nos. 3 and 4 in comparison with the pure YBCO film (No. 1) is not completely understood. This effect may possibly be explained as follows. A YBCO film in contact with air after deposit loses oxygen. If a film of the insulator STO is deposited on the film, these losses do not occur (or are sharply diminished), and T_c corresponds to the value obtained in the deposition chamber.

2. The lowering of j_c at high temperatures in structure No. 2 in comparison with the pure YBCO film is not very significant. The cause of this might lie in the fact that the substrate temperature during deposition of the films was 760–780 °C, i.e., the diffusional range was rather large. Because of this, some of the LCMO molecules penetrated deeper into the YBCO film, creating additional pinning centers. In thin YBCO films the critical current is determined by the pinning of the vortex structure. The LCMO exchange field leads to a partial destruction of the superconducting correlations induced by the YBCO film and hence to a decrease of j_c. At the same time, the appearance of strong new pinning centers because of the ferromagnetic inclusions that have diffused into the YBCO film should lead to an increase in j_c. The competition between these two effects probably leads to a slight increase in j_c in film No. 2 in comparison with the pure YBCO film.

3. The increase of the critical current at high temperatures in heterostructure No. 3 in comparison with the pure YBCO film can probably be attributed to the circumstance that the insulating layer in this structure is only 2 nm thick and is not continuous but perforated. The degree of continuity of the coating depends on the roughness of the film and on the growth conditions. In this structure the diffusion of LCMO into the YBCO film is much less than in the case of direct LCMO–YBCO contact (film No. 2), and the decrease of j_c is determined by the degree of transparency of the interface between LCMO and YBCO. The ''needles'' of the ferromagnet LCMO that penetrate through the pores of the STO can create fringe fields of rather small spatial size, capable of pinning vortices. We note that these penetrating ''needles'' can have ''up'' or ''down'' magnetization because of the domain structure of the demagnetized LCMO layer. The interaction of differently magnetized ''needles'' with vortices of identical polarity causes the vortices to concentrate near the needles with magnetization antiparallel to the magnetization of the vortices. Such a picture was observed in Ref. 15 when ferromagnetic droplets 0.4 μm in diameter were deposited on a Pb film. The mechanism described above is probably what causes the increase in $j_c(0)$ and $j_c(77\ \text{K})$, which are obtained by extrapolation. At low temperatures, when the potential wells of the edge and screw dislocations become deep and narrow, those wells begin to give the main contribution to j_c, and the influence of the magnetized ''needles,'' which are considerably fewer in number than the dislocations, is sharply reduced.

4. In the case of a 7-nm thick insulating spacer layer between LCMO and YBCO (sample No. 4) the STO layer is now continuous, and there is no diffusion of LCMO into the YBCO film, nor are there any ferromagnetic ''needles'' penetrating into the YBCO film. The decrease of j_c in this case can again be explained by the circumstance that the superconducting correlations induced by the YBCO film are destroyed by the LCMO exchange field to a degree that depends on the transparency of the interface. At the same time, the value of the critical current in this film is lower than in film No. 2, in which there is direct LCMO–YBCO contact, where the transparency of the interface should be higher and j_c should accordingly be lower (see Table I). It seems likely that this discrepancy can only be explained by the diffusion of LCMO particles into the YBCO film, which creates additional strong pinning centers. Thus for film No. 4 one observes the direct influence of the LCMO exchange field on the superconducting properties of the YBCO film.

In summary, the results of our studies lead us to conclude that the magnetic behavior of $F–I–S$ heterostructures is the result of a competition between the suppression of superconductivity in the YBCO film due to the circumstance that the superconducting correlations induced in the YBCO film are destroyed by the LCMO exchange field and the contrary increase in j_c due to the circumstance that ferromagnetic inclusions form potential wells of a size close to that of the vortices at high temperatures. These ferromagnetic inclusions, like the LCMO ''needles'' that penetrate into the YBCO film in the case of a ''perforated'' STO insulating

layer, are strong centers of vortex pinning on account of their purely magnetic interaction with the vortices. The role of ferromagnetic inclusions and ''needles'' (in the case of a perforated insulating layer) in the pinning of vortices having a large size for $T \rightarrow T_{\text{onset}}$ decreases with decreasing temperature, while the role of dislocations in the pinning of vortices, on the contrary, increases. Thus with decreasing temperature there is a change of the dominant mechanism of vortex pinning.

*E-mail: ayup@ua.fm

[1] P. G. de Gennes, Rev. Mod. Phys. **36**, 225 (1964).
[2] B. Y. Jin and J. B. Kettorson, Adv. Phys. **38**, 189 (1989).
[3] Yu. A. Izyumov, Yu. N. Proshin, and M. G. Khuseĭnov, Usp. Fiz. Nauk **172**, 113 (2002).
[4] N. C. Yen, R. P. Vasquez, C. C. Fu, A. V. Samoilov, Y. Li, and K. Vakili, Phys. Rev. B **60**, 10522 (1999).
[5] M. Johnson and R. H. Silbce, Phys. Rev. Lett. **55**, 1970 (1985); Phys. Rev. B **35**, 4957 (1987).
[6] Yu. I. Bezpyatnykh, V. Vasilevskiĭ, A. I. Buzdin, and L. N. Bulaevskiĭ, Adv. Phys. **34**, 176 (1985); Zh. Éksp. Teor. Fiz. **94**, 256 (1988) [*sic*].
[7] M. M. Goldman, V. A. Vas'ko, P. A. Kraus, K. R. Nikolaev, and V. A. Larkin, J. Magn. Magn. Mater. **200**, 69 (1999).
[8] R. M. Stroud, J. Kim, C. R. Eddy, D. B. Chrisley, J. S. Horwitz, D. Koller, M. S. Osofsky, R. J. Soulen, and R. C. Y. Auyeung, J. Appl. Phys. **83**, 7189 (1988).
[9] E. H. Brandt, Phys. Rev. B **55**, 14513 (1997).
[10] A. Gurevich and E. A. Pashitskii, Phys. Rev. B **56**, 6213 (1997).
[11] Y. Gao, K. L. Merkle, G. Bai, H. L. M. Chang, and D. J. Lam, Physica C **174**, 1 (1991).
[12] V. M. Pan, UFM **1**, 3 (2000).
[13] V. Svetchnikov, V. Pan, Ch. Traeholt, and H. W. Zandbergen, IEEE Trans. Appl. Supercond. **AS-7**, 1396 (1997); S.-W. Chan, J. Phys. Chem. Solids **55**, 1415 (1999).
[14] R. Prozorov and E. B. Sonin, Phys. Rev. B **57**, 13845 (1999).
[15] B. Dam, J. M. Huijbregtse, F. C. Klaassen, and R. C. F. van der Geest, Nature (London) **339**, 439 (1999).
[16] Q. Lu, C. C. Chen, and A. Lozanne, Science **276**, 2006 (1997).

Translated by Steve Torstveit

ELECTRONIC PROPERTIES OF METALS AND ALLOYS

Observation of the strain-driven charge-ordered state in a $La_{0.7}Ca_{0.3}MnO_{3-\delta}$ thin film with oxygen deficiency

V. G. Prokhorov,* V. A. Komashko, and G. G. Kaminsky

Institute of Metal Physics, National Academy of Sciences of Ukraine, 36 Vernadsky Ave., Kiev, 03142, Ukraine

V. L. Svetchnikov and H. W. Zandbergen

NCHREM, Rotterdamseweg 137, 2628AL, Delft, The Netherlands

Y. P. Lee and J. S. Park

Department of Physics, Hanyang University, Seoul, 133-791 Korea

K. W. Kim

Department of Physics, Sunmoon University, Choongnam, 336-840 Korea

(Submitted May 31, 2002)
Fiz. Nizk. Temp. **29**, 161–168 (February 2003)

The magnetic and transport properties of $La_{0.7}Ca_{0.3}MnO_{3-\delta}$ films with an oxygen deficiency ($\delta \simeq 0.1$) and a $La_{0.9}Ca_{0.1}MnO_3$ film with the stoichiometric oxygen content are investigated in a wide temperature range. It is shown that the charge-ordered insulating (COI) state is observed for a $La_{0.7}Ca_{0.3}MnO_{2.9}$ film with thickness $d \leqslant 30$ nm, which manifests mainly a cubic crystal structure with an anomalously small lattice parameter for this composition. An increase in the film thickness ($d \simeq 60$ nm) leads to a structural transition from the lattice-strained cubic to the relaxed rhombohedral phase and is accompanied by a shift of the Curie point (T_C) to lower temperature and a frustration of the COI state. The magnetic and transport properties of the $La_{0.7}Ca_{0.3}MnO_{2.9}$ film with $d \simeq 60$ nm are similar to those exhibited by the optimally oxygen-doped $La_{0.9}Ca_{0.1}MnO_3$ film. It is concluded that the formation of the COI state in the $La_{0.7}Ca_{0.3}MnO_{3-\delta}$ compound is governed by a compression of the crystal lattice rather than accumulation of oxygen vacancies, the low doping of the substituted divalent ions, or electronic phase separation. [DOI: 10.1063/1.1542410]

1. INTRODUCTION

The hole-doped perovskite manganites are of great current interest not only because of their interesting fundamental science, connected with the discovery of colossal magnetoresistance (CMR), but also in connection with their potential applications to new devices such as magnetic read heads, field sensors, and memories. Recently evidence was presented for the coexistence at low temperatures of ferromagnetic metallic (FMM) and charge-ordered insulating (COI) phases in $La_{0.67}Ca_{0.33}MnO_3$ films, governed by the lattice strains accumulated during the deposition.[1,2] That is contradicted by the common knowledge that the phenomenon of charge ordering (CO) is observed only in compounds with a small average *A*-site cation radius, $\langle r_A \rangle \leqslant 0.118$ nm. However, in view of the very similar energies of the COI and FMM states in these compounds,[3] one might expect the appearance of COI regions in a compound with a larger $\langle r_A \rangle$ induced by a structural distortion away from the ideal cubic perovskite lattice.[2] It is believed that the stoichiometric compound $LaMnO_3$ (Mn^{3+};$t_{2g}^3 e_g^1$) is antiferromagnetic due to the superexchange coupling between Mn^{3+} ions. A partial substitution of the trivalent La^{3+} by divalent Ca^{2+} ions is balanced by a conversion of the Mn valence states between Mn^{3+} and Mn^{4+}, which leads, first, to an increase of the Curie point (T_C) and, second, to the formation of the FMM state in the temperature range $T \leqslant T_C$ at a certain concentration of Ca. However, a change in the Mn^{3+}:Mn^{4+} ratio can be produced by the creation of vacancies at the oxygen sites, as well. The oxygen deficiency leads to a degradation in the Curie point and in the temperature of the metal-insulator (MI) transition, providing the formation of the COI state in the manganites.[4–11] The other point of view is based on the idea of the electronic phase separation between phases with different hole densities in the low-doped manganites, which can also induce the coexisting nano-scale metallic and insulating clusters.[12] Therefore, it is not clear what is the main reason for the appearance of the COI state in these materials-lattice strains, oxygen vacancies, or low doping of the substituted divalent ions.

In this paper we report experimental results for $La_{0.7}Ca_{0.3}MnO_{3-\delta}$ films with an oxygen deficiency ($\delta \simeq 0.1$) and $La_{0.9}Ca_{0.1}MnO_3$ film with the stoichiometric oxygen content. It was found that the COI state is observed only for $La_{0.7}Ca_{0.3}MnO_{2.9}$ films with thickness $d \leqslant 30$ nm,

which manifest mainly a cubic crystal structure with an anomalously small lattice parameter for this composition. The increase in the film thickness ($d \simeq 60$ nm) leads to a structural transition from the lattice-strained cubic to the relaxed rhombohedral phase, which is accompanied by a shift of the Curie point to lower temperature and a frustration of the COI state. The magnetic and transport properties of the $La_{0.7}Ca_{0.3}MnO_{2.9}$ film with $d \simeq 60$ nm become similar to those exhibited by the optimally oxygen-doped $La_{0.9}Ca_{0.1}MnO_3$ film. Therefore the formation of the COI state in the $La_{0.7}Ca_{0.3}MnO_{3-\delta}$ compound is governed by a compression of the crystal lattice rather than accumulation of oxygen vacancies, the low doping of the substituted divalent ions, or electronic phase separation.

2. EXPERIMENTAL TECHNIQUES

All the films were prepared by rf magnetron sputtering using a so-called "soft" (or powder) target.[13] The total pressure in the chamber was $5 \cdot 10^{-2}$ Torr, with a gas mixture of Ar and O_2 (3:1). The substrate was a $LaAlO_3$ (001) single crystal with a lattice parameter $a \simeq 0.379$ nm for the pseudocubic symmetry. The substrate temperature during deposition was 750 °C. Under these conditions we deposited two $La_{0.7}Ca_{0.3}MnO_{3-\delta}$ films with different thickness: $d \leqslant 30$ nm (LCM1) and $d \simeq 60$ nm (LCM2). The stoichiometric $La_{0.9}Ca_{0.1}MnO_3$ (LCM3) film with $d \simeq 60$ nm was made by additional postannealing at 800 °C in 1-atm O_2 for 1.5 h. The θ–2θ x-ray diffraction (XRD) patterns were obtained using a Rigaku diffractometer with CuK_α radiation. The lattice parameters evaluated directly from the XRD data were plotted against $\cos^2\theta/\sin\theta$. With an extrapolated straight line to $\cos^2\theta/\sin\theta = 0$, a more precise determination of the lattice parameter was obtained. The high-resolution electron microscopy (HREM) studies were carried out using a Philips CM300UT-FEG microscope with a field emission gun operated at 300 kV. The point resolution of the microscope is of the order of 0.12 nm. Cross-section specimens were prepared by the standard techniques using mechanical polishing followed by ion-beam milling under grazing incidence. The resistance measurements were carried out by the four-point-probe method in a temperature range of 4.2–300 K and a magnetic field up to 5 T. The magnetization in a field up to 100 Oe were taken with a Quantum Design SQUID magnetometer in a temperature range of 4.2–300 K.

3. MICROSTRUCTURE OF THE FILMS

Figure 1a presents the (002) Bragg peaks for the LCM1 (*1*), LCM2 (*2*), and LCM3 (*3*) films. It is seen that the LCM2 and LCM3 films display only one peak, which corresponds to an out-of-plane lattice parameter for the cubic symmetry c of 0.3947 nm and 0.3923 nm, respectively. The thinner LCM1 film exhibits two Bragg peaks. The first of them (lower-intensity) indicates $c \simeq 0.394$ nm, which is almost coincident with the lattice parameters of the LCM2 and LCM3 films. The second is located very close to the substrate peak and corresponds to $c \simeq 0.3795$ nm. Figures 1a and 1b show the high-angle peaks of the (002) and (003) reflections, respectively, in detail for the LCM1 film. It is noteworthy that a similar asymmetry of the substrate Bragg peak was observed recently by Li *et al.*,[9] but without discussion. Therefore, the XRD data attest that the LCM1 film contains two crystalline phases with different lattice parameters, in contrast to the LCM2 and LCM3 films. The first phase with a larger c belongs to a relaxed state of the crystal lattice for $La_{0.7}Ca_{0.3}MnO_{3-\delta}$ with oxygen deficiency (*A* phase). This interpretation is supported by the large value for the out-of-plane lattice parameter, which differs greatly from the stoichiometric one for this composition ($c \simeq 0.3849$ nm).[7] Using the empirical ratio between the oxygen deficiency δ and the out-of-plane lattice parameter,[11] we estimated the value of δ for the *A* phase to be $\delta \simeq 0.1$. The second crystalline phase (*B* phase), with an unusually small lattice parameter, in view of the large peak intensity can be considered as the primary peak of the LCM1 film. The small value for the lattice parameter is provided by epitaxial growth of the film and the accumulation of a biaxial compressive lattice strain. An increase in the film thickness leads to a recrystallization during deposition or cooling of the film and results in the disappearance of the *B* phase, which is inferred from the absence of the second Bragg peak (curve 2 in Fig. 1a). The estimated value for the oxygen deficiency of the LCM2 film is $\delta \simeq 0.11$ and is almost identical with that for the *A* phase of LCM1. Note that the results obtained coincide excellently with the published data for similarly oxygen-deficit films.[14]

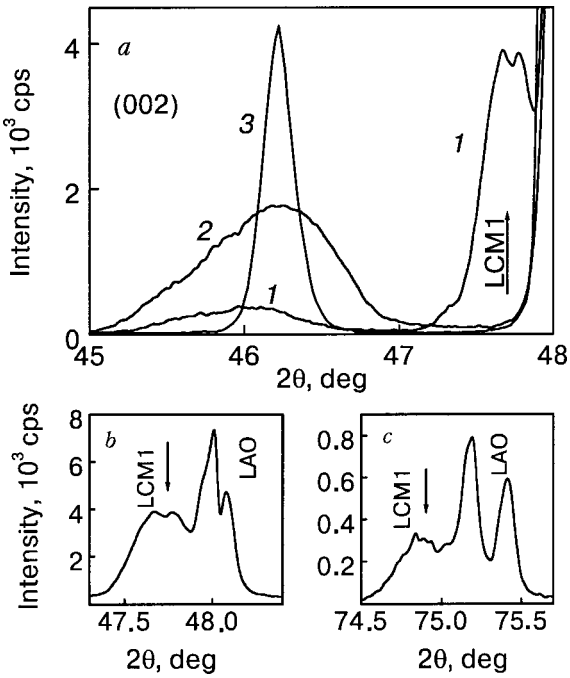

FIG. 1. a—The (002) XRD peaks for LCM1 (*1*), LCM2 (*2*), and LCM3 (*3*) films. b,c—the (002) and (003) peaks, respectively, of the LCM1 film.

The cross-section low-magnification HREM images of the films studied are shown in Fig. 2. They were obtained with the incident beam parallel to a cube direction of the substrate and parallel to the film/substrate interface. All films are epitaxial and exhibit sharp, flat, and well-defined interfaces. However, it is seen that the structure changes slightly for different films. The LCM1 film with smallest thickness (Fig. 2a) exhibits a perfect single-crystal structure. It shows uniform contrast; neither dislocations nor domains were observed. The LCM2 and LCM3 films (Figs. 2b and 2c, respec-

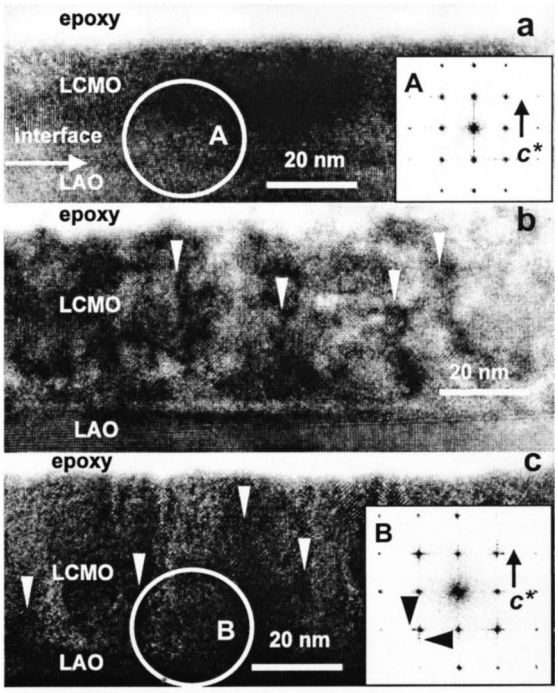

FIG. 2. Low-magnification HREM images of a cross section for LCM1 (a), LCM2 (b), and LCM3 (c) films. The insets are the FFT of the areas A and B containing the interface for the LCM1 and LCM3 films, respectively.

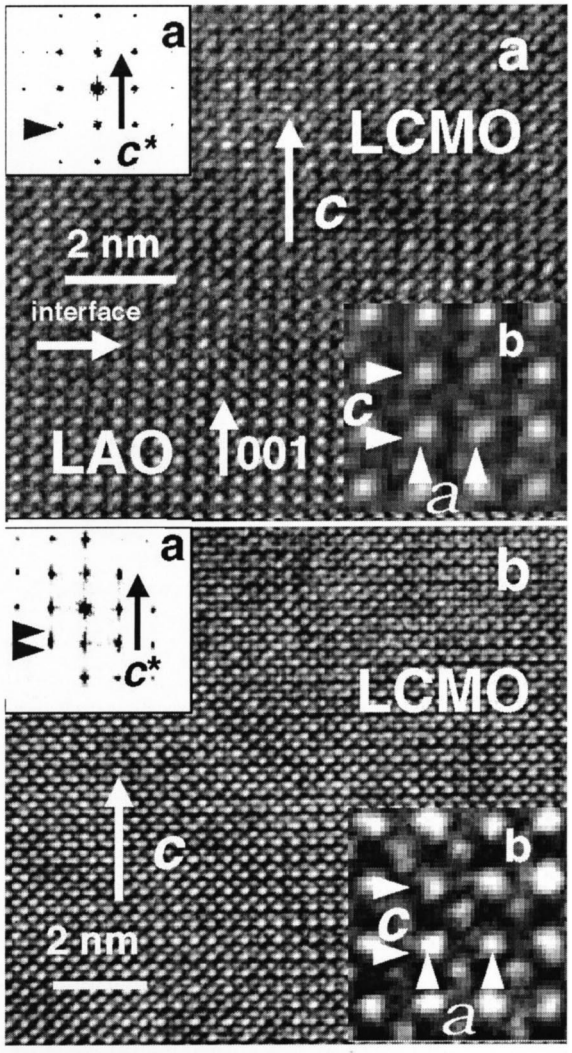

FIG. 3. HREM images of a cross section for LCM2 film near the interface (a) and 30 nm above it (b). The insets *a* are the FFT of the corresponding areas of the film. The insets *b* are high-magnification HREM images for the substrate (top) and the film (bottom).

tively) exhibit a set of regions with a slightly different brightness, which can be treated as the presence of crystalline domains separated by the lattice strain (shown by the white arrows).[15] Moreover, in the LCM2 film the dark contrast demonstrates the more or less disordered zones, suggesting the formation of chaotic domain structure, while in the LCM3 film the columnar microstructure occurs with columns parallel to the interface normal. The inset in Fig. 2a shows the fast Fourier transform (FFT) of the HREM image (area A) for the LCM1 film selected across the interface. It is seen that the FFT of an area containing the interface produces a rectangular pattern of the circled and unsplit spots. Therefore, the out-of-plane (c) and in-plane (a) lattice parameters are the same for both the substrate and the film. Their value is coincident with the XRD data for the *B* phase of the LCM1 film with the smallest lattice parameter $c \simeq 0.3795$ nm. A more detailed analysis of the HREM images of the LCM1 film shows that inclusions of the *A* phase with the lattice parameter $c \simeq 0.39$ nm are present near the top of the film.

The inset in Fig. 2c shows the FFT of the HREM image (area B) for the LCM3 film selected across the interface, as well. In this case the FFT pattern for the similar area containing the interface displays the spots elongated and slightly split in the c (along to the interface normal) and a (along to the interface) directions (shown by black arrows). One can conclude that the interface is incoherent in the LCM3 film, providing the difference in the lattice parameters of the substrate and the film. A similar FFT pattern was obtained for the area of the LCM2 film containing the interface, which is reproduced in inset *a* of Fig. 3a. In contrast to that, the FFT pattern for the area of the film located 30 nm above the interface exhibits spots elongated only in the c direction (see inset *b* in Fig. 3b). We attribute these features to the slight tetragonal deformation of the crystal lattice in the LCM2 film.

The insets *b* in Figs. 3a and 3b show high-magnification HREM images of LCM2 film for the substrate and the film, respectively. The brightest dots represent La(Ca) atoms in the film as well as in the substrate. The less bright dots at the centers of the squares of brightest dots represent AlO chains in the substrate and MnO chains in the film. The measurement of a large number of interdot spacings allow us to obtain the average values of the lattice parameters from the HREM images. According to an analysis one can conclude that the $LaAlO_3$ substrate has a pseudocubic crystal lattice with $c \simeq a \simeq 0.379$ nm and angle of the cell $\alpha_C \simeq 90°$, and the greater part of the LCM1 film has also a pseudocubic crystal lattice with $c \simeq a \simeq 0.379$ nm and $\alpha_C \simeq 90°$ (except for local areas near the top of the film, which have a rhombohedral crystal structure with $c \simeq a \simeq 0.39$ nm and $\alpha_C \simeq 90.4°$). The LCM2 and LCM3 films have a similar rhombohedral crystal structure with $c \simeq a \simeq 0.395$ nm and $\alpha_C \simeq 90.6°$, and $c \simeq a \simeq 0.391$ nm and $\alpha_C \simeq 90.6°$, respectively. It is seen that re-

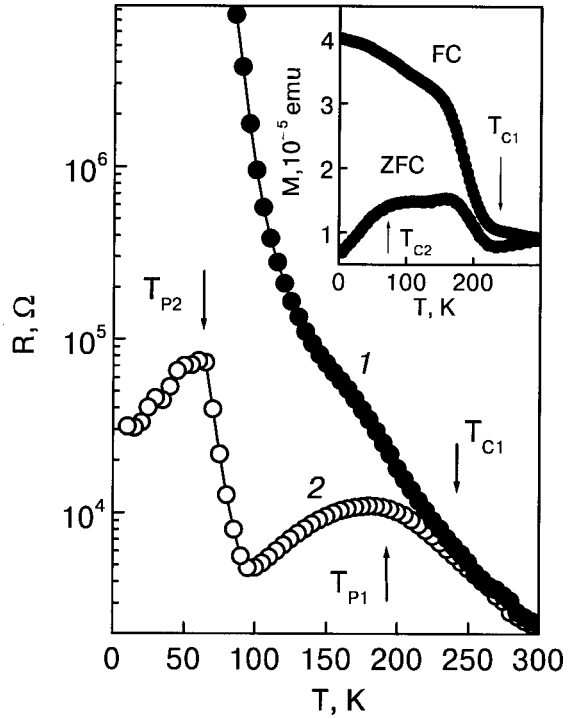

FIG. 4. Temperature dependence of the resistance of the LCM1 film without (*1*) and with (*2*) an applied magnetic field of 5 T. The lines are a guide to the eye. The inset displays the temperature dependence of the field-cooled and zero-field-cooled magnetization for this film.

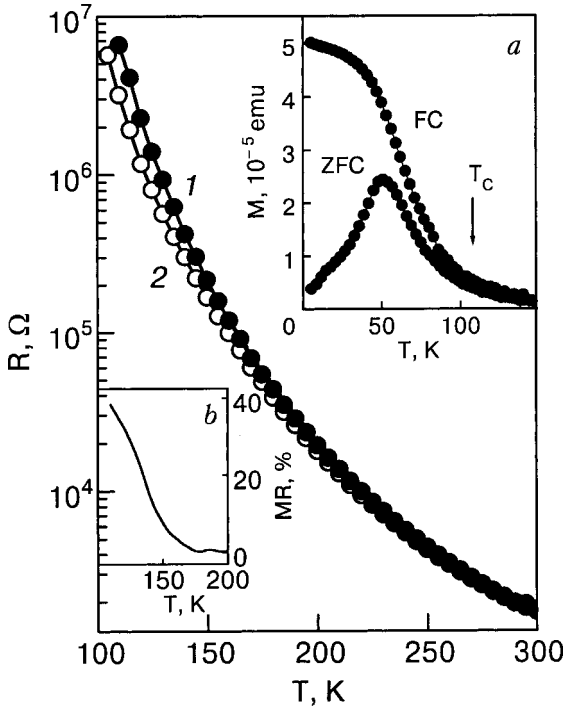

FIG. 5. Temperature dependence of the resistance of the LCM2 film without (*1*) and with (*2*) an applied magnetic field of 5 T. The lines are a guide to the eye. The inset *a* displays the temperature dependence of the FC and the ZFC magnetization. The inset *b* shows the temperature dependence of the magnetoresistance in an applied magnetic field of 5 T.

sults obtained agree very perfectly with the XRD data for the investigated films.

Therefore, both the cubic (*B*-phase) and the rhombohedral (*A*-phase) crystalline phases coexist in LCM1, while only the rhombohedral phase exists in LCM2 and LCM3. An estimation of the average crystallite size (D) using the Scherrer formula for the Bragg peak broadening shows that the LCM1 film consists of large grains ($D \approx 50$ nm) belonging to the *B* phase and small clusters ($D \approx 7-10$ nm) in the *A* phase. For LCM2 and LCM3 the average size of the crystallites turns out to be about $D \approx 10-12$ nm and 60 nm, respectively. The sizes obtained are supported by the peculiarities of the contrast in the HREM images (Fig. 2) and agree with the published results for thin films of similar compositions.[16,17] The large difference in crystallite size between the *A* and *B* phase indicates that the cubic *B* phase is formed directly during deposition, while the rhombohedral *A* phase is made during the recrystallization afterwards.

4. EXPERIMENTAL RESULTS

Figure 4 displays the temperature dependence of the resistance $R(T)$ for the LCM1 film without (*1*) and with (*2*) an applied magnetic field of 5 T. The magnetic field was directed at right angles to both the film surface and the transport current. The experimental curves attest to the existence of two phases with different temperatures for the MI transition in the applied magnetic field. The first phase undergoes a transition from the insulating to the metallike state at $T_{P1} \approx 200$ K, which agree perfectly with recently published results obtained for a similar thin film with oxygen stoichiometry.[2] The second phase manifests the MI transition at $T_{P2} \simeq 80$ K. In zero applied magnetic field both phases display an exponential growth of the resistance with decreasing temperature. Unfortunately, our setup was limited to 10^7 Ω and we could not measure $R(T)$ down to the lowest temperature. The inset in Fig. 4 reveals that both field-cooled (FC) and zero-field-cooled (ZFC) magnetization curves represent a superposition of the two magnetic transitions belonging to the different phases. The onset of the magnetic transition is observed at $T_{C1} \simeq 230$ K for the first phase and at $T_{C2} \approx 100$ K for the second phase.

Figure 5 shows that the LCM2 film does not undergo the MI transition in the investigated temperature range, even though negative magnetoresistance (MR) appears at $T \leqslant 150$ K, as in inset *b*. The MR value is defined by $\mathrm{MR} = 100\%\ [R(0) - R(H)]/R(H)$, where $R(0)$ and $R(H)$ are resistances with and without magnetic field, respectively. Inset *a* of Fig. 5 shows that the magnetic transition in this film begins at $T_C \simeq 120$ K; that is coincident with the onset of the second magnetic transition in LCM1. Because the lattice parameter *c* of the LCM2 film is similar to that for the *A* phase of the LCM1 film, it is reasonable to assert that the *A* phase shows the magnetic and electronic transitions at a low temperature (T_{C2} and T_{P2} in Fig. 4).

Figure 6 exhibits the magnetic and transport properties for the LCM3 film. Inset *b* shows that the MR(T) demonstrates a peaklike behavior with $T_P \simeq 150$ K that is coincident with the temperature of the magnetic transition, T_C. The unusual FC curve of $M(T)$, revealing a drop of the magnetization at $T \leqslant 120$ K (inset *a* in Fig. 6) can be explained by the existence of a second ferromagnetic→canted antiferromagnetic transition in this film, with $T_N \simeq 118$ K.[18] We suggest that it is the main reason for the peaklike behavior of MR(T) for the LCM3 film.

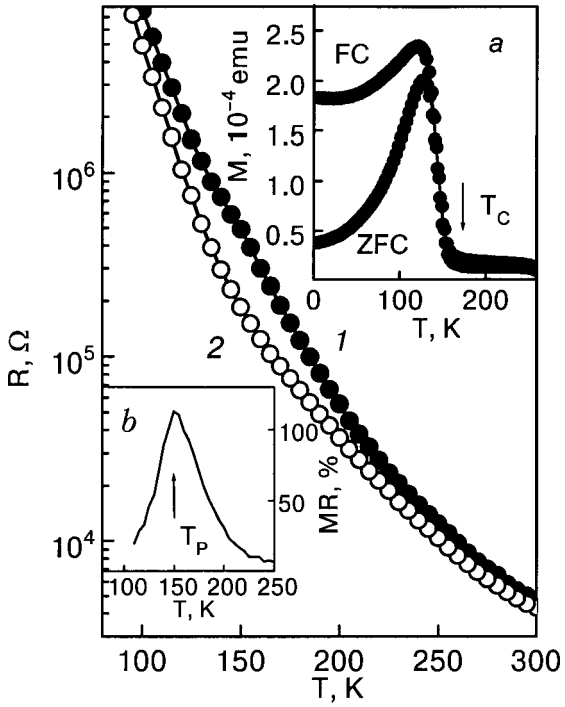

FIG. 6. Temperature dependence of the resistance of the LCM3 film without (*1*) and with (*2*) an applied magnetic field of 5 T. The lines are a guide to the eye. The inset *a* shows the temperature dependence of the FC and ZFC magnetization. The inset *b* displays the temperature dependence of the magnetoresistance in an applied magnetic field of 5 T.

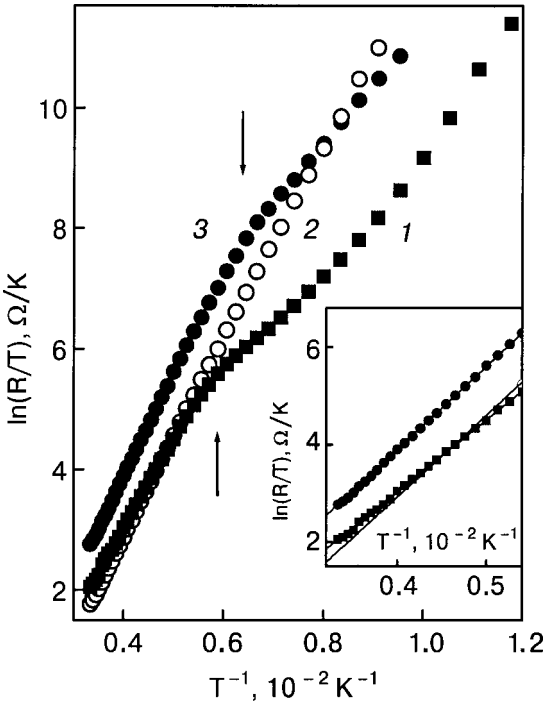

FIG. 7. ln(*R*/*T*) versus T^{-1} for the LCM1 (1), LCM2 (2), and LCM3 (3) films without an applied magnetic field. The inset displays the high-temperature range. The solid lines are fitting curves based on the TAC model.

5. DISCUSSION

The temperature behavior of the resistance for the *B* phase of the LCM1 film in an applied magnetic field (curve 2 in Fig. 2) is very similar to that for a thin $La_{0.67}Ca_{0.33}MnO_3$ film in the COI state as reported by Biswas *et al.*[2] Consequently, the transition of the *B* phase at $T \leqslant 210$ K from the insulating to the metallic state under applied magnetic field (curve 2 in Fig. 4) can be treated as melting of the COI state and nucleation of the FMM phase with decreasing temperature. The observed increase in resistance at $T \leqslant 100$ K (curve 2 in Fig. 4) attests that the inclusions of the *A* phase remain in the paramagnetic insulating (or semiconducting) state up to $T_{P2} \simeq 80$ K. The authors of Refs. 1 and 2 presented an explanation for the appearance of the COI state in thin manganite films, based on the idea of a nonuniform distribution of the lattice strain that resulted from a transition from a two- to a three-dimensional growth mode. It was suggested that the two-phase state is formed by separation of the film into high-strain and strain-free regions which possess different transport and magnetic behaviors at low temperatures. However, in our case the oxygen-deficit $La_{0.7}Ca_{0.3}MnO_{2.9}$ thin film is separated into two different *crystalline* phases, and only the cubic phase with an anomalously small lattice parameter gives evidence for the COI state. It is reasonable to claim that the forced reduction of the lattice parameter, induced by the epitaxial growth mode, is equivalent to a decrease in the average *A*-site cation radius, $\langle r_A \rangle$, which makes this compound similar to $Pr_{0.7}Ca_{0.3}MnO_3$. It was shown recently that an increase of the out-of-plane lattice parameter of a $Pr_{0.65}Ca_{0.35}MnO_3$ film leads to frustration of the COI state.[8–20] Here we observe the opposite phenomenon, which is connected with the appearance of the COI state in the $La_{0.7}Ca_{0.3}MnO_{2.9}$ thin film with an artificially reduced lattice parameter.

$La^{3+}_{1-x}Ca^{2+}_{x}Mn^{3+}_{1-x-2\delta}Mn^{4+}_{x-2\delta}O^{2-}_{3-\delta}V^{0}_{\delta}$ is the ionic structure of manganites according to Jonker and van Santen,[21] where V^0_δ stands for the ratio of oxygen vacancies. Consequently, the real Mn^{3+}: Mn^{4+} ratio in the LCM1 and LCM2 films is about 0.9:0.1 instead of 0.7:0.3. A similar Mn^{3+}: Mn^{4+} ratio is applies to the LCM3 film with the optimum oxygen doping. Therefore, the concentration of Mn^{4+} ions in the *A* phase of LCM1 is about equal to that in the LCM2 and LCM3 films. However, the manganese valency is provided by the oxygen deficiency in the case of LCM1 (*A* phase) and LCM2 but by the concentration of the substituted divalent ions in the case of LCM3. In both cases the decrease in the concentration of Mn^{4+} ions reduces the Curie temperature and leads to suppression of the MI transition for this compound.[11,22] On the other hand, our results show that the artificial compression of the unit cell volume leads to a significant increase in the Curie temperature (down to the value of the lattice parameter which is typical for the stoichiometric composition), in spite of the remaining deficiency of Mn^{4+} ions.

Figure 7 shows the ln(*R*/*T*) versus T^{-1} plots for the LCM1 (*1*), LCM2 (*2*), and LCM3 (*3*) films. In the high-temperature range the plots can be described on the basis of thermally-activated-conductivity (TAC) model, which predicts an expression $R(T) = R_0 T \exp(T_A/T)$, where T_A is the activation energy in units of temperature. The inset displays that the best agreement between the experiment and the theory (solid lines) is seen with the following fitting parameters: $R_0 \simeq 5.78 \cdot 10^{-2}$ Ω and $T_A \simeq 1470$ K for LCM1, $R_0 \simeq 2.38 \cdot 10^{-2}$ Ω and $T_A \simeq 1680$ K for LCM2, and $R_0 \simeq 4.5$

$\cdot 10^{-2}\ \Omega$ and $T_A \simeq 1700$ K for LCM3. The values for the activation energy turn out to be almost identical for the LCM2 and LCM3 films. Taking into account that both films have a rhombohedral crystal structure and similar hole densities (similar Mn^{3+}:Mn^{4+} ratios), the result obtained is absolutely expected. The LCM1 film, most of which is in a cubic *B* phase, shows a smaller value of T_A. It can be explained by the significant difference in the Mn–O–Mn angle between these two kinds of films, which plays a key role for the mechanism of transport in manganites. The arrows in Fig. 7 indicate the onset of magnetic transitions in the LCM3 film and the *B* phase of the LCM1 film. Near these temperatures the $R(T)$ behavior is changed for both films. The absence of such a peculiarity in $R(T)$ for the LCM2 film is explained by the limited capability for measurements in the low-temperature region or a very small value of the magnetization compared with the LCM3 film (see insets *a* in Figs. 5 and 6).

6. CONCLUSION

The magnetic and transport properties of $La_{0.7}Ca_{0.3}MnO_{3-\delta}$ films with an oxygen deficiency ($\delta \simeq 0.1$) and a $La_{0.9}Ca_{0.1}MnO_3$ film with the stoichiometric oxygen content have been investigated in a wide temperature range.

It was shown that the COI state is observed for $La_{0.7}Ca_{0.3}MnO_{2.9}$ film with thickness $d \leqslant 30$ nm, which manifests mainly a cubic crystal structure with an anomalously small lattice parameter for this composition. In addition, the artificial compression of the crystal lattice due to the epitaxial growth of the film leads to a significant increase in the Curie temperature (down to the value of the lattice parameter which is typical for the stoichiometric composition) and to the recovery of magnetic ordering at high temperature. Increasing in the film thickness ($d \simeq 60$ nm) leads to a structural transition from the lattice-strained cubic to the relaxed rhombohedral phase, which is accompanied by a shift of the Curie point to lower temperatures and a frustration of the COI state.

The magnetic and transport properties of the film with $d \simeq 60$ nm are similar to those exhibited by the optimally oxygen-doped $La_{0.9}Ca_{0.1}MnO_3$ film. This is confirmed by the roughly equal temperatures of the magnetic transition and the almost identical values of the activation energy. In contrast, the cubic modification of the $La_{0.7}Ca_{0.3}MnO_{2.9}$ film with $d \leqslant 30$ nm has a smaller value of the activation energy, which can be explained by the change in the Mn–O–Mn angle or the reduced distance between the Mn ions.

We conclude that the formation of the COI state in the oxygen-deficit $La_{0.9}Ca_{0.1}MnO_{3-\delta}$ films is governed by a compression of the crystal lattice rather than accumulation of the oxygen vacancies, the low doping of the substituted divalent ions, or electronic phase separation.

This work was supported by the KOSEF through the Quantum Photonic Science Research Center and a Korea Research Foundation Grant (KRF-2001-015-DS0015).

*E-mail: pvg@imp.kiev.ua

[1] A. Biswas, M. Rajeswari, R. C. Srivastava, Y. H. Li, T. Venkatesan, R. L. Green, and A. J. Millis, Phys. Rev. B **61**, 9665 (2000).
[2] A. Biswas, M. Rajeswari, R. C. Srivastava, T. Venkatesan, R. L. Green, Q. Lu, A. L. de Lozanne, and A. J. Millis, *cond-mat/0102321*.
[3] M. Uehara, S. Mori, C. H. Chen, and S.-W. Cheong, Nature (London) **399**, 560 (1999).
[4] K. M. Satyalakshmi, S. S. Manoharan, M. S. Hegde, V. Prasad, and S. V. Subramanyam, J. Appl. Phys. **78**, 6861 (1995).
[5] W. Zhang, W. Boyd, M. Elliot, and W. Herrenden-Harkerand, Appl. Phys. Lett. **69**, 3929 (1996).
[6] J.-M. Liu and C. K. Ong, Appl. Phys. Lett. **73**, 1047 (1998).
[7] R. Mahendiran, S. K. Tiwary, A. K. Raychaudhuri, and T. V. Ramakrishnan, Phys. Rev. B **53**, 3348 (1996).
[8] J.-M. Liu and C. K. Ong, J. Appl. Phys. **84**, 5560 (1998).
[9] J. Li, C. K. Ong, J.-M. Liu, Q. Huang, and S. J. Wang, Appl. Phys. Lett. **76**, 1051 (2000).
[10] N. Abdelmoula, K. Guidara, A. Cheikh-Rouhou, E. Dhahri, and J. C. Joubert, J. Solid State Chem. **151**, 139 (2000).
[11] J. R. Sun, C. F. Yeung, K. Zhao, L. Z. Zhuo, C. H. Leung, H. K. Wong, and B. G. Shen, Appl. Phys. Lett. **76**, 1164 (2000).
[12] E. Dagotto, T. Hotta, and A. Moreo, *cond-mat/0012117*.
[13] V. G. Prokhorov, G. G. Kaminsky, V. A. Komashko, J. S. Park, and Y. P. Lee, J. Appl. Phys. **90**, 1055 (2001).
[14] K. Dörr, J. M. De Teresa, K.-H. Müller, D. Eckert, T. Walter, E. Vlakhov, and L. Schultz, J. Phys.: Condens. Matter **12**, 7099 (2000).
[15] O. I. Lebedev, G. Van Tendeloo, S. Amelinkx, H. L. Ju, and K. M. Krishnan, Philos. Mag. A **80**, 673 (2000).
[16] J. Aarts, S. Freibem, R. Hendrikx, and H. W. Zandbergen, Appl. Phys. Lett. **72**, 2975 (1998).
[17] W. Z. Gong, B. R. Zhao, C. Cai, and Y. Lin, Appl. Phys. Lett. **79**, 827 (2001).
[18] G. Biotteau, M. Hennion, F. Moussa, J. Rodriguez-Carvajal, L. Pinsard, and A. Revcolevschi, Physica B **259–261**, 826 (1999).
[19] Y. P. Lee, V. G. Prokhorov, J. Y. Rhee, K. W. Kim, G. G. Kaminsky, and V. S. Flis, J. Phys.: Condens. Matter **12**, L133 (2000).
[20] V. G. Prokhorov, G. G. Kaminsky, V. S. Flis, Y. P. Lee, K. W. Kim, and I. I. Kravchenko, Physica B **307**, 239 (2001).
[21] Y. P. Lee, V. G. Prokhorov, K. W. Kim, and J. Y. Rhee, J. Phys.: Condens. Matter **13**, 9673 (2001).
[22] G. H. Jonker and J. H. van Santen, Physica (Amsterdam) **19**, 120 (1953).
[23] W. Prellier, M. Rajeswari, T. Venkatesan, and R. L. Greene, Appl. Phys. Lett. **75**, 1446 (1999).

This article was published in English in the original Russian journal. Reproduced here with stylistic changes by AIP.

Point-contact spectroscopy of the relaxation dynamics of two-level systems upon structural changes in Ni–Nb glasses

O. P. Balkashin* and I. K. Yanson

B. Verkin Institute for Low Temperature Physics and Engineering, National Academy of Sciences of Ukraine, pr. Lenina 47, 61103 Kharkov, Ukraine

A. Halbritter and G. Mihály

Institute of Physics of the University of Technology and Economics, ul. Budafoki 8, Budapest 1111, Hungary
(Submitted August 27, 2002)
Fiz. Nizk. Temp. **29**, 169–178 (February 2003)

The point-contact spectra (the energy dependence of the second derivatives of the current–voltage characteristics) of bimetal contacts of the amorphous alloy $Ni_{59}Nb_{41}$ with silver are investigated in the frequency range $10^3-5\times10^9$ Hz. At low energies the spectral feature due to the scattering of conduction electrons on two-level tunneling systems in point contacts of the quenched alloy is clearly observed in the microwave region. This confirms the conclusion reached previously by the authors for homocontacts [O. P. Balkashin *et al.*, Solid State Commun. **118**, 623 (2001)] that rapidly relaxing two-level systems with a characteristic relaxation frequency $\Gamma>10^{11}$ Hz are present in metallic glasses. After a high-temperature annealing of the amorphous alloy (for 1 hour at $T=800\,^\circ$C) and its crystallization, the intensity of the spectral feature in the region of low voltages across the contact increases substantially. A sharp frequency dispersion of the amplitude of this feature is observed; it vanishes completely for measurements at frequencies below $\sim5\times10^9$ Hz. The data attest to the formation of qualitatively new, slowly relaxing two-level systems in the annealed Ni–Nb amorphous alloys. An estimate of the characteristic relaxation frequency of the two-level systems from the frequency dispersion of the measured signal gives a value $\Gamma/2\pi\approx0.7\times10^9$ Hz. The possible causes of the formation of two-level systems in point contacts are discussed. © *2003 American Institute of Physics.* [DOI: 10.1063/1.1542411]

INTRODUCTION

The model of two-level tunneling systems (TLSs)—dynamic defect centers with internal degrees of freedom—as a new class of low-energy excitations in solids was originally proposed[1] to explain the linear trend of the temperature dependence of the heat capacity of amorphous insulators at low temperatures ($T\leqslant1$ K). It was subsequently learned[2] that the low-temperature properties of amorphous metals and alloys are also well explained by the presence of TLSs, and an important role in this is played by the interaction of these structural defects with conduction electrons. In addition, as has been shown by point-contact (PC) spectroscopy of plastically deformed pure metals,[3,4] the scattering of electrons on TLSs cause of the low-energy features in the PC spectra (zero-bias anomalies).

Although the exact microscopic structure of the TLSs is unknown—they could be special parts of dislocation lines, intercluster or grain boundaries, interstitial atoms, etc., a simple model of a particle in a double-well potential field gives a good description of the properties of disordered (amorphous) systems of completely different natures. According to the model of Ref. 1, a TLS can be represented as an atom moving in a potential well with two minima, created by its nearest-neighbor environment, or as a group of atoms which can form two or more almost equivalent configurations in space with slightly different energies. Suppose that the difference of the energy levels of the lowermost states in each well differs by Δ (asymmetric double-well potential) and that the wells are separated by a rectangular potential barrier with a characteristic height V and width W. Although at low temperatures ($T\sim1-10$ K) the thermally activated classical above-barrier transitions are forbidden, quantum tunneling between states in the individual wells can occur. The frequency of these tunneling transitions is determined by the parameters of the barrier and the mass of the tunneling particle:

$$\omega_t=\omega_0\exp(-W\sqrt{2mV/\hbar^2}), \tag{1}$$

where $\hbar\omega_0$ is the characteristic energy of oscillations in an individual minimum, and m is the effective mass of the tunneling atoms or individual atom. The distance between energy levels of a TLS (the excitation energy), corresponding to two configurations of the atomic structure, is given by $E=\sqrt{\Delta^2+\Delta_0^2}$, where $\Delta_0=\hbar\omega_t$. It is assumed that because of the amorphous nature of the medium the TLSs are uniformly distributed over values of the parameter Δ, and the properties of the sample are determined by the average over the whole random ensemble of TLSs. This as is confirmed by measurements of various thermodynamic and kinetic characteristics at $T\sim1$ K.[2,5]

The interaction of TLSs with phonons in amorphous insulators is taken into account in the theory as a perturbation of the asymmetry parameter Δ. In amorphous metals it is also necessary to take into account the interaction of the

TLSs with conduction electrons in order to explain the faster (by 4–5 orders of magnitude) relaxation in metals as compared to insulators.[2]

Starting from the results of numerous experiments on the measurement of the time dependence of the electrical conductivity and PC spectroscopy studies of mesoscopic conductors, and also ultrasound experiments on bulk samples, the TLSs can be classified[6] according to the rates of transitions between the potential minima.

1. Slow TLSs (relaxation time $\tau > 10^{-8}$ s), which are sometimes called two-level fluctuators, are characterized by a high barrier and a negligibly small value of Δ_0. Transitions between the potential wells are brought about by thermal activation or incoherent quantum tunneling.

2. Fast TLSs (10^{-8} s$> \tau > 10^{-12}$ s) have a small barrier and rather large values of Δ_0 ($10^{-4}-1$ meV, according to the uncertainty principle); this makes for coherent quantum transitions between two states.

3. Ultrafast TLSs ($\tau < 10^{-12}$ s) have such large values of Δ_0 that E is also large, and the physical behavior of the system is determined by the uniformly distributed ground state.

The relaxation frequency Γ of a TLS is proportional to the square of the ratio of the tunneling energy to the excitation energy $(\Delta_0/E)^2$ (see, e.g., Ref. 7). The distribution function of the TLSs in the model of Refs. 1 and 2 is given by the expression

$$P(E,u) = 1/2\overline{P}(1-u)^{-1/2}/u, u = (\Delta_0/E)^2, \tag{2}$$

and therefore in the amorphous state the slow defect centers ($E > \Delta_0$) with an asymmetric two-level potential relief should basically be dominant. Thus the distribution function of the TLSs over energy and relaxation frequencies should have the form[8]:

$$P(E,\Gamma) = P(E)\Gamma^{-1}\left(1-\frac{\Gamma}{\Gamma_{\max}}\right)^{-1/2},$$

$$\int P(E,\Gamma)\,dE\,d\Gamma = 1. \tag{3}$$

Two different mechanisms have been proposed for the interaction of conduction electrons with TLSs in amorphous metals. The theory of Zawadowski and Vladar (Refs. 9 and 10; see also Ref. 6) considers a mechanism of nonmagnetic two-channel Kondo scattering for rapidly relaxing TLSs with an almost symmetric ($\Delta_0 \gg \Delta$) double-well potential. In contrast to the formalism of the conventional one-channel theory of the Kondo effect, which describes the scattering of electrons on static magnetic impurities, this model treats a TLS as a dynamic defect with two quasi-spin values corresponding to the two states of the TLS. The two channels are associated with the two values of the real spin of the conduction electrons. Fluctuations of the electron density change the barrier height in the potential relief of the TLSs and thereby alter the probability of tunneling transitions. With decreasing temperature this mechanism leads to logarithmic growth of the electronic resistivity in the low-temperature region and, consequently, gives rise to negative features[1)] on the PC spectra for $eV_0 \to 0$ (V_0 is the dc voltage across the contact).

In the alternative theory of Kozub and Kulik[11] both inelastic and elastic processes of electron scattering on asymmetric ($\Delta_0 \ll \Delta$) TLSs in point contacts are taken into account. The inelastic processes cause a positive anomaly on the PC spectrum (i.e., on the curve of $d^2V/dI^2(eV_0)$, which is usually what is recorded in experiments), whereas the contribution from elastic scattering can have either sign, depending on the sign of the difference $(\sigma^+ - \sigma^-)$ of the elastic scattering cross sections for electrons on TLSs found in two spatial configurations. The contribution of elastic processes to the current through a microcontact at $T=0$ is determined by the expression

$$\begin{aligned}\Delta I &= \frac{V_0}{2R_0}\frac{1}{S_c}\sum_j \mathbf{M}(\mathbf{r}_j)[\sigma_j^+(1-N_j)+\sigma_j^- N_j] \\ &= \frac{V_0}{2R_0}\sum_j \mathbf{M}(\mathbf{r}_j)\frac{\sigma_j^+-\sigma_j^-}{2S_c} \\ &\quad\times\left[\Theta(E_j-eV_0)+\frac{E}{E+q(eV_0-E)}\Theta(eV_0-E_j)\right],\end{aligned} \tag{4}$$

$$q = \frac{1}{2}[1-(2\varphi(\mathbf{r}_j)/V)^2],$$

where R_0 is the resistance of the point contact in the absence of TLSs, S_c is the transverse cross-sectional area of the contact, $\mathbf{M}(\mathbf{r}_j)$ is a geometric factor that depends on the position of the jth TLS, N_j are the occupation numbers of the lower energy levels of the TLSs, which depend on the voltage applied to the contact because of the inelastic interaction of TLSs with conduction electrons,[2)] Θ is the Heaviside step function, and $\varphi(\mathbf{r}_j)$ is the electric potential at the site of the individual TLS. The dependence of the occupation numbers N_j on the electron energy makes it possible to implement the elastic spectroscopy of TLS occupation numbers which was proposed in Ref. 11.

Thus both of the mechanisms discussed above for the scattering of electrons on TLSs will give rise to low-energy features on the PC spectra. However, the characteristic relaxation times for the two processes are substantially different: $\tau \sim 10^{-12}$ s for nonmagnetic Kondo scattering and $10^{-3}-10^{-8}$ s for occupation-number spectroscopy.

The universality conferred on the low-temperature behavior of a wide class of amorphous solids by the presence of TLSs in them is attracting considerable interest in such systems and is stimulating the adoption of diverse experimental methods, including point-contact spectroscopy, for studying the properties of these specific structural formations. In particular, it has been established by means of rf point-contact spectroscopy in measurements in the microwave region up to frequencies $\omega \sim 10^{11}$ Hz ($\omega \leqslant \Gamma$) that for metallic glasses of various compositions in the systems Fe–B (Ref. 12) and Ni–Nb (Refs. 13 and 14) it is rapidly relaxing TLSs that are mainly realized, with characteristic relaxation frequencies exceeding 10^{11} Hz. Analogous results have also been obtained for PCs based on imperfect polycrystalline thin films of pure copper.[15]

The goal of the present study was to investigate how the frequency dispersion of the amplitude of the low-temperature

feature on the PC spectra due to the scattering of electrons on the TLSs is affected by the crystallization of the amorphous alloy $Ni_{59}Nb_{41}$ during high-temperature annealing. The method of rf PC spectroscopy in the frequency range $10^3-5\times10^9$ Hz was used to measure the spectrum of contacts of silver with the initial amorphous alloy $Ni_{59}Nb_{41}$ and with the same alloy after it had been annealed for 1 hour at 800 °C. It turned out that, unlike the amorphous state for contacts with the annealed alloy, the amplitude of the low-energy features for $eV_0\to0$ depend substantially on the irradiation frequency.

EXPERIMENTAL TECHNIQUES

The studies were done on samples of the metallic amorphous alloys $Ni_{59}Nb_{41}$ obtained by fast quenching of the melt and having the shape of thin (~20 μm) ribbons 1–2 mm wide. Thermal annealing of the ribbons was done in an inert atmosphere of helium or argon for 1 hour at a temperature of 800 °C with a subsequent slow (5–7 h) cooling to room temperature. According to published data,[16] such a heat-treatment regime leads to the formation of an equilibrium crystalline phase. For the quenched samples of metallic glasses the point contacts were made between the ends of the alloy ribbon and the sharp edge of a bar of pure silver. After annealing, the ribbon became exceptionally brittle, and it was therefore attached with silver paste to a flat copper surface, and the point contacts were formed between the surface of the ribbon and a silver tip with a radius of curvature of several microns. The surface of the ribbon after annealing was treated by mechanical polishing and chemical etching.

The massive electrodes of the point contact were mounted in the holders of two independent micrometer movements to permit changing their relative position in space and varying the pressing force. This technique made it possible to create contacts of different geometric sizes on different parts of the electrode surfaces.

The point-contact studies were done by the standard technique of recording the amplitude V_2 of the second harmonic of a low-frequency (1623 Hz) modulating current as a function of the dc voltage applied to the contact (energy).[17] In the high-frequency measurements the contact was irradiated by an rf alternating field of low power, delivered to the contact by a coaxial cable. The radiation of the rf oscillator was chopped at a sonic frequency (2433 Hz), and the dc voltage different across the point contact—the video detection signal V_d—was amplified and registered by a phase detector at the chopping frequency in both the presence and absence of rf irradiation of the point contact. In both cases the measured signals $V_2(V_0)$ and $V_d(V_0)$, with an amplitude of around 1 μV, are proportional to the values of the second derivative of the current–voltage characteristic of the point contact, $d^2V/dI^2(eV_0)$.[12] All of the experiments were done at a temperature of 4.2 K. A detailed description of the measurement technique is given in Refs. 12–14.

PRESENTATION AND DISCUSSION OF THE MAIN RESULTS

In Fig. 1 we show typical PC spectra obtained for several bimetal contacts of silver with the unannealed $Ni_{59}Nb_{41}$ alloy. The jumplike decrease of the signal amplitude at high

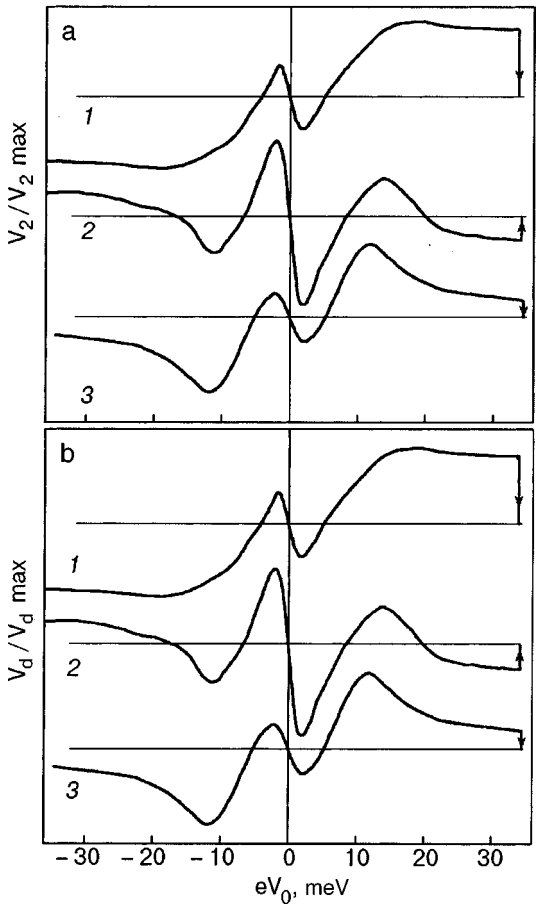

FIG. 1. Point-contact spectra of heterocontacts of the quenched alloy $Ni_{59}Nb_{41}$ with silver, measured at a sonic frequency (a) and at 5.12×10^9 Hz (b) for different contact resistances R [Ω]: 8 (*1*), 19 (*2*), and 36 (*3*). The curves have been shifted vertically, but the scales are the same for all curves.

biases ($V_0>30$ mV) is due to the turning off of the low- and high-frequency modulations for precise fixing of the zero signal level. The characteristic spectral feature at low voltages ($V_0\to0$) due to the scattering of electrons on TLSs is clearly manifested in the PC spectrum at a sonic frequency of ~3 kHz (Fig. 1a) and has practically the same form in measurements at microwave frequencies $\sim5\times10^9$ Hz (Fig. 1b). In its general aspects this feature reproduces well the data for homocontacts of metallic amorphous alloys of different compositions in the systems Fe–B and Ni–Nb, which were studied in Refs. 12–14 in the sonic and microwave (6×10^{10} Hz) regions. Then, as the voltage is increased the signal amplitude varies smoothly and for some contacts passes through a maximum. In the spectra shown in Fig. 1 (curves *2* and *3*) this peak at $eV_0\sim12$ meV coincides in position with the maximum in the density of states of transversely polarized phonons in silver,[17] whereas the characteristic energies of the corresponding phonons for Nb and Ni are equal to 16 and 25 meV.[17] However, for unambiguous confirmation of the phonon nature of the feature at $eV_0\sim12$ meV it is necessary to make special measurements on $Ni_{59}Nb_{41}$ contacts with other pure metals. One notices the different behavior of the signal at high energies ($eV_0>20$ meV) in Fig. 1. In spectra *1* and *3* the values of V_2 and V_d in this region are positive ($d^2V/dI^2>0$, i.e., the contact

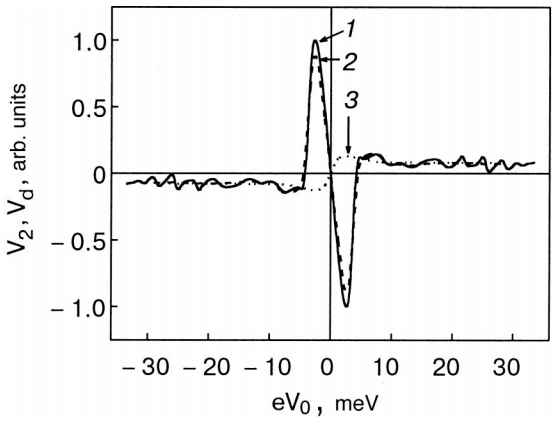

FIG. 2. Point-contact spectra of a heterocontact of the annealed alloy $Ni_{59}Nb_{41}$ with silver, measured at a sonic frequency (*1*) and at the microwave frequencies ω [Hz]: 0.48×10^9 (*2*) and 4.79×10^9 (*3*). The contact resistance $R=7\ \Omega$.

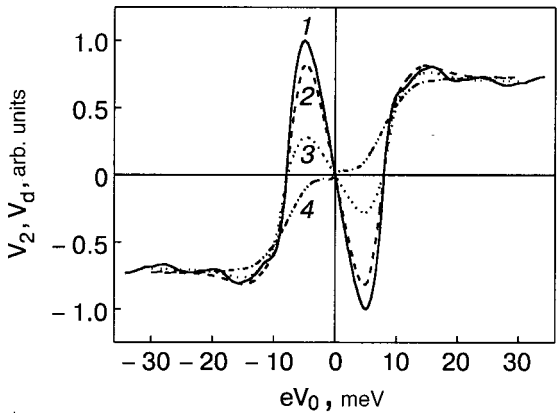

FIG. 3. Evolution of the PC spectra of a contact of the annealed alloy $Ni_{59}Nb_{41}$ with Ag in measurements at different frequencies: a sonic frequency (*1*) and microwave frequencies ω [10^9 Hz]: 0.48 (*2*), 2.036 (*3*), and 4.72 (*4*). The contact resistance $R=14\ \Omega$.

resistance increases with increasing voltage), as is typical for an electron–phonon scattering mechanism.[17] The nonlinearity of the current–voltage characteristic is due to processes of multiphonon generation, which take place in dirty contacts[18] with the high relaxation frequencies typical of relaxation of the electronic subsystem in the contact ($\sim10^{13}$ Hz). Therefore, the measurements at much lower frequencies ($\omega\sim10^9$ Hz) cannot affect the shape of the recorded curves. The influence of slower processes of reabsorption of nonequilibrium phonons with frequencies $\sim10^9$–10^{10} Hz, which take place in clean contacts,[19,20] are not observed in the measured spectra. The negative values of d^2V/dI^2 at $eV_0>20$ meV observed in spectrum *2* are possibly due to the destruction of the spatial localization of the electronic states in electron–electron or electron–phonon collisions.[21,22] The slight differences of the amplitude and shape of the spectra at $eV_0\to0$, like the behavior of the signal at high voltages, for contacts with different resistances and, hence, different geometric sizes should be attributed to different relationships between the contributions of several scattering mechanisms: electron–TLS, electron–phonon, and electron–electron.

The measurements showed that asymmetry of the PC spectra for different polarities of the applied voltage due to the thermoelectric effects inherent to bimetal contacts was practically absent. It is known[23,24] that the asymmetry depends on the difference of the thermopowers of the metals in contact and the on the growth rate of the temperature of the point contact as the voltage applied to it is increased. The temperature of the contacts studied can increase significantly with increasing voltage because of the short mean free path of electrons in an amorphous alloy. However, the thermopower of metallic glasses[5,21] have the same sign and nearly the same magnitude as that of pure silver (0.3–1 μV/deg) in the low-temperature region ($T\leqslant30$ K),[25] and that leads to a negative asymmetry of the spectra for different polarities of the bias voltage.

Upon high-temperature annealing of the alloy $Ni_{59}Nb_{41}$ the topological and compositional disorders inherent to the amorphous state are substantially decreased. Crystallization of the alloy duration annealing results in an increase in the degree of regularity of the atomic lattice and, consequently, should lead to a decrease in the concentration of TLSs. This, in turn, should decrease the intensity of the corresponding feature on the PC spectra to such an extent that it vanishes completely in a perfect crystal. Experiments have shown that the shape of the PC spectra are not fundamentally altered after annealing. However, for practically the same values of the low-frequency modulation (0.5–1.0 mV) the amplitude of the spectral feature at $eV_0\to0$ was 3–5 times larger. The PC spectra for two contacts of silver with the annealed alloy $Ni_{59}Nb_{41}$ are shown in Figs. 2 and 3. The spectra obtained for different measurement frequencies are normalized to the low-frequency curve in the high-voltage region, where the characteristic frequency of electron–phonon scattering is substantially greater than the frequency of the rf irradiation. In the figures one can clearly discern the decrease of the amplitude of the low-energy line in the spectrum with increasing irradiation frequency. The corresponding curves for measurement of the differential resistance of these contacts are shown in Fig. 4. The increase in the resistance of the contact with increasing bias confirms an electron–phonon scattering mechanism at high voltages. It follows from Figs.

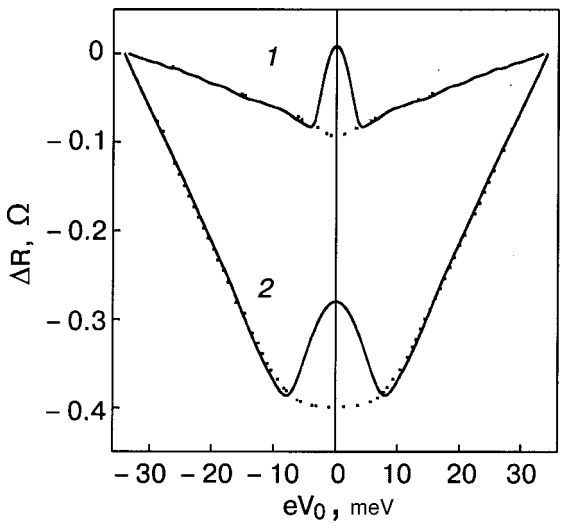

FIG. 4. Measurement of the differential resistance of the contacts in Fig. 2 (curve *1*) and Fig. 3 (curve *2*) in measurements at a sonic frequency (solid curves) and at a microwave frequency (dashed curves).

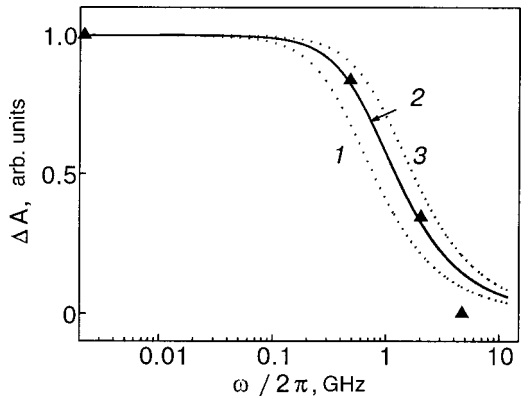

FIG. 5. Frequency dispersion of the amplitude of the low-energy spectral feature. The symbols are experimental data points. The curves show the frequency dependence of the signal amplitude calculated for $\Gamma/2\pi$ [10^9 Hz]: 0.4 (*1*), 0.7 (*2*), and 1.0 (*3*).

2–4 that in contacts with the annealed alloy the amplitude of the low-energy features (zero-bias anomalies) depend substantially on the frequency of the rf irradiation. At frequencies of around 5×10^9 Hz this feature vanishes from the spectrum completely.

The spectra in Figs. 2 and 3 do not have the phonon feature that is observed for the quenched alloys in the region $eV_0\sim12$ meV (see Fig. 1) and which retains its shape for different measurement frequencies. Point contacts with the quenched alloy were created by touching the sharp edges of electrodes; this apparently led to a larger fraction of pure silver in the volume of the contact. In the contacts with the annealed alloy, which were created by the tip–plane method, the region in which the current is concentrated probably consists of $Ni_{59}Nb_{41}$ with a finely disperse structure, which makes for a short mean free path for the electrons and thus degrades the spectroscopic properties of the contact. The concentration of the components in the alloy $Ni_{59}Nb_{41}$ is close to the eutectic composition $Ni_{60}Nb_{40}$ (Ref. 16). Eutectic alloys have a finely disperse structure and even after prolonged high-temperature annealing have an elevated resistivity (see, e.g., Ref. 26) because of the significant influence of interphase boundaries. The eutectic alloy in the Ni–Nb system consists of a mixture of two phases: the μ phase and a metallic compound Ni_3Nb with complex rhombohedral and orthorhombic structures with several atoms in the unit cell.[27] For these alloys the coordination numbers and the distances between neighboring atoms in the amorphous and crystalline states are only slightly different.[28] The complexity of the crystal structure of $Ni_{59}N_{41}$ makes it hard to carry out PC spectroscopy of phonons in these alloys.

Figure 5 shows a semilogarithmic plot of the relative changes ΔA in the intensity of the spectral line versus the frequency ω for $|eV_0|\approx5$ meV. The symbols in the figure represent the experimental values of the quantity

$$\Delta A=(A_\omega-A_{\min})/(A_{\max}-A_{\min}),$$

where $A_{\max}$ and $A_{\min}$ are the amplitudes of the peaks measured at the sonic frequency and at 4.72×10^9 Hz, respectively. The theory of Ref. 11 predicts that the nonlinear conversion signal will fall off with frequency as $\sim\omega^{-1}$ for point contacts in which electron–TLS scattering occurs. The same sort of behavior of the signal was predicted earlier[19] for the electron–phonon interaction. In that case the amplitude of the rectified rf current for an electron–phonon mechanism of nonlinear electrical conduction of a contact will decrease as $[1+(\omega/\omega_{ph})^2]^{-1/2}$ (Refs. 19 and 20), where ω_{ph} is the characteristic phonon relaxation frequency. It is reasonable to suppose that the amplitude of the rectified current, which we measured in the experiments, will have behavior analogous to that for the nonlinear mechanism due to the interaction of electrons with two-level defects. The curves in Fig. 5 show the function $\Delta A\sim[1+(\omega/\Gamma)^2]^{-1/2}$ calculated for three different values of the characteristic TLS relaxation frequency Γ. It is seen in the figure that the function calculated with $\Gamma/2\pi=0.7\times10^9$ Hz (curve *2* in Fig. 5) is in good agreement with the experimental points. An estimate of the number of TLSs in the contacts studied gives values of 10^2-10^4 (Ref. 14), and therefore the results in Fig. 5 and the value $\Gamma/2\pi=0.7\times10^9$ Hz do not pertain to an individual TLS but represent a certain effective characteristic of the whole set of two-level dynamic defects in the contact, distributed over relaxation frequencies according to the law (3).

The results presented above unambiguously point to the presence of slowly relaxing TLSs in the point contacts with the annealed alloys. As we have said, the scattering of electrons on slow TLSs in the point contacts was considered in the Kozub–Kulik theory.[11] Those authors paid particular attention to the importance of elastic scattering processes, which do not change the state of the TLS, unlike inelastic processes, which are accompanied by a transition of the TLS to an excited state. The contribution of inelastic scattering to the PC spectrum, according to the results of Ref. 7, is proportional to $(\Delta_0/E)^2$, while the ratio of the intensities of the inelastic and elastic processes depends linearly on the ratio Δ_0/E (Ref. 11). Therefore, if slow TLSs are present in the contact, the elastic contribution to the nonlinear feature in the PC spectrum at low energies $eV_0\sim E$ will be the governing one. Thus elastic scattering processes occur mainly on slow TLSs having an asymmetric potential ($\Delta_0\gg E$), whereas inelastic processes mainly involve rapidly relaxing structural defects with an almost symmetric potential ($\Delta_0\ll E$).[11]

For comparison of our experimental results with the theory of Ref. 11, we calculated the contributions of inelastic and elastic scattering to the PC spectrum, i.e., the values of the second derivatives $d^2V/dI^2(eV_0)$, using the corresponding expressions from Ref. 29. The calculations were done for $T=4.2$ K for an isolated structural defect with $E=1$ meV at the center of a clean point contact with a ballistic regime of electron motion. Only the scattering of electrons on the TLS was taken into account, while the interaction of the TLS with phonons was ignored (see footnote 2). The results of the calculation are presented in Fig. 6. Since the experimental PC spectra exhibit spectral features of negative sign for $eV_0>0$, while inelastic processes give a positive contribution to the spectrum (the contact resistance increases with increasing bias because of the growing electron energy loss to excitation of the TLSs), a negative sign of the difference of the cross sections for elastic scattering of electrons on TLSs in the ground and excited states $[(\sigma^+-\sigma^-)<0]$ is adopted in the calculations. As was mentioned in Ref. 11, the

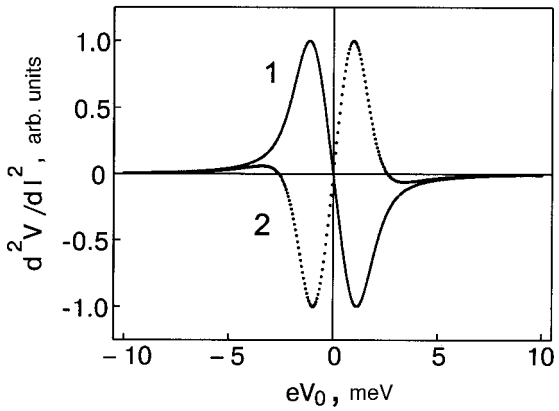

FIG. 6. Form of the features in the PC spectra calculated according to the theory of Ref. 11 for elastic (*1*) and inelastic (*2*) processes of electron scattering on an isolated two-level system found at the center of the contact ($T=4.2$ K, $E=1$ meV).

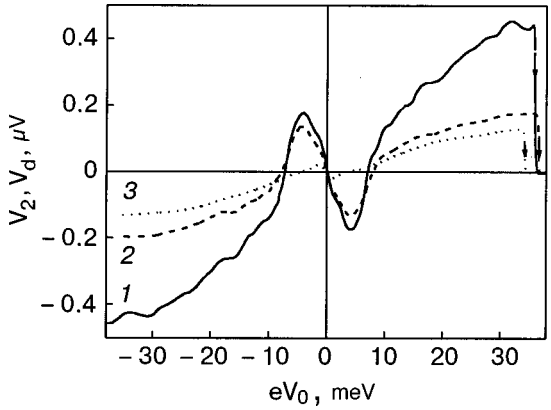

FIG. 7. Point-contact spectrum of the annealed alloy $Ni_{59}Nb_{41}$ with Ag for a contact with an appreciable contribution from thermal effects, measured at a sonic frequency (*1*) and at the microwave frequencies ω [10^9 Hz]: 0.48 (*2*) and 5.11 (*3*). The amplitude of the low-frequency modulation for curve *1* was $V_{10}=0.93$ μV. The contact resistance $R=7$ Ω.

spectral line caused by elastic scattering has an asymmetric shape with respect to $eV_0=E$ (curve *1* in Fig. 6), with a descending wing in the energy region $eV_0>E$. At the same time, we note that there is also an analogous wing but of positive sign for the inelastic scattering line (curve *2* in Fig. 6). Behavior of this kind has been observed previously[30,31] in PC spectra in the electron-beam excitation of crystal-field levels in $YbBe_{13}$ and $PrNi_5$. A comparison of the calculated spectra (Fig. 6) with the data of the experimental measurements (Figs. 2 and 3), together with the experimentally established frequency dispersion of the signal (Fig. 5), proves that high-temperature annealing of the amorphous alloy $Ni_{59}Nb_{41}$ has led to the formation of slowly relaxing TLSs.

Let us discuss the possible nature of the fast and slow two-level structural defects. In Ref. 32 the molecular dynamics method was used to calculate the atomic structure, the parameters of the energy barriers, the effective masses, and the probabilities of quantum tunneling for the anomalous regions of the lines of screw dislocations in a copper crystal. It was found that the motion of a kink in a dislocation line when the dislocation line is displaced smoothly by a lattice constant[33] involves the movement of hundreds of atoms. Each atom is shifted by a very small distance ~ 0.01Å. As a result, the effective mass and the parameters of the tunneling barrier turn out to be insignificant, and that makes for a high frequency of tunneling transitions [see formula (1)]. In the motion of jogs on a dislocation line, the jumplike transition of the dislocation line to an adjacent slip plane[33] involves the tunneling of only a few atoms. Therefore, for such a structural defect the effective mass and the barrier parameters are appreciable, and the frequency of transitions is substantially lower. Thus a step on a dislocation line can be associated with a slow two-level system. It should be noted, however, that in a multicomponent alloy the dislocation cores are of a more complex structure containing different kinds of atoms. Moreover, the surface of the sample may have an influence because of the possible enrichment of the surface layer in one of the elements of the alloy and segregation of the components at interphase boundaries.[21]

In amorphous alloys the situation is fundamentally altered, since a dislocation line cannot be defined as an extended spatial defect. For this reason a special role in the formation of rapidly relaxing TLSs in such materials may be played by intercluster boundaries of locally ordered nanoclusters.[34] The size of an individual cluster in Ni–Nb metallic glasses is determined in Ref. 16 from a comparison of the results of x-ray and electron diffraction scattering with model calculations for different atomic structures. According to the estimates of Ref. 16, a cluster contains up to 150 atoms and has an effective diameter of ~ 1.5 nm. The point contacts studied here, with a diameter $d\sim 50-100$ nm, contain around 10^4-10^5 clusters, which in turn should govern the electron scattering picture.

Let us consider the PC spectra for a contact that can manifest thermal effects (Fig. 7). Unlike the data in Figs. 2 and 3, in Fig. 7 the experimentally curves of the measured signals for different frequencies are plotted in absolute units. The amplitudes of the low- and high-frequency modulation currents for this contact were standard and close to the analogous quantities for the contact in Fig. 2, which had the same resistance $R=7$ Ω. However, the values of the signals obtained in the low- and high-frequency measurements at high voltages ($V_0>30$ mV) differed severalfold for this contact, rather than by 20–30% as is usually observed. The monotonic growth of the signal amplitude with increasing voltage applied to the contact instead of the saturation of the signal seen in Figs. 2 and 3 can be attributed to heating of the contact, i.e., a rise in its temperature as the bias is increased. Here the strong attenuation of the signal with increasing measurement frequency is logically explained by a significant decrease of the thermal contribution to the signal at frequencies exceeding the thermal relaxation frequency $\omega\geqslant\omega_T\sim 10^8-10^9$ Hz.[14] We note that for the given contact we also observed a substantial suppression of the zero-bias anomaly, similar to that in Figs. 2 and 3, but, unlike the case in Figs. 2 and 3, the shape of the feature observed at different measurement frequencies is modified by thermal effects, as was shown in Ref. 35.

CONCLUSION

In this paper we have investigated the influence of high-temperature annealing of $Ni_{59}Nb_{41}$ amorphous alloys on the electrical conduction processes in $Ni_{59}Nb_{41}$–Ag contacts.

The results demonstrate that annealed samples of the alloy in the resistivity range 10^8 Hz$<\omega/2\pi\leqslant 5\times10^9$ Hz exhibit a substantial decrease of the intensity of the low-energy spectral feature associated with electron scattering on two-level systems. The characteristic relaxation frequency of the TLSs in the annealed samples is estimated as $\Gamma/2\pi\approx 0.7\times10^9$ Hz, as opposed to $\Gamma/2\pi>10^{11}$ Hz for the quenched amorphous $Ni_{59}Nb_{41}$ alloys.

Until now the available experimental results on the zero-bias anomalies[4,6] have been interpreted in the framework of the Vladar–Zawadowski model[10] for rapidly relaxing TLSs or, as in Ref. 3, have admitted a satisfactory explanation on the basis of both the models of Refs. 10 and 11. A subsequent annealing of the samples, unlike our results here, have led to a significant decrease or even to the complete vanishing of the low-energy feature in the PC spectra.[3,4] A small contribution of slowly relaxing TLSs to the zero-bias anomaly has been successfully detected experimentally only for high-frequency studies of point contacts of amorphous alloys.[12,13]

Thus we have shown for the first time that crystallization of the amorphous alloy $Ni_{59}Nb_{41}$ leads to the formation of qualitatively new defect structures. The interaction of conduction electrons with this new type of TLS in point contacts is described well by the theoretical model of Kozub and Kulik.[11] However, the microscopic atomic structure of these dynamic defects remains unknown. The metallic glass region on the phase diagram of the Ni–Nb system is extends to 30–40 at. %. Therefore, definite information about the internal nature of the TLSs could be obtained from further studies by the method of rf PC spectroscopy at different temperatures on samples of different composition subjected to different heat treatment, i.e., having different degrees of crystallinity of the atomic lattice.

*E-mail: balkashin@ilt.kharkov.ua

[1)]The polarity of a feature on the PC spectrum is the sign of the second derivative of the current–voltage characteristic of the point contact. In this context it should be kept in mind that the electron–phonon interaction gives rise to a positive feature in the spectrum, i.e., $d^2V/dI^2(eV_0)>0$.

[2)]The interaction of the TLSs with phonons can be neglected because of their low density at temperatures $T<5$ K and low contact voltages $V_0<3-5$ mV.

[1] P. W. Anderson, B. I. Halperin, and C. M. Varma, Philos. Mag. **25**, 1 (1972).
[2] J. L. Black, in *Glassy Metals I*, H. J. Guntherodt and H. Beck (Eds.) Springer-Verlag, New York (1981), p. 167.
[3] R. J. P. Keijsers, O. I. Shklyarevskii, and H. van Kempen, Phys. Rev. B **51**, 5628 (1995).
[4] J. von Delft, D. C. Ralph, R. A. Buhrman, S. K. Upadhyay, R. N. Louie, A. W. W. Ludwig, and V. Ambegaokar, cond-mat/9702048 (1998).
[5] R. Harris and J. O. Strom-Olsen, in *Glassy metals II*, H. J. Guntherodt and H. Beck (Eds.) Springer-Verlag, New York (1981), p. 325.
[6] D. L. Cox and A. Zawadowski, Adv. Phys. **47**, 599 (1998).
[7] V. I. Kozub, Fiz. Tverd. Tela (Leningrad) **26**, 1955 (1984) [Sov. Phys. Solid State **26**, 1186 (1984)].
[8] A. M. Zagoskin, I. O. Kulik, and A. N. Omel'yanchuk, Fiz. Nizk. Temp. **13**, 589 (1987) [Sov. J. Low Temp. Phys. **13**, 332 (1987)].
[9] A. Zawadowski, Phys. Rev. Lett. **45**, 211 (1980).
[10] K. Vladar and A. Zawadowski, Phys. Rev. B **28**, 1564,1582,1596 (1983).
[11] V. I. Kozub and I. O. Kulik, Zh. Eksp. Teor. Fiz. **91**, 2243 (1986) [Sov. Phys. JETP **64**, 1332 (1986)].
[12] O. P. Balkashin, R. J. P. Keijsers, H. van Kempen, Yu. A. Kolesnichenko, and O. I. Shklyarevskii, Phys. Rev. B **58**, 1294 (1998).
[13] O. P. Balkashin, I. K. Yanson, A. Halbritter, and G. Mihály, Solid State Commun. **118**, 623 (2001).
[14] O. P. Balkashin, I. K. Yanson, A. Halbritter, and G. Mikhály, Fiz. Nizk. Temp. **27**, 1386 (2001) [Low Temp. Phys. **27**, 1021 (2001)].
[15] O. P. Balkashin and Yu. A. Pilipenko, Fiz. Tverd. Tela (Leningrad) **33**, 2584 (1991) [Phys. Solid State **33**, 1460 (1991)].
[16] R. C. Ruhl, B. C. Giessen, M. Cohen, and N. J. Grant, Acta Metall. **15**, 1693 (1967).
[17] A. V. Khotkevich and I. K. Yanson, *Atlas of Point Contact Spectra and Electron-Phonon Interactions in Metals*, Klewer, Dordrech (1995), Naukova Dumka, Kiev (1986).
[18] I. O. Kulik and M. V. Moskalets, Fiz. Nizk. Temp. **15**, 405 (1989) [Sov. J. Low Temp. Phys. **15**, 229 (1989)].
[19] I. O. Kulik, JETP Lett. **41**, 370 (1985).
[20] I. K. Yanson, O. P. Balkashin, and Yu. A. Pilipenko, JETP Lett. **41**, 373 (1985).
[21] V. V. Nemoshkalenko, A. V. Romanova, A. G. Il'inskiĭ, A. V. Maslov, D. Yu. Paderno, Yu. V. Kornyushin, B. G. Nikitin, M. E. Osinovskiĭ, I. Ya. Dekhtyar, É. G. Madatova, M. A. Vasil'ev, T. I. Bratus', V. M. Pan, A. S. Shpigel', and M. P. Voron'ko, *Amorphous Metallic Alloys* [in Russian], Naukova Dumka, Kiev (1987).
[22] O. P. Balkashin and I. I. Kulik, Fiz. Nizk. Temp. **21**, 45 (1995) [Low Temp. Phys. **21**, 32 (1995)].
[23] Yu. G. Naĭdyuk, N. N. Gribov, O. I. Shklyarevskiĭ, A. G. M. Yansen, and I. K. Yanson, Fiz. Nizk. Temp. **11**, 1053 (1985) [Sov. J. Low Temp. Phys. **11**, 580 (1985)].
[24] O. P. Balkashin, Fiz. Nizk. Temp. **24**, 1151 (1998) [Low Temp. Phys. **24**, 863 (1998)].
[25] F. J. Blatt, *Physics of Electronic Conduction in Solids*, McGraw-Hill, New York (1968), Mir, Moscow (1971).
[26] B. G. Livshits, *Physical Properties of Metals and Alloys* [in Russian], Gos. Nauchno-Tekh. Izd. Mashinostr. Lit., Moscow (1959).
[27] P. I. Kripyakevich, *Structural Types of Intermetallic Compounds* [in Russian], Nauka, Moscow (1977).
[28] G. Kreuch and J. Hafner, J. Non-Cryst. Solids **189**, 227 (1995).
[29] L. Borda, A. Halbritter, and A. Zawadowski, cond-mat/0107590 (2001).
[30] O. P. Balkashin, G. L. Sukhodub, and I. K. Yanson, *XXXI Conference on Low Temperature Physics* [in Russian], Moscow (1998), p. 29.
[31] O. P. Balkashin, T. M. Brill, A. G. M. Jansen, G. L. Sukhodub, P. Wyder, and I. K. Yanson, Fiz. Nizk. Temp. **27**, 90 (2001) [Low Temp. Phys. **27**, 69 (2001)].
[32] T. Vegge, J. P. Sethna, Siew-Ann Cheong, K. W. Jacobsen, C. R. Myers, and D. C. Ralph, Phys. Rev. Lett. **86**, 1546 (2001).
[33] A. N. Orlov, *Introduction to the Theory of Defects in Crystals* [in Russian], Vysshaya Shkola, Moscow (1983).
[34] A. S. Bakaĭ, *Polycluster Amorphous Solids* [in Russian], Énergoatomizdat, Moscow (1987).
[35] O. P. Balkashin, I. K. Yanson, V. S. Solov'ev, and A. Yu. Krasnogorov, Zh. Tekh. Fiz. **52**, 811 (1982) [Sov. Phys. Tech. Phys. **27**, 522 (1982)].

Translated by Steve Torstveit

LOW-DIMENSIONAL AND DISORDERED SYSTEMS

On the nature of the contributions to the entropy of Pauling ice

T. V. Lokotosh and O. M. Gorun

*I. I. Mechnikov Odessa National University, ul. Dvoryanskaya 2, 65026 Odessa, Ukraine**
(Submitted November 5, 2001; revised September 13, 2002)
Fiz. Nizk. Temp. **29**, 179–188 (February 2003)

A calculation is presented for the entropy and correlation functions of Pauling ice—a model in which the energy of the microstates can take only two values: zero or infinity. The central point of the proposed approach is the use of a canonical expansion of the thermodynamic functions in irreducible multiparticle correlations. Reduction rules are formulated which establish the relation between the correlation functions of orders $1,\ldots,k-1$ and the kth-order correlation function of the system. The latter is calculated on the basis of the assumption of equal probabilities of all allowed configurations of a compact group of k particles and the normalization condition. The order of approximation is determined by the number of particles k for which the correlations between states is taken into account. It is shown that with increasing k the values of the entropy of two-dimensional ''square ice'' converge nonmonotonically to its exact value obtained by Lieb. The best agreement corresponds to those approximations in which the group of k particles has the lattice symmetry and contains closed loops of hydrogen bonds. The method can be extended to arbitrary lattice systems. © *2003 American Institute of Physics.* [DOI: 10.1063/1.1542412]

INTRODUCTION

Water in the liquid and solid states is a unique substance in terms of the number of behavioral anomalies.[1–3] For example, ordinary ice I_h is not a crystal in the exact meaning of the word, since, while being ordered in respect to the positions of the centers of mass of the molecules, it is completely disordered in respect to the positions of the protons on the hydrogen bond lines.[4,5] With decreasing temperature the spontaneous transition to an ordered state, as required by the third law of thermodynamics, does not occur—hexagonal ice at temperatures $T<T_*$, where $T_*\approx 70$ K is the temperature of the equilibrium phase transition,[2,3] remains in a metastable proton-disordered state. At the same time, for ice with the body-centered cubic lattice the transition to a state of ordering occurs without difficulty.[6]

An important characteristic of hexagonal ice is its residual entropy. Calculations according to the data of calorimetric measurements have shown that ice I_h has a large residual entropy $\Delta s_{\rm res}\approx(0.566\pm 0.032)\times 10^{-23}$ J/K per molecule.[7] This value is close to the value $k_B\ln(3/2)$ obtained by Pauling in 1935[4] in the framework of a simple model of disordered ice and the mean field approximation for pairs of neighboring molecules. This agreement has stimulated a number of papers[8,9] devoted to the theoretical calculation of the residual entropy of ice. A new spike of interest in the calculation of the residual entropy flared up in the late 1960s and early 1970s[10–13] and was motivated not by refinement of the Pauling model but by the intensive development of general mathematical methods of statistical physics. Therefore the calculation of the residual entropy of Pauling ice has been the subject of a much larger number of theoretical papers than has the problem of determining the ground state of hexagonal ice or explaining the negative coefficient of thermal expansion of ice at nitrogen temperatures. Lieb[14] obtained an exact value for the entropy of two-dimensional ice on a square lattice (''square ice''); the result, like the Pauling approximation, had a remarkably simple form: $s_L=(3/2)\ln(4/3)\approx 0.4314$ (in units of k_B). Unfortunately, it has not been possible to generalize Lieb's matrix method to lattices of other types. The presence of an exact solution has made it possible to assess the correctness and rate of convergence of various other statistical approaches that have been used to solve this problem. We shall briefly characterize these approaches.

The most widely used method for calculating the entropy of Pauling ice is the diagram method,[10,12,13] which corresponds to a formal expansion of the entropy in a series in powers of 1/3. Specific calculations of the entropy of ice for three types of lattice—two-dimensional square, face-centered cubic, and hexagonal—have been carried out to the twelfth order of perturbation theory. At the same time, it should be pointed out that the partition function and correlation functions are represented by diagrams of different types,[15] and it is therefore difficult to identify the type of correlations responsible for some particular contribution to the partition function.

In the Kikuchi method of pseudoparticle ensembles[8] the thermodynamic potentials and correlation functions are calculated in a self-consistent manner. However, the procedure of eliminating incompatible states of the pseudoparticles is extremely cumbersome. Although in principle the method permits one to take into account correctly the correlations between states of arbitrarily remote molecules for an arbitrary character of the interaction in the system, in reality it is

possible to calculate only the contributions to the thermodynamic functions due to the correlations of nearest and next-nearest neighbors. This approximation has also been used in a calculation of the residual entropy of Pauling ice (see Ref. 8).

In view of what we have said, it seems advisable to advance the development of correlation methods for construction of the thermodynamic potentials.

The goal of the present study was to calculate the bulk entropy of Pauling ice in the framework of a statistical method based on a consistent accounting of the contributions of the irreducible correlations, which play a decisive role in systems with strong hydrogen (highly directional) bonds. The idea of this method originated in the works by Ruelle,[16] but it was not developed further in those or in subsequent works.

The proposed approach consists in: a) expansion of the entropy in a series in multiparticle correlation functions; b) transformation of a fragment of the series on the basis of reduction rules (relations between the multiparticle probabilities); c) the assertion that the probabilities of all allowed states of a k-particle cluster are equally probable; d) a self-consistent calculation of the correlation functions of orders lower than the number of particles in the cluster. The number k determines the order of perturbation theory. Concrete calculations were done for the cases of a simple square and a three-dimensional hexagonal lattice. A comparison with the results obtained previously by other approaches attest to the good convergence of the series for the entropy.

It should be emphasized that there is a weighty reason to return to the problem of the entropy of Pauling ice. This is the problem of describing the structure and properties of amorphous and highly viscous states of water, in which multiparticle clusters play a decisive role. Our proposed method of irreducible multiparticle correlations is a reliable tool for constructing equations of state of clustered systems. In addition, a model for supercooled water is much more naturally constructed as an expansion of the Pauling ice model rather than an expansion of the liquid–vapor model ordinarily used for the purpose.

1. PAULING MODEL OF PROTON-DISORDERED ICE

It is well known that the main feature of liquid water and ices is the existence of an infinite network of hydrogen bonds, which is regular in ice and irregular in the liquid phase. This is due to the structure of the water molecule, which has two pronounced maxima each in the densities of positive and negative charge, the directions to these maxima from the oxygen atom having a practically tetrahedral coordination. In ice each water molecule forms four hydrogen bonds. In all modifications of ice the hydrogen bonds are close to linear, i.e., they are such that the protons lie practically on the line connecting the two adjacent oxygen atoms.

The allowed distributions of protons can be described by the Bernal–Fowler rules:[17] 1) two hydrogen atoms are found close to each oxygen atom; 2) one and only one proton is located on each bond. Places where these rules are broken are identified as defects. The Bernal–Fowler rules do not uniquely fix the positions of the protons in the system, or, in other words, the orientation of the water molecule.[4] However, as we mentioned above, the transition to the proton-ordered state corresponding to the minimum energy takes tens of thousands of years on account of the low rate of conversion. Therefore, the residual entropy of ice near absolute zero practically coincides with the entropy of the proton disorder near the melting point of ice. The contributions of libron–phonon oscillations to $\Delta s_{\rm res}$ play a subordinate role and can be neglected.[18] The next simplification of the calculations derives from the fact that the energy of the multipole interactions is not only much less than the hydrogen bonding energy of the molecules but also much less than the thermal energy at the melting point ($k_B T_{\rm melt}$). This means that to a first approximation the energy of all the Bernal–Fowler configurations can be assumed equal in a calculation of the entropy of ice. This is the assumption on which Pauling based his model of proton-disordered ice. Let us mention the main approximations that allowed Pauling to evaluate the entropy of ice in the model he proposed.

Each H_2O molecule forms four hydrogen bonds with its nearest neighbors, so that its two protons can be distributed six ways on the four bond lines (see Fig. 1a). Since the number of bonds in the crystal is twice the number of molecules, two of the bonds of a molecule can formally be treated as being attached to it and the other two as being attached to the neighboring molecules. The probability that a proton will be present (or absent) on each of the bonds is equal to 1/2. Accordingly, the probability that two bonds belonging to adjacent molecules will admit a given configuration of a chosen molecule (or, equivalently, a given distribution of its protons) is equal to $(1/2)^2$. Thus the number of states ω and the entropy s per molecule have the following approximate values:

$$\omega \approx \frac{3}{2}, \quad s = \ln \omega \approx \frac{3}{2} \approx 0.405 \quad (\text{in units of } k_B). \qquad (1)$$

These same values were obtained by Slater as a first approximation in a different approach.[9]

We see that the Pauling result is determined solely by the local properties of the network of hydrogen bonds, which are the same for all ices, and corresponds to a situation in which the molecules linked by hydrogen bonds form a Cayley tree. Formulas (1) can be refined, first, by taking into account the correlations between states of remote molecules and the dependence of the entropy of proton disorder on the topological properties of the network of hydrogen bonds, which are determined by the type of crystal lattice[13] (even in the Pauling model).

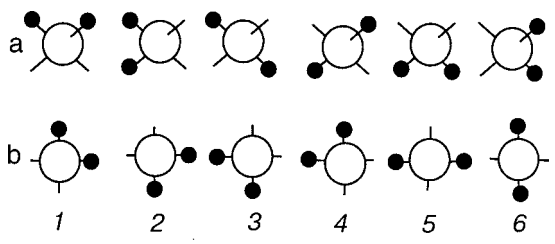

FIG. 1. The six possible ways of distributing two protons of the H_2O molecule on the hydrogen bonds it forms in the three-dimensional (a) and two-dimensional (b) cases. The numbers *1–6* label the states of the molecule corresponding to the different distributions of protons.

An additional reason why the Pauling model is attractive is the probability of constructing a ''square ice'' model on the basis of it. One actually needs only to drop the requirement of tetrahedral coordination of the hydrogen bonds forming each molecule (Fig. 1b). As we have said, this circumstance is unimportant in the Pauling approximation and is not explicitly used in it.

2. CONSTRUCTION OF CORRELATION FUNCTIONS FOR SYSTEMS WITH STRICT EXCLUSION RULES

In the case of Pauling ice we are dealing with a specific system with strict exclusion rules (SSER). By SSER we mean a model system in which the energy of a microstate can only take on two values: zero or infinity. Other examples of SSERs include hard spheres (disks) and long, non-self-intersecting polymer chains (the Flory–Huggins problem). The study of the mathematical properties of SSERs is important because they can be regarded as acceptable zeroth approximations for real systems.

In Pauling ice the energies of all Bernal–Fowler configurations are identical and taken to be zero, while the energies of the configurations containing Bjerrum defects are assumed to be infinite. States with infinite energy are interpreted as forbidden, and therefore the total energy of the system is equal to zero. The nontrivial thermodynamic characteristic of a SSER is its entropy.

The entropy of a system of N particles is expressed in terms of its distribution function $\rho_N(\{\xi_i\})$:

$$S=-\sum_i \sum_{\xi_i} \rho_N(\{\xi_i\})\ln \rho_N(\{\xi_i\}), \tag{2}$$

where $\{\xi_i\}$ is a complete set of variables which uniquely determine the microscopic state of the system, and the index i enumerates the lattice sites.

It is physically obvious that a large part of the information about the state of a system is contained in the low-order correlation functions $\rho_1(\xi_i)$, $\rho_2(\xi_i,\xi_j)$, etc., which are related to $\rho_N(\{\xi_i\})$ by well-known relations. In view of this, it is expedient to write the expression for the entropy in the form of a series (see Ref. 19):

$$S=S_1-S_2-S_3+\ldots, \tag{3}$$

$$S_1=-\sum_i \sum_{\xi_i} \rho_1(\xi_i)\ln \rho_1(\xi_i)=-N\sum_{\xi_1} \rho_1(\xi_1)\ln \rho_1(\xi_1),$$

$$S_2=-\sum_{\langle ij\rangle} \sum_{\xi_i,\xi_j} \rho_2(\xi_i,\xi_j)\ln \frac{\rho_2(\xi_i,\xi_j)}{\rho_1(\xi_i)\rho_1(\xi_j)},$$

$$S_3=-\sum_{\langle ijk\rangle} \sum_{\xi_i,\xi_j,\xi_k} \rho_3(\xi_i,\xi_j,\xi_k) \times \ln \frac{\rho_3(\xi_i,\xi_j,\xi_k)\rho_1(\xi_i)\rho_1(\xi_j)\rho_1(\xi_k)}{\rho_2(\xi_i,\xi_k)\rho_2(\xi_i,\xi_j)\rho_2(\xi_j,\xi_k)}, \tag{4}$$

in which the symbols $\langle ij\rangle$, $\langle ijk\rangle$,... denote all possible samples of particle pairs, triples, etc. Series (3) is an expansion of the entropy in irreducible multiparticle correlations.

The meaning of the term ''irreducible'' is most simply illustrated by the example of a set of three particles. If the state of one of them (k) is statistically independent of the states of the other two particles, then $\rho_3(ijk)$ decomposes into a product $\rho_2(ij)\rho_1(k)$, and a binary correlation function of the type $\rho_2(ik)$ decomposes into a product $\rho_1(i)\rho_1(k)$. As a result, the expression in the argument of the logarithm in the formula for S_3 becomes unity, and the corresponding contribution to the energy is zero. Although no subgroup in a system of interacting particles is exactly statistically independent, the principle of decay of correlations[20] allows one to state that with increasing distance between the various pairs of particles in a subgroup, the irreducible correlations between their states rapidly decay, and the corresponding contributions to the entropy tend toward zero.

Let us consider an approximation in which series (3) is truncated at the kth term. In other words, we shall neglect all the irreducible correlation effects above the kth order. Let us discuss the character of the different distributions to the kth term of series (3) in more detail. All possible samples of k particles can be divided into linked and unlinked. In a linked sample any two molecules can be connected by broken lines (forming the ''bonds'' of the lattice) that pass only through sites of the sample itself. Further, on the set of linked k-samples one can always identify a configuration that is the most compact (i.e., the configuration with minimum diameter).

From a physical standpoint the main role is played by the contributions of compact configurations of k particles. For such configurations the behavior of the k-particle correlation function is determined mainly by interactions taking place within the sample itself (we shall call it a k-cluster). In this case $\rho_k^{(k)}(\ldots)$ (the upper index here and below will denote the order of approximation) can be constructed directly from ''first principles.'' In particular, in a SSER one can use the principle of equal probability of all allowed configurations of a k-cluster to determine the highest-order correlation function. All the lower-order correlation functions, $m<k$, are determined on the basis of the higher-order ones with the aid of rigorous reduction relations.

A formula for calculating the approximate value of the entropy $S^{(k)}$ for different values of k can be written in the form

$$S^{(k)}=S_1^{(k)}+S_2^{(k)}+S_3^{(k)}+\ldots+S_k^{(k)}, \tag{5}$$

where $S_m^{(k)}$ is the sum of irreducible contributions over all possible sets of m particles belonging to a compact k-cluster. With increasing k the value of $S^{(k)}$ approaches a limit which naturally coincides with the entropy of the system.

The stated approach is internally consistent, since we are neglecting irreducible correlation effects higher than kth order both in truncating the entropy series (3) and in determining the highest-order correlation function. We note that its consistency is a consequence of the fact that only compact configurations are reflected in it. In the noncompact groups of particles the correlations do not have such a direct (energy-related) character, since they are mediated by correlations with molecules that do not belong to the sample. The highest-order correlation function of such a sample must be determined by a correlation function of higher order.

The optimal value of k depends on the specifics of the interparticle interactions. For Pauling ice and other SSERs, k should be larger than unity. This is because the single-

particle approximation (actually the mean field approximation) is inapplicable, since it is unable to incorporate the exclusion rule. It follows from physical considerations that the best approximation for the correlation function and entropy should be obtained for values of k that correspond to clusters whose symmetry coincides with the point symmetry of the lattice. For a square lattice this requirement is satisfied by clusters with $k=4,5,9,\ldots$, which are square ($k=4,9$) and cross-shaped ($k=5$) (see below). The requirements of compactness and symmetry do not depend on the specifics of the interaction. In the case of systems with hydrogen bonds an additional factor influencing the accuracy of the calculations is the presence of closed loops of hydrogen bonds in the cluster. In particular, in 4- and 9-particle clusters all the loops of hydrogen bonds are closed, while in the 5-particle cluster there are no closed loops. The leading role of clusters with closed loops of hydrogen bonds is explained by the fact that for them the multiparticle correlations are taken into account most completely.

In systems with a strong anisotropic interaction, in which microscopically nonuniform structures can arise, the value of k should be matched with the size of the region of nonuniformity.

The entropy $S^{(k)}$ of Pauling ice will take on its maximum value in the case when all the allowed states of the k-cluster are assumed equiprobable.[20] Thus for a SSER the principle of maximum entropy allows us to approximate the k-particle correlation function of the system by the expression

$$\rho_k^{(k)}(\xi_1,\xi_2,\ldots,\xi_k)=\begin{cases}1/P_k & \text{for allowed states,}\\ 0 & \text{for forbidden states,}\end{cases} \tag{6}$$

where $P_k=\Sigma_{\xi_1,\ldots,\xi_k}\Delta(0,\varepsilon(\xi_1,\ldots,\xi_k))$ is the number of allowed states of the compact group of k molecules. Here $\Delta(0,\varepsilon)$ is the Kronecker delta. The upper index in $\rho_m^{(k)}$ indicates the order of approximation, and the lower index is the order of the correlation function.

Let us consider a way of finding the values of the low-order correlation functions of a k-cluster for a specific example, when $k=5$. On a two-dimensional square lattice in the five-particle approximation the most compact distribution of molecules corresponds to the situation when the central molecule (see Fig. 2) is considered together with its four nearest neighbors (a cross-shaped configuration). The total number of different states of the 5-cluster is $P_5=6\cdot 3^4$. In particular, let us find the correlation function $\rho_2'^{(5)}$ of the molecules lying at opposite vertices of the minimal square. Of the two possible variants of the distribution of the vertices, we choose the one corresponding to the unit vector $\mathbf{n}_0$ in Fig. 2. Let the molecule in the lower right-hand corner of the square be found in the state labeled *1* in Fig. 1, and let the molecule in the upper left-hand corner be in state *4*.

Two pairs of molecules in the cross $(1,2$ and $1',2')$ are arranged in the required way. These two pairs should both be taken into account on an equal footing in the calculation of $\rho_2'^{(5)}(1,4)$. The number of states of the 5-cluster in which molecules 1 and 2 are found in states *1* and *4* is $P_{12}(1,4)=9$. At the same time, for molecules $1'$ and $2'$ this number is $P_{1'2'}(1,4)=18$. This difference is due to the different number of allowed states of the central molecule 0 in the specified states of the molecules at the indicated vertices of the square. Therefore, $\rho_2'^{(5)}(1,4)$, defined as the ratio of the number of favorable outcomes to the total number, is given by

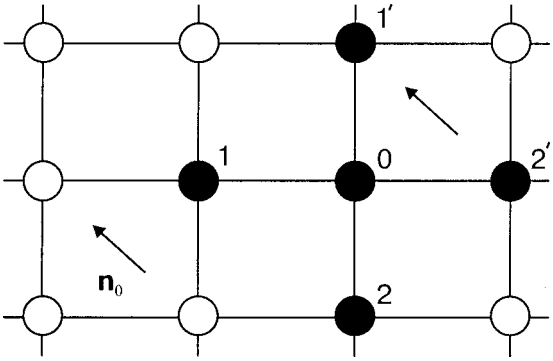

FIG. 2. Five-particle cluster (“cross”). It contains two pairs of molecules connected by horizontal hydrogen bonds (1–0 and 0–2′) and two equivalent pairs of next-nearest neighbors (1–2 and 1′–2′).

$$\rho_2'^{(5)}(1,4)=\frac{P_{12}(1,4)+P_{1'2'}(1,4)}{2P_5}=\frac{1}{36}\ .$$

It can be verified that for the pairs of molecules distributed as indicated above, the correlation function $\rho_2'^{(5)}$ assumes this same value for 16 out of the 36 possible states of a pair. In ten states $\rho_2'^{(5)}=1/27$, and in the remaining 10 states it equals 1/54.

This method of calculating the correlation function can also be applied for all the other groups of molecules with $m<5$ of the five-particle cluster and also in the general case. The basic feature of this method is the determination of all the correlation functions $\rho_m^{(k)}(\ldots)$, $m<k$ from the correlation function $\rho_k^{(k)}$ of the cluster as a whole. The relations between $\rho_m^{(k)}$, $m<k$ and $\rho_k^{(k)}$ have the meaning of reduction rules.

It is important to note that these reduction rules have a substantially different character from the standard relations

$$\rho_{k-1}(\xi_1,\ldots,\xi_{k-1})=\sum_{\xi_k}\rho_k(\xi_1,\ldots,\xi_k) \tag{7}$$

for the exact correlation functions of a system. Indeed, it follows from (7) that

$$\rho_{k-2}(\xi_1,\ldots,\xi_{k-2})=\sum_{\xi_{k-1}\xi_k}\rho_k(\xi_1,\ldots\xi_k).$$

In our approach the relation between the correlation functions $\rho_{k-1}^{(k)}$ and $\rho_k^{(k)}$ is given by a formula similar to (7):

$$\rho_{k-1}^{(k)}(\xi_1,\ldots\xi_{k-1})=\sum_{\xi_k}\rho_k^{(k)}(\xi_1,\ldots,\xi_k),$$

but the relation

$$\rho_{k-2}^{(k)}(\xi_1,\ldots,\xi_{k-2})=\sum_{\xi_{k-1}}\rho_k^{(k)}(\xi_1,\ldots,\xi_k)$$

is no longer valid. This is because adding a particle to a subgroup of $(k-1)$ particles to bring it to a compact k-cluster ($k\sim 10$) can only be done in one way. At the same time, to obtain a k-particle cluster by adding two particles to a subgroup of $(k-2)$ particles can be done in several ways.

In constructing $\rho_{k-2}^{(k)}$ one must take all of these possibilities into account. This way of calculating $\rho_{k-2}^{(k)}$ turns out to be completely consistent with the probabilisitic meaning of the correlation function. What we have said applies to all the lower-order correlation functions.

When all the possible correlations in an ensemble of $N\sim 10^{23}$ particles are taken into account, such problems do not arise, and relation (7) does apply.

3. CALCULATION OF THE ENTROPY OF "SQUARE ICE" IN DIFFERENT APPROXIMATIONS FROM THE IRREDUCIBLE CORRELATION FUNCTIONS

The features of the calculation of the bulk entropy of Pauling ice by the method of series expansion in irreducible correlation functions are most conveniently discussed for the extremely simple example of square ice.

When the physical equivalence of all the lattice sites is taken into account, the single-particle contribution to the entropy per site is given by the formula

$$s_1^{(1)}=-\sum_{\xi_1}\rho_1^{(1)}(\xi_1)\ln\rho_1^{(1)}(\xi_1). \tag{8}$$

A molecule at a site can be found in six different states (see Fig. 1), which in the single-particle approximation should be treated as equiprobable. Therefore

$$\rho_1^{(1)}(\xi_1)=1/6, \quad \xi=1,...,6 \tag{9}$$

and

$$s^{(1)}=\tilde{s}_1^{(1)}=\ln 6\approx 1.792. \tag{10}$$

This value of the entropy is more than four times as large as the exact value,[14] since in the single-particle approximation the restrictions on the states of pairs of hydrogen-bonded molecules are not taken into account.

In the two-particle approximation we must consider pairs of nearest neighbors. For any state of the first molecule of a pair, the second can be found in only three of the six possible states. Thus, of the 36 states of a pair, only 18 are allowed, so that

$$\rho_2^{(2)}(\xi_1,\xi_2)=\begin{cases}1/18 & \text{for allowed states,}\\ 0 & \text{for forbidden states.}\end{cases} \tag{11}$$

The single-particle probabilities $\rho_1^{(2)}(\xi)$, as may easily be seen, remain the same in the two-particle as in the single-particle approximation.

Taking into account the reduction rules, the equivalence of all pairs of molecules, and also the fact that the number of pairs of nearest neighbors is twice the number of lattice sites, we can write the entropy per molecule in the two-particle approximation [see formula (4)] in the form:

$$s^{(2)}=2\tilde{s}_2^{(2)}-3\tilde{s}_1^{(2)}, \tag{12}$$

where

$$\tilde{s}_1^{(2)}=s_1^{(1)}, \quad \tilde{s}_2^{(2)}=-\sum_{\xi_1,\xi_2}\rho_2^{(2)}(\xi_1,\xi_2)\ln\rho_2^{(2)}(\xi_i,\xi_2).$$

Substituting (9) and (11) into the expressions for $\tilde{s}_1^{(2)}$ and $\tilde{s}_2^{(2)}$, we obtain $\tilde{s}_2^{(2)}=\ln 18\approx 2.8904$ and $\tilde{s}_1^{(2)}=\ln 6\approx 1.7918$ and the value

$$s^{(2)}\approx 0.405, \tag{13}$$

which agrees with the Pauling result.[4] It is somewhat smaller than the exact value.[14] We note that in the case of a two-dimensional square lattice the correlations between all the nearest neighbors are taken into account completely only starting in the five-particle and higher approximations.

The next correction to the value of the entropy comes from taking into account the correlations in the states of three "mutually nearest" molecules. There exist two physically different types of such configurations: 1) a "corner"—the configuration formed by molecules $1-0-1'$ in Fig. 2; and 2) a "segment"—three molecules lying on a straight line, like molecules $1-0-2'$ in Fig. 2. In the three-particle approximation these configurations are statistically equivalent. Taking into account that the numbers of "corners" and "segments" are, respectively, four times and twice the number of lattice sites, we find

$$s^{(3)}=6\tilde{s}_3^{(3)}-10\tilde{s}_2^{(3)}-2\tilde{s}_{2'}^{(3)}+7\tilde{s}_1^{(3)}, \tag{14}$$

where

$$\tilde{s}_3^{(3)}=-\sum_{\xi_1,\xi_2,\xi_3}\rho_3^{(3)}(\xi_1,\xi_2,\xi_3)\ln\rho_3^{(3)}(\xi_1,\xi_2,\xi_3),$$
$$\tilde{s}_{2'}^{(3)}=-\sum_{\xi_1,\xi_2}\rho_{2'}^{(3)}(\xi_1,\xi_2)\ln\rho_{2'}^{(3)}(\xi_1,\xi_2). \tag{15}$$

In $\tilde{s}_3^{(3)}$ and $\tilde{s}_{2'}^{(3)}$ the summation is over states of particles in the "corners" and "segments," and the prime denotes the pair correlation function for non-hydrogen-bonded molecules in these same configurations.

It is easy to see that in formula (6) one has $P_3=54$, while $\rho_1^{(3)}$ and $\rho_2^{(3)}$ have the same values as in the two-particle approximation. At the same time, the pair correlation function $\rho_2^{(3)}$ takes the value 1/54 for 18 orientations of the pair of molecules, and 1/27 for the other 18. Accordingly,

$$\tilde{s}_3^{(3)}=\ln 54, \ \tilde{s}_2^{(3)}=\ln 18,$$
$$\tilde{s}_{2'}^{(3)}=\frac{1}{3}\ln 54+\frac{2}{3}\ln 27, \ \tilde{s}_1^{(3)}=\ln 6.$$

Substituting the values of $\tilde{s}_p^{(3)}$, $p=1,2,2',3$ into formula (14), we obtain $s^{(3)}\approx 0.519$. We see that taking three-particle correlations into account leads to a worsening of the agreement of the approximate and exact values of the entropy.

We note that the topological properties of the lattice do not play a role in the two- and three-particle approximations. This is because of the absence of closed loops of hydrogen bonds in the k-clusters for $k=2,3$. We encounter a different situation in the four-particle approximation, in which the 4-cluster represents 4 molecules lying at the vertices of the square and forming a closed loop of bonds.

For any state of the molecule A in Fig. 3, molecules B and D can each be found in three different states. However, depending on the states B and D, molecule C can be found either in one or in two states. A simple calculation shows that $P_4=82$, so that the probability of each allowed state is equal to 1/82. If the four molecules formed an unclosed chain of three bonds, the number of states would be equal to $6\cdot 3^3$. Another important consequence of the existence of a closed

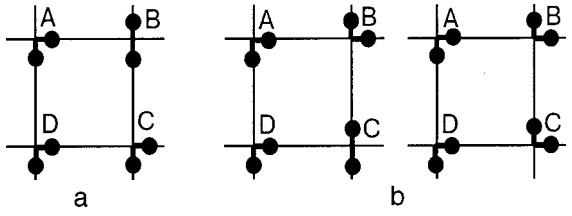

FIG. 3. Examples of configurations of the 4-cluster (''square''): the states of molecules A, B, and D uniquely determine the state of molecule C (a); there are two allowed orientations of molecule C (b).

loop of hydrogen bonds is that the single-particle probabilities $\rho_1^{(4)}$ are different from 1/6, and the two-particle probabilities for the allowed states of a pair of nearest neighbors is different from the values in the two- and three-particle approximations ($\rho_2^{(2)}=\rho_2^{(3)}=1/18$). One can readily verify by a direct calculation that the preferred states of a molecule are those with the protons lying in a straight line, for which $\rho_1^{(4)}=28/164$. The states with protons on perpendicular straight lines, labeled *1–4* in Fig. 1, are more rarely encountered: $\rho_1^{(4)}=27/164$. Among the five physically nonequivalent configurations of a pair, the most common configuration is that in which the protons of each of the molecules lie in a straight line. Its probability is equal to 10/164.

By simple identity transformations the explicit expression for $s^{(4)}$ is brought to the form

$$s^{(4)}=\tilde{s}_4^{(4)}-2\tilde{s}_2^{(4)}+\tilde{s}_1^{(4)}, \tag{16}$$

$$\tilde{s}_4^{(4)}=-\sum_{\xi_1,\ldots,\xi_4}\rho_4^{(4)}(\xi_1,\xi_2,\xi_3,\xi_4)\ln\rho_4^{(4)}(\xi_1,\xi_2,\xi_3,\xi_4). \tag{17}$$

We see that the three-particle correlation functions do not appear in $s^{(4)}$, nor do the pair correlation functions for the states of the molecules lying on the diagonals of the square. The latter belong to four 4-clusters simultaneously (Fig. 4). We note that expression (16) is in complete agreement with the result obtained by the Kikuchi pseudoensembles method,[8] but, unlike that method, it is derived without elaborate lines of reasoning and mathematical complexities. With the numerical values of the corresponding correlation functions substituted in, we have

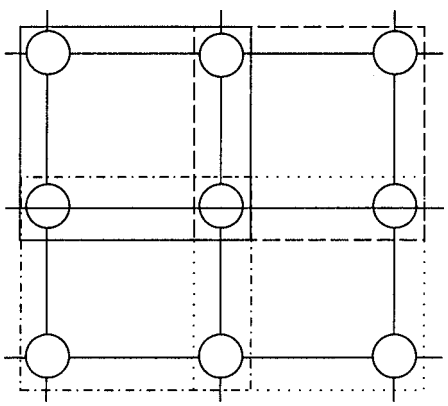

FIG. 4. Four adjacent 4-clusters. The common elements are pairs of adjacent molecules and individual molecules (each site belongs to four clusters).

$$\tilde{s}_4^{(4)}=\ln 82\approx 4.4067,$$

$$\tilde{s}_2^{(4)}=\frac{15}{41}\ln\frac{82}{5}-\frac{18}{41}\ln\frac{164}{9}+\frac{8}{41}\ln\frac{41}{2}\approx 2.8871,$$

$$\tilde{s}_1^{(4)}=\frac{14}{41}\ln\frac{41}{7}-\frac{27}{41}\ln\frac{164}{27}\approx 1.7916.$$

These values together with (16) lead to an estimate $s^{(4)}\approx 0.424$. Thus taking into account the configurations forming closed loops of hydrogen bonds leads to a significant improvement in the result, which, by the way, is now practically in agreement with the values of the entropy found by the diagram method in Refs. 10–13.

In the five-particle approximation the 5-cluster is cross-shaped (see Fig. 2), and in the six-particle approximation it is a 2×1 rectangle. It is clear that although these approximations are very different qualitatively, one can assume beforehand that neither will improve upon the result obtained in the four-particle approximation. Indeed, in the case of the ''cross'' there are no closed loops of hydrogen bonds. In the six-particle approximation we have two types of closed loops, but the symmetry of the compact cluster is lower than the symmetry of the lattice. The values of P_5 and P_6 are equal to $6\cdot 3^4$ and 374, respectively. We shall omit the intermediate calculations and just give the results for the entropy in these approximations:

$$s^{(5)}=\tilde{s}_5^{(5)}-2\tilde{s}_2^{(5)}-2\tilde{s}_{2'}^{(5)}+4\tilde{s}_1^{(5)},$$

$$s^{(6)}=2\tilde{s}_6^{(6)}-3\tilde{s}_4^{(6)}-2\tilde{s}_3^{(6)}+4\tilde{s}_2^{(6)}-\tilde{s}_1^{(6)}, \tag{18}$$

where the notation has the same meaning as before. Plugging in the numerical values,

$$\tilde{s}_5^{(5)}=\ln 486\approx 6.1862m \quad \tilde{s}_2^{(5)}=\ln 18\approx 2.8904,$$

$$\tilde{s}_{2'}^{(5)}\approx 3.5520, \quad \tilde{s}_1^{(5)}=\ln 6\approx 1.7918,$$

we find $s^{(5)}\approx 0.469$. Similarly, with

$$\tilde{s}_6^{(6)}=\ln 374\approx 5.9243,\ \tilde{s}_4^{(6)}\approx 4.4049,\ \tilde{s}_3^{(6)}\approx 3.9820,$$

$$\tilde{s}_2^{(6)}\approx 2.8760, \quad \tilde{s}_1^{(6)}\approx 1.7915$$

we get $s^{(6)}\approx 0.383$.

The single-particle probabilities in the six-particle approximation $\rho_1^{(6)}$ for the equivalent states *1–4* and *5, 6* are equal to 0.164 and 0.172, respectively.

Thus we can conclude that the best approximation corresponds to the situation when the compact cluster contains various closed loops of hydrogen bonds and the symmetries of the cluster and lattice coincide. After the four-particle cluster, these properties are possessed by the 9-particle cluster, which is a 2×2 square, for which $P_9=2604$. In this approximation the entropy is given by the formula

$$s^{(9)}=\tilde{s}_9^{(9)}-2\tilde{s}_6^{(9)}+\tilde{s}_4^{(9)}. \tag{19}$$

Determining the numerical values of the correlation functions for the different allowed configurations of compact clusters of six, four, three, and two molecules and the probabilities of single-particle states of the two types, we find

$$s^{(9)}=7.864804-2\cdot 5.921714-4.407329\approx 0.4287.$$

TABLE I.

k	1	2	3	4	5	6	9
P_k	6	18	54	82	486	374	2604
$s^{(k)}$	1.7918	0.4055	0.5187	0.4242	0.4684	0.3825	0.4287
ρ_1^k(I)	0.16(6)	0.16(6)	0.16(6)	0.170	0.16(6)	0.172	0.174
ρ_1^k(II)	0.16(6)	0.16(6)	0.16(6)	0.165	0.16(6)	0.164	0.163

The relative error is around 0.7%. A very similar value was found in Ref. 13 in the twelfth order of perturbation theory: $S_{\text{diagr}}^{(12)} \approx 0.4283$.

The results obtained for the entropy and the single-particle averages $\rho_1^{(k)}$(I) and $\rho_1^{(k)}$(II), where I=5 or 6 and II takes one of the values *1–4*, are collected in Table I.

It is seen that with increasing size of the cluster within which the irreducible multiparticle correlations are taken into account, the entropy and the single-particle averages change nonmonotonically. The smallest deviation from the exact results[14] corresponds to clusters with $k=4$ and 9, the symmetry of which coincides with the lattice symmetry and in which the hydrogen bonds form closed loops. From this standpoint one expects that for further refinement of the entropy value it will be necessary to consider a 16-particle cluster (a 3×3 square).

The values of the single-particle averages $\rho_1^{(9)}$(I) and $\rho_1^{(9)}$(II) can be compared only with the results obtained in Ref. 15 by the diagram method in the approximation of loops containing 12 hydrogen bonds: $\rho_1^{(12)}(\text{I})=0.190$ and $\rho_1^{(12)}(\text{II})=0.155$. We stress that in the approach taken here, the calculation of the correlation functions $\rho_m^{(k)}$ with $m \leqslant k$ precedes the calculation of the entropy, and therefore the accuracies to which the entropy and correlation functions are determined are assumed to be the same. In the diagram methods the correlation functions are constructed independently of the partition function, and there is thus no consistent control of the random errors. Moreover, in the method of irreducible correlation functions the normalization condition is imposed on the correlation functions of all orders $m \leqslant k$, making it possible to avoid omissions or repeated counting of physically equivalent states of the samples. In the diagram method there is no analogous ''sum rule'' for the topologically nonequivalent loops with a specified number of ''bonds,'' and that makes it harder to monitor the random errors.

4. ENTROPY OF HEXAGONAL ICE

Let us turn to a calculation of the entropy of three-dimensional hexagonal Pauling ice. As we have said, the values of the entropy in the pair and three-particle approximations, $s^{(2)}$ and $s^{(3)}$, do not depend on the topology of the lattice and therefore are the same for the square and hexagonal ices. In hexagonal ice the minimal closed contour of hydrogen bonds is formed by six molecules, and we shall therefore calculate the entropy in the six-particle approximation. We note that the molecules making up a hexagonal ring of hydrogen bonds do not form the most compact group of particles. Both requirements—the presence of closed loops of hydrogen bonds and the coincidence of the cluster and lattice symmetries—are satisfied only for a 26-particle cluster.

We take into account that hexagonal ice has two types of closed rings of six hydrogen bonds (Fig. 5), the so-called ''armchair'' and ''hat.''[3] The numbers of ''armchairs'' and ''hats'' are half and 1.5 times the number of lattice sites, respectively. The number of possible states of the ''armchair'' (a) and ''hat'' (h) types are the same, $P_6(a) = P_6(h) = 730$, so that the probability of each allowed state of the six molecules of a ring is equal to 1/730.

After some identity transformations, the extremely awkward initial expression for $s^{(6)}$ takes the form

$$s^{(6)} = \frac{1}{2}\tilde{s}_6(a) + \frac{3}{2}\tilde{s}_6(h) - \frac{3}{2}\tilde{s}_4(h) - 3\tilde{s}_3(a) + \frac{3}{2}\tilde{s}_2(a) - \tilde{s}_2(h) + \frac{1}{2}\tilde{s}_{2'}(h) + 2\tilde{s}_1, \tag{20}$$

where the symbols a and h label the contributions belonging to the ''armchair'' and ''hat'' conformations, respectively. The calculation gives $s^{(6)} \approx 0.409$.

This value agrees to an accuracy of 2% with the result of Ref. 13, which was found by the diagram method with all the closed loops containing 12 hydrogen bonds taken into account. A very close value for the entropy of cubic ice was obtained in Ref. 12 by a semiphenomenological method with the minimal closed loops, also containing 6 bonds, taken into account: $s_{\text{cub}}^{(6)} \approx 0.408$.

Thus we are convinced of the good convergence of the sequence $s^{(k)}$ of approximate values of the entropy obtained from consideration of the truncated series (3). In addition, the results of the calculation directly attest to the largeness of the irreducible multiparticle correlation effects in ice or, more generally, in systems with strong hydrogen bonds. Effects of this kind may be responsible for the formation of clusters of mesoscopic size in liquid water.

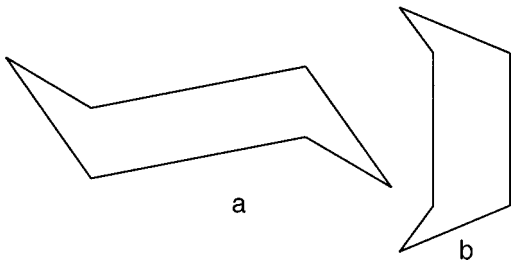

FIG. 5. Conformations of the minimal closed loops of hydrogen bonds in hexagonal ice: the ''armchair'' type (a) and the ''hat'' type (b).

CONCLUSION

In this paper we have calculated the bulk entropy of proton-disordered ice in the framework of the Pauling model on the basis of a series expansion of the entropy in the contributions of irreducible multiparticle correlations. We have shown that a leading role is played by the contributions of compact groups of molecules and that the sequence of approximate values $s^{(k)}$ of the entropy is not a monotonic function of the cluster size. The best approximations correspond to situations in which the k-cluster has the symmetry of the lattice and contains several types of closed loops of hydrogen bonds.

The method of expanding the entropy in a series in irreducible multiparticle correlation functions (IMCFs) is conceptually similar to the Kikuchi pseudoensembles method,[8] which is also based on examining the correlations within compact groups of molecules. However, the mathematical implementation of the Kikuchi algorithm is considerably more complicated.

The IMCF method is also extremely efficient for constructing the equation of state of the two- and three-dimensional Ising models. There, however, it is necessary to take into account the interaction of the boundary spins of the clusters with the spins that do not belong to the clusters. From a physical standpoint this step is necessitated by the presence of a long-range magnetic interaction, which makes that problem different from the Pauling ice problem.

The first results in the IMCF method were obtained for a system of hard disks.[20] The dependence of the entropy and isothermal compressibility on the relative area φ occupied by the disks, $S \approx S^{(k)}(\varphi)$ and $\beta \approx \beta^{(k)}(\varphi)$, was determined for $k=2,3,4$. These functions can be used to estimate the maximum admissible value $\overline{\varphi}$ that limits the existence of the isotropic phase. An estimate of $\overline{\varphi}$ for $k=4$ is in satisfactory agreement with the computer data.

The statistical approach proposed in this paper also works successfully for finding the entropy of another well-known SSER model—a solution of ideal polymer chains.

The authors thank Prof. N. P. Malomuzh for helpful discussions and criticism.

*E-mail: mnp@uk2.net

[1] E. H. Stanley, S. V. Buldyrev, M. Canpolat, M. Meyer, O. Mishima, M.-R. Sadr-Lahijany, A. Scala, and F. W. Starr, Physica D **133**, 453 (1999).
[2] E. Whalley, ''Structure problems of ice,'' in *Physics of Ice*, Plenum Press, New York (1969), p. 19.
[3] V. F. Petrenko and R. W. Whitworth, *Physics of Ice*, Oxford University Press (1999), p. 252.
[4] L. Pauling, J. Am. Chem. Soc. **57**, 2680 (1935).
[5] V. M. Nield, J.-C. Li, D. K. Ross, and R. W. Whitworth, Phys. Scr. T **57**, 179 (1955).
[6] Ph. Pruzan, J. C. Chervin, and B. Canny, J. Chem. Phys. **97**, 718 (1992).
[7] O. Haida, T. Matsuo, H. Suga, and S. Seki, J. Chem. Thermodyn. **6**, 815 (1974).
[8] R. Kikuchi, Phys. Rev. **81**, 988 (1951).
[9] J. C. Slater, J. Chem. Phys. **9**, 16 (1941).
[10] E. A. DiMarzio and F. H. Stillinger, J. Chem. Phys. **40**, 1577 (1964).
[11] L. Onsager and M. Dupuis, Rend. Scoula Intern. FS. Corso **10**, 294 (1960).
[12] G. T. Hollins, Proc. Phys. Soc. **84**, 1001 (1964).
[13] J. F. Nagle, J. Math. Phys. **7**, 1484 (1966).
[14] E. H. Lieb, Phys. Rev. Lett. **18**, 435 (1967).
[15] A. Yanagawa and J. F. Nagle, Chem. Phys. **43**, 329 (1979).
[16] D. Ruelle, *Statistical Mechanics: Rigorous Results*, Benjamin, New York (1969), Mir, Moscow (1971).
[17] J. D. Bernal and R. H. Fowler, J. Chem. Phys. **1**, 515 (1933).
[18] R. Howe and R. W. Whitworth, J. Chem. Phys. **90**, 4450 (1989).
[19] I. Z. Fisher, *Statistical Theory of Liquids* [in Russian], Gos. Izd. Fiz.-Mat. Lit., Moscow (1961).
[20] T. V. Lokotosh and N. P. Malomuzh, J. Mol. Liq. (2002) (to be published).

Translated by Steve Torstveit

One-dimensional model of a vortex in an easy-plane ferromagnet

A. S. Kovalev* and J. E. Prilepsky

B. Verkin Institute for Low Temperature Physics and Engineering, National Academy of Sciences of Ukraine, pr. Lenina 47, 61103 Kharkov, Ukraine

(Submitted August 14, 2002)
Fiz. Nizk. Temp. **29**, 189–204 (February 2003)

A simple one-dimensional model of a ferromagnet in a vortex configuration is proposed for qualitative description of the structure and dynamics of a vortex in a two-dimensional magnetic system. The model describes a system of four parallel spin chains with single-ion anisotropy of the easy-plane type and includes elements of both the continuum (along the chains) and discrete (perpendicular to the chains) descriptions. An analytical study is made of the static vortices and moving vortex solutions of stationary profile. The analytical results of a calculation of the static structure of the vortices are supplemented by a numerical analysis for the analogous discrete systems and are in good agreement with the numerical data. The approach is generalized to the case of the description of gyrotropic motion of vortices of stationary profile in the framework of the collective variables method for the combined continuum–discrete description. The results are analyzed and compared with the data for two-dimensional magnets. © *2003 American Institute of Physics.* [DOI: 10.1063/1.1542413]

1. INTRODUCTION

Studies of the structure and dynamics of magnetic vortices in two-dimensional ferromagnets with anisotropy of the easy-plane type have recently been attracting significant attention on account of the fact that the magnetic phase transition in such systems takes place in accordance with the Berezinskiĭ–Kosterlitz–Thouless mechanism and is accompanied by the formation of a large number of vortices.[1] On the other hand, a significant number of two-dimensional and quasi-two-dimensional compounds have now been obtained (a list of references and a brief review are given in Ref. 2), and so there is a heightened interest in studying them. In very recent years the experimental study of magnetic nanodots[3,4] and artificial two-dimensional lattices of them[5] has become one of the most interesting areas in the physics of magnetic phenomena, as these might serve as a basic element of new technical devices. Experiments show that for certain ratios of the the transverse dimensions to the thickness of the magnetic dots, magnetic vortices are observed in them. However, the theoretical study of two-dimensional magnetic vortices is a rather complicated problem. Although the structure of the vortices and their motion and internal dynamics have been investigated in some detail in a number of studies (see, e.g., Refs. 2 and 6–9), the majority of the results have been obtained in the collective variables method (CVM) or by direct numerical integration of the equations of spin dynamics of the lattice. At the same time, in any approach important information can be lost concerning the dependence of the dynamics and structural properties of the vortices on the parameters of the system, so that models which admit an analytical treatment are extremely important for gaining a qualitative understanding and finding an explanation of the results of experiments and numerical simulations.

The simplest models of this kind describe small fragments of the spin lattice—spin plaquettes.[10] In recent years the theoretical study of spin plaquettes has acquired additional significance in connection with experimental research on some new objects in the physics of magnets: magnetic molecules.[11] An exact analytical treatment of spin plaquettes[10] gives a rather clear explanation of the phenomena related to the internal modes of such a system in a vortex configuration. However, because of the small size of a plaquette, one cannot consider the motion of a vortex in such a model.

In this paper we propose a one-dimensional model for describing the vortex properties in an anisotropic easy-plane Heisenberg ferromagnet. The model admits solutions of the vortex type and can give a qualitative explanation of the features of vortex dynamics in a two-dimensional magnetic system. The first one-dimensional model of two-dimensional topological defects was proposed by Frenkel and Kontorova[12] for describing dislocations in a crystal lattice. In spite of its one-dimensional character, that model gives a rather accurate description of the core structure of a dislocation and its dynamics and has been used successfully for more than 60 years.[13] Later a similar 1D model was proposed[14] for describing complex magnetostructural topological defects. In our case the study of the proposed 1D model is also of important methodological significance: it is simultaneously a continuum and a discrete model, depending on the direction, and it is therefore possible to study the influence of the discreteness of the system on the topological characteristics of defects (their ''topological charges'').

The main feature of the proposed model and the dynamical equations for the magnetization are described in Sec. 2. Section 3 is devoted to an analysis of the static in-plane vortex (IPV) solution in the model: analytical expressions are obtained for the distribution of the spins in IPV, and the stability of this vortex solution is investigated. In addition to the analytical treatment, for the analogous discrete systems of finite size we present numerical results on the determina-

tion of the value of the anisotropy parameter at which the IPV becomes unstable. We examine the static out-of-plane vortex (OPV) solution arising in the proposed model (see Sec. 4). An analytical treatment for the case of weak easy-plane anisotropy is also supplemented by data from a numerical analysis of the analogous discrete systems of finite size. The dynamical properties of the OPV are investigated (Sec. 5). Expressions for the magnetization distribution in a vortex of stationary profile are obtained for the cases of ''fast'' and ''slow'' vortices. It is emphasized that the moving OPV exhibits the characteristic asymmetry of gyrotropic motion. A version of the CVM approach[2,27] is proposed for the case of a combined continuum–discrete description of the system, and a simplified effective equation of motion for the center of the vortex is derived. The results are summarized and compared to those from an analysis of two-dimensional systems (Sec. 6).

2. MODEL AND EQUATIONS OF SPIN DYNAMICS

The simplest model that admits an analytical treatment of the statics and dynamics of magnetic vortices is a system of two ferromagnetic spin chains with easy-plane anisotropy (only single-ion anisotropy is considered). Such a model admits a solution with a vortex configuration in which all the spins lie in the easy plane. However, such an extremely simplified model cannot be used to describe a more interesting type of vortex, in which the magnetization vector can deviate from the easy planes. It is therefore necessary to use a more complicated model in which the existence of both types of vortex solutions are possible, depending on the value of the anisotropy.

The simplest model that generalizes our previous plaquette models[10] to the quasi-one-dimensional case and which admits analysis of the OPV solutions is illustrated in Fig. 1. The system includes four parallel spin chains with fixed spins in the boundary chains (labeled *0* and *3*). Similar models have been proposed previously[14] for describing the properties of complex topological magnetostructural defects. The fixed spin chains *0* and *3* model the two spin spaces surrounding chains *1* and *2*, which contain the core of the vortex. In our case the spins of the outer chains are fixed in the easy plane (the xy plane in Fig. 1) and are directed along the x axis for chain *0* and in the opposite direction for chain *3* (in the standard notation the chosen spin direction corresponds to an ''antivortex''). This simplification of the boundary chains leads to an additional effective anisotropy for the inner chains *1* and *2* which makes the OPV stable. The spins of the inner chains *1* and *2* are free and can assume any position in the easy plane and can also deviate from the plane. The proposed model is capable of describing a vortex configuration if the corresponding static solution has the following properties: the spins in *1* have positive x and y projections for $x\to-\infty$, while for $x\to+\infty$ they have positive x but negative y projections. In chain *2* the x projections of the spins change sign (Fig. 1). In such a configuration the total circulation of the spin vector along a closed contour is equal to 2π. In other words, this solution possesses an analog of topological charge around the vortex center $x=y=0$, but, unlike the continuum system, in one passage around the center of the vortex the magnetization vector in magnetic space does not follow a continuous circle but takes on only six discrete values on the unit circle.

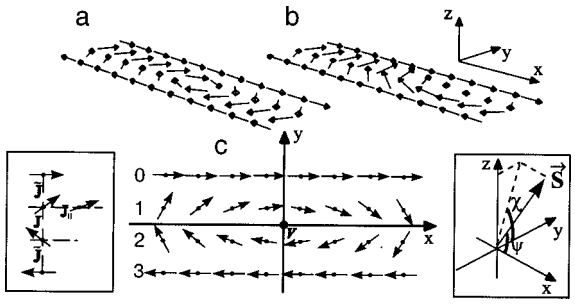

FIG. 1. One-dimensional model of an easy-plane ferromagnet in a vortex configuration: the three-dimensional form of the static in-plane vortex configuration (a); the three-dimensional form of the static out-of-plane vortex configuration (b); the xy projection of the central part of the out-of-plane vortex (the lengths of the arrows correspond to the values of the spin projection) (c). The center of the vortex is found at the point V.

In the framework of the classical Heisenberg model this system is described by a Hamiltonian

$$\mathcal{H}=-\sum_n\left[J_\parallel(\mathbf{S}_n^1\cdot\mathbf{S}_{n+1}^1+\mathbf{S}_n^2\cdot\mathbf{S}_{n+1}^2)-\frac{\beta}{2}(S_{nz}^1)^2-\frac{\beta}{2}(S_{nz}^2)^2+\tilde{J}S_{nx}^1-\tilde{J}S_{nx}^2+J\mathbf{S}_n^1\cdot\mathbf{S}_n^2\right],\tag{1}$$

where the index n is the number of a pair of neighboring spins from the first and second free chains along the x axis, $\mathbf{S}_n^i$ is the classical spin vector of the nth pair of the ith chain, where $i=1,2$ ($|\mathbf{S}|=1$); $J_\parallel$ is the exchange interaction constant between the spins of each individual free chain, $\tilde{J}$ corresponds to the exchange between the fixed boundary spins and the spins of a free chain, and J is the exchange between spins of different free chains (all of the exchange constants are positive). The parameter β is the single-ion anisotropy constant, with $\beta>0$ for the case of easy-plane symmetry. From here on we shall assume that all the magnetic parameters are normalized to the value of $J_\parallel$, i.e., $J_\parallel=1$. Since the single-ion anisotropy energy is much less than the exchange interaction energy, the so-called magnetic length $l=(J_\parallel/\beta)^{1/2}$ is much greater than the interatomic distance, and we can thus use the long-wavelength continuum description for the magnetization distribution along the chains. On the other hand, in the direction of the y axis the discreteness of the system is taken into account, since the angles between spins in this direction can be of the order of π. Ordinarily the orientation of the spin vector is described in terms of spherical projections referred to the symmetry axis (the z axis in the present case):

$$\mathbf{S}=(\sin\theta\cos\varphi,\sin\theta\sin\varphi,\cos\theta).\tag{2}$$

In terms of the spherical angles (φ and θ) the total energy is written as

$$E=\int_{-\infty}^{\infty}dx\Bigg(\frac{1}{2}\sum_{i=1}^{2}\left[(\theta_i')^2+\sin^2\theta_i(\varphi_i')^2+\beta\cos^2\theta_i\right]$$
$$-\tilde{J}[\sin\theta_1\cos\varphi_1-\sin\theta_2\cos\varphi_2]$$
$$-J[\cos\theta_1\cos\theta_2+\sin\theta_1\sin\theta_2\cos(\varphi_1-\varphi_2)]\Bigg), \quad (3)$$

where a prime denotes the partial derivative $\partial/\partial x$ (x is the coordinate along the chains). However, in the Sections devoted to analysis of the OPV solution, it will be convenient for us to use different angle variables:

$$\mathbf{S}=(\cos\psi,\sin\psi\cos\chi,\sin\psi\sin\chi), \quad (4)$$

i.e., a spherical coordinate system referred to the x axis (see Fig. 1). In such a coordinate system, expression (3) for the energy is rewritten as

$$E=\int_{-\infty}^{\infty}dx\Bigg(\frac{1}{2}\sum_{i=1}^{2}\left[(\psi_i')^2+\sin^2\psi_i(\chi_i')^2\right.$$
$$\left.+\beta\sin^2\psi_i\sin^2\chi_i\right]-\tilde{J}[\cos\psi_1-\cos\psi_2]$$
$$-J[\cos\psi_1\cos\psi_2+\sin\psi_1\sin\psi_2\cos(\chi_1-\chi_2)]\Bigg). \quad (5)$$

In the expressions for the energy density (3), (5) we have dropped a constant term $-2J_{\|}$. The variables (φ,θ) and (χ,ψ) are related by

$$S_z=\cos\theta=\sin\psi\sin\chi, \quad \tan\varphi=\tan\psi\cos\chi. \quad (6)$$

In the angle variables, the equations of spin dynamics (the Landau–Lifshitz equations) lool like

$$\sin\psi_{1,2}\frac{\partial\chi_{1,2}}{\partial t}=\frac{\delta E}{\delta\psi_{1,2}}, \quad \sin\psi_{1,2}\frac{\partial\psi_{1,2}}{\partial t}=-\frac{\delta E}{\delta\chi_{1,2}}, \quad (7)$$

$$\sin\theta_{1,2}\frac{\partial\varphi_{1,2}}{\partial t}=\frac{\delta E}{\delta\theta_{1,2}}, \quad \sin\theta_{1,2}\frac{\partial\theta_{1,2}}{\partial t}=-\frac{\delta E}{\delta\varphi_{1,2}}, \quad (8)$$

or, in explicit form,

$$\begin{cases}\psi_{1,2}''-[\beta\sin^2\chi_{1,2}+(\chi_{1,2}')^2]\sin\psi_{1,2}\cos\psi_{1,2}\\ \mp\tilde{J}\sin\psi_{1,2}-J[\sin\psi_{1,2}\cos\psi_{2,1}\\ -\sin\psi_{2,1}\cos\psi_{1,2}\cos(\chi_{2,1}-\chi_{1,2})]+\sin\psi_{1,2}\dot{\chi}_{1,2}=0,\\ \\ (\sin^2\psi_{1,2}\chi_{1,2}')'-\beta\sin^2\psi_{1,2}\sin\chi_{1,2}\cos\chi_{1,2}\\ -J\sin\psi_{1,2}\sin\psi_{2,1}\sin(\chi_{1,2}-\chi_{2,1})-\sin\psi_{1,2}\dot{\psi}_{1,2}=0;\end{cases} \quad (9)$$

$$\begin{cases}\theta_{1,2}''+[\beta-(\varphi_{1,2}')^2]\sin\theta_{1,2}\cos\theta_{1,2}\\ \pm\tilde{J}\cos\theta_{1,2}\cos\varphi_{1,2}-J[\sin\theta_{1,2}\cos\theta_{2,1}\\ -\cos\theta_{1,2}\sin\theta_{2,1}\cos(\varphi_{1,2}-\varphi_{2,1})]+\sin\theta_{1,2}\dot{\varphi}_{1,2}=0,\\ \\ (\sin^2\theta_{1,2}\varphi_{1,2}')'\mp\tilde{J}\sin\theta_{1,2}\sin\varphi_{1,2}\\ -J\sin\theta_{1,2}\sin\theta_{2,1}\sin(\varphi_{1,2}-\varphi_{2,1})-\sin\theta_{1,2}\dot{\theta}_{1,2}=0\end{cases} \quad (10)$$

Here the subscripts denote the number of the free chain, and the upper of the two signs in $\pm$ or $\mp$ corresponds to the first of the pair of indices. Below we consider only the case of equal exchange between all chains, $\tilde{J}=J$.

As we have pointed out, in a discrete two-dimensional ferromagnet with easy-plane anisotropy there are two types of vortices: IPVs and OPVS. In a continuous medium (continuum description) an OPV always has a lower energy than an IPV.[15] Thus, unlike an IPV, an OPV is stable in the continuum limit. However, when the discreteness of the spin lattice is taken into account, there is a critical value of the easy-plane anisotropy, β_c, and for $\beta>\beta_c$ (strong anisotropy) the IPV corresponds to the stable configuration of the system. In the other case, when $0<\beta<\beta_c$, the OPV is stable.[6,7,9] This effect is due to the competition between the anisotropy energy and exchange energy or, in other words, it is due to the presence of two characteristic spatial scales—the radius of a vortex (the magnetic length) and the interatomic distance. In this paper we will be mainly interested in the case of weak anisotropy, $0<\beta\ll J$ (recall that all the parameters are normalized to $J_{\|}$), which corresponds to the actual physical situation. Because of this, the treatment can be substantially simplified thanks to the possibility of using perturbation theory. However, we shall first study the IPV solution and analyze the stability of the IPV configuration to determine the critical value of the anisotropy parameter.

3. STATIC IN-PLANE VORTEX

In considering the IPV solution, we limit ourselves to finding the static structure and stability region of a vortex of that type. We note, however, that in the model under study the meaning of the IPV solution differs from that in the case of a 2D system: as we have shown, in our model a IPV is a solitonlike solution of a nonlinear equation, while in the 2D case the IPV is the solution of a linear equation of the Poisson type. In the IPV all of the spins of the inner chains *1* and *2* have a z component of zero, i.e., in terms of the angle variables we have introduced, $\chi_{1,2}(x)=0$. It follows from Eq. (6) that in this case $\psi_{1,2}(x)\equiv\varphi_{1,2}(x)$. Far from the vortex core the magnetization distribution is uniform, and Eqs. (9) and (10) are transformed to

$$\sin\psi_{1,2}+\sin(\psi_{1,2}-\psi_{2,1})=0. \quad (11)$$

These equations have two different solutions:

$$\psi_1=\psi_2=0,\pi \quad (12)$$

and

$$\psi_1=\pi-\psi_2=\pm\frac{\pi}{3}. \quad (13)$$

For solution (12) the energy of the system falls off with increasing longitudinal size L of the system as $E\sim-L$, and for solution (13) it falls off as $E\sim-3L/2$, and thus solution (13) describes a twofold degenerate ground state of the system. In our model the vortex solution actually corresponds to a one-dimensional domain wall[18] separating uniform domains. At the same time, as will be shown below, this solution manifests vortex properties, and the so-called vorticity corresponding to this solution is nonzero.

Assuming that $\psi_1(x)=\psi(x)$ and $\psi_2(x)=\pi-\psi(x)$ for an IPV, we can obtain from Eqs. (9) [or Eqs. (10)] a static equation determining the magnetization distribution for an IPV in the easy plane xy:

$$\psi_{xx} - J\sin\psi + J\sin 2\psi = 0, \tag{14}$$

which is the same as the well-studied static double sine-Gordon equation (see, e.g., Refs. 17 and 18). The topological localized solution (14) with the vortical asymptotic behavior found here (13) has the form

$$\psi_{\mathrm{IPV}} = \varphi_{\mathrm{IPV}} = -2\tan^{-1}\left[\frac{1}{\sqrt{3}}\tanh\left(\sqrt{\frac{3J}{8}}(x-x_0)\right)\right], \tag{15}$$

where x_0 is the coordinate of the center of the vortex, and the lattice constant is set equal to unity. It should be noted, however, that this expression is a good approximation for the spin distribution in an IPV only under the condition that the characteristic magnetic length $l \sim J^{-1/2}$ is much larger than the interatomic spacing. Using solution (15), we easily obtain an expression for the energy of the system in the IPV configuration:

$$E_{\mathrm{IPV}} = \alpha\sqrt{J} - \frac{3}{2}JL, \tag{16}$$

where the first term describes the characteristic energy of the vortex, and the second term corresponds to the ground state; the numerical value of the constant a is given by

$$\alpha = \frac{2}{\sqrt{J}}\int_{-\infty}^{\infty}(\varphi'_{\mathrm{IPV}})^2 dx = \sqrt{6} - \frac{\sqrt{2}\pi}{3} \approx 0.967.$$

We note that while in the two-dimensional case the energy of a vortex diverges logarithmically with increasing size of the system,[1] in the system considered here the vortex solution separates two degenerate ground states and corresponds to a one-dimensional domain wall, the energy of which is finite.[16,18,24] In a certain sense the situation is similar to the ''collapse'' of a magnetic vortex in a Bloch line in a domain wall in a 2D easy-plane ferromagnet when the additional anisotropy in the easy plane is taken into account. It is well known that the existence of the IPV configuration is possible only when the discreteness of the system in the core of the vortex is taken into account[6] (in which case the logarithmic divergence of the vortex energy at the center of the vortex solution is removed). In view of that fact it is of interest to examine the question of the existence of an IPV–OPV transition in a model in which the longitudinal distribution of the magnetization is described in the continuum limit and only the interaction between chains is taken into account in a discrete manner. As will be shown below, the energy of the OPV configuration is less than the energy of the IPV under the condition of weak anisotropy $\beta \ll J$, and thus the OPV should be stable for small values of β. On the other hand, this conclusion becomes invalid if the anisotropy is not small. Moreover, since the energy of the IPV configuration increases with increasing anisotropy parameter β [see Eq. (35)], one expects that the IPV should be energetically preferred in the case of weak anisotropy. This question can be investigated by using the method of Vakhiov and Kolokolov[19] and performing a stability analysis of the IPV configuration.

Following Ref. 19, we must linearize the initial equations (10) with respect to small time- and coordinate-dependent corrections to the static IPV solution. There are two modes that must be analyzed:

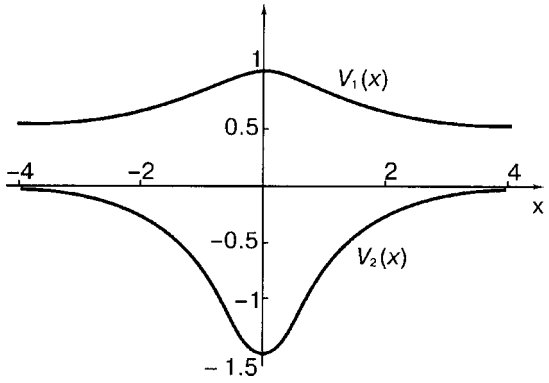

FIG. 2. Profiles of the effective potentials $V_1(x)$ and $V_2(x)$ as functions of the renormalized coordinate (25) and (26).

1) a symmetric mode with small corrections, of the form

$$\theta_1 = \frac{\pi}{2} - \vartheta(x,t), \quad \theta_2 = \frac{\pi}{2} - \vartheta(x,t), \tag{17}$$

$$\varphi_1 = \varphi_{\mathrm{IPV}}(x) + \phi(x,t), \quad \varphi_2 = \pi - \varphi_{\mathrm{IPV}}(x) + \phi(x,t);$$

2) an antisymmetric mode with

$$\theta_1 = \frac{\pi}{2} - \vartheta(x,t), \quad \theta_2 = \frac{\pi}{2} + \vartheta(x,t), \tag{18}$$

$$\varphi_1 = \varphi_{\mathrm{IPV}}(x) - \phi(x,t), \quad \varphi_2 = \pi - \varphi_{\mathrm{IPV}}(x) + \phi(x,t),$$

where φ_{IPV} is given by expression (15).

The IPV–OPV phase transition should result from instability of the symmetric mode, as is attested to by the symmetry of the OPV solution. This assertion is also in agreement with previous results[7,10] for two-dimensional systems with a fixed boundary. Substituting expression (17) into (9), we obtain the following system of equations in a linear approximation in the small corrections:

$$-\phi'' + \cos\varphi_{\mathrm{IPV}}\phi = \dot{\vartheta}, \tag{19}$$

$$\vartheta'' + [\cos\varphi_{\mathrm{IPV}} - 2\cos^2\varphi_{\mathrm{IPV}} - (\varphi'_{\mathrm{IPV}})^2 + \beta]\vartheta = -\dot{\phi}, \tag{20}$$

where for convenience the time, coordinate, and anisotropy parameter are renormalized as follows: $Jt \to t$, $J^{1/2}x \to x$, $\beta/J \to \beta (J > 0)$, and the dots over the symbols on the right-hand sides stand for $\partial/\partial t$. For solutions of this system with the form

$$\phi(x,t) = \tilde{\phi}(x)\exp(\nu t), \quad \vartheta(x,t) = \tilde{\vartheta}(x)\exp(\nu t), \tag{21}$$

we obtain the coupled equations

$$\hat{\mathcal{L}}_1\tilde{\phi} = \nu\tilde{\vartheta}, \quad \hat{\mathcal{L}}_2\tilde{\vartheta} = -\nu\tilde{\phi}, \tag{22}$$

where $\hat{\mathcal{L}}_1$ and $\hat{\mathcal{L}}_2$ are Hermitean operators of the Schrödinger type:

$$\hat{\mathcal{L}}_1 = -\frac{d^2}{dx^2} + V_1(x), \tag{23}$$

$$\hat{\mathcal{L}}_2 = -\frac{d^2}{dx^2} + V_2(x) + \beta, \tag{24}$$

with the effective potentials $V_1(x)$ and $V_2(x)$ [see Fig. 2]:

$$V_1(x)=\frac{2+\cosh\left(\sqrt{\frac{3}{2}}x\right)}{1+2\cosh\left(\sqrt{\frac{3}{2}}x\right)}, \tag{25}$$

$$V_2(x)=-\frac{3}{2}\frac{7+2\cosh\left(\sqrt{\frac{3}{2}}x\right)}{\left(1+2\cosh\left(\sqrt{\frac{3}{2}}x\right)\right)^2}. \tag{26}$$

We thus arrive at the eigenvalue problem

$$\hat{\mathcal{L}}_1\hat{\mathcal{L}}_2\tilde{\vartheta}=-\nu^2\tilde{\vartheta}, \tag{27}$$

with the condition that the eigenfunctions be finite at infinity. We must analyze the sign of the lowest eigenvalue of the operator $\hat{\mathcal{L}}_1\hat{\mathcal{L}}_2$, which corresponds to the ground-state eigenfunction, as a function of the value of the anisotropy parameter. If the lowest eigenvalue of the operator (27) is positive, then ν is imaginary, and the initial problem does not contain solutions which grow exponentially in time, and the IPV is stable. In the opposite case a solution appears which grows exponentially with time, and the IPV is unstable. Consequently, it is necessary to find the dependence of the lowest eigenvalue on the anisotropy parameter and the value of the anisotropy parameter at which the eigenvalue changes sign. This value β_c will be the IPV–OPV phase transition point.

Since $V_1(x)>0$ for any x, the operator $\hat{\mathcal{L}}_1$ is nondegenerate and possesses a continuous spectrum of positive definite eigenvalues. In that case the inverse operator $\hat{\mathcal{L}}_1^{-1}$ exists and is also positive definite. Taking this circumstance into account, we can reduce the variational problem

$$-\nu_0^2=\min\frac{\langle\tilde{\vartheta}|\hat{\mathcal{L}}_2|\tilde{\vartheta}\rangle}{\langle\tilde{\vartheta}|\hat{\mathcal{L}}_1^{-1}|\tilde{\vartheta}\rangle} \tag{28}$$

to investigation of the eigenvalue spectrum of the operator $\hat{\mathcal{L}}_2$, since the sign of its eigenvalues determines the signature of the initial operator from (27). In expression (28) the subscript 0 corresponds to the lowest eigenvalue, and the standard quantum-mechanical notation for the scalar product is used.

As can be seen in Fig. 2, an upper estimate for the IPV–OPV phase transition point in the system under study is $\beta=-V_2(0)=1.5$. Indeed, for all $\beta>1.5$, the whole potential well for the Schrödinger operator $\hat{\mathcal{L}}_2$ is shifted above the x axis, and the ground-state eigenvalue is positive. This means that not all of the solutions of the initial set of equations (19), (20) are growing ones, and the IPV is stable for any $\beta>1.5$. To obtain the value of the IPV–OPV transition point to high accuracy, one can use an approximate variational procedure for studying the lowest eigenvalue of the operator $(\hat{\mathcal{L}}_2-\beta)$, which corresponds to a symmetric eigenfunction without nodes and with exponentially damped asymptotic behavior at infinity. By choosing the comparison function for the ground state in the form $\vartheta=\mathrm{sech}(\gamma x)$, where γ is the variational parameter, we satisfy the conditions imposed. The variational procedure leads to a critical value of the anisotropy parameter $\beta_c\approx0.73$. Since the operator $(\hat{\mathcal{L}}_2-\beta)$ is negative definite on a manifold of functions with the symmetry of the ground state, one can conclude that the true value of β_c for our system should be slightly smaller than the value found.

To check our results and to track the connection of the proposed system with purely discrete systems, we carried out a series of numerical computations for completely discrete systems of finite size, analogous to that shown in Fig. 1. Using the Hamiltonian of the discrete system (1) directly, we determined numerically the vortex configuration with minimum energy for systems containing 40, 60, and 100 free spins (in the inner chains). It is known that for a very small two-dimensional system, the critical value of the anisotropy parameter for the IPV–OPV transition depends substantially on the size of the system.[7,10] However, as the size of the system increases, the critical value of the anisotropy parameter rapidly approaches a certain limiting value. For all the 40-, 60- and 100-spin systems it was found that the transition point lies in the interval $0.695<\beta_c<0.7$. This result is in good agreement with the analytical estimate obtained.

4. STATIC OUT-OF-PLANE VORTEX CONFIGURATION

As we have shown above, the IPV is stable if the anisotropy parameter is greater than a critical value $\beta_c\approx0.7J$ (in this Section we use an unrenormalized parameter β). The OPV is stable in the interval of anisotropy parameters $0<\beta<\beta_c$. The structure of the OPV is much more complicated to study than that of the IPV, but the discussion can be simplified considerably by assuming that $\beta\ll J$. In our subsequent treatment we shall therefore use perturbation theory in the small parameter β.

4.1. Magnetization distribution in a static out-of-plane vortex

We use the angle variables for the spin in the form (4). In the case of weak anisotropy ($\beta\ll1$) the distribution for the fields $\psi(x)$ and $\chi(x)$ can be found in the form of a power series in the parameter β. For an OPV the characteristic spatial scale (magnetic length) is of the order of $\beta^{1/2}$, and, as will be shown below, $\partial/\partial x\sim\beta^{1/2}$. As in the IPV case, in a static OPV $\psi_1=\pi-\psi_2=\psi$. In addition, for a static vortex we have $\chi_1=\chi_2=\chi$ (see Fig. 1b, 1c). Taking these symmetry relations into account, we can reduce Eqs. (9) to a pair of coupled nonlinear equations:

$$\chi''-\frac{\beta}{2}\sin2\chi+2\chi'\psi'\cot\psi=0, \tag{29}$$

$$\psi''-[\beta\sin^2\chi+(\chi')^2]\sin\psi\cos\psi-J[\sin\psi-\sin2\psi]=0. \tag{30}$$

The vortex solution of equations (29), (30) corresponds to a spatial rotation of the spin vector from the position $\psi=\pi/3$, $\chi=0$ for $x\to-\infty$ to the position $\psi=\pi/3$, $\chi=\pi$ for $x\to+\infty$; here the spins rotate practically along a conical surface (see Fig. 3). In accordance with this assumption the value of χ remains of the order of unity, while $\chi'\sim\beta^{1/2}$. For the second field $\psi=\pi/3+O(\beta)$ and $\psi'\sim\beta^{3/2}$. In Eq. (29) in

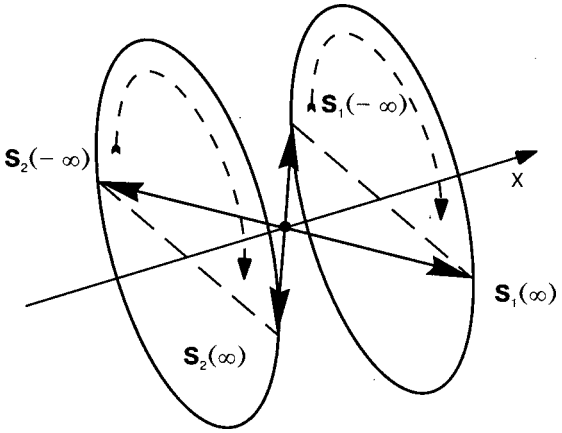

FIG. 3. Spatial rotation of the spin vector in the free chains as the coordinate varies from $-\infty$ to $+\infty$.

the leading approximation one can drop the last term and obtain the well-known static sine-Gordon equation, with the soliton solution

$$\chi^{(0)}=2\tan^{-1}(\exp\sqrt{\beta}x). \tag{31}$$

The last term in Eq. (30) is of order β. Thus this analysis demonstrates the correctness of the initial assumption that we made as to the order of smallness of ψ'. Using the leading approximation for the field X, we obtain the first corrections for ψ:

$$\psi(x)=\frac{\pi}{3}-\frac{1}{\sqrt{3}}\frac{\beta}{J}\frac{1}{\cosh^2\sqrt{\beta}x}+O(\beta^2), \tag{32}$$

and using Eq. (32), we obtain an expression for χ accurate to order β^2 in the form

$$\chi(x)=2\tan^{-1}\exp\sqrt{\beta}x+\frac{1}{3}\frac{\beta}{J}\frac{\sinh\sqrt{\beta}x}{\cosh^2\sqrt{\beta}x}+O(\beta)^2. \tag{33}$$

From Eqs. (29) and (30) we can also obtain the asymptotic behavior of the fields $\chi(x)$ and $\psi(x)$ in the OPV without making the assumption that β is small. For $x\to\pm\infty$ one can linearize these equations above the ground state [see Eq. (13)] and obtain

$$\chi(x)\approx C\exp(\mp\sqrt{\beta}x),$$
$$\psi(x)\approx\mp\frac{\pi}{3}\pm C^2\frac{\sqrt{3}\beta}{8\beta-3J}\exp(\mp 2\sqrt{\beta}x), \tag{34}$$

where the constant of integration C depends on β and J and for small β can be represented in the form $C\approx 2+\beta(3J)^{-1}+O(\beta^2)$.

It follows from the form of solutions (32), (33) and the asymptotic expression (34) that the size of the core of an OPV is of order $l_{\mathrm{OPV}}\sim\beta^{-1/2}$, i.e., in the case of small β it is substantially larger than for an IPV: $l_{\mathrm{IPV}}\sim J^{-1/2}\ll l_{\mathrm{OPV}}$ [see Eq. (15)].

It is of interest to compare the results with the data from an analysis of two-dimensional systems. Far from the core of a vortex the asymptotic expression for the z component of the magnetization falls off exponentially, so that in the two-dimensional case $S_z\sim\exp(-\sqrt{\beta}x)$. However, the field φ also tends exponentially toward its limiting value $[\varphi\approx\pi/3-O(\exp(2\sqrt{\beta}x)]$, which differs from the 2D case, in which at large distances $\varphi(y=a,\ x\gg a)\sim a/x$. This difference demonstrates the one-dimensional character of the proposed model.

Substituting the solutions (32) and (33) for the fields $\psi(x)$ and $\chi(x)$ into the energy expression (5), we obtain with an accuracy to terms of order β

$$E_{\mathrm{OPV}}=12\sqrt{\beta}-\frac{3}{2}JL, \tag{35}$$

where L, as before, denotes the longitudinal size of the system. The OPV eigenenergy $12\beta^{1/2}$ at small β is substantially less than the energy of an IPV [see Eq. (16)].

For understanding the physical nature of the vortex solution obtained, it is convenient to make a change of variables from (χ,ψ) to (S^z,φ). Substituting (32) and (33) into the expressions (6) for the z component of the magnetization, we obtain with an accuracy to order β

$$S^z_{1,2}=\frac{\sqrt{3}}{2}\frac{1}{\cosh(\sqrt{\beta}x)}-\frac{1}{2\sqrt{3}}\frac{\beta}{J}\left(\frac{2}{\cosh^3(\sqrt{\beta}x)}-\frac{1}{\cosh(\sqrt{\beta}x)}\right). \tag{36}$$

The dependence of the total out-of-plane magnetization of the OPV on the anisotropy parameter looks like:

$$M_\infty=\pi\sqrt{\frac{3}{\beta}}+O(\beta^{3/2}), \tag{37}$$

and in the leading approximation the expression for the field φ is

$$\varphi_1=-\tan^{-1}\sqrt{3}\tan(\sqrt{\beta}x),\quad \varphi_2=-\pi-\varphi_1. \tag{38}$$

Using the expressions obtained for the fields S^z and φ, we can find an expression for the density of vorticity of this solution, which is an important characteristic of the OPV. For a two-dimensional magnet in the continuum description, the density of vorticity has the form (see, e.g., Ref. 22)

$$\Upsilon=\frac{\partial S^z}{\partial x}\frac{\partial\varphi}{\partial y}-\frac{\partial S^z}{\partial y}\frac{\partial\varphi}{\partial x}, \tag{39}$$

and the total vorticity of the OPV in an infinite 2D magnet is given by $\Gamma=\int_V\Upsilon dxdy=2\pi S^z(0)$, where $S^z(0)$ is the z component of the magnetization at the center of the vortex. For the combined model under study the y coordinate takes on discrete values $y=0,1,2,3$ and the derivative $\partial/\partial y$ should be replaced by symmetrized finite differences: $\partial f/\partial y\to(f_0-f_2)/2,(f_1-f_3)/2$. To calculate the discrete analog of the total vorticity it is necessary to use the symmetry properties of the OPV: $S^z_0=S^z_3=0$, $S^z_1=S^z_2$, $\varphi_0=0$, $\varphi_3=-\pi$, and $\varphi_2=-\pi-\varphi_1$ (for $x>0$); $\varphi_2=\pi-\varphi_1$ (for $x<0$). The latter relation takes into account the rotation of the spin vector by an angle of 2π in traversing a closed contour around the center of the vortex. Thus we finally get for the vorticity density (the indices give the number of the chain)

$$\Upsilon_1=\Upsilon_2=\frac{1}{2}\frac{\partial}{\partial x}(S^2_1\varphi_1)+\frac{\pi}{2}\frac{\partial S^z_1}{\partial x}\mathrm{sgn}(x), \tag{40}$$

and for the total vorticity

$$\Gamma = \int_{-\infty}^{\infty} dx(\Upsilon_1 + \Upsilon_2) + 2\pi S_1^z(0). \tag{41}$$

This result agrees with the result for an OPV in a two-dimensional continuum system.

Since we will later be discussing the numerical treatment of discrete systems of finite size along the x axis, it is helpful to lead off with an analytical discussion of the effects of finiteness of the chains. First it is necessary the rewrite the leading approximation of the solution for the field χ (31) in order to satisfy the boundary conditions (for the sake of definiteness we have chosen Neumann boundary conditions) at the ends of chains *1* and *2* (i.e., at the points $x = \pm L/2$, where L denotes the total length of each chain). In the leading approximation $\psi^{(0)} \approx \pi/3$, and $\chi^{(0)}$ satisfies the sine-Gordon equation. In order to satisfy the boundary conditions we must choose the periodic cnoidal solution of the sine-Gordon equation:

$$\chi^{(0)} = \frac{\pi}{2} + \sin^{-1} \kappa \mathrm{sn}(\sqrt{\beta}x|\kappa), \tag{42}$$

where $\mathrm{sn}(z|\kappa)$ is the Jacobi elliptic sine[20] with argument z and modulus κ. The modulus κ is uniquely determined by the length of the chains and the value of the anisotropy parameter:

$$\frac{\sqrt{\beta}L}{2} = K(\kappa). \tag{43}$$

Here K is the complete elliptic integral of the first kind. Taking into account that the minimum value $K(0) = \pi/2$ and that $K(\kappa)$ is a monotonic function of its argument κ, we can find the value of the anisotropy parameter β at which the vortex configuration vanishes. Indeed, as $\kappa \to 0$ the value of β remains finite and approaches $\beta_* = (\pi/L)^2$. For values of β less than β_* there exists only the uniform spin ordering (in the direction of the x axis) with no vortex. An analogous influence of the finite size of the system on the structure of an OPV was also noted previously in a study of a two-dimensional spin plaquette with a free boundary.[10] The bifurcational splitting-off of the localized state from the uniform state for systems of finite size is a well-known fact. It occurs at a finite critical value of the bifurcation parameter, and in two-dimensional systems this critical value is of order L^{-2} (Ref. 21). Let us calculate the out-of-plane magnetization for a system of finite size L in the OPV configuration. Expressions for the local z component of the spins can be obtained by substituting the expressions for the fields $\chi^{(0)}$ and $\psi^{(0)}$ into relation (6):

$$S_z^{1,2} = \frac{\sqrt{3}}{2} \mathrm{dn}(\sqrt{\beta}x|\kappa), \tag{44}$$

where the elliptic function $\mathrm{dn}(z|\kappa)$ is defined as $\mathrm{dn}(z|\kappa) = (1 - \kappa^2 \mathrm{sn}^2(z|\kappa))^{1/2}$. Then the total out-of-plane magnetization of a finite system takes the form

$$M_L = \int_{-L/2}^{L/2} [S_1^z(x) + S_2^z(x)]dx = \pi \sqrt{\frac{3}{\beta}}. \tag{45}$$

In the limit $\beta \to \beta_*$ it approaches the value

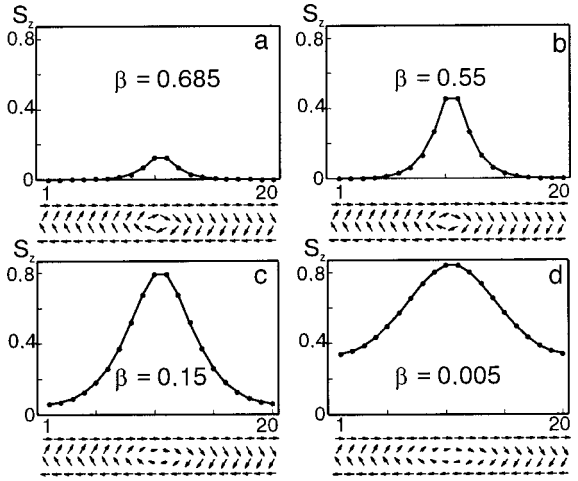

FIG. 4. Change of the distribution of S_z and the structure of the ordering of the spins in the easy plane as the value of β decreases for a discrete system consisting of 40 spins in the out-of-plane vortex configuration.

$$M_L^* = 2L \frac{\sqrt{3}}{2}. \tag{46}$$

In the treatment of a discrete system the factor $2L$ in expression (46) must be replaced by the number of spins N in the mobile chains *1* and *2*.

4.2. Numerical analysis of a static out-of-plane vortex in a discrete system of finite size

It is helpful to supplement the analytical treatment by numerical calculations for discrete systems of analogous geometry for the purpose of extending the analysis to the whole region of stability of the OPV without restricting consideration to the case of small β only, and to study the vortex structure at values of the anisotropy parameter close to the point of the IPV–OPV transition. For finding the minimum-energy configuration, expression (1) for the energy of the discrete system was used directly and the random relaxation procedure was employed for different values of the anisotropy. As the initial configuration we chose the distribution described by formula (15), where the center of the vortex coincides with the center of the system (the coordinate origin in Fig. 1c) and we set $J = 1$. We note that solution (15) was obtained in the long-wavelength approximation and is correct only for small J. Only relaxation to configurations with the vortex symmetry was allowed. We investigated systems containing 40, 60, and 100 spins, but because of the almost complete similarity of the results, in this Section we shall consider the results of the analysis only for a system with 40 mobile spins [Neumann (i.e., free) boundary conditions were chosen at the ends of the chains].

In the first step, relaxation was permitted only in the easy plane, and in that way the true IPV configuration for the chosen values of the parameters of the system was obtained. The corresponding IPV distribution is very close to the spin distribution in the easy plane in Fig. 4a. The discreteness of the system, the influence of the finite lengths of the chains, and the rather large value of J used all led as a result to the transformation of the chosen initial IPV distribution (obtained analytically in the continuum limit for an infinite sys-

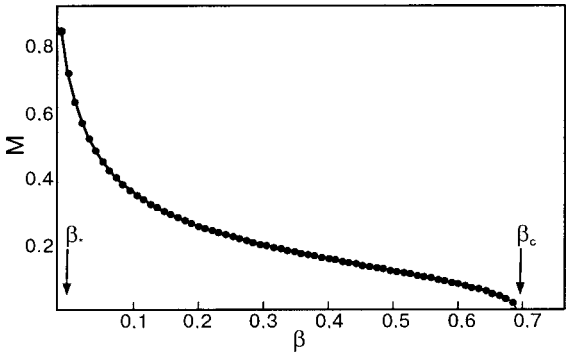

FIG. 5. The out-of-plane magnetization for one atom as a function of the anisotropy parameter β for a system of 40 spins.

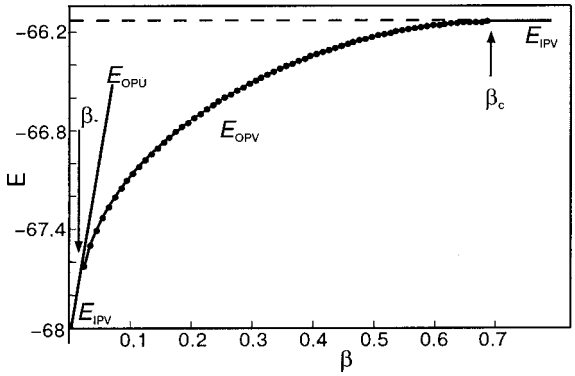

FIG. 6. Total energy in a system of 40 mobile spins as a function of the parameter β for the out-of-plane (OPV) and in-plane (IPV) vortex configurations and the uniform out-of-plane (OPU) and in-plane (IPU) configurations.

tem). In spite of this, the difference of the initial configuration and that obtained after the relaxation procedure was not very substantial.

In the next step the spins were allowed to leave the easy plane, and spin configuration in three dimensions was found (recall that the length of the spin vector remains constant). This was done for values of the anisotropy parameter in the interval $0.02<\beta<1.5$ with a step of 0.01 (for values of β less than 0.02 the system did not relax to a vortex configuration).

A graphical illustration of the distribution of the z projection of the magnetization and the distribution of spins in the easy plane xy is given in Fig. 4. Analysis showed that for $\beta<\beta_c\approx 0.695$ the vortex solution acquired an out-of-plane component, strongly localized in the vicinity of the vortex core for small deviations of the values of β from the critical value β_c. For such values of β the distribution of spins in the xy plane does not differ substantially from that in the IPV. With increasing deviation of β from the critical value (in the direction of lower β) the in-plane ordering of the spins changed in accordance with the results of the analytical treatment [see Eqs. (15), (32), and (33)]. The profile of the out-of-plane magnetization simultaneously acquired an increasingly smooth bell-shaped form. Similar behavior of the z projection of the magnetization with decreasing anisotropy is observed in two-dimensional systems.

Figure 5 shows the out-of-plane magnetization per spin of the system as a function of the anisotropy parameter. The curve has the characteristic bifurcational form and is in good agreement with the data for two-dimensional systems: it arises at the point β_c with a square-root singularity and tends monotonically toward its limiting value $M_L/N=\sqrt{3}/2$ for $\beta\to\beta_*$ (we note that the maximum value of M/N in a two-dimensional system is equal to unity). The numerical $M(\beta)$ dependence is in good agreement with the analytical result $M=\pi(3/\beta)^{1/2}$ (for small β).

Figure 6 shows $E(\beta)$ for the OPV. At small β the curve obtained numerically (see Fig. 6) is in good agreement with the result of the analytical treatment. $E(\beta)$ splits off in a bifurcational manner at the point $\beta=\beta_c$ from the the IPV energy value $E_{IPV}\cong\approx 66.1$ (for $N=40$). For $\beta<\beta_c$ the energy of an OPV is less than the energy of an IPV, and at these values of the anisotropy the IPV is unstable. The OPV energy decreases with decreasing β and reaches a value $E_*\approx -67.6$ at a second bifurcation point $\beta=\beta_*\approx(\pi/L)^2\approx 0.02$, at which the vortex loses its topological properties and undergoes a transition to a uniform out-of-plane state (OPU) with a nonzero z component of the spins ($S^z_{1,2}=\sin(\pi/3)=\sqrt{3}/2$, $S^x_1=-S^x_2=\cos(\pi/3)=1/2$, $S^y_1=S^y_2=0$). The dependence of the OPV energy $E_{OPV}(\beta)$ splits off at the point (β_*,E_*) from the energy curve $E_{OPU}(\beta)$ of this uniform state. For each $\beta<\beta_*$ in a system of finite size, only the uniform states are stable: in the case considered here, these are the uniform out-of-plane (OPU) and uniform in-plane (IPU) states.

The spin distribution in the latter is given by expression (13). The global energy minimum for any positive β corresponds to the IPU state with energy $E_{IPU}=-68$ for $N=40$. The OPU configuration, in turn, corresponds to a local minimum of the energy. For $\beta=0$ the energies of the OPU and IPU states are equal to each other.

5. DYNAMICS OF AN OUT-OF-PLANE VORTEX

Let us consider the dynamical properties of an OPV in the case of weak anisotropy ($\beta\ll J$). The difficulty in treating the dynamics of an OPV in the proposed model lies in the fact that motion of the OPV is possible only under the condition that the center of the vortex is displaced in the direction of the y axis from the symmetric position. This, in turn, makes it necessary to consider a system of four coupled equations for the fields $\psi_{1,2}$ and $\chi_{1,2}$. We note that in an infinite two-dimensional system an OPV cannot move (it is ''frozen'' in the ground state), and motion is possible only in systems of finite size, even if they are bounded in only one dimension. (The problem of the motion of Pitaevskiĭ vortices in a superfluid liquid in systems with a similar geometry is examined in Ref. 23.)

Let us start by analyzing the spectrum of linear spin waves propagating along the chains. To obtain the spectrum it is necessary to linearize the set of equations (9) above the uniform ground state with respect to $\chi_{1,2}\ll 1$ and $\varepsilon_{1,2}\ll 1$, where $\psi_1=\pi/3+\varepsilon_1$ and $\psi_2=2\pi/3-\varepsilon_2$:

$$\chi''_{1,2}-\beta\chi_{1,2}=J(\chi_{1,2}-\chi_{2,1})\pm\frac{2}{\sqrt{3}}\dot{\varepsilon}_{1,2}, \tag{47}$$

$$\varepsilon''_{1,2}-J\varepsilon_{1,2}=\frac{J}{2}\varepsilon_{1,2}\mp\frac{2}{\sqrt{3}}\dot{\chi}_{1,2}. \tag{48}$$

Then, substituting

$$\chi_i(x,t)=\chi_i\sin(kx-\omega t),$$
$$\varepsilon_i(x,t)=\varepsilon_i\cos(kx-\omega t),$$

we arrive at the dispersion relation

$$\omega_s^2=(\beta+k^2)\left(\frac{J}{2}+k^2\right), \tag{49}$$

for the symmetric mode s with $\chi_1=\chi_2$, $\varepsilon_1=-\varepsilon_2$, and

$$\omega_a^2=(\beta+2J+k^2)\left(\frac{3J}{2}+k^2\right), \tag{50}$$

for the antisymmetric mode a with $\chi_1=-\chi_2$, $\varepsilon_1=\varepsilon_2$. We emphasize that the dispersion relations obtained correspond to spin waves in a system with a special type of boundary conditions (with opposite directions of the fixed spins in chains *0* and *3*). If the spins in the boundary chains are fixed in the same direction, then the dispersion relation for the symmetric mode would be $\omega_s^2=[(\beta+J)+k^2][J+k^2]$, just as in the antisymmetric mode. The dispersion relations obtained have qualitatively the same form as the dispersion relation for spin waves in a two-dimensional easy-plane ferromagnet with fixed boundary conditions (of the Dirichlet type). The lowest symmetric mode coincides with the spectrum of a two-dimensional magnet if the size of the two-dimensional system in one direction is $\pi/2$. The dispersion relations obtained are also reminiscent of that for a biaxial ferromagnet.[24]

It follows from Eq. (49) that the minimum spin-wave phase velocity is approximately $V_{\rm ph}^{\min}\approx(J/2)^2=c$. It is well known[24] that the motion of nonlinear localized excitations of stationary profile is possible only at velocities lower than the minimum phase velocity of linear excitations ($V<c$). From here on we will be interested only in the case of vortex motion at low velocities $V\ll c$.

In a static OPV the spatial rotation of the spins as x goes from $-\infty$ to $+\infty$ occurs almost along a conical surface with a vertex angle $\psi_1=\pi-\psi_2\approx\pi/3$. This fact demonstrates the convenience of using the new variables $\varepsilon_{1,2}$. By linearizing Eqs. (9) with respect to small $\varepsilon_{1,2}$, one can express $\varepsilon_{1,2}$ in terms of $\chi_{1,2}$ and derive simplified equations containing only $\chi_{1,2}$ (the details of this procedure and of the spin-wave spectrum are given in the Appendix). Thus in this Section we consider only the simplified equations for the fields $\chi_{1,2}$:

$$\chi''_{1,2}-\frac{\beta}{2}\sin 2\chi_{1,2}-J\sin(\chi_{1,2}-\chi_{2,1})=\frac{2}{3J}\{2\ddot{\chi}_{1,2}+\ddot{\chi}_{2,1}\}$$
$$\pm\frac{\beta}{3J}\dot{\chi}_{2,1}(\sin 2\chi_{1,2}+\sin 2\chi_{2,1})\mp\frac{2}{3J}[2\chi''_{1,2}\dot{\chi}_{1,2}$$
$$+3\chi'_{1,2}\dot{\chi}'_{1,2}+(\chi'_{1,2}\dot{\chi}_{2,1})'-\chi'_{2,1}]\dot{\chi}'_{2,1}]. \tag{51}$$

Such a simplification is possible only at small β.

The equations obtained are easily analyzed for the cases $V\ll\beta^{1/2}$ and $\beta^{1/2}\ll V\ll c$ (we assume that $\beta\ll J\sim 1$). Since the system of equations (51) was derived for motion with velocities $V\ll c$, those equations can be used to study linear waves with a group velocity satisfying the relation $V_{\rm gr}\ll c$, or, in other words, with wave numbers $k\ll\beta^{1/2}$. With the given accuracy the dispersion relations (49) and (50) lead to (see also the Appendix):

$$\omega_s^2=\frac{\beta J}{2}+ck^2,\quad \omega_a^2=\left(3J^2+\frac{3\beta J}{2}\right). \tag{52}$$

In these relations the indices s and a, as before, characterize the symmetry of the fields $\chi_{1,2}$.

5.1. Motion of an out-of-plane vortex of stationary profile

Let us give an estimate of the different terms on the right-hand side of system (51). It follows from the static solutions (32) and (33) that the characteristic spatial scale of the magnetization distribution is of order $\beta^{1/2}$, i.e., the spatial gradients are of order $\partial/\partial x\sim\beta^{1/2}$. The time derivatives are of order $V\beta^{1/2}$. Then the terms on the right-hand side of (51) have the following orders: $V^2\beta$ for the term in the curly brackets, and $V\beta^{3/2}$ for the terms in the parentheses and square brackets. As long as the vortex velocity lies in the interval $\beta^{1/2}=c_2\ll V\ll c=(J/2)^{1/2}$ (''fast'' vortices) the term in the curly brackets on the right-hand side of Eq. (51) is the main term. Otherwise, for ''slow'' vortices with velocities $V\ll c_2$, this term can be dropped.

Let us consider slow vortices moving with velocities $V\ll\beta^{1/2}=c_2$. In this case one can use perturbation theory, taking the solution (31) for the static OPV as the leading approximation:

$$\chi_{1,2}=2\tan^{-1}e^{\eta}+\mu_{1,2},\quad \mu_{1,2}\ll 1, \tag{53}$$

where $\eta=\sqrt{\beta}(x-Vt)$. Substituting expression (53) into the right-hand side of (51) and linearizing the left-hand side of system (51) with respect to small $\mu_{1,2}$, we obtain the following system of equations:

$$\mu''_{1,2}-\beta\left(1-\frac{2}{\cosh^2\eta}\right)\mu_{1,2}-J(\mu_{1,2}-\mu_{2,1})$$
$$=\mp\frac{8}{3}\frac{V\beta^{3/2}}{J}\frac{\sinh\eta}{\cosh^3\eta}. \tag{54}$$

Taking the particular solution of this inhomogeneous system, we find that to the accuracy used the expressions for $\chi_{1,2}$ have the form

$$\chi_{1,2}=2\tan^{-1}e^{\eta}\pm\frac{4}{3}\frac{V\beta^{3/2}}{J^2}\frac{\sinh\eta}{\cosh^3\eta}. \tag{55}$$

The expressions for $\psi_{1,2}$ are as follows:

$$\psi_1=\frac{\pi}{3}-\frac{\beta}{\sqrt{3}J}\operatorname{sech}^2\eta+\sqrt{\frac{3\beta}{2J}}\frac{V}{c}\operatorname{sech}\eta,$$
$$\psi_2=\frac{2\pi}{3}+\frac{\beta}{\sqrt{3}J}\operatorname{sech}^2\eta+\sqrt{\frac{3\beta}{2J}}\frac{V}{c}\operatorname{sech}\eta. \tag{56}$$

The solution obtained for the slow vortices goes over to the static OPV solution (32), (33) in the limit $V\to 0$.

For fast vortices we introduce the new pair of variables $u=\chi_1+\chi_2$, $w=\chi_1-\chi_2$, in terms of which we can rewrite system (51) in the leading approximation as

$$\left[1-\left(\frac{V}{c}\right)^2\right]u''-\beta\sin u\cos w=0,$$
$$\left[1-\frac{1}{3}\left(\frac{V}{c}\right)^2\right]\omega''-\beta\sin w\cos u-2J\sin w=0. \tag{57}$$

This system has a unique solution for moving vortices of stationary profile with $w=0$, and it reduces to the standard sine–Gordon equation with a solution in the form a kink:

$$\chi_1=\chi_2=2\tan^{-1}e^{\xi}, \tag{58}$$

where ξ differs from η by the Lorentzian denominator:

$$\xi=\sqrt{\beta}\frac{x-Vt}{\sqrt{1-(V/c)^2}}.$$

In this approximation we obtain from Eq. (A3) (see Appendix)

$$\psi_1=\frac{\pi}{3}+\sqrt{\frac{3\beta}{2J}}\frac{V/c}{\sqrt{1-(V/c)^2}}\operatorname{sech}\xi,$$
$$\psi_2=\frac{2\pi}{3}+\sqrt{\frac{3\beta}{2J}}\frac{V/c}{\sqrt{1-(V/c)^2}}\operatorname{sech}\xi. \tag{59}$$

In these solutions we have dropped terms $\sim\beta\operatorname{sech}^2\eta$, since for velocities in the interval $c_2\ll V\ll c$ they are substantially smaller than the ''dynamical'' terms (proportional to V). Consequently, the solutions (55) and (56) can be used as an approximating formula in the entire range of velocities $V\ll c$.

Substituting solutions (55), (56) into relations (6), we find the distribution of the z component of the magnetization in the moving vortex (we are neglecting corrections $\sim\beta$ to the static distribution):

$$S^z_{1,2}\approx\frac{\sqrt{3}}{2}\operatorname{sech}\eta\left(1\pm\sqrt{\frac{\beta}{2Jc}}V\operatorname{sech}\eta\right). \tag{60}$$

A more accurate expression can be obtained using the higher static corrections from expressions (36). From the solution (60) we see that $S^z_1\neq S^z_2$, i.e., the magnetization distribution is asymmetric. Asymmetry proportional to the vortex velocity in a moving vortex solution is also observed in the motion of a vortex in a 2D system.[2,6] For the system under discussion this asymmetry leads to an effective shift of the center of the vortex in the y direction.

Let us also consider the solution for a vortex with the other sign of its topological charge (see the remarks at the beginning of Sec. 2). It can be obtained by replacing $\chi_{1,2}$ by $\pi-\chi_{1,2}$. Thus the signs in front of the terms in the parentheses and square brackets in system (51) would be changed to the opposite. However, the equation of motion is conserved under the substitution $V\to -V$, and the final solution looks like:

$$S^{z(AV)}_{1,2}\approx\frac{\sqrt{3}}{2}\operatorname{sech}\xi\left(1\mp\sqrt{\frac{\beta}{2J}}\frac{V}{c}\operatorname{sech}\xi\right). \tag{61}$$

Consequently, vortices with topological charges of different signs moving in the same direction are shifted in opposite directions along the y axis.

5.2. Description of the dynamics of an out-of plane vortex in the framework of the collective variables method

A simplified description of the 2D dynamics of an OPV is usually given in the framework of the collective variables method (CVM), in which the coordinates of the center of the OPV $\mathbf{R}(t)=(X(t),Y(t))$ are used as these collective variables. This procedure leads to the well-known equations of Thiele for $(X(t),Y(t))$.[25,26] (The corresponding equations for Pitaevskiĭ vortices are obtained in Ref. 23). Generalization of Thiele's analysis for $\mathbf{S}=\mathbf{S}(\mathbf{r},\mathbf{R},\dot{\mathbf{R}})$ gives the following equation of motion for the vortex:[2,27]

$$\hat{M}\ddot{\mathbf{R}}+\hat{G}\dot{\mathbf{R}}=\mathbf{F}. \tag{62}$$

Here $\hat{M}$ is the effective mass tensor for the OPV, $\mathbf{F}=-\partial E/\partial\mathbf{R}$ is the force acting on the OPV, and $\hat{G}$ is a so-called antisymmetric gyrotensor with the components

$$G_{xy}=-G_{yx}=\int_V dxdy\left(\frac{\partial\varphi}{\partial Y}\frac{\partial S^z}{\partial X}-\frac{\partial S^z}{\partial Y}\frac{\partial\varphi}{\partial X}\right). \tag{63}$$

For an OPV in an infinite two-dimensional magnet, where $\mathbf{S}=\mathbf{S}(\mathbf{r}-\mathbf{R})$, one can make the substitution $\partial/\partial X$, $\partial/\partial Y\to-\partial/\partial x$, $-\partial/\partial y$. After that, the definition (63) coincides with the expression for the total density of vorticity for a static vortex, $\Gamma=G_{xy}=2\pi qS^z(\mathbf{r})|_{\mathbf{r}=\mathbf{R}}$, where q is the topological charge of the OPV (in the case considered, $q=-1$). Since in our case $\mathbf{S}\neq\mathbf{S}(\mathbf{r}-\mathbf{R})$, the gyrotensor component G_{xy} is not equal to the total vorticity. This component can be found by using the solution obtained for a moving vortex.

In this Section we propose a variant of the generalization of the CVM to the case of systems like the one under discussion. The procedure used to derive the simplified equations of motion is extremely similar to that described in Refs. 2, 25, and 27, but in our case the approximate solution for the moving vortex is known, and the problem consists in determining the coordinates of its center (the collective variables). For the coordinate $X(t)$ this can be done rather simply: it is sufficient to replace x in the solutions for the moving OPV by the combination $x-X(t)$. However, the Y coordinate of the center of the vortex is not uniquely defined. In Ref. 27 the authors proposed to define the center of a vortex from the distribution of the field φ. We consider a more consistent definition in terms of the distribution of the field S^z. Since the z projection of the magnetization is coupled to the magnon density, it seems natural to us to choose the Y coordinate of the vortex as the magnon center of mass, by analogy with the introduction of the center of mass in classical mechanics. The definition of the collective coordinate Y for the center of the moving OPV then has the form

$$Y=\frac{\int_{-\infty}^{\infty}(S^z_1-S^z_2)dx}{\int_{-\infty}^{\infty}(S^z_1+S^z_2)dx}. \tag{64}$$

Substituting expression (60) for S^z into this definition, we obtain a relation between the Y coordinate of the IPV and its velocity:

$$Y=\frac{2}{\pi}\frac{\sqrt{\beta}}{J}\dot{X}. \tag{65}$$

We rewrite our moving solutions (59) and (60) as functions of $x-X(t)$ and $Y(t)$:

$$S^z_{1,2}=\frac{\sqrt{3}}{2}\operatorname{sech}\,\eta\pm\frac{\sqrt{3}}{4}\pi Y\operatorname{sech}^2\,\eta,$$

$$\varphi_1=-\tan^{-1}\sqrt{3}\tanh\,\eta-2\sqrt{3}\pi Y\frac{\sinh\,\eta}{\cosh^2\,\eta+3\sinh^2\,\eta}, \tag{66}$$

$$\varphi_2=-\pi+\tan^{-1}\sqrt{3}\tanh\,\eta-2\sqrt{3}\pi Y\frac{\sinh\,\eta}{\cosh^2\,\eta+3\,\sinh^2\,\eta},$$

where $\nu=\sqrt{\beta}(x-X(t))$.

The expressions found for the dependence of the solutions on the collective variables (the coordinates of the center of the OPV) can be used to drive an effective equation for these variables in the usual way. However, the definition of the gyrotensor (63) must be modified:

$$G_{xy}=-G_{yx}=\int_{-\infty}^{\infty}dx\sum_{k=1}^{2}\left(\frac{\partial\varphi_k}{\partial x}\frac{\partial S^z_k}{\partial Y}-\frac{\partial S^z_k}{\partial x}\frac{\partial\varphi_k}{\partial Y}\right). \tag{67}$$

Substituting (66) into this formula, we obtain an expression for the gyrotensor $G_{xy}=-G_{yx}=3\pi$, which differs from the expression for the gyrotensor in a two-dimensional infinite ferromagnet, $G_{xy}=-G_{yx}=2\pi$. This difference is due to the fact that the extremely simple substitution $\mathbf{S}=\mathbf{S}(\mathbf{r}-\mathbf{R})$ is not suitable for the system under study, where it is necessary to use $\mathbf{S}=\mathbf{S}(\mathbf{r},\mathbf{R})$.

The generalized Thiele equation (62) that follows from the generalized ansatz $\mathbf{S}=\mathbf{S}(\mathbf{r}-\mathbf{R},\dot{\mathbf{R}})$ was obtained in Refs. 2 and 27. In our system the combined description we have used leads to a modification of the definition of the mass tensor, which contains derivatives with respect to the velocity of the center of the vortex, and since the explicit form of the solution for an OPV moving in the x direction is known, the components M_{xx} are found in a rather obvious way:

$$M_{xx}=\int_{-\infty}^{\infty}dx\sum_{k=1}^{2}\left(\frac{\partial\varphi_k}{\partial V}\frac{\partial S^z_k}{\partial x}-\frac{\partial S^z_k}{\partial V}\frac{\partial\varphi_k}{\partial x}\right), \tag{68}$$

where $\dot{X}=V$. Using the solution in the initial form (without substituting the expression for the velocity in terms of Y into it), we obtain the vortex mass in the form

$$M_{xx}=\frac{6\sqrt{\beta}}{J}. \tag{69}$$

We note that this component of the mass tensor is finite, unlike the infinite mass of a vortex in a two-dimensional system. However, one can show[28] that for a ferromagnet of finite size the effective mass of a vortex is of the order of $\ln L$, where L is the distance from the center of the OPV to the nearest boundary; this is the reason why the vortex mass is finite in our model.

6. CONCLUSION

In this paper we have proposed a quasi-one-dimensional model for describing the vortex structure of IPVs and OPVs and the dynamic properties of OPVs in an easy-plane ferromagnet. Unlike the two-dimensional case, where the IPV has been studied only in a discrete approach, here the continuum description of the magnetization distribution along the chains forming the one-dimensional system is preserved. Taking into account the discreteness of the magnetic lattice in one direction is sufficient for the existence of two types of vortices in this approach: in-plane and out-of plane, i.e., in the combined description one can study fundamentally discrete features. We have found the critical value of the anisotropy (the point of the IPV–OPV transition) in the framework of the proposed model. The result is supported by numerical studies of discrete systems with an analogous geometry.

We have obtained analytical expressions for the magnetization distributions in the IPV and OPV (the latter in the case of weak anisotropy) and discussed the features of the vortex solution which stem from the special properties of the proposed model. For the system under study the gradient of the azimuthal angle φ falls off exponentially at large distances from the vortex core, and the difference between the spin directions of the mobile chains tends toward a finite value. The one-dimensional character of the model leads to finite values of the vortex mass and energy, in contrast to the case of an infinite two-dimensional system. At the same time, the vortex solution obtained has many of the properties of vortices in a two-dimensional system.

We have analyzed the motion of ''fast'' and ''slow'' OPVs of stationary profile. We have shown that a moving vortex has an asymmetric structure, as in two-dimensional systems. We have obtained analytical expressions for vortices moving with velocities $V\ll c$. We have also developed a generalization of the collective variables method which takes into account the combined description of the system, and we have obtained expressions for the gyrotensor and xx component of the vortex mass tensor.

The results presented here may be important for considering two-dimensional magnetic systems with a strong difference of the spatial sizes.

Some of the materials of this paper were presented at the conferences EASTMAG-2001 (Ekaterinburg) and Nonlinear Lattice Structure and Dynamics (Dresden), 2001. The authors thank M. MBogdan for helpful comments and additions in regard to the analysis of the stability of the IPV.

APPENDIX

For derivation of a simplified system of dynamical equations containing only the variables $\chi_{1,2}$, we need to retain in Eqs. (9) only the nonlinear terms in the small quantities $\varepsilon_{1,2}$. Then for the first pair of equations we obtain

$$J\varepsilon_{1,2}+\frac{J}{2}\varepsilon_{2,1}\mp\dot{\chi}_{1,2}+\frac{J\sqrt{3}}{2}\sin^2\frac{1}{2}(\chi_{1,2}-\chi_{2,1})$$
$$+\frac{\sqrt{3}}{4}(\beta\sin^2\chi_{1,2}+(\chi'_{1,2})^2)=\varepsilon'_{1,2}, \quad \text{(A1)}$$

and for the second pair

$$\chi''_{1,2}-\frac{\beta}{2}\sin 2\chi_{1,2}-J\sin(\chi_{1,2}-\chi_{2,1})$$
$$\pm\dot{\varepsilon}_{1,2}=-\frac{2}{\sqrt{3}}(\varepsilon_{1,2}\chi'_{1,2})'+\frac{\beta}{\sqrt{3}}\varepsilon_{1,2}\sin 2\chi_{1,2}$$
$$+\frac{J}{\sqrt{3}}(\varepsilon_{1,2}+\varepsilon_{2,1})\sin(\chi_{1,2}-\chi_{2,1}). \quad \text{(A2)}$$

The exact expressions for $\varepsilon_{1,2}$ are as follows:

$$\varepsilon_{1,2}=\pm\frac{1}{\sqrt{3}J}(2\dot{\chi}_{1,2}+\dot{\chi}_{2,1})-\frac{1}{\sqrt{3}}\sin^2\frac{1}{2}(\chi_{1,2}-\chi_{2,1})$$
$$-\frac{\beta}{2\sqrt{3}J}(2\sin^2\chi_{1,2}-\sin^2\chi_{2,1})-\frac{1}{2\sqrt{3}J}[(\chi'_{1,2})^2$$
$$-(\chi'_{2,1})^2]\pm\frac{2}{3\sqrt{3}J^2}(5\dot{\chi}_{1,2}+4\dot{\chi}_{2,1})''. \quad \text{(A3)}$$

As was shown above, for localized solutions of stationary profile of the form $\mathbf{S}=\mathbf{S}(x-Vt)$ we have $\partial/\partial t\sim V\beta^{1/2}$, $\partial/\partial x\sim\beta^{1/2}$, and $(\chi_1-\chi_2)\sim V\beta^{3/2}$. In order to obtain the asymptotic form of the solution for a moving vortex it is necessary to keep only the terms of the leading approximation in (A3).

Let us turn to an analysis of the spin-wave spectrum in the framework of the simplified equations. After linearization of equations (51) in small $\chi_{1,2}$ and making the substitution $\chi_{1,2}(x,t)=\chi_{1,2}\sin(kx-\omega t)$, we obtain

$$\omega_s^2=\frac{\beta J}{2}+c^2k^2,\quad \omega_a^2=\left(3J^2+\frac{3\beta J}{2}\right)+3c^2k^2, \quad \text{(A4)}$$

where $c=(J/2)^{1/2}$. Thus these dispersion relations differ from the exact ones (49) by terms of order Jk^2. The reason for this is that these dispersion relations can be used only under the condition that the magnon group velocity $V_{\rm gr}=\partial\omega/\partial k\ll c$, i.e., for $k\ll\beta^{1/2}$. Consequently, these relations can be used only in the leading approximation, and then the dispersion relations obtained agree with the exact relations (49) and (50) for $k\ll\beta^{1/2}$. To obtain a result which would give better agreement with the exact relations (49), (50) it is necessary to correct the above-described derivation procedure, keeping terms which we have previously neglected in the expressions for $\varepsilon_{1,2}$. As a result, in the linear approximation we obtain from (A3) the more exact relations for $\varepsilon_{1,2}$:

$$\varepsilon_{1,2}=\pm\frac{1}{J\sqrt{3}}(2\dot{\chi}_{1,2}+\dot{\chi}_{2,1})\pm\frac{2}{J^2 3\sqrt{3}}(5\dot{\chi}_{1,2}+4\dot{\chi}_{2,1})'' \quad \text{(A5)}$$

and the corresponding set of equations for $\chi_{1,2}$:

$$\chi''_{1,2}-\beta\chi_{1,2}=J(\chi_{1,2}-\chi_{2,1})+\frac{2}{3J}(2\ddot{\chi}_{1,2}+\ddot{\chi}_{2,1})$$
$$+\frac{4}{9J^2}(5\ddot{\chi}''_{1,2}+4\ddot{\chi}''_{1,2}). \quad \text{(A6)}$$

Then for the symmetric ($\chi_1=\chi_2$) mode we obtain

$$\omega_s^2=\left(\frac{J}{2}k^2+\frac{J\beta}{2}\right)\Big/\left(1-\frac{2}{J}k^2\right)\approx(\beta+k^2)\left(\frac{J}{2}+k^2\right), \quad \text{(A7)}$$

and for the antisymmetric mode ($\chi_1-\chi_2$)

$$\omega_a^2=\left(\frac{3J}{2}k^2+\frac{3J}{2}\beta+3J^2\right)\Big/\left(1-\frac{2}{3J}k^2\right)$$
$$\approx(\beta+2J+k^2)\left(\frac{3J}{2}+k^2\right). \quad \text{(A8)}$$

These relations agree with the exact values to terms of order k^4.

[a)]E-mail: kovalev@ilt.kharkov.ua

[1] J. M. Kosterlitz and D. J. Thouless, J. Phys. C **6**, 1181 (1973).
[2] F. G. Mertens and A. R. Bishop, *Nonlinear Sciences at the Dawn of the 21st Century*, Lecture Notes in Physics, P. L. Christiansen, M. P. Soerensen, and A. C. Scott (Eds.), Springer, Berlin (2000), p. 137.
[3] R. P. Cowburn, D. K. Koltsov, A. O. Adeyeye, M. E. Welland, and D. M. Tricker, Phys. Rev. Lett. **83**, 1042 (1999); R. P. Cowburn, J. Phys. D **33**, R1 (2000).
[4] T. Shinjo, T. Okuno, R. Hassdorf, K. Shigeto, and T. Ono, Science **289**, 930 (2000); ICR Ann. Rep. **7**, 16 (2000).
[5] H. Shima, K. Yu. Guslienko, V. Novosad, Y. Otani, K. Fukamichi, N. Kikuchi, O. Kitakami, and J. Shimada, J. Appl. Phys. **91**, 6952 (2002).
[6] M. E. Gouvea, G. M. Wysin, A. R. Bishop, and F. G. Mertens, Phys. Rev. B **39**, 11840 (1989).
[7] G. M. Wysin, Phys. Rev. B **49**, 8780 (1994).
[8] B. A. Ivanov, H. J. Schnitzer, F. G. Mertens, and G. M. Wysin, Phys. Rev. B **58**, 8464 (1998).
[9] G. M. Wysin and A. R. Völkel, Phys. Rev. B **52**, 7412 (1995).
[10] A. S. Kovalev and J. E. Prilepsky, Vestnik KhGU, Ser. Fizika **417**, 32 (1998); **440**, 25 (1999); Fiz. Nizk. Temp. **29**, 71 (2003) [Low Temp. Phys. **29**, 65 (2003)].
[11] L. Thomas, F. Lionti, R. Ballou, D. Gatteschi, R. Sessoli, and B. Barbara, Nature **383**, 145 (1996); J. Kortus, M. R. Pedersen, C. S. Hellberg, and S. N. Khanna, Eur. Phys. J. D **16**, 177 (2001); N. Fujima, *ibid.* , 185 (2001).
[12] T. A. Kontorova and Ya. I. Frenkel', Zh. Eksp. Teor. Fiz. **8**, 89 (1938)].
[13] O. M. Braun and Yu. S. Kivshar, Phys. Rep. **306**, 1 (1998).
[14] A. S. Kovalev, Fiz. Nizk. Temp. **20**, 1034 (1994) [Low Temp. Phys. **20**, 1034 (1994)].
[15] A. M. Kosevich, V. P. Voronov, and I. V. Manzhos, Zh. Éksp. Teor. Fiz. **84**, 148 (1983) [Sov. Phys. JETP **57**, 86 (1983)].
[16] L. M. Pismen, *Vortices in Nonlinear Fields*, Clarendon Press, Oxford (1999).
[17] D. K. Campbell, M. Peyrard, and P. Sodano, Physica D **19**, 165 (1986).
[18] A. J. Mikeska and M. Steiner, Adv. Phys. **90**, 191 (1991).
[19] N. G. Vakhitov, A. A. Kolokolov, Izv. Vyssh. Uchebn. Zaved., Radiofiz. **16**, 1020 (1973); M. M. Bogdan and A. M. Kosevich, in *Proceedings of the 4th International Workshop on Nonlinear and Turbulent Processes in Physics (Kiev)*, Vol. 1, edited by A. G. Sitenko and V. E. Zakharov, Naukova Dumka, Kiev (1989), p. 50.
[20] E. Jahnke, F. Emde, and F. Lösch, *Tables of Higher Functions*, McGraw-Hill, New York (1960), Nauka, Moscow (1964).
[21] A. S. Kovalev, Teor. Mat. Fiz. **37**, 135 (1979).
[22] N. Papanicolaou, Phys. Lett. A **186**, 119 (1994).
[23] T. I. Zueva, Fiz. Nizk. Temp. **26**, 119 (2000) [Low Temp. Phys. **26**, 85 (2000)].
[24] A. M. Kosevich, B. A. Ivanov, and A. S. Kovalev, Phys. Rep. **194**, 117 (1990).
[25] A. A. Thiele, Phys. Rev. Lett. **30**, 230 (1973).
[26] D. L. Hubert, Phys. Rev. B **26**, 3758 (1982).

[27] F. G. Mertens, H.-J. Schnitzer, and A. R. Bishop, Phys. Rev. B **56**, 2510 (1997).
[28] A. S. Kovalev, F. G. Mertens, and H.-J. Schnintzer (submitted to Eur. Phys. J. B., 2003).
[29] B. N. Filippov, Fiz. Nizk. Temp. **28**, 991 (2002) [Low Temp. Phys. **28**, 707 (2002)].

Translated by Steve Torstveit

LATTICE DYNAMICS

Elastic properties and phonon spectra of quasi-two-dimensional VSe_2

I. A. Gospodarev, A. V. Eremenko, T. V. Ignatova, G. V. Kamarchuk, I. G. Kolobov, P. A. Minaev, E. S. Syrkin,* S. B. Feodosyev, and V. D. Fil'

B. Verkin Institute for Low Temperature Physics and Engineering, National Academy of Sciences of Ukraine, pr. Lenina 47, 61103 Kharkov, Ukraine

A. Soreau-Leblanc, P. Molinie, and E. C. Faulques

Institut differences Materiaux Jean Rouxel, 2 reu de la Houssiniere, BP32229, F-44322 Nantes Cedex 3, France

(Submitted July 3, 2002; revised August 23, 2002)
Fiz. Nizk. Temp. **29**, 205–210 (February 2003)

A recently developed method is used to make acoustic measurements of VSe_2 single crystals. The components of the elastic constant tensor are determined from the data of these measurements. The experimental data are used to calculate the total and partial phonon densities of VSe_2, which permit an explanation of the vibrational spectra of this compound. © *2003 American Institute of Physics.* [DOI: 10.1063/1.1542414]

The vanadium dichalcogenide VSe_2, whose point-contact and Raman spectra have recently been obtained,[1] are quasi-two-dimensional layered structures which are now being actively studied because of a number of interesting properties (see, e.g., Refs. 2 and 3). Since the study of the phonon spectrum of VSe_2 by neutron-diffraction methods is difficult on account of the practically total transparency of vanadium for neutrons,[4–7] the present problem can be solved by recovering the interatomic interaction constants from the results of acoustic measurements and a subsequent theoretical calculation of the phonon density of states. Additional information about the phonon spectrum of VSe_2, which, because of the complexity of its crystal structure, should have an abundance of various kinds of features in the form of rather sharp spikes similar to those mentioned in Ref. 8, can be found in the data obtained by point-contact and Raman spectroscopy.

In this report we present the results of measurements of the elastic constants of VSe_2 and of a calculation based on those measurements for the density of phonon states of this compound; these results can be used to give an adequate interpretation of the results of Ref. 1.

The VSe_2 crystal consists of a set of planar structural formations—''sandwiches'' stacked on one another. Each of these elements consists of three layers, the upper and lower formed by selenium atoms and the middle an interlayer of vanadium atoms (Fig. 1). The layers of the metal and chalcogen in VSe_2 are displaced relative to one another in such a way that within a ''sandwich'' the vanadium atoms are found in an octahedral environment of selenium atoms. Although VSe_2 is an intensively studied compound, the absolute values of the sound velocities (and the elastic constants) in it have not been measured before.

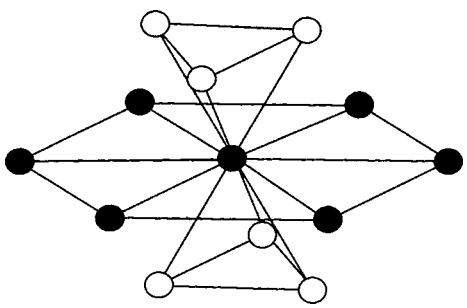

FIG. 1. Structure of the vanadium dichalcogenide VSe_2: V (●), Se (○).

The technology for growing VSe_2 single crystals can produce flakes with a size of $\sim 50-200$ μm in the direction perpendicular to the layers. In the preparation of x-ray-oriented samples for the acoustical studies, plane-parallel faces perpendicular to the [100] and [010] axes were obtained by mechanical polishing in a special miniature vise. The working faces, perpendicular to the [001] axis, were cleavage planes. As a result of this treatment the acoustical path length in the plane of the layers was 1–2 mm and that in the perpendicular direction was 40–100 μm. For determining the sound velocity we developed a new version of the phase technique, representing a kind of ''Nonius'' measurement procedure. Initially by recording the phase–frequency characteristic of the sample (frequencies near 54 MHz) we obtain a rough estimate of the value of the sound velocity, which allows us to estimate the number n of whole wavelengths that fit in the sample. The total phase delay created by the sample is found from the relation $\Phi = n360° + A$, where A is the reading of the phase meter ($0° \leqslant A \leqslant 360°$).

It was established by special studies that the irreproducibility of the phase measurements when the same sample is remounted is not more than 20°, and therefore the accuracy of the measurements is estimated as $\delta \sim 20°/\Phi$, i.e., $\sim 0.3\%$ for acoustic path lengths in the millimeter range, and 2–5% in the direction perpendicular to the layers. The ''Nonius''

TABLE I. Sound velocities and elastic constants in VSe_2 single crystals at $T=77$ K.

Mode	Sound velocity, 10^5 cm/s	Elastic constants, 10^{11} dyn/cm
[001] T	1.70 ± 0.05	$c_{44} = 1.69$
[001] L	2.67 ± 0.27	$c_{33} = 4.17$
[010] T	2.53 ± 0.01	$c_{12} = 1.42$
$\mathbf{q} \parallel [100]$	–	$c_{66} = 3.74$
[010] T	1.52 ± 0.01	$\lvert c_{14}\rvert = 2$
$\mathbf{q} \parallel [001]$	–	–
[100] L	3.9 ± 0.1	$c_{11}=8.9$

technique for acoustical measurements will be set forth in detail in a separate paper.

In the plane parallel to the threefold axis the samples are quite thin (with characteristic dimensions of 0.047 and 0.038 mm). In this direction the absolute values of the velocities are determined by comparison of the phases of the signals that have passed through samples of different lengths. The values of the sound velocities measured at a temperature $T=77$ K and the elastic constants calculated on the basis of them are presented in Table I.

From the results of the acoustical measurements of the elastic constants we calculated the ratios between the force constants of the interatomic interaction. Using the $\mathcal{J}$-matrix method[9,10] with the continued-fraction technique,[11,12] we found the total (Fig. 2) and partial phonon densities corresponding to the contributions from displacements of selenium atoms (Fig. 3) and vanadium atoms (Fig. 4) to the vibrational spectrum of the VSe_2 lattice both along the layers and in the perpendicular direction.

The partial phonon densities $\nu_i^{(q)}(\omega)$ (where the index q labels the atom and the index i the direction of displacement) are determined as (see, e.g., Ref. 13)

$$\nu_i^{(q)}(\omega)=\frac{V_0}{(2\pi)^3}\sum_{\alpha=1}^{3q}{}_{\omega_\alpha}\oint_{(\mathbf{k})=\omega}\frac{dS_\alpha}{v_\alpha}|e_i^{(q)}(\mathbf{k})|^2, \qquad (1)$$

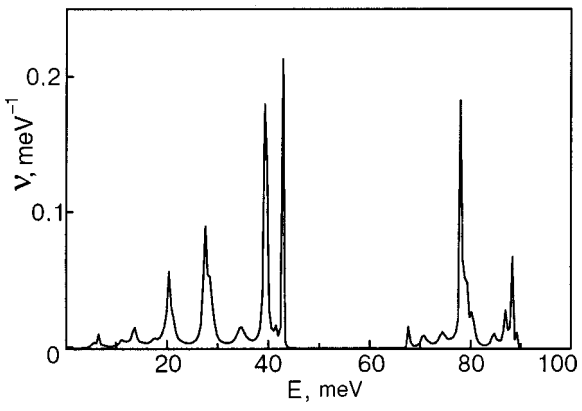

FIG. 2. Total phonon density calculated by the $\mathcal{J}$-matrix method from the data of acoustical measurements.

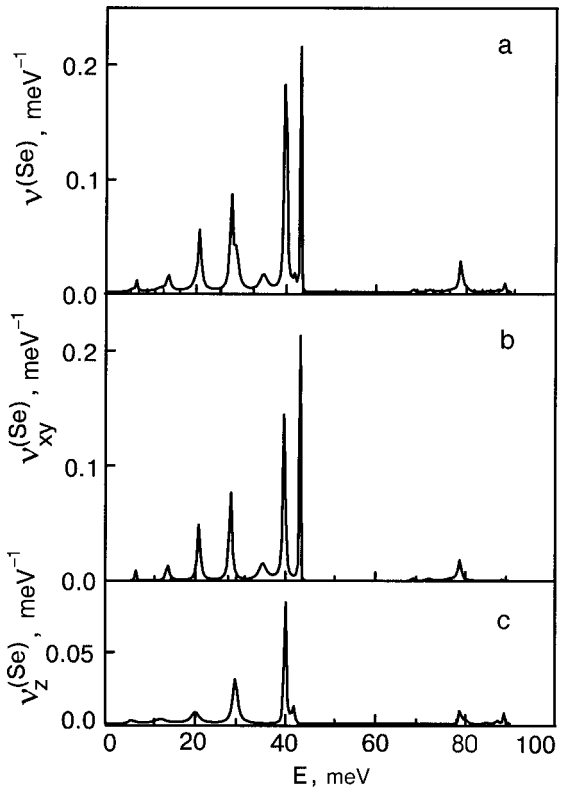

FIG. 3. Contributions to the phonon density from vibrations of the Se atoms: the total contribution (a) and the contributions of vibrations along the layers (b) and perpendicular to the layers (c).

where V_0 is the unit cell volume, $\omega_\alpha(\mathbf{k})$ is the dispersion relation of the vibrational mode of index α, $e^{(q)}$ are the polarization vectors, the integral is taken over an isofrequency surface in $\mathbf{k}$ space, dS_α is an element of that surface, and $v_\alpha=|\mathbf{v}_\alpha(\mathbf{k})|=|\nabla_\mathbf{k}\omega_\alpha(\mathbf{k})|$ is the absolute value of the phonon group velocity. The total phonon density is the sum of the partial densities:

$$\nu(\omega)=\sum_q \nu^{(q)}(\omega)=\sum_{q,i}\nu_i^{(q)}(\omega)$$

$$=\frac{V_0}{(2\pi)^3}\sum_{\alpha=1}^{3q}{}_{\omega_\alpha}\oint_{(\mathbf{k})=\omega}\frac{dS_\alpha}{v_\alpha}. \qquad (2)$$

We note that the partial densities $\nu^{(q)}(\omega)=\Sigma_{i=1}^3\nu_i^{(q)}(\omega)$ for many compounds are determined by neutron diffraction, by the isotopic contrast method.[14,15] Because of the weak interaction between the individual ''sandwiches'' of the Se–V–Se type, the lattice period of VSe_2 in the direction perpendicular to the layers can be considered to be much larger than the characteristic interatomic interaction radius (in fact, atoms separated by one lattice period along the C axis are practically noninteracting). As a result, the vibrational density of this compound exhibits characteristic features of both crystalline and disordered compounds, viz., the presence of a large number of quasilocalized vibrations (in a defect-free lattice) on diverse parts of the continuous spectrum band. Such features, though much more pronounced, are inherent to the spectra of high-T_c superconductors and similar compounds, the lattice period of which along the C axis is substantially larger.[8,14,15] In the case of VSe_2 the comparatively

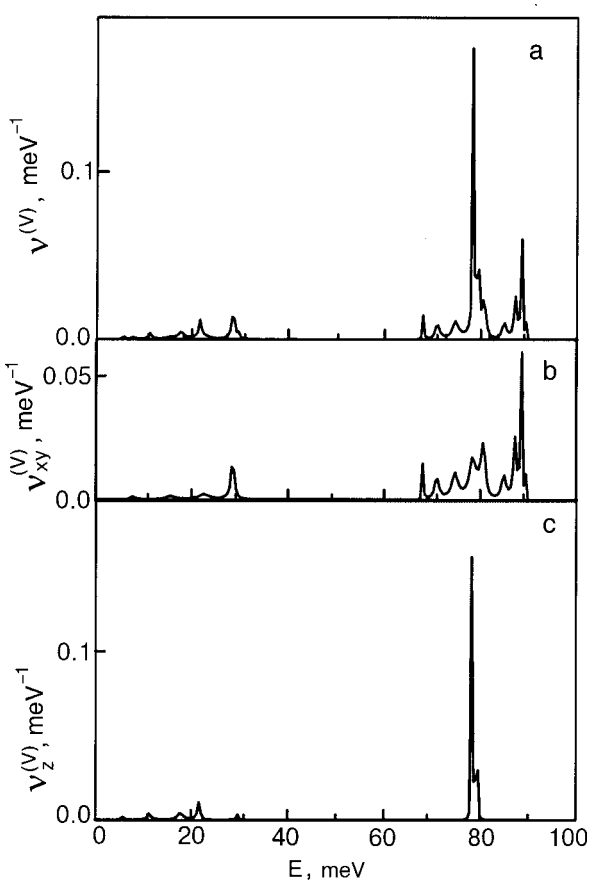

FIG. 4. Contributions to the phonon density from vibrations of the V atoms: the total contribution (a) and the contributions of vibrations of the V atoms along the layer (b) and perpendicular to the layer (c).

small lattice period in this direction is ''compensated'' by the strong anisotropy of the interatomic interaction. As a result, the vibrational spectrum of VSe_2 contains slowly propagating modes which form sharp resonance peaks on the phonon density.

The partial densities $\nu_i^{(Se)}(\omega)$ in VSe_2 are similar to those found in highly anisotropic layered crystals (see, e.g., Ref. 16, and for concrete models see Refs. 13, 17, and 18). The fact that the role of the layers is played by three-atom Se–V–Se ''sandwiches'' leads to changes in the behavior of the partial density $\nu_z^{(Se)}(\omega)$ (the z axis is chosen along the C axis) and also analogous changes due to the bending stiffness of the monolayers, i.e., to smearing of the low-frequency peaks.

The sharp peaks on the partial density $\nu^{(Se)}(\omega)$ are due to both Van Hove singularities for various vibrational modes and to the presence of weak-dispersion segments on the optical branches, which are characteristic for highly anisotropic layered crystals,[19] especially for values of the wave vector $\mathbf{k}$ close to zero. These are the vibrations that are manifested in the Raman spectra.

Let us first consider the two sharp peaks at $E \approx 40$ meV and $E \approx 43$ meV. Each of them corresponds to a weak-dispersion optical mode corresponding (for $\mathbf{k}=0$) to the Raman-active antiphase vibrations of the selenium atoms lying in the same plane, since the partial densities $\nu_i^{(V)}(\omega)$ (Fig. 4) show no traces of these peaks. The maximum at the lower frequency $E \approx 40$ meV corresponds to transverse vibrations, and is therefore clearly observed on both $\nu_{xy}^{(Se)}(\omega)$ and $\nu_z^{(Se)}(\omega)$. The peak at the higher frequency $E \approx 43$ meV corresponds to longitudinal vibrations, and it is therefore present on the curve of the partial density $\nu_{xy}^{(Se)}(\omega)$ but is extremely weak on the $\nu_z^{(Se)}(\omega)$ curve because of the very small interaction between the corresponding weak-dispersion vibrational modes.

These two peaks coincide in frequency with the peaks on the Raman spectra given in Ref. 1. The substantial difference in the height and width of the Raman peaks as compared to the peaks under discussion (they are substantially higher and narrower on the theoretical curves of Fig. 3) is explained, on the one hand, by the fact that we have considered an ideal lattice, and the presence of any defects and even the natural isotopic composition of Se can lead to smearing of the narrow peaks, and, on the other hand, by the fact that Raman spectroscopy does not detect the short-wavelength phonons which in this case have the same frequencies.

At $E \approx 21$ meV and 28 meV there are peaks observed on the partial densities both for vibrations of the vanadium atoms and of the selenium atoms, and they correspond to antiphase displacements of the V and Se found in adjacent layers. These peaks are broader and lower than those discussed above, and they correspond to modes with stronger dispersion. The fact that the peaks due both to the longitudinal ($E \approx 28$ meV) and transverse ($E \approx 21$ meV) vibrations are present on the functions $\nu_{xy}^{(q)}(\omega)$ and $\nu_z^{(q)}(\omega)$ is also due to the fact that the polarization direction of these modes does not coincide with the principal axes of the crystal and to the stronger interaction of these modes with each other. While in the previous case (vibrations in the plane of a close-packed layer) structural defects did not lead to mixing of the longitudinally and transversely polarized vibrational branches, for the modes under discussion now such interference, due in particular to the stresses caused by the various defects, is inevitable. Therefore, the Raman spectra given in Ref. 1 have a single large maximum at an intermediate frequency ($E \approx 28$ meV) instead of the two peaks.

Of course, since information for determining the force constants of VSe_2 came from acoustical measurements, there cannot be complete assurance that the phonon density in the high-frequency region has been recovered precisely. However, because of the weak interaction between Se–V–Se ''sandwiches,'' the partial densities $\nu_i^{(V)}(\omega)$ have the characteristic features of an isolated light impurity monolayer (vanadium is only about half as heavy as selenium).

Thus in our view the almost complete localization of these partial densities in the high-frequency region of the continuous spectrum is therefore completely explainable.

It should also be noted that in real VSe_2 crystals the partial density should not have as pronounced a resonance form because of the smearing due to various structural defects.

The position of the characteristic peaks on the total phonon density agrees with the results of measurements of the point-contact spectra.[1] For example, the point-contact spectra and the theoretical densities of states for selenium atoms have a characteristic low-frequency peak ($\sim 5-7$ meV), which should appear in all the low-temperature characteristics of the compound under study. This peak is the termina-

tion of the ''quasi-Debye'' segment on the density of states, $\nu(\omega)\sim\omega^2$, and it is therefore present on all the partial phonon densities. The frequency of this peak corresponds to the transition from closed isofrequency surfaces in the acoustic mode polarized perpendicular to the layers. In crystals for which the anisotropy of the interatomic interaction is small, this segment ends in a Van Hove singularity of the ''kink'' type,[16] while in highly anisotropic layered crystals this kink is transformed into a sharp resonance peak due to the presence of an extended weak-dispersion segment on the acoustic vibrational mode polarized along the weak-coupling direction.[20]

We note that the frequency of this peak has nothing to do with the Debye frequency of VSe_2. An estimate of the Debye temperature from the results of ultrasonic measurements gives $\Theta_D\approx 221$ K, which agrees completely with the value obtained for it in Ref. 20 ($\Theta_D=220\pm 5$ K).

The correspondence between the point-contact and Raman data near $E\approx 25$ meV and $E\approx 40-43$ is discussed in Ref. 1. We note only that the temperature and modulation broadening leads to smearing of the shape of the spectral lines in the point-contact spectra.[21] This explains why the point-contact spectra have broader peaks and even a ''shoulder'' ($E\approx 25$ meV) as compared to the calculated density of states. In making a comparison of the intensities, which for the point-contact and Raman spectra in Ref. 1 are given in arbitrary units (since the data of point-contact measurements only give information about the relative intensity of the peaks), one must take into account the influence of the point-contact form factor. It is expressed in a relative enhancement of the intensities at low frequencies and a diminution of the intensities at high frequencies in the point-contact spectra[22] (for VSe_2 this aspect is discussed in Ref. 1).

The agreement between the positions of the ''shoulders'' appearing at $E\approx 72$ meV and 82 meV against the background of the main maximum and the positions of the features in our calculated density of states (Fig. 2), at $E\approx 68$ meV and 80 meV, can be regarded as satisfactory in view of the inevitable distortions of the crystal structure and the stresses that arise in the lattice during the formation of point contacts.

In conclusion, it should be noted that the comparatively simple model proposed in this study for describing the phonon spectrum of the VSe_2 lattice can be augmented and refined on the basis of experimental data on the vibrational thermodynamic characteristics—heat capacity, Debye–Waller factor, coefficient of thermal expansion, etc. Neutron diffraction studies would be of great interest, in spite of the fact, mentioned at the beginning of this paper, that the total phonon spectrum of the compound under study cannot be obtained by neutron diffraction. And, for example, the application of the isotopic contrast method[15] for selenium would yield direct information about the partial densities $\nu^{(Se)}(\omega)$.

The authors thank K. R. Zhekov and A. N. Zholobenko for assistance in the measurements of the elastic constants.

This study was supported in part by NATO (CLG.PST 972846), the Ministry of Education and Science of Ukraine (2M-201/2001), and the Science and Technology Center of Ukraine (2276).

*E-mail: syrkin@ilt.kharkov.ua

[1] G. V. Kamarchuk, A. V. Khotkevich, V. M. Bagatskiĭ, A. Leblanc, P. Molinie, and E. Faulques, Fiz. Nizk. Temp. **27**, 71 (2001) [Low Temp. Phys. **27**, 56 (2001)].
[2] H. Mutka, in *Advances in the Crystallographic and Microstructural Analysis of Charge Density Wave Modulated Crystals*, edited by F. W. Boswell and J. C. Bennett, Kluwer, Dordrecht (1999), p. 153.
[3] P. Molinie, A. Leblanc, E. Faulques, Z. Ouili, J.-C. Jumas, and C. Ayache, in *Spectroscopy of Superconducting Materials*, edited by E. Faulques, American Chemical Society Symposium Series, Vol. 730, Washington (1999), Ch. 2, p. 21.
[4] D. J. Hughes, *Neutron Cross Sections*, Pergamon Press, Oxford (1957), Izd. Inostr. Lit., Moscow (1959).
[5] G. E. Bacon, *Neutron Diffraction Commission Data*, IUC (1978).
[6] G. E. Bacon, *Neutron Diffraction*, Clarendon Press, Oxford (1975).
[7] Yu. Z. Nozik, R. P. Ozerov, K. Khennig, in *Neutrons and the Solid State*, edited by R. P. Ozerov, Atomizdat, Moscow (1979).
[8] I. A. Gospodarev, A. M. Kosevich, E. S. Syrkin, and S. B. Feodos'ev, Fiz. Nizk. Temp. **22**, 593 (1996) [Low Temp. Phys. **22**, 457 (1996)].
[9] V. I. Peresada, in *Physics of the Condensed State* [in Russian], Kharkov (1968), p. 172.
[10] V. I. Peresada and V. N. Afanas'ev, Zh. Éksp. Teor. Fiz. **58**, 135 (1970) [Sov. Phys. JETP **31**, 78 (1970)].
[11] V. I. Peresada, V. N. Afanas'ev, and V. S. Borovikov, Fiz. Nizk. Temp. **1**, 461 (1975) [Sov. J. Low Temp. Phys. **1**, 227 (1975)].
[12] R. Haydock, in *Solid State Physics*, Vol. 35, H. Ehrenreich, F. Seitz, and D. Turnbull (Eds.), Academic Press, New York (1980), p. 129.
[13] A. M. Kosevich, E. S. Syrkin, and S. B. Feodosyev, Phys. Low-Dimens. Semicond. Struct. **3**, 47 (1994).
[14] I. Natkanets, E. S. Syrkin, S. B. Feodos'ev, and V. K. Fedotov, *Abstracts of the Conference on Low Temperature Physics*, September 6–9, 1994, JINR, Dubna [in Russian], Part 2, p. 189.
[15] V. K. Fedotov, A. I. Kolesnikov, V. I. Kulakov, E. G. Ponyatovskiĭ, I. Natkanets, Ya. Maĭer, and Ya. Krawczyk, Fiz. Tverd. Tela. (St. Pertersburg) **35**, 310 (1993) [Phys. Solid State **35**, 156 (1993)].
[16] A. M. Kosevich, *Theory of the Crystal Lattice (Physical Mechanics of Crystals)* [in Russian], Vishcha Shkola, Kharkov (1988).
[17] E. S. Syrkin, S. B. Feodos'ev, and O. Ya. Shamfarova, Fiz. Nizk. Temp. **17**, 746 (1991) [Sov. J. Low Temp. Phys. **17**, 393 (1991)].
[18] S. B. Feodos'ev and E. S. Syrkin, Fiz. Nizk. Temp. **9**, 528 (1983) [Sov. J. Low Temp. Phys. **9**, 268 (1983)].
[19] G. Smith and N. Wakabayashi, in Dynamics of Solids and Liquids by Neutron Scattering, edited by S.W. Lovesey and T. Springer, Springer-Verlag, Berlin–Heidelberg–New York (1977), Mir, Moscow (1980), p. 97.
[20] Yu. A. Kosevich and E. S. Syrkin, Fiz. Nizk. Temp. **9**, 624 (1983) [Sov. J. Low Temp. Phys. **9**, 317 (1983)].
[21] A. V. Khotkevich and I. K. Yanson, *Atlas of Point Contact Spectra of Electron-Phonon Interactions in Metals*, Kluwer, Dordrecht (1995).
[22] I. O. Kulik, A. N. Omel'yanchuk, and R. I. Shekhter, Fiz. Nizk. Temp. **3**, 1543 (1977) [Sov. J. Low Temp. Phys. **3**, 740 (1977)].

Translated by Steve Torstveit

NEW METHODS OF LOW-TEMPERATURE EXPERIMENT

High-T_c rf SQUID for magnetic microscopy

S. S. Khvostov, V. P. Timofeev,* A. S. Garbuz, and V. I. Shnyrkov

B. Verkin Institute for Low Temperature Physics and Engineering, National Academy of Sciences of Ukraine, pr. Lenina 47, 61103 Kharkov, Ukraine
(Submitted July 17, 2002)
Fiz. Nizk. Temp. **29**, 211–215 (February 2003)

The spectral density of magnetic flux noise $S_\Phi^{1/2}(f)$ is investigated for high-T_c rf SQUIDs with a pumping frequency of 390–457 MHz, placed inside three-layer Permalloy and superconducting shields. A superconducting interferometer with inner dimensions of the pickup loop of 100×100 μm is prepared by thin-film technology with a YBaCuO–PrBaCuO–YBaCuO Josephson junction of the ramp-edge type. It is shown that with the use of a cooled preamplifier, the energy sensitivity of SQUIDs in the ''white'' noise region (at frequencies above 1 kHz) is 4×10^{-30} J/Hz and is mainly determined by the intrinsic noise of the high-T_c superconducting interferometer and the shields. At low frequencies the predominant noise is from external fields penetrating directly into the shields. The addition of a ferromagnetic antenna to the SQUID microscope increases the intrinsic noise of the magnetometer to 8×10^{-30} J/Hz at frequencies above 1 kHz. [DOI: 10.1063/1.1542415]

INTRODUCTION

The creation of SQUID microscopes[1,2] with high spatial resolution requires increasing the signal-to-noise ratio and, hence, the sensitivity of high-T_c rf SQUIDs. This is because of the fact that when scanning an object, for any algorithm used to solve the inverse problem of magnetic defectometry, the accuracy of location, classification, and determination of its parameters all depend on the signal-to-noise ratio in the compilation of the data base.

In the room-temperature study of objects containing spontaneous or induced magnetic moments, the spectral density of external magnetic noise at the sample is much greater than the typical sensitivity of a high-T_c SQUID microscope. Therefore, to improve the signal-to-noise ratio the sensitive element and the sample are placed in a Permalloy shield. The working frequency f of the microscope is chosen in the ''white'' noise region, which for the usual shielding conditions starts at hundreds of hertz. In such a microscope the intrinsic $1/f$ noise of a high-T_c SQUID has practically no effect on the quality of reconstruction of the characteristics of the object under study, which is determined by the sensitivity of the SQUID in the ''white'' noise region, the shielding coefficient for external electromagnetic fields, and the gain factor for the magnetic flux from the sample to the SQUID. Since a high-T_c SQUID is found at a temperature of 77 K while the object of study is at room temperature, so that they have to be separated by a gap for thermal isolation, the spatial resolution of a SQUID microscope can be improved by using a magnetic antenna—a magnetic circuit made of a ferromagnetic material (e.g., in the shape of a cone).

For improving the sensitivity to magnetic field and the gain factor for the magnetic flux from the object to the high-T_c SQUID, the geometric inductance L of the superconducting quantum interferometer is made quite large. However, as follows from the classical theory of SQUIDs,[3,4] an increase of the inductance will lead to a rapid decrease of the modulation index of the output voltage, a decrease in the conversion transconductance, and an increase in the intrinsic noise, which depends on the ratio L/L_F, where $L_F=(\Phi_0/2\pi)^2/k_BT$ is the fluctuational inductance, Φ_0 is the magnetic flux quantum, k_B is Boltzmann's constant, and T is the temperature.

For SQUIDs with nitrogen cooling ($T=77$ K) the fluctuational inductance $L_F=1.02\times10^{-10}$ H, and in the usual film technology for preparation of interferometers the value L/L_F is close to unity in all published studies. This means that the so-called nonhysteretic operating regime ($\beta_L=2\pi LI_c/\Phi_0<1$) the is realized for high-T_c rf SQUIDs with $L>10^{-10}$ H and $T=77$ K under conditions such that the thermal fluctuation energy k_BT exceeds the characteristic Josephson junction coupling energy $I_c\Phi_0/2\pi$. Here I_c is the critical current. In other words, for high-T_c SQUIDs with $\beta_L\leqslant1$ the dimensionless parameter

$$\gamma=2\pi k_BT/l_c\Phi_0 \tag{1}$$

is greater than 1 in practically all published studies.

For $\gamma\gg1$, $L/L_F\sim1$, and $\beta_L\leqslant1$, it follows from the theory[3] that the average value of the current $\langle I\rangle$ circulating in the interferometer of the SQUID at a fixed phase difference φ across the contact is sharply reduced:

$$\langle I\rangle\approx I_c\exp(-L/2L_F)\sin\varphi, \tag{2}$$

and this leads to the above-mentioned rapid falloff of the sensitivity of high-T_c rf SQUIDs with increasing inductance of the pickup loop. In the nonhysteretic regime, when the nonlinearity is small, expression (2) should describe a high-T_c rf SQUID to good accuracy, and in the limit of not very large values of γ, e.g., $\gamma\sim1$, one has $L/L_F\sim1$ and β_L

$\ll 1$.[5] This is easily understood by formally replacing the microwave energy in Ref. 5 by the thermal fluctuation energy k_BT in the analytical expressions for the amplitude–frequency characteristics of the SQUID in the nonhysteretic regime.

To take into account the influence of the large thermal fluctuations on a high-T_c rf SQUID operating in the hysteretic ($\beta_L > 1$) regime, it is necessary to carry out an analysis of the Fokker–Planck equation in this limit. Such theoretical studies for the region $\gamma \sim 1$, $L/L_F \sim 1$, and $\beta_L \sim 1$ were carried out in Ref. 6. A more detailed analysis, also based on numerical solution of the Fokker–Plank equation, and experimental studies of the characteristics of high-T_c rf SQUIDs[7,8] have made it possible to extend these results to practically arbitrary values of γ, L/L_F, and β_L. For example, for the region $L/L_F \sim 1$ it has been shown that thermal fluctuations in rf SQUIDs lead to a more complicated renormalization of the average circulating current and dimensionless inductance β_L, which in this case can be written in the form

$$\beta_{\text{eff}} \sim B_L \left[2\gamma \exp\left(-\frac{L}{2L_F} \right) \frac{J_1(1/\gamma)}{J_0(1/\gamma)} \right], \tag{3}$$

where $J_1(1/\gamma)$ and $J_0(1/\gamma)$ are modified Bessel functions. It follows from expression (3) that for $\gamma \gg 1$ the average value of the circulating current practically coincides with the results of a previous study,[3] while for $\gamma \leqslant 1$ it is modified in a rather complicated way. This effective decrease in the nonlinearity of the interferometer in Eqs. (2) and (3) is due to the influence of thermal fluctuations, which lead to a change in the current–voltage and signal characteristics of the SQUID,[8] and, in the final analysis, to a degradation (proportional to β_{eff}) of its sensitivity.

It was shown in Ref. 9 that for optimization of the signal characteristics and sensitivity of an rf SQUID working in the large-fluctuation limit ($\gamma \sim 1$, $L/L_F \sim 1$), it is necessary to increase significantly the coupling coefficient k between the resonance circuit, with Q factor Q, and the pickup loop. For the hysteretic regime $\beta_L > 1$ the usual matching condition $k^2Q \cong 1$, $\gamma \ll 1$ must be rewritten as $k^2Q\beta_{\text{eff}} \cong 1$. This reflects the fact that in this limit the nonlinearity of the current–voltage characteristics of the SQUID is strongly reduced on account of the influence of thermal fluctuations, and its working regime becomes similar to the nonhysteretic regime.

It is known[4] from the classical theory that the sensitivity of an rf SQUID improves significantly with increasing excitation frequency $\omega/2\pi$, and this improvement can to a certain degree compensate the influence of thermal fluctuations in the region $\gamma > 1$, $L/L_F \sim 1$. For example, in Ref. 10, in a study of a high-T_c rf SQUID in the regime of large fluctuations, $L/L_F \sim 1$, $\gamma > 1$, at an excitation frequency of 850 MHz, the energy sensitivity in the ''white'' noise region was found to be

$$\delta\varepsilon = S_\Phi(f)/2L \sim 5.6 \times 10^{-31}\ \text{J/Hz}, \tag{4}$$

where S_Φ is the square of the spectral density of magnetic flux noise.

A calculation of the total sensitivity of a high-T_c rf SQUID microscope in the limit of large fluctuations with the intrinsic noise of the interferometer and the noise of the oscillator circuit, preamplifier, magnetic antenna, and shields taken into account is an extremely complicated problem even if one ignores the influence of the noise that is specifically related to the features of high-T_c materials. Therefore, in this paper we have made a direct experimental study of $S_\Phi^{1/2}(f)$ for two variants of a film-type high-T_c rf SQUID magnetometer (with and without a ferromagnetic antenna) placed in a shielded space.

EXPERIMENTAL RESULTS

The pickup loop of the high-T_c SQUID, with an area of 100×100 μm, was made from a $YBa_2Cu_3O_{7-\delta}$ epitaxial film 150 nm thick, deposited on a $SrTiO_3$ substrate by the method of laser ablation. To increase the coupling with the external antenna of the microscope, the interferometer was made in the form of a magnetic flux concentrator with dimensions of 3×3 mm. For such a geometry of the device the period of the output voltage of the SQUID magnetometer with respect to magnetic field was $\Delta B/\Phi_0 = 1.3 \times 10^{-8}$ T/Φ_0. The characteristic voltage $V_c = I_cR_N$ (the product of the critical current times the contact resistance R_N in the normal, nonsuperconducting state) for Josephson junctions of the ramp-edge type made from YBaCuO–PrBaCuO–YBaCuO epitaxial films with a barrier thickness of 5–10 nm has values of around 20 μV at 77 K ($I_c = 10$–15 μA, $R_N = 1.5$–2 Ω). Thus for these interferometers the ratio of the energy of thermal fluctuations to the Josephson junction coupling energy has a value $\gamma = 0.7$ for $L/L_F = 1.6$ and $\beta_L = 2$–5. The comparatively low values of R_N for PrBaCuO-based junctions limits how much one can increase the excitation frequency $1/2\pi$ of high-T_c SQUIDs (because of the onset of strong nonadiabatic phenomena in the pickup loop) at a level of ~ 500 MHz. Indeed, for $R_N \sim 1$ Ω the characteristic time of the interferometer, $\tau = L/R_N$, becomes comparable to $1/\omega$ at $1/2\pi \sim 1$ GHz.

To decrease the influence of the noise temperature of the relaxation circuit and reduce the contribution of the noise of the subsequent cascades of the measurement circuit, we used a cooled two-cascade preamplifier based on GaAs field-effect transistors. The noise temperature T_N of the amplifier unit, measured by the method of ''hot'' and ''cold'' loads, was 35 K at room temperature. Although the noise temperature of the unit was not measured when the preamplifier was cooled to 77 K, we can state that it did not exceed the value indicated above. At a frequency of 400 MHz the gain of the cooled cascade was 30 dB in a 20 MHz band. For matching of the input impedance of the amplifier with the resonance circuit we used a partial connection scheme. The amplified signal at the output of the second cascade of the cooled preamplifier was detected by a wideband amplitude detector with a working frequency bandwidth of more than 40 kHz. Figure 1 shows the main elements of the resonance circuit (a) and the circuit of the cooled preamplifier (b).

The inductance of the the single-ply coil of the resonance circuit, which was made of copper wire with a diameter of 0.07 mm, was 7.2×10^{-8}H. The loaded Q factor of the resonance circuit was $Q \sim 100$ at the maximum coupling coefficient $k \sim 0.1$. Increasing the coupling coefficient further led to a loss of stability of the gain, i.e., to regenerative amplification.

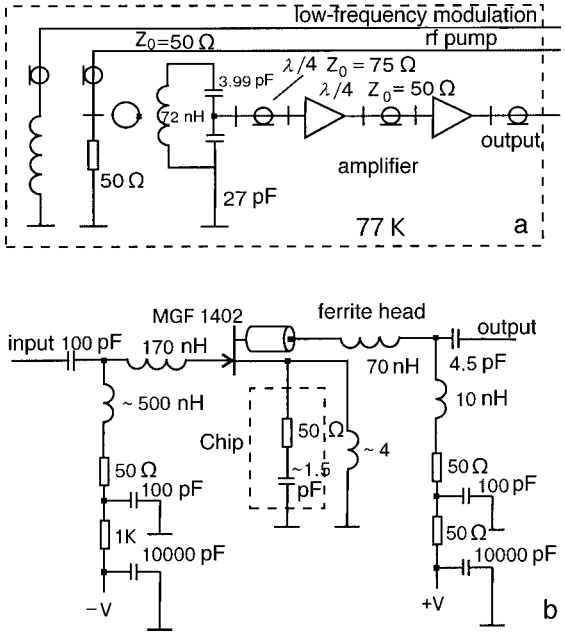

FIG. 1. Main elements of the resonance circuit of the high-T_c rf SQUID and cooled two-cascade preamplifier (a) and the electrical circuit of the amplifier cascade (b). The special use of a filter in the form a chip in the source circuit, together with the use of absorbing ferrite beads at selected fixed positions in the drain circuit made stable operation of the cascade possible in the specified frequency band.

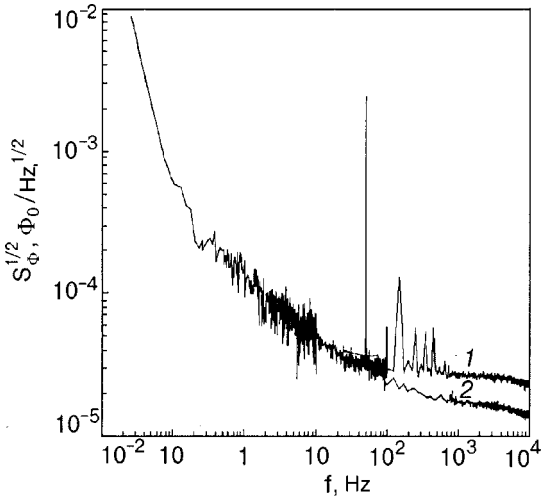

FIG. 2. Spectral density of magnetic flux noise $S_\Phi^{1/2}$ versus frequency f for high-T_c rf SQUID magnetometers in a three-layer Permalloy shield: SQUID magnetometer with a magnetic antenna (*1*) and without an antenna (*2*).

For studies of the the intrinsic noise (the spectral density of magnetic flux noise) the high-T_c SQUID was placed inside a special compact glass-reinforced plastic cryostat with a volume of 1 liter. In turn, the cryostat was mounted with the SQUID in a cylindrical three-layer Permalloy shield made from the alloy NM-79. The shielding coefficient of the static component of the Earth's magnetic field with respect to the z coordinate was measured by means of a ferroprobe magnetometer in the place where the SQUID and magnetic antenna were located and was found be 62–65 dB. For analysis of how the spectral density of the noise of the high-T_c SQUID depends on the choice of working point and the type of magnetometer, we used a B&K Type 2033 low-frequency analyzer with a frequency band from 0 to 20 kHz.

Figure 2 shows the spectral density of the magnetic flux noise as a function of frequency, obtained for two variants of the SQUID magnetometer. For the SQUID magnetometer without the magnetic antenna at the input the energy sensitivity in the frequency range 10^3–10^4 Hz reaches values $\delta\varepsilon = 4\times10^{-30}$ J/Hz, which corresponds to a magnetic-field resolution $S_B^{1/2} = 2\times10^{-13}$ T/Hz$^{1/2}$ in the "white" noise region. It is seen from the graph that at frequencies below 10^3 Hz the total noise can be represented in the form $1/f^\alpha$, where the exponent α varies from 1 to 0.5 (at frequencies of 0.03 to 300 Hz). The large spikes at frequencies of 50, 100, and 150 Hz are due to the penetration of external noise (which are apparently harmonics of the grid voltage supplied to the leads) indicate the presence of magnetic fields in the shielded space at the levels of 10^{-11} T/Hz$^{1/2}$ and 8×10^{-13} T/Hz$^{1/2}$, respectively.

For a SQUID magnetometer inductively coupled to a conical rod with a minimum diameter of ~0.5 mm and a length of 2 mm, made from a weakly conducting ferrite, the spectral density of the noise at frequencies above 100 Hz increases by a factor of 3.5–4 (see Fig. 2). Below 100 Hz the noise is the same for both magnetometers and is determined by the magnetic field in the shield. The increase in the intrinsic noise of a SQUID magnetometer having a ferrite antenna can be attributed to an increase in the inductance of the pickup loop [Eqs. (2) and (3)] and to the direct insertion noise of the magnetic antenna.

DISCUSSION OF THE RESULTS

If a small ($r \ll R$) dipole with magnetic moment **m** is found in the sample under study, the magnetic induction **B** produced by this dipole will fall off with distance as $\mathbf{B}(R) \sim \mu\mu_0\mathbf{m}/2\pi R^3$. Here μ is the magnetic permeability of the medium, $\mu_0 = 4\pi\cdot10^{-7}$ H/m, and R is the distance to the SQUID along the axis of the dipole of radius r. The design of our cryostat allows one to place the high-T_c rf SQUID magnetometer a distance 2 mm from the object, which is at room temperature. Since the characteristic values of the radii of the magnetic dipoles to be investigated lie in the range $r = 0.1$–1.0 mm, in order to increase the magnetic induction **B** produced by the dipole at the point where the SQUID is located it is necessary to increase the magnetic permeability μ of the medium. In other words, a magnetic circuit made of a material with $\mu \gg 1$ should be placed between the magnetic dipole and the SQUID magnetometer. Then the magnetic induction will be

$$\mathbf{B}(R) = \mu_{\text{eff}}\mu_0\mathbf{m}/2\pi R^3. \tag{5}$$

Depending on the material and construction of the rod, the effective magnetic permeability μ_{eff} can increase the conversion ratio of the signal to the SQUID magnetometer while simultaneously increasing the inductance of the pickup loop. On the other hand, the high magnetic permeability of the magnetic circuit acts as a kind of concentrator of magnetic noise, and at low shielding coefficients the magnetic antenna becomes ineffective. In the experiment under discussion the spectral density of the magnetic flux noise of the SQUID with the ferromagnetic antenna increased by a factor of

3.5–4, while the conversion ratio for some dipoles increased by a factor of 5–10. Another very important consideration is that the shape of the magnetic antenna and the effective decrease in the distance between the dipole and the SQUID can greatly improve the spatial resolution of the SQUID microscope.

For classical low-temperature rf SQUIDs, which operate in the limit of small fluctuations, $L/L_F \ll 1$ and $\gamma \ll 1$, the increase in the inductance L of the pickup loop (due to the influence of the magnetic antenna) always leads to a degradation of the sensitivity of the SQUID magnetometer to magnetic field. This is easily shown by differentiating the well-known expressions for the sensitivity of a SQUID as a function of energy $\varepsilon\varepsilon$ and the magnetic induction δB with respect to the inductance L.[4,11] It is interesting to note that in high-T_c rf SQUIDs, which operate in the limit of large fluctuations, the minima with respect to L for the analogous expressions cannot coincide because of the presence of the additional factor $\sim \exp(-L/2L_F)$, which depends on the inductance of the pickup loop [Eqs. (2) and (3)].

In this study the period with respect to magnetic field for the high-T_c SQUID magnetometer with the magnetic antenna was not measured, but if its value is estimated as $\Delta B/\Phi_0 < 10^{-8}$ T/Φ_0 (the magnetic antenna increases the effective area), the sensitivity with respect to the magnetic induction would be $\delta B < 4 \times 10^{-13}$ T/Hz$^{1/2}$, and for $\mu_{\text{eff}}/\mu \sim 10$ one could register magnetic dipoles of area 100×100 μm with a current of several microamperes.

The authors thank S. I. Bondarenko, A. A. Shablo, and P. P. Pavlov for helpful discussions.

*E-mail: timofeev@ilt.kharkov.ua

[1] T. S. Lee, G. Dantsker, and J. Clarke, Rev. Sci. Instrum. **67**, 4208 (1996).
[2] J. Banchet, J. Jouglar, P. L. Vuillermoz, P. Waltz, and H. Weinstok, Rev. Prog. Quant. Nondestr. Eval. **14**, 1675 (1995).
[3] V. A. Khlus and I. O. Kulik, Zh. Tekh. Fiz. **45**, 449 (1975) [Sov. Phys. Tech. Phys. **20**, 283 (1975)].
[4] K. K. Likharev, *Introduction to the Dynamics of Josephson Junctions* [in Russian], Nauka, Moscow (1985).
[5] V. I. Shnyrkov, V. A. Khlus, and G. M. Tsoi, J. Low Temp. Phys. **39**, 477 (1980).
[6] B. Chesca, J. Low Temp. Phys. **110**, 963 (1998).
[7] Ya. S. Greenberg, J. Low Temp. Phys. **114**, 297 (1999).
[8] X. H. Zeng, Y. Zhang, B. Chesca, K. Barthel, Ya. S. Greenberg, and A. I. Braginski, J. Appl. Phys. **88**, 11 (2000)
[9] V. I. Shnyrkov, V. P. Timofeev, A. S. Garbuz, and Cheol Gi Kim, Fiz. Nizk. Temp. **25**, 1103 (1999) [Low Temp. Phys. **25**, 826 (1999)].
[10] Y. Zhang, W. Zander, J. Schubert, F. Rüders, H. Soltner, M. Banzet, N. Wolters, X. H. Zeng, and A. I. Braginski, J. Appl. Phys. **71**, 704 (1997).
[11] T. Ryhanen, H. Seppa, R. Ilmoniemi, and J. Knuutila, J. Low Temp. Phys. **76**, 287 (1989).

Translated by Steve Torstveit

LETTER TO THE EDITOR

Detection of nuclear spin conversion of CD_4 molecules in a solid solution of deuteromethane in krypton

M. I. Bagatskiĭ,* V. G. Manzheliĭ, D. A. Mashchenko, and V. V. Dudkin

B. Verkin Institute for Low Temperature Physics and Engineering, National Academy of Sciences of Ukraine, pr. Lenina 47, 61103 Kharkov, Ukraine
(Submitted November 29, 2002)
Fiz. Nizk. Temp. **29**, 216–218 (February 2003)

The heat capacity of the solid solutions $(CD_4)_{0.05}Kr_{0.95}$ and $(CD_4)_{0.05}Kr_{0.948}(O_2)_{0.002}$ are investigated in the temperature interval 0.7–1.6 K. The contribution to the heat capacity of the solutions from the rotational subsystem is separated out. Conversion between the A and T nuclear spin species of CD_4 is detected. It is shown that in unconcentrated solutions of methane isotopes in krypton the rate of conversion is larger for the deuteromethane molecules than for the methane molecules. © *2003 American Institute of Physics.* [DOI: 10.1063/1.1542416]

Research on the physical properties of $(CH_4)_nKr_{1-n}$ and $(CD_4)_nKr_{1-n}$ solid solutions yields information about quantum effects in the dynamics of spherical rotors. A clear quantum effect manifested on a macroscopic level is conversion—transitions between the A, T, and E nuclear spin species of the CH_4 and CD_4 rotors, with total spins of the nuclei of $I=2$, 1, 0 and $I=4$, 2, 0, respectively. Equilibrium is established between spicies through conversion. The study of conversion in solid methane and solid solutions of methane in rare gases has been the subject of a large number of experimental and theoretical works (see Refs. 1–3, the handbooks,[4,5] and the literature cited therein). At the same time, there are no reliable experimental data on the observation of conversion in solid deuteromethane and in solid solutions containing deuteromethane.[3–5] For a long time it was thought that the conversion of CD_4 must occur very slowly because of the relatively small magnetic moment of the deuterium atoms and for that reason is not manifested in real experiments.

The main result of the present study is the detection of nuclear spin conversion of CD_4 molecules in a krypton matrix. Calorimetric studies were done for a 5% solution of CD_4 in Kr and for the same solution doped with 0.2% O_2. It had been established previously[1] that a 0.2% O_2 concentration accelerates conversion in a weak solution of methane in krypton by at least an order of magnitude while having practically no effect on the phonon subsystem and spectrum of rotational motion of the CH_4 rotors.

The heat capacity of these solutions was determined by means of an adiabatic calorimeter[6] in the temperature interval 0.7–1.6 K. The calorimetric heating time was $t_h=2-4$ min. The effective time for one measurement of the heat capacity was $t_m=t_h+t_e\sim 40$ min, where t_e is the time for establishment of a steady temperature trend of the calorimeter from the time the heater was turned on. The gases used for preparing the samples had the following compositions: CD_4—isotopic purity 99%, purity with respect to other gases 99.20% (N_2—0.5%, O_2—0.2%, CO—0.1%, and Ar $<0.01\%$); Kr—purity 99.79% (Xe—0.2%, N_2—0.01%, O_2 and Ar$<0.01\%$); O_2—purity 99.99% ($N_2<0.01\%$). Prior to the experiments the samples were held for about a day at the lowest temperature of the measurements. The error of measurement of the heat capacity of the solutions was 6% at 0.8 K, 2% at 1 K, and 1.5% at 1.6 K.

The contribution to the heat capacity from the rotational subsystem $C_{\rm rot}$ was separated out. The temperature dependence of the experimentally determined heat capacity of the rotational subsystem $C_{\rm rot}$ of the solutions, normalized by the CD_4 concentration n and the universal gas constant R ($C_{\rm rot}/nR$ is the reduced heat capacity of a mole of rotors) is presented in Fig. 1. Also shown in Fig. 1 is the temperature dependence of the rotational heat capacity calculated from the spectrum indicated below for the equilibrium $C_{\rm rot,equilib}$ (solid curve) and high-temperature $C_{\rm rot,high}$ (dotted curve) contributions of the nuclear spin species of CD_4. $C_{\rm rot,equilib}$ was calculated on the assumption of rapid conversion, for characteristic conversion times $\tau \ll t_m$. $C_{\rm rot,high}$ was calculated on the assumption that conversion does not take place at all, and the relationship between the nuclear spin species of CD_4 remains at the equilibrium value for high temperatures and free molecules of CD_4 ($x_A:x_T:x_E=15:54:12$).

The lower rotational energy levels of a CD_4 rotor in the crystalline field of krypton were calculated in Ref. 7 and are as follows (the energy levels are in kelvins, and the degeneracy of the levels is given in parentheses):

Species A: 0 K (15), 22.5 K (45).

Species T: 4.7 K (54), 11.0 K (36).

Species E: 11.0 K (36), 34.4 K (24).

It is easy to see that at low temperatures and in the presence of conversion the largest contribution to the heat capacity $C_{\rm rot}$ is from transitions between the lowest levels of the A (0 K) and T (4.7 K) species. In the experiment the indicated contribution to the heat capacity $C_{\rm rot}$ is determined by the number of molecules that have undergone transition from level A (0 K) to level T (4.7 K) over the time t_m of one heat capacity measurement. In the case of rapid conversion

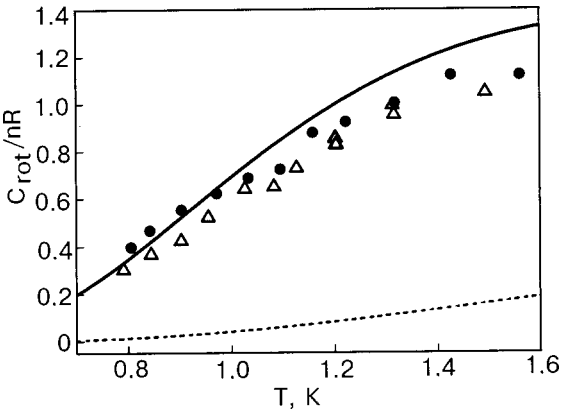

FIG. 1. Temperature dependence of the normalized heat capacities $C_{\rm rot}/nR$ of the solid solutions $(CD_4)_{0.05}Kr_{0.95}$ (○) and $(CD_4)_{0.05}Kr_{0.948}(O_2)_{0.002}$ (●). The solid and dotted curves were calculated from the spectrum of Ref. 7 for the equilibrium and high-temperature ($x_A:x_T:x_E=15:54:12$) distributions of the nuclear spin species of CD_4, respectively.

equilibrium will be established over the time t_m ($C_{\rm rot}$ will be maximal). In the limiting case of no conversion the ratio of the concentrations of the species correspond to the high-temperature distribution, and $C_{\rm rot}=C_{A,\rm rot}+C_{T,\rm rot}+C_{E,\rm rot}$, where the heat capacities $C_{A,\rm rot}$, $C_{T,\rm rot}$, and $C_{E,\rm rot}$ are determined solely by transitions within each species.

The influence of conversion on the results of the measurements is evidenced by the following circumstances (see Fig. 1). In the solid solution $(CD_4)_{0.05}Kr_{0.95}$ the experimental values of $C_{\rm rot}/nR$ are several times higher than the calculated values $C_{\rm rot,high}$ for the high-temperature distribution of the nuclear spin species. The fact that a 0.2% O_2 admixture has an insignificant effect on the experimental values of $C_{\rm rot}/nR$ indicates that the distribution of the nuclear spin species of CD_4 is close to the equilibrium distribution in the samples studied. It should also be noted that the experimental data are close to the calculated temperature dependence for the case of an equilibrium distribution of the species.

Thus in this study we have for the first time detected nuclear spin conversion of the CD_4 molecule.

It is important to note that the rate of conversion of the CD_4 rotor in the solution $(CD_4)_{0.05}Kr_{0.95}$ (the ratio $(C_{\rm rot}/nR)/C_{\rm rot,equilib}=85\%$) is notably larger than the rate of conversion of the more quantum rotor CH_4 in the solution $(CH_4)_{0.05}Kr_{0.95}$ at $T<1.6$ K (in the latter case the ratio $(C_{\rm rot}/nR)/C_{\rm rot,equilib}$ is equal to 12%; Ref. 2).

It is natural to assume that in the CD_4-Kr solutions, as in the CH_4-Kr solution, the dominant mechanism of conversion at low temperatures is a hybrid mechanism,[8] according to which the conversion rate is determined by the simultaneous intramolecular magnetic interaction between the nuclear spins of the H (D) atoms and the intermolecular octupole–octupole (OO) interaction between nearest-neighbor CH_4 (CD_4) molecules in the lattice. The intramolecular interaction mixes the nuclear spin states, while the intermolecular OO interaction brings about transitions between rotational states with a transfer of the energy of conversion to the lattice.

In CH_4-Kr solutions the magnetic moment of the proton is greater than the magnetic moment of the deuteron, and the contribution of the intramolecular magnetic interaction is larger. On the other hand, the intermolecular OO interaction should give a larger contribution to conversion in the CD_4-Kr solution for the following reasons. The noncentral interaction between CH_4 molecules in the solid phase is smaller than that between CD_4 molecules, since in the lowest state of the A species the octupole moment of the quantum rotor CH_4 is smaller than that of the rotor CD_4, and the amplitude of the zero-point orientation vibrations (librations) of CD_4 is substantially smaller than for CH_4. The noncentral interaction between rotors decreases with increasing libration amplitude. According to Ref. 8, for weakly braked rotors the conversion rate increases with increasing octupole–octupole interaction.

Our results indicate that the ''bottleneck'' governing the conversion rate in CH_4-Kr and CD_4-Kr solid solutions is the intermolecular interaction and the related probability of transfer of the conversion energy to phonons.

We plan to continue our calorimetric studies of CD_4-Kr solid solutions by expanding the region of CD_4 concentrations in the solutions and the temperature interval of the measurements.

The authors thank M. A. Strzhemechny for a discussion of the results.

*E-mail: bagatskii@ilt.kharkov.ua

[1] I. Ya. Minchina, V. G. Manzhelii, M. I. Bagatskii, O. V. Sklyar, D. A. Mashchenko, and M. A. Pokhodenko, Fiz. Nizk. Temp. **27**, 773 (2001) [Low Temp. Phys. **27**, 568 (2001)].
[2] M. I. Bagatskii, V. G. Manzhelii, I. Ya. Minchina, D. A. Mashchenko, and I. A. Gospodarev, J. Low Temp. Phys. **127**, No. 3 (2003).
[3] W. Press, *Single-Particle Rotations in Molecular Crystals*, Vol. 92 of Springer Tracts in Modern Physics, Springer-Verlag, Berlin–Heidelberg–New York (1981).
[4] V. G. Manzhelii, A. I. Prokhvatilov, V. G. Gavrilko, and A. P. Isakina, *Structure and Thermodynamic Properties of Cryocrystals, Handbook*, Begell House, New York–Wallingford, UK (1998).
[5] V. G. Manzhelii, A. I. Prokhvatilov, I. Ya. Minchina, and L. D. Yantsevich, *Handbook of Binary Solutions of Cryocrystals*, Begell House, New York–Wallingford, UK (1996).
[6] M. I. Bagatskiĭ, I. Ya. Minchina, and V. G. Manzheliĭ, Fiz. Nizk. Temp. **10**, 1039 (1984) [Sov. J. Low Temp. Phys. **10**, 542 (1984)].
[7] K. Nishiyama, J. Chem. Phys. **56**, 5096 (1972).
[8] A. J. Nijman and A. J. Berlinsky, Can. J. Phys. **58**, 1049 (1980).

Translated by Steve Torstveit

ERRATA

Erratum: Magnetic properties of a $LaMn_{0.46}Co_{0.54}O_3$ single crystal

S. N. Barilo, V. I. Gatal'skaya, S. V. Shiryaev, and L. A. Kurochkin

Institute of Solid State Physics and Semiconductors, Belorussian National Academy of Sciences, ul. l. Brovki, 17, Minsk, 220072, Belorus

R. Shimchak and M. Baran

Institute of Physics, Polish Academy of Sciences, Al. Lotnikow 32/46, 02-668 Warsaw, Poland
Fiz. Nizk. Temp. **28**, 853–855 (2002)

The following corrections were reported by the authors.

On page 853, the authors names should read: ''S. N. Barilo, V. I. Gatalskaya, S. V. Shiryaev, L. A. Kurochkin, R. Szymczak, and M. Baran.''

On page 853, the affiliation for the first four authors should read: ''Institute of Solid State Physics and Semiconductors, Belorussian National Academy of Sciences, ul. P. Brovki, 17, Minsk, 220072, Belorus.''

On page 853, in the first paragraph, line 8 from top, the sentence should read: ''The colossal magnetoresistance (CMR) observed in substituted manganites is ordinarily explained by the double-exchange model in combination with Jahn–Teller (JT) distortions of the crystal structure.''

On page 853, in the left column, line 5 from the bottom, the sentence should read: ''LMCO single crystals with Co content close to 0.5 were obtained by electrochemical deposition in a platinum crucible from a fluxed melt of the binary system $Cs_2MoO_4-MoO_3$.''

On page 853, in the right column, line 3 from bottom, the sentence should read: ''The susceptibility $\chi_{FC}=M/H$ increases as temperature decreases and is close to saturation at low temperatures.''

On page 854, in the left column, line 11 from bottom, the sentence should read: ''The value $\mu_s=1.75\mu_B$ which we obtained for a LMCO crystal is identical to the theoretical value of the magnetic moment for $x=0.54$,[10] associated with the $Mn^{4+}-Co^{2+}$ interaction[7] giving rise to FM in a LMCO crystal.''

On page 854, in Figure 2 the caption should read: ''Temperature dependence of χ of a LMCO single crystal in a 50 kOe field: χ_{FC} (○), χ_{ZFC} (△); solid line—fit of a Langevin function.''

One-dimensional and zero-dimensional electron systems on liquid helium (Review)

Yu. Z. Kovdrya*

B. Verkin Institute for Low Temperature Physics and Engineering, National Academy of Sciences of Ukraine, pr. Lenina 47, 61103 Kharkov, Ukraine

(Submitted July 12, 2002)
Fiz. Nizk. Temp. **29**, 107–144 (February 2003)

A review of the experimental and theoretical research on one-dimensional and zero-dimensional electron systems localized near a liquid helium surface is given. The properties of the electronic states on a flat liquid helium surface, including the surface of thin helium layers, are briefly considered. Ways of realizing one-dimensional and zero-dimensional electron systems and the results of experimental and theoretical studies of their properties are discussed. Experiments on the investigation of localization processes in quasi-one-dimensional electron systems are described. Collective effects in systems of this kind are considered, and the possibilities for the use of low-dimensional electron systems on the surface of liquid helium for creating electronic devices and quantum computers are explored. © *2003 American Institute of Physics.* [DOI: 10.1063/1.1542406]

INTRODUCTION

Systematic research on two-dimensional electron systems on liquid helium began almost immediately after the publication of the first theoretical papers of Cole and Cohen[1] and Shikin[2] predicting surface electron states on liquid helium. Two-dimensional electron systems on the surfaces of quantum liquids have proved to be practically ideal for experimental and theoretical research on low-dimensional systems by virtue of their exceptional uniformity and cleanliness. An important feature of this system is that it obeys classical Boltzmann statistics and consists of particles with a strong, unscreened Coulomb interaction. This last circumstance makes for such interesting behavior features of the system as Wigner crystallization, for example. Furthermore, the substrate (the liquid helium surface) on which the two-dimensional electron layer is formed is ''soft'' and can be deformed by the electrons.

The study of two-dimensional electron systems on liquid helium has been the subject of a number of reviews and monographs.[3,4]

In the present review we discuss the properties of one-dimensional and zero-dimensional electron systems near a liquid helium surface, i.e., systems in which, besides localization of particles perpendicular to the surface of the liquid there is also an additional localization along the liquid–vapor interfacial surface.

A two-dimensional electron system on liquid helium is among the simplest of physical systems. Many of its properties can be calculated to high accuracy, permitting reliable comparison of the results of calculations and experiments. In recent years interest in the study of systems of lower dimensionality—one-dimensional and zero-dimensional charge systems—has risen sharply. Such studies are important not only from the standpoint of understanding the fundamental physical regularities but also in connection with various technical applications. One-dimensional and quasi-one-dimensional electron systems are usually realized in thin metal wires and semiconductor structures, while zero-dimensional systems are created by means of complex technological processes based on semiconductor materials. The preparation of both metal wires and high-quality semiconductor structures presents a rather complicated technical problem. Dissipative processes in such systems are determined by many poorly controlled factors, such as the presence of impurities, the method of preparation, etc. For this reason it is of interest to obtain and study one-dimensional and zero-dimensional electron systems on liquid helium, which will have all the advantages of surface electrons in comparison with other low-dimensional systems. In particular, in systems with dimensionality lowered through the use of surface electrons, by virtue of the weak interaction of the electrons with the liquid helium surface, one can expect low dissipative carrier losses, high mobilities, and rather narrow electron interlevel transition lines. One further advantage of this type of low-dimensional systems is the possibility of easy control of their properties: the characteristics of the potential wells in which the particles are localized, carrier concentration, degree of dissipation, etc. Research on one-dimensional and zero-dimensional electron systems on liquid helium has recently come under intensive development, and interesting new results have been obtained.

In this review we shall briefly list the main properties of a two-dimensional electron system on liquid helium which are necessary for understanding the behavior of electron systems with lower dimensionality, and we shall discuss the main studies, both experimental and theoretical, pertaining to quasi-one-dimensional, one-dimensional, and zero-dimensional electron systems on liquid helium.

1. SURFACE ELECTRONS ON A FLAT HELIUM–VAPOR INTERFACE

1.1. Spectrum of electrons on liquid helium

The formation of surface electronic states on liquid helium is due to the presence of electrostatic attractive forces of a polarization nature which are exerted on an electron by the

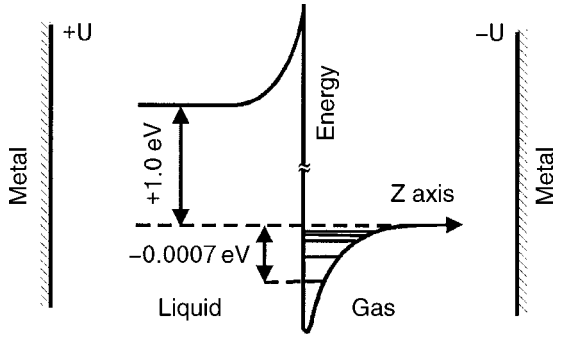

FIG. 1. Schematic arrangement of electron levels near the surface of liquid helium.

liquid helium and the existence of a potential barrier preventing the penetration of the electron into the liquid. Thus an electron is trapped in a one-dimensional potential well, and its motion is free along the surface of the liquid and is quantized in the direction perpendicular to the surface (see Fig. 1). The energy spectrum of electrons localized on the liquid helium surface has been calculated by Cole and Cohen[1] and independently by Shikin.[2]

The potential energy of an electron near the liquid helium surface can be written approximately in the form

$$V(z)=\begin{cases} -\dfrac{\Lambda}{z}, & z\geqslant 0, \\ V_0, & z<0. \end{cases} \tag{1}$$

Here

$$\Lambda=\frac{e^2(\varepsilon-1)}{4(\varepsilon+1)}$$

(where e is the electron charge and ε is the dielectric constant of liquid helium) and z is the coordinate perpendicular to the surface of the liquid. The value of Λ for liquid helium is small by virtue of the fact that its dielectric constant is close to unity ($\varepsilon=1.057$).

The value of the potential barrier V_0 preventing penetration of the electron into the liquid was measured by Woolf and Rayfield[5] and turns out to be rather large (~ 1 eV), and one can let $V_0\to\infty$ in the calculations.

The energy spectrum of the surface electrons can be calculated by solving the Schrödinger equation and assuming the potential energy is given by (1) with $V_0=\infty$. The electron spectrum then has the form

$$\varepsilon_l(k)=\Delta_l^{(0)}+\hbar^2k^2/2m, \quad \Delta_l^{(0)}=-\Delta/l^2, \qquad \Delta=m\Lambda^2/2\hbar^2. \tag{2}$$

Here m is the electron mass, $\hbar$ is Planck's constant, k is the two-dimensional wave vector of the electron along the surface of the liquid, and $l=1,2,3...$ is the number of the state. The first term describes the quantized motion of the electron perpendicular to the surface of the liquid, and the second term is due to the free motion of the electron along the surface. We see that the spectrum describing the motion of the electron perpendicular to the liquid surface is hydrogenlike. Then the wave functions of the ground and first excited states have the form

$$\psi_l(\mathbf{r},z)=f_l(z)e^{i\mathbf{k}\cdot\mathbf{r}}; \quad f_1(z)=2\gamma^{3/2}z\exp(-\gamma z), \qquad f_2(z)=\frac{1}{\sqrt{2}}\gamma^{3/2}z\left(1-\frac{\gamma z}{2}\right)\exp\left(-\frac{\gamma z}{2}\right), \quad \gamma=\frac{m\Lambda}{\hbar^2}. \tag{3}$$

The electron binding energy in the ground state is $\Delta\approx 8$ K, and the average distance of the electron from the liquid surface in the energy ground state, $\langle z\rangle_1$, is much larger than the interatomic distance in liquid helium. For liquid ^{4}He one has $\langle z\rangle_1=114$ Å, $\langle z\rangle_2=456$ Å. For liquid ^{3}He the corresponding distances are somewhat larger, since its dielectric constant is smaller than that of ^{4}He.

For a more exact treatment of the problem it is necessary to take into account the finiteness of the potential barrier V_0 and the distortion of the potential at small distances from the surface. This leads to certain corrections in the energy spectrum.[6]

Importantly, the existence of surface electronic states requires the presence of a potential barrier preventing penetration of the electron into the medium. The other substances besides helium in which such a potential barrier exists are liquid and solid hydrogen and neon, for which surface electronic states have been observed by Troyanovskiĭ, Volodin, and Khaĭkin.[7,8] However, since the dielectric constant of those substances is larger than that of liquid helium, the electron binding energy with the medium is substantially greater than in the case of liquid helium, and $\langle z\rangle_l$ is much smaller. For example, for solid hydrogen $\Delta=150$ K and $\langle z\rangle_1=25$ Å.

Experiments with surface electrons on liquid helium are usually done in pressing (or ''holding'') electric fields. In the presence of an electric field $E_\perp$ perpendicular to the surface of the liquid, the potential energy $V(z)$ can be written as

$$V(z)=\begin{cases} -\dfrac{\Lambda}{z}+eE_\perp z & \text{for } z>0, \\ \infty & \text{for } z<0. \end{cases} \tag{4}$$

Calculations show that the pressing field causes deformation in the discrete part of the spectrum. Calculations of this kind are simpler to do for a strong pressing field. In that limit the electron energy spectrum and wave functions have the form

$$\Delta_l=\xi_l\frac{eE_\perp}{\gamma^*}; \quad f_l(z)=\frac{\sqrt{\gamma^*}}{|\mathrm{Ai}'(-\xi_l)|}\mathrm{Ai}(\gamma^*z-\xi_l), \qquad \gamma^*=\left(\frac{2meE_\perp}{\hbar^2}\right)^{1/3}. \tag{5}$$

Here $\mathrm{Ai}(x)$ and $\mathrm{Ai}'(x)$ are the Airy function and its derivative, and ξ_l are the absolute values of its zeros ($\xi_1=2.238$, $\xi_2=4.088$). Equation (5) is valid under the condition $\Lambda\gamma^*\ll\Delta_l$. The influence of the pressing electric field on the spectrum of surface electrons was considered by Grimes, Brown, Burns, and Zipfel.[6]

The first experiments with surface electrons on liquid helium involved the investigation of features of their motion along the surface of the liquid. Shikin, Kovdrya, and Rybalko[9] used a time-of-flight method to measure the mobility μ of electrons on liquid helium in a weak pressing electric field. It was found that at relatively high temperatures the value of μ is practically the same as the mobility of electrons

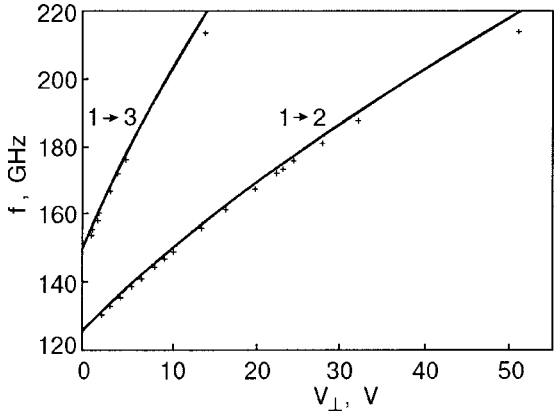

FIG. 2. The transitions $1\rightarrow 2$ and $1\rightarrow 3$ for electrons on liquid ^{4}He versus the pressing potential.[6] The points are experimental and the curves are theoretical.

in gaseous helium in the three-dimensional case. Measurements of the mobility of surface electrons at temperatures in the region 1.2–4 K were made by Sommer and Tanner[10] by a capacitive method, which permitted the use of rather high pressing electric fields. They observed a noticeable difference in the mobility from the three-dimensional case. The first measurements of the energy spectrum of surface electrons on liquid ^{4}He were made by Grimes and Brown,[11] and those measurements were continued in Ref. 6. The results, in the form of curves of the frequency f of electron transitions from one energy level to another are presented in Fig. 2. The solid curves show the theoretical dependence. Good agreement is seen between the experimental data and theoretical calculation. The energy spectrum of surface electrons in high pressing fields was measured by Lambert and Richards.[12] They found that the transition frequencies increased several-fold when the pressing field was increased to 2000 V/cm. The energy spectrum of surface electrons on liquid ^{3}He was measured by Volodin and Édel'man.[13]

The mobility of surface electrons at relatively high temperatures is governed by their scattering on helium atoms in the vapor, while for $T<0.8$ K it is determined by the interaction of electrons with thermal excitations of the liquid helium surface (ripplons). The mobility of surface electrons was considered theoretically by Saitoh in the gas scattering region and by Shikin and Monarkha in the ripplon scattering region (see Refs. 3 and 4). Experimentally the influence of the electron–ripplon interaction was first observed by Rybalko, Kovdrya, and Esel'son[14] and by Grimes and Adams.[15] The study of electron transport in a 2D system on liquid helium in a magnetic field was begun with the work of van der Sanden, van der Heijden, de Waele, and Gijsman[16] and of Stone, Fozooni, Lea, and Abdul-Gader[17] and has since been the subject of a large number of papers (see, e.g., Refs. 18 and 19).

The study of a two-dimensional system of electrons on liquid helium gives information about the properties of the surface of the quantum liquid, on the one hand, and about the behavior of the two-dimensional electron system itself—in particular, about the collective effects that are observed in a two-dimensional electron layer—on the other. Plasma oscillations in a 2D surface-electron layer have been detected and investigated by Grimes and Adams.[15] Mast, Dahm, and Fetter[20] and Glattli, Andrei, Deville, Poitrenaud, and Williams[21] observed edge magnetoplasmons in a 2D electron system, and it turned out that there are several branches of magnetoplasma oscillations that propagate along the boundary of the electron layer.[22,23]

Perhaps the most interesting phenomenon arising in a 2D system of surface electrons is the transition to a crystalline state. The possibility of existence of an electron crystal was considered back in 1934 by Wigner.[24] A system of surface electrons on liquid helium has turned out to be the most suitable object for studying this phenomenon. Crystallization in an electric field was first observed by Grimes and Adams[25] from the appearance of coupled phonon–ripplon resonances, and then later by Rybalko, Esel'son, and Kovdrya[26] and by Dahm and co-workers[27] from the onset of features in the behavior of the electron mobility in different pressing electric fields. The kinetic and dynamic properties of electrons on liquid ^{3}He, including in the region of the crystalline state, have been studied by Kono and co-workers.[28]

1.2. Electrons on thin layers of liquid helium

An electron found near the surface of a liquid helium film covering a solid substrate is acted upon by an attractive force from both the helium and the substrate. The dielectric constant of the majority of solid substances is much larger than that of liquid helium. The attractive polarization force is accordingly stronger, and that leads to a substantial change in the energy spectrum of the surface electrons.

The first theoretical calculation of the spectrum of electron surface states on a helium film was done by Shikin and Monarkha.[29] According to Ref. 29, the potential of the image forces can be written to a good approximation as

$$V(z)=-\frac{\Lambda}{z}-\frac{\Lambda_1}{d}+F_d z,\quad z>0, \tag{6}$$

$$\Lambda_1=\frac{e^2\varepsilon(\varepsilon_d-\varepsilon)}{(1+\varepsilon)^2(\varepsilon_d+\varepsilon)},\quad F_d=\frac{\Lambda_1}{d^2},$$

where ε_d is the dielectric constant of the substrate. From this we see that the presence of the substrate reduces to the appearance of an additional pressing electric field. For films $\sim$300 Å thick the effective pressing field is rather large, and the spectrum of the surface electrons has the form

$$\Delta_l=-\frac{\Lambda_1}{d}+\xi_l\left(\frac{\hbar^2}{2m}\right)^{1/3}F_d^{2/3}, \tag{7}$$

where ξ_l are the zeros of the Airy function of Eq. (5).

It follows from Eq. (7) that the spectrum of surface electrons on a helium film is analogous to the spectrum of surface electrons on bulk helium in the presence of a pressing field. We note that the typical values of the binding energy differ quite substantially from those for electrons on bulk helium. For example, the binding energy of electrons on a film $\sim$300 Å thick is $\sim$100 K for $\varepsilon_d=5$, a typical value of the dielectric constant of a solid substrate.

The energy spectrum of surface electrons for very thin layers of liquid helium on a metallic substrate were calculated by Gabovich, Il'chenko, and Pashiitskiĭ.[30] In that case the electron spectrum differs from (7) and has the form

$$\Delta_l=\frac{e^2}{32a_0}\left[1-\frac{3}{4}+\frac{1}{\pi}\left(\frac{2d}{a_0}\right)^{1/2}\right]^{-2},\quad l>1, \tag{8}$$

where $a_0=\hbar^2/me^2$. According to this calculation, for $d=65$ Å the distance between levels 1 and 2 is $E_{12}\approx 1200$ K; the corresponding transition frequency lies in the submillimeter range of microwave oscillations.

Surface electrons on a film of liquid helium were first registered by observing the drainage of charge to the liquid helium surface from the film-coated dielectric walls of an experimental cell.[31] Electronic bound states were also detected on a metal substrate by Volodin, Khaĭkin, and Édel'man using a similar technique.[32]

Importantly, the binding energy of the surface electrons on a helium film is high and depends on the film thickness. In reality the surfaces of solid substances are rough, with a characteristic roughness size of 10^{-5}–10^{-6} cm. Therefore, the electrons on a helium film are found in a random potential consisting of a set of potential wells and humps. In this case the electrons can be localized in the potential wells. Therefore, the mobility of electrons on a helium film is ordinarily very low. The kinetic properties of electrons on a helium film can be influenced by another effect, which was predicted by Monarkha.[33] A large pressing field exerted on the electron by the substrate can lead to the formation of a dimple, which is a sort of polaron, the motion of which is due to the flow of the normal component in the helium film. According to theoretical estimates, the mobility of such a polaron should be low. These effects will be considered in Sec. 4. The mobility of electrons on a helium film in a microwave field was first investigated by Karamushko, Kovdrya, Mende, and Nikolaenko,[34] and the mobility in the low-frequency limit, by Andrei.[35] Jiang and Dahm[36] found that the mobility of electrons on a helium film covering a very smooth glass surface is much higher than that obtained in Refs. 34 and 35.

2. ONE-DIMENSIONAL AND QUASI-ONE-DIMENSIONAL ELECTRON SYSTEMS ON LIQUID HELIUM

2.1. Characteristics of a one-dimensional electron system. Electron spectrum. Influence of magnetic field

There are several ways of obtaining a one-dimensional electron system using surface electrons on liquid helium. Ginzburg and Monarkha[37] proposed to use a dielectric substrate with a system of sharp linear prominances lying parallel to one another. The substrate lies beneath the surface of the liquid helium. When the liquid is charged, the large image forces exerted by the dielectric cause the electrons above the substrate to accumulate over the prominances on it, forming a linear structure. However, in order to obtain sufficiently deep and narrow potential wells, the height of the liquid over the prominances must be very small ($\sim 10^{-5}$ cm), and because of the unavoidable roughness and nonuniformity of the substrate, that should lead to appreciable uncontrolled variation of the potential relief. Chaplik[38] proposed to create a one-dimensional electron system on liquid helium with the electrons localized over thin metal wires lying under the surface of the liquid. However, in that case it is also hard to achieve good uniformity.

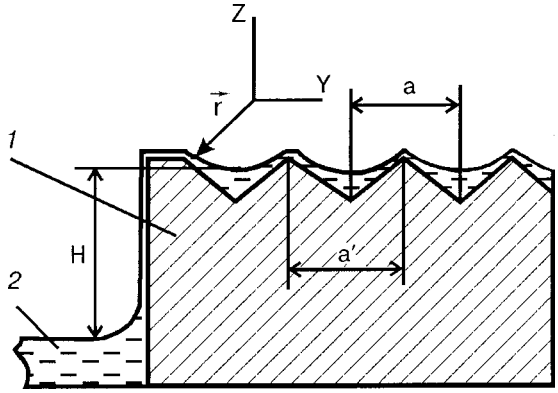

FIG. 3. One-dimensional electron system on liquid helium:[39] *1*—dielectric substrate with a linear profile; *2*—liquid helium (the thickness of the helium film is exaggerated in the drawing).

Kovdrya and Monarkha[39] proposed a method of creating a one-dimensional electron system which might offer the same advantages (cleanliness, uniformity, the possibility of wide variation of the parameters) as for the two-dimensional system on bulk helium. To achieve this goal it was proposed to use a curved liquid surface arising when the superfluid helium leaks under capillary forces into grooves in the dielectric substrate lying at a height H above the liquid level (Fig. 3). The curvature of the surface of the liquid in the ''troughs'' formed in this case is

$$r=\frac{\alpha}{\rho g H}, \tag{9}$$

where α and ρ are the surface tension and density of liquid helium and g is the acceleration of gravity.

When these ''troughs'' on the surface of liquid helium are charged, the polarization forces of the substrate tend to confine the electrons, localizing them above the prominances of the substrate, and the external pressing electric field $E_\perp$ will move them to the bottom of the ''troughs,'' the potential energy of an electron upon its displacement by a distance y from the center perpendicular to the axis of the ''trough'' increases by an amount

$$V(y)=\frac{eE_\perp}{2r}y^2 \tag{10}$$

(the liquid channel is directed along the x axis). The motion of the potential along the y axis in such a potential well will be oscillatory, with a frequency

$$\omega_0=\left(\frac{eE_\perp}{mr}\right)^{1/2} \tag{11}$$

and, consequently, under the condition $\hbar\omega_0>k_BT$ (k_B is Boltzmann's constant) will be quantized. The electron motion along the x axis will remain quasi-free.

For surface electrons on liquid helium the effective ''Bohr'' radius is

$$r_B=\frac{1}{\gamma}=\frac{4\hbar^2(\varepsilon+1)}{me^2(\varepsilon-1)}=80\ \text{Å}.$$

Since in real experiments $r=10^{-3}-10^{-4}$ cm, one always has $r_B \ll r$. Therefore the wave functions of electrons localized in the linear potential wells under consideration can be written in the form

$$\psi_{l,n,k_x}=e^{ik_x x}Y_n(y)f_l(z), \quad n=0,1,2,...$$
$$Y_1(y)=\pi^{-1/4}y_0^{-1/2}e^{-y^2/2y_0^2}, \quad y_0=\left(\frac{\hbar}{m\omega_0}\right)^{1/2}. \tag{12}$$

Here k_x is the one-dimensional wave vector of the electron along the axis of the channel. The functions $f_1(z)$ and $f_2(z)$ are given, as before, by expression (3), where now γ depends on $E_\perp$ and is determined by a variational method. The energy spectrum of the electrons can be written as

$$\varepsilon_{l,n}(k_x)=-\frac{\Delta}{l^2}+\left(n+\frac{1}{2}\right)\hbar\omega_0+\frac{\hbar^2k_x^2}{2m}. \tag{13}$$

For $H=5$ cm, $r=5\times10^{-4}$ cm, and $E_\perp=2000$ V/cm we obtain $\omega_0=8\times10^{10}$ s^{-1} and a localization length of the particle in the direction transverse to the channel $y_0=4\times10^{-6}$ cm. The distance between energy levels will be $\Delta E=\hbar\omega_0=0.5$ K. Thus the system under discussion can be considered one-dimensional to good accuracy at sufficiently low temperatures.

An advantage of this one-dimensional system is that it can be quite uniform. The electrons in the liquid channels lie at a large distance from the solid substrate, and their behavior is therefore unaffected by roughness and irregularities of the substrate. Indeed, substrate roughness with period A and amplitude ξ will give rise at distances $z>A$ to a polarization potential

$$\delta V\approx-\frac{e^2(\varepsilon_d-1)}{4(\varepsilon_d+1)z}\frac{\pi\xi}{A}\left(\frac{A}{z}\right)^{1/2}\exp\left(-\frac{2\pi z}{A}\right), \tag{14}$$

which is exponentially decaying. Estimates by this formula for $z\sim A$ give $\delta V\leqslant10^{-3}$ K. A more substantial influence on the uniformity of the system can be exerted by electrons localized on the thin film over prominances of the grooved substrate. Under certain conditions they can have the predominant influence on the carrier transport. However, as will be shown below, the use of substrates with a smooth surface and low dielectric constant makes it possible for all the electrons to be removed from the prominances to the bottom of the liquid channels grooves and thus to obtain a rather clean, uniform system.

By studying the influence of magnetic field on the characteristics of a one-dimensional electron system, Sokolov and Studart[40] calculated the wave functions and spectrum of the electrons for a magnetic field directed along the z and y axes. It was found that a magnetic field substantially alters not only the parameters but also the form of the energy spectrum. In the case when the magnetic field is directed along the z axis, the electron energy spectrum has the form

$$\varepsilon_{l,n}(k_x)=-\frac{\Delta}{l^2}+\left(n+\frac{1}{2}\right)\hbar\Omega+\frac{\hbar^2\omega_0^2k_x^2}{2m\Omega^2}, \tag{15}$$
$$\Omega=\sqrt{\omega_0^2+\omega_c^2},$$

where ω_c is the cyclotron frequency. Spectrum (15) reflects the facts that, first, the distance between energy levels changes, and, second, the mass of the electron is replaced by an effective mass $m^*=m(1+\omega_c^2/\omega_0^2)$.

2.2. Realization of a quasi-one-dimensional electron system on liquid helium

A two-dimensional electron system on liquid helium in a channel 35 μm wide (quasi-two-dimensional system) was obtained by Marty.[41] A meander line was used for making the measurements. The width of the electron layer in which the electron density was approximately uniform was $\sim20\mu$m. As a result of studies of the stability of the charged surface in the channel it was shown that the maximum attainable electron density was greater than the corresponding value for bulk helium and equalled 4×10^9 cm^{-2}.

A quasi-one-dimensional electron system on liquid helium was first obtained by Kovdrya and Nikolaenko[42] using an optical diffraction grating as a substrate. The grating material was glass with a dielectric film of naphthogene deposited on its surface. The distance between rulings of the grating was 1.25 μm, and the depth of the grooves was 0.3 μm. Experiments were done at a temperature of 1.5 K and a frequency of 1.1 MHz. In measurements of the electron mobility a strong anisotropy of the conductivity of surface electrons moving along and transverse to the channels was found. The value of ΔE was ~0.1 K. Since $\Delta E<k_BT$, the electrons occupied not only the ground level but also higher-lying levels. This system therefore cannot be considered strictly one-dimensional. However, since the width of the liquid strips charged with electrons was 10^{-4} cm, which corresponds approximately to the average distance between electrons, one can speak of a one-dimensional chain of charges.

A quasi-one-dimensional electron system on liquid helium was also obtained by Yayama and Tomokiyo with the use of an optical diffraction grating.[43]

Kirichek, Monarkha, Kovdrya, and Grigor'ev[44] proposed a simple method of creating a single conducting channel of highly mobile electrons through curvature of the liquid helium surface; the channel was formed at the acute-angle junction of two planes of a weakly polarized polymer film mounted on metal electrodes. The polymer film used was Mylar, which has a dielectric constant of ~1.5 at helium temperatures. In zero pressing electric field the electrons are found mainly on the helium film, where their conductivity is low and they do not contribute to the signal. When a pressing potential is applied, the electrons accumulate on the highly curved surface of the liquid helium. Then a noticeable signal appears, and one can determine the conductivity of the channel with the electrons. The electron density and the effective width of the conducting channel were calculated. A method of creating quasi-one-dimensional and quasi-two-dimensional electron systems in single channels with the use of lithography was proposed by Valkering, Sommerfeld, Richardson, van der Heijden, and de Waele[45] and also by Lea and co-workers.[46]

In experiments with quasi-one-dimensional systems created using dielectric substrates it is important to know the electron density n in the channels. To calculate n one must

solve an electrostatics problems on the assumption that the potential is constant over the whole liquid helium surface, including both the film and the thick layers of helium found in the channels. Such a method of determining the electron density was used by Kovdrya, Nikolaenko, and Sommerfeld.[47] There are also experimental methods of finding n. Hu and Dahm[48] determined the electron density over a thin helium film by measuring the signal excited in an electrode moving perpendicular to the surface of the charged liquid. Here the value of the signal is proportional to the electron density. This method, which was applied to a uniformly charged surface, also can be used to measure the average electron density in a system of quasi-one-dimensional channels. For determining the electron density in a single quasi-one-dimensional channel, Lea and co-workers[46] used a simple and elegant method. They applied a negative potential to an intermediate electrode in the experimental cell, and at a certain value of the applied potential the electrons were removed from part of the drift space of the cell, and the electron signal vanished. From the value of this potential one can calculate the electron density.

The shape of the liquid channel—in particular, its curvature, determined by expression (9)—can vary under the influence of the pressure exerted on the liquid by the layer of electrons. Valkering, Klier, and Leiderer,[49] by using an interference method to measure the profile of the surface of the charged liquid in channels 300 μm wide, showed that in the presence of a layer of electrons of density n on the surface of the liquid in the channel, the radius of curvature is given approximately by the expression

$$r=\alpha\left[\rho g H+\frac{2\pi n^2 e^2}{\varepsilon}\right]^{-1}. \tag{16}$$

A calculation of the change in height of the liquid helium level by formula (16) for the values of the pressing electric fields used in Refs. 42 and 47 showed that the position of the liquid level in the channel changes by no more than 3×10^{-6} cm, which is much less than the depth of the channel.

2.3. Electron transport in quasi-one-dimensional electron systems

Electron transport in quasi-one-dimensional systems created on liquid helium with the use of diffraction gratings has been investigated[47,50–52] in the temperature region 0.05–1.8 K at frequencies of 100 kHz and 1.1 MHz in pressing electric fields of up to 2.5 kV/cm on two types of diffraction gratings. Grating I had a distance between grooves $a=1.25$ μm, and grating II had $a=5$ μm. The groove depth h was 0.2–0.3 μm in both, and the groove width was 1.25 μm in grating I and 1.7 μm in grating II. The glass surface of grating I was coated with naphthogene, onto which grooves were ruled, while grating II was glass. A typical experimental cell used for measurement of the mobility is shown in Fig. 4. The liquid helium lies a distance H from the upper surface of the gratings. Voltage from a generator is supplied to the electrodes so that the driving electric field is directed along the grooves of the gratings.

The changes of the amplitude ΔU and phase $\Delta\varphi$ of the signal passed through the experimental cell upon charging

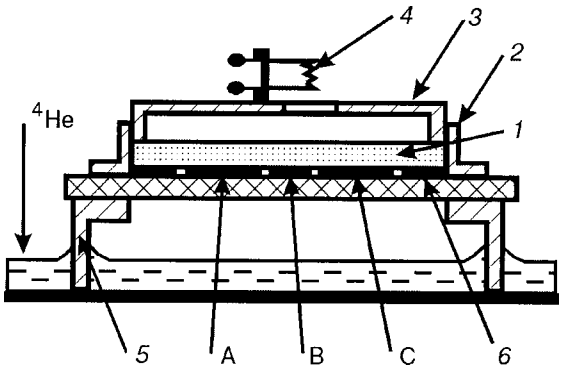

FIG. 4. Measurement cell: *1*—substrate; *2,3*—electrodes; *4*—heating filament; *5*—copper casing; *6*—guard electrode; A,B,C—the driving, intermediate, and receiving electrodes.[51]

with electrons were measured. Data on the values of ΔU and $\Delta\varphi$ can be used to determine the real G_r and imaginary G_i parts of the conductance of the cell and thence to find the real part of the resistivity ρ of the electron layer and, accordingly, the electron mobility μ. The method of calculating ρ was analogous to that used in Ref. 53.

Figure 5 gives the temperature dependence of the electron mobility μ in the conducting channels for gratings I (curves *2–4*) and II (curves *5,6*). The curves pertain to different heights H of the gratings above the liquid helium level. Here for comparison we also show the temperature dependence of μ for bulk helium, taken from Ref. 27 (curve *1*). It is seen that the electron mobility for the quasi-one-dimensional channels is less than that for bulk helium. For both gratings μ decreases with increasing H, although for a given value of H the value of μ is higher for grating I. This is because the dielectric constant of naphthogene, into which the grooves of the grating were cut, is less than that of glass. For grating I at small values of H the electron mobility increases with decreasing temperature, and for $T<0.8$ K it ceases to depend on temperature. At large values of H the

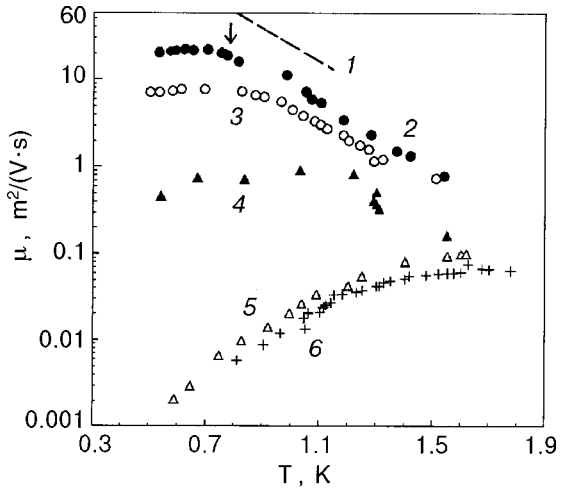

FIG. 5. Electron mobility versus temperature in a quasi-one-dimensional system on liquid helium.[52] Curve *1* is for a 2D electron layer.[27] Grating I: curves *2*, *3* and *4* correspond to values $H=0.6$, 4, and 6 mm, respectively. Grating II: curves *5* and *6* pertain to $H=0.8$ and 1.7 mm. The arrow indicates the temperature of the transition to the crystalline state at the average electron density in the conducting channels.

value of μ initially increases with decreasing temperature and then, after passing through a maximum, begins to decrease.

For grating II the behavior of the mobility is different: the value of μ decreases exponentially with decreasing temperature. Curve *6* is described by the equation

$$\mu = \frac{\tilde{\alpha}_0}{T} \exp\left(-\frac{E}{k_B T} \right) \tag{17}$$

with the coefficients $\tilde{\alpha}_0 = (2.5 \pm 0.1) \times 10^2$ m^{2}K/(V·s) and $E = (6.0 \pm 0.1)$ K. Curve *5* is well approximated by the expression

$$\mu = \frac{\tilde{\alpha}_1}{T} \exp\left(-\frac{E_1}{k_B T} \right) + \frac{\tilde{\alpha}_2}{T} \exp\left(-\frac{E_2}{k_B T} \right), \tag{18}$$

where $\tilde{\alpha}_1 = (4.9 \pm 0.2) \times 10^2$ m^{2}K/(V·s), $E_1 = (5.4 \pm 0.1)$ K, $\tilde{\alpha}_2 = (4.4 \pm 0.3) \times 10^2$ m^{2}K/(V·s), and $E_2 \approx 0.05$ K.

The experimental values of the electron mobility μ in a quasi-one-dimensional system is lower than the value calculated theoretically by Sokolov, Hai, and Studart,[54] and the temperature curves differ from those found there.[54] In Refs. 47 and 50–52 it is conjectured that this difference is due to localization of the electrons in quasi-one-dimensional channels under the influence of the random potential in which they move. This potential arises because the channels, except in the region of ''deep'' liquid at the center, have strips of thin film along the sides. Localization of electrons occurs in places where the film is thin. The mobility of such electrons is extremely low.[34,35] The localized electrons on the film create a random potential in which the electrons found in the deep part of the channels move. If the variation δV of the random potential along the channel is less than $k_B T$, it will have a weak effect on the electron motion, but if $\delta V \gtrsim k_B T$ the effect can become strong. With increasing H there is a decrease in the radius of curvature of the liquid channels and an increase in the area occupied by the thin film. The electrons localized on the film lie closer to the center of the channel, and the variation of the potential increases; this leads to a decrease of the mobility.

It is seen from Fig. 5 (curves *2–4*) that an increase in H and, hence, in δV substantially alters the character of the carrier motion, especially at low temperatures. It has been conjectured that the fact that μ is independent of T for $T < 0.8$ K and also the small drop in μ in that temperature region (curves *2–4*) are due to the quantum character of the transport of the surface electrons in the random potential. At the same time, the character of curves *5* and *6* attests to a thermally activated transport mechanism: the variation of the potential amounts to $\delta V = 5-6$ K.

Experimental data for G_r and G_i can also be used, as in the case of a helium film in Ref. 35, to find the value $K_p = m\omega_p$, which is determined by the Coulomb restoring force in the electron system (ω_p is the frequency of plasma oscillations propagating in the system of conducting channels). Upon localization of the electrons the plasma spectrum acquires a term corresponding to the natural frequency ω_α of the electron oscillations in the potential wells: $\tilde{\omega}_p = \sqrt{\omega_a^2 + \omega_p^2}$, which is analogous to an optical mode of an electron crystal (see Ref. 3). If the signal frequency ω at which the measurements are made is much less than the ripplon frequency $\omega_r(q)$ corresponding to a ripplon wave vector $q \approx 1/L$ (where L is the characteristic localization length of the electron), then m should be replaced by an effective carrier mass M^*, and $K_p \to K_p + K^*$, where K^* is determined by the restoring force due to the presence of the dimple.[35]

Experiments show that the value of $K_p + K^*$ found in Refs. 47 and 50–52 is higher than the value corresponding to free motion of the carriers and is an increasing function of H. This circumstance can serve as additional evidence of carrier localization.

Localization of the electrons in the random potential of the substrate has also been observed over a helium film of thickness $d < 700$ Å.[34,35] At the same time, the channel depth in Refs. 47 and 50–52 is ~ 2400 Å, i.e., this is essentially bulk helium.

In the case of strong localization the carrier motion is thermally activated, and the mobility is determined by the expression

$$\mu = \frac{e \nu_0 \tilde{a}_0^2}{k_B T} e^{-E/k_B T}, \tag{19}$$

where $\tilde{a}_0$ is the average distance between potential wells, which is approximately equal to the distance between electrons localized on the film; ν_0 is the oscillation frequency of the particles in the potential wells. The values of ν_0 found from the experimental data are 10^{10} and 5×10^{10} s^{-1} for curves *5* and *6*, respectively. Thus in the case of strong localization the natural frequencies of the electron oscillations in the potential wells are rather high.

The quasi-one-dimensional channels studied in Refs. 47 and 50–52 are not strictly one-dimensional. Estimates show that the distance between energy levels in them, determined by relation (13), is 0.05–0.1 K, which is much less than the temperature of the experiment. In addition, the electron density in experiments is often such that 2–4 electrons lie across the width of a channel. The quantitative interpretation of the results obtained is further complicated by the fact that electron localization can be accompanied by polaron effects on the liquid helium surface (the properties of the polarons will be considered in Sec. 4.1).

2.4. Kinetic properties of electrons in systems close to one-dimensional

Quasi-one-dimensional electron systems on liquid helium were obtained in Refs. 47, and 50–52. A high mobility could be achieved only for wide channels, across which several electrons were located. For narrow channels, where the influence of the electrons localized on the thin film is great, carrier localization effects arose and the mobility decreased. In a single channel formed by two Mylar films[44] it was necessary to accumulate a rather large amount of charge in order to register the signal from the electrons, and that made for a large number of electrons across such a channel also.

Kovdrya, Nikolaenko, and Gladchenko[55–59] obtained and studied a low-dimensional, close to one-dimensional, electron system in which there was only one electron across the channel. The grooves into which the liquid helium was leaked were made from a dielectric with a small dielectric constant and a smooth surface. This made it possible to col-

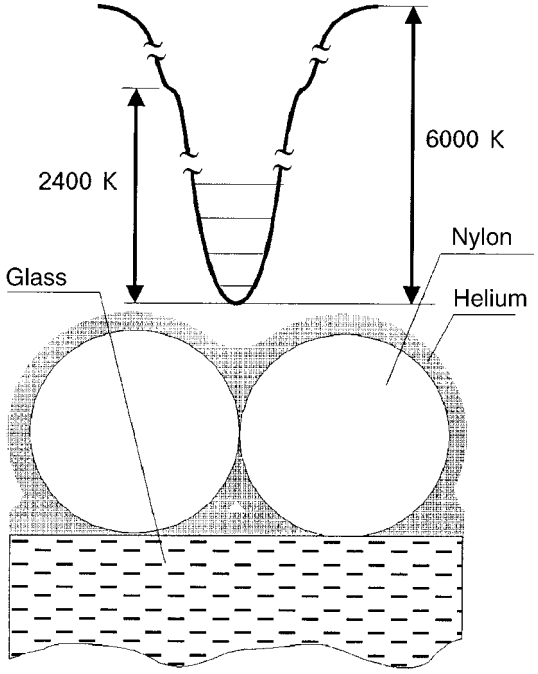

FIG. 6. Schematic illustration of the profile of the potential energy of an electron in a liquid channel at $E_\perp = 450$ V/cm.[59]

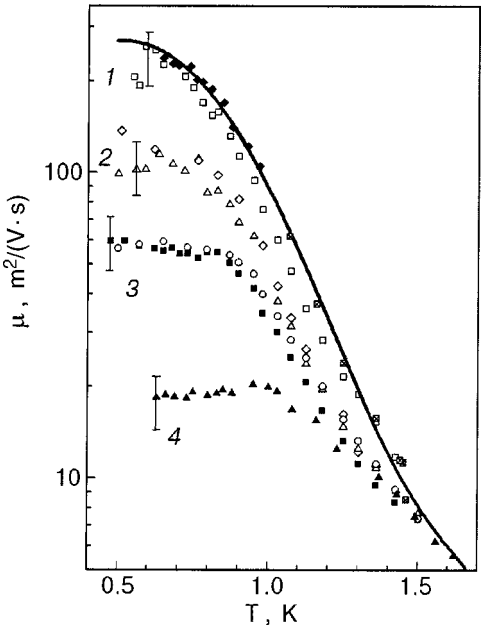

FIG. 7. Temperature dependence of the mobility of electrons in a 1D system on liquid helium for various states of the substrate:[59] *1*—as-prepared substrate, $n_l = 6\times10^4$ (□), 8×10^3 (◆), 5.6×10^4 cm^{-1} (⊠); *2–4*—substrates with charge and defects on the surface, $n_l = 6.6\times10^3$ (◇,○), 4.8×10^3 (△), 1.5×10^4 (■), 10^5 cm^{-1} (▲). The solid curve is a theoretical calculation for $r = 5\times10^{-4}$ cm and $E_\perp = 450$ V/cm.[54]

lect the charge from the helium film covering the substrate by means of the pressing electric field and to obtain a rather pure one-dimensional system.

The experimental cell is analogous to that used in Ref. 51 (see Fig. 4). The dielectric substrate was a glass slab 1 mm thick on which a nylon filament 0.1 mm in diameter was compactly wound. The tops of the nylon filaments were covered by a helium film $\sim 2.5\times10^{-6}$ cm thick, and ''troughs'' of liquid helium formed between the filaments. The radius of curvature of the surface of the liquid in the ''troughs'' was $r = 35$ μm, and there were 150 conducting channels in the cell.

The dielectric constant of nylon at helium temperatures is approximately 1.5.

The form of the potential well in which the electrons are localized and the energy levels at a pressing electric field $E_\perp = 450$ V/cm are shown in Fig. 6. The potential well is quite deep ($\sim$6000 K). On its upper part we see the feature due to image forces exerted on the electron by the solid substrate in those places where the thickness of the film becomes small. There is practically no potential barrier which might confine the electrons over the film. This makes it possible to remove all the electrons from the thin-film layers to the liquid ''troughs,'' where the electrons are found over a thick layer of helium, and thus to ensure a rather good uniformity of the one-dimensional system. Estimates show that the potential barrier vanishes at a pressing electric fields $E_\perp > 200$ V/cm.

Measurements of the 0° and 90° components of the signal passed through the cell when it is charged with electrons were made at a frequency of 100 kHz. The electron density per unit length, n_l, was determined at 1.5 K from the ratio of the resistances of the channels in the unsaturated case (incomplete compensation of $E_\perp$ by the self-field of the electrons) to the resistance of the channel in the saturated case, when the value of n_l is known, and also by tying the data on the conductance of the channels at 1.5 K to the theoretical value of μ obtained on the basis of an exact calculation.[54] The values of n_l determined by the two methods agreed to within 30%. The interval of linear densities in the conducting channels was $5\times10^3 - 2.5\times10^4$ cm^{-1}, which corresponded to a largest distance between electrons $a = 2\times10^{-4}$ cm.

Figure 7 shows the mobility μ as a function of temperature T in a one-dimensional electron system on liquid helium for a clean, as-prepared substrate and for a substrate with defects and charge on the surface. We see that initially μ increases sharply with decreasing temperature for all the substrates; at $T < 0.9$ K the increase of μ with decreasing T for the clean substrate becomes more gradual, while for charged substrates or substrates with defects the mobility either becomes practically independent of T (curves *2,3*) or actually decreases with decreasing temperature (curve *4*). We see that for $T = 0.5$ K the mobility for the clean substrate is more than an order of magnitude higher than that in the case of a large amount of charge (curve 4).

The sharp increase in the electron mobility for the clean substrate at relatively high temperatures is due to the fact that in the temperature region 0.9–1.5 K the carrier mobility in the absence of localization, as in the case of a two-dimensional electron system on liquid helium, is determined by the predominant scattering of electrons by helium atoms in the vapor, the number of which decreases exponentially with decreasing temperature. For $T < 0.8$ K the value of μ is determined by the interaction of the electrons with ripplons, and this dependence is less sharp.

Figure 8 shows the value of the parameter $K_p + K^*$ (see Sec. 2.3) for substrates with different carrier mobilities. It is seen that the substrate with the low value of μ has a larger

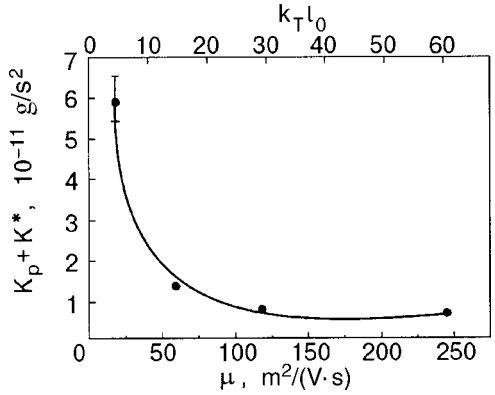

FIG. 8. The parameter K_p+K^* characterizing the restoring force in systems of conducting channels with different values of the mobility.

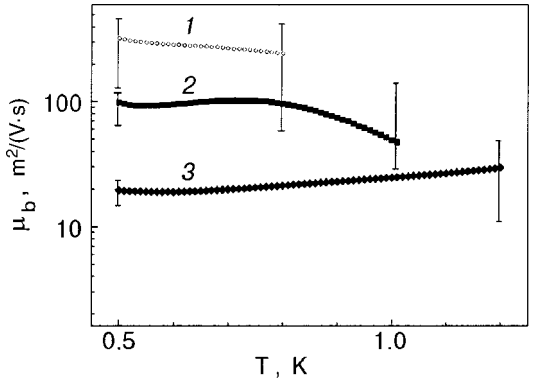

FIG. 9. Temperature dependence of μ_b (curves *1–3*) for the data corresponding to curves *2*, *3*, and *4* in Fig. 7.[59]

value of K_p+K^* than the clean substrate. The experimental value of K_p+K^* is practically independent of temperature.

The typical potential well depth for the one-dimensional electron system under discussion is approximately equal to 6000 K in each of the conducting channels; the characteristic localization length in the direction transverse to the channel for electrons on the ground energy level, $y_0=\sqrt{\hbar/(m\omega_0)}$, had a value of $\sim 10^{-5}$ cm for the pressing field used in Refs. 55–59. For $a\approx 2\times 10^{-4}$ cm the electron–electron interaction energy $V_{ee}=7-8$ K. Unfortunately, the distance between energy levels $\Delta E=0.13$ K, so that the condition $\Delta E > k_B T$ did not hold, and the electrons were found not only on the ground energy level but also at higher-lying levels. This increased the average transverse dimension of the channel, since the characteristic scale for the localization of electrons found on a level n is given approximately by $y_n \approx y_0\sqrt{n+1/2}$ (Ref. 54), where for $n\gg 1$ we use the approximation $n\simeq k_B T/\hbar\omega_0$. For 0.5 K it has a value $y_n=3\times 10^{-5}$ cm, and at $T=1.5$ K it is somewhat larger.

The characteristics of the electron system under study are presented in Table I.

It is seen that for a clean substrate at $T<1$ K the carrier mean free path $l_0>y_n$, while for $T\geqslant 1$ K, on the contrary, $l_0<y_n$. At the same time, for substrates with conducting channels characterized by the lowest mobility (curve *4*), $l_0<y_n$ in the entire temperature region investigated.

The experiments made it possible to isolate the influence of the random potential on the carrier mobility. Here it was assumed that the contributions to the scattering of electrons on helium atoms in the vapor and on ripplons and the processes by which the random potential limits the motion of the carriers are additive. Then the mobility limited by the influence of the random potential is determined by the expression $\mu_b^{-1}=\mu^{-1}-\mu_c^{-1}$, where μ is the electron mobility for a substrate with charge and defects, and μ_c is the electron mobility for the clean substrate.

TABLE I. Characteristics of the electron system.

T, K	Clean substrate (curve *1*, Fig. 7)		Substrate with defects (curve *4*, Fig. 7)		
	μ, m^2/(V·s)	l_0, 10^{-5} cm	μ, m^2/(V·s)	l_0, 10^{-5} cm	y_n, 10^{-5} cm
0.5	250	3.1	19	0.24	1.6
1.0	65	1.1	20	0.35	2.3
1.5	7	0.15	7	0.15	2.8

Figure 9 shows the temperature dependence of μ_b calculated with the use of the smoothed experimental curves *1–4* in Fig. 7. Although the accuracy of determination of μ_b was low, especially at high temperatures, one can nevertheless notice that to within the error limits of the calculation, a slight growth of μ_b with decreasing temperature is observed for curves *1* and *2*, while for curve *3* a decrease of μ_b is observed.

The character of the motion of the carriers in a 1D channel should depend strongly on whether localization occurs or if the influence of the random potential reduces merely to the appearance of an additional scattering mechanism. In Ref. 59 it was assumed that for the experimental curve *2* in Fig. 7 and, accordingly, curve *1* in Fig. 9 one observes only an additional scattering on the random potential, while for experimental curves *3* and *4* in Fig. 7 and, accordingly, *2* and *3* in Fig. 9 a localization of the carriers apparently occurs.

Evidence in favor of this assumption is provided by the behavior of the parameter K_p+K^* for substrates with charge and defects on the surface (Fig. 8). It is seen that at large values of μ the parameter K_p+K^* has the same value for channels with different values of μ. This corresponds to nonlocalized motion of the electrons. However, for channels with $\mu<100$ m^2/(V·s) the value of K_p+K^* is larger for channels with smaller μ; this may be evidence of localization of the carriers. The upper scale in Fig. 8 shows the values of $k_T l_0$ (k_T is the electron wave vector corresponding to the thermal motion). It is seen that the increase of K_p+K^* starts from a value $k_T l_0\approx 20$, so that one can assume that the localization in the 1D channels under study begins to be manifested at $k_T l_0\approx 15-20$. The increase of K_p+K^*, as in the quasi-one-dimensional systems considered in Sec. 2.3, can be thought of as being due to the appearance of an optical mode of plasma oscillations as a result of the localization of the electrons.

The mean free paths of electrons in their scattering by helium atoms in the vapor and by ripplons have been obtained in a theoretical analysis of the mobility of electrons at the ground energy level in a 1D system.[39] Accordingly, the

mobility of surface electrons in a 1D system in the gas scattering region can be written as

$$\mu_{1D}=\frac{\sqrt{2}}{3\sqrt{\pi^3}}\,\frac{e(k_BT)^{1/2}y_0r_Bm^{1/2}}{\hbar^2N_ga_0^2}. \tag{20}$$

Here N_g is the density of the helium atoms in the vapor, and a_0 is the electron scattering length for helium atoms. It is interesting to compare expression (20) with the corresponding expressions for the mobility μ_{2D} and μ_{3D} of electrons in the three-dimensional and two-dimensional cases:

$$\mu_{3D}N_g=\frac{1}{3}\,\frac{e}{\pi a_0^2(2\pi mk_BT)^{1/2}},\quad \mu_{2D}N_g=\frac{2e}{3\pi^2a_0^2\hbar\gamma}. \tag{21}$$

We see that in the three-dimensional case $\mu_{3D}N_g\sim T^{-1/2}$, in the two-dimensional case $\mu_{2D}N_g$ is independent of temperature, and in the one-dimensional case $\mu_{1D}N_g\sim T^{1/2}$. The mobility of electrons in a 1D system in the ripplon scattering region at high pressing electric fields is independent of temperature and is described by the expression

$$\mu_{1D}=\frac{6\alpha\hbar}{meE_\perp^2}, \tag{22}$$

which agrees to within a constant factor with the mobility of electrons on liquid helium in the two-dimensional case.[3]

The mobility of electrons in quasi-one-dimensional conducting channels on the surface of superfluid helium in the case when the electrons occupy several energy levels was considered in Ref. 54. The effects on the mobility from electron scattering on helium atoms in the vapor and on ripplons were investigated in the one-electron approximation, in which the electron–electron interaction is ignored, and in the so-called ''complete control'' regime, when the electron–electron collision frequency ν_{ee} is much higher than the electron–ripplon collision frequency ν_{er} and the collision frequency ν_{eg} of electrons with helium atoms in the vapor. The expressions obtained for the mobility are very complicated and cannot be written in analytical form. The results of the calculation for the complete control regime (which is the most important limit from an experimental standpoint) are presented in Fig. 10, which shows the temperature dependence of the mobility for various pressing electric fields. It follows from the figure that the value of μ in a 1D system decreases substantially with increasing $E_\perp$. For $T<0.1$ K one observes a decrease of μ with decreasing temperature. This behavior of μ is due to transitions of the electrons from level to level, the probability of which increases with increasing temperature.

The nonlinear transport of electrons in 1D channels on liquid helium was studied theoretically in Ref. 60. It was shown that in the electron–ripplon interaction region the electron mobility begins to increase at a certain value of the driving field. It follows from the calculation that this effect takes place both for small electron densities per unit length (the one-electron approximation) and for relatively high densities (the complete control regime). From the theoretical dependence of the electron mobility on the driving electric field $E_\parallel$, which is shown in Fig. 11, we see that μ begins to increase at $E_\parallel\approx 10$ mV/cm. It is appropriate to compare this

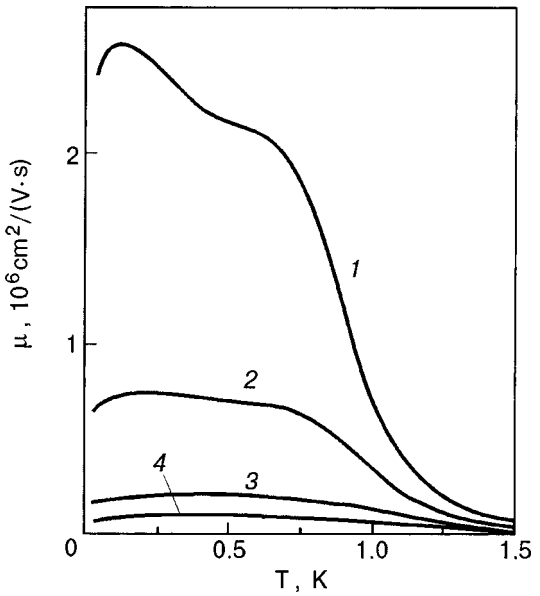

FIG. 10. Calculated mobility of electrons in a quasi-one-dimensional system in the ''complete control'' regime as a function of temperature for different values of the pressing electric field $E_\perp$ [V/cm]: 500 (*1*), 1000 (*2*), 2000 (*3*), 3000 (*4*).[54]

result with the experiment of Ref. 59, where it was shown that the mobility in a 1D system is independent of the generator signal up to values $V_g=200$ mV. However, the value of the driving electric field acting on the electrons at this value of the signal was not determined in Ref. 59; it could have been extremely small on account of screening, and it is therefore impossible to make a quantitative comparison of the results of the experiment and the calculation.

2.5. Electron transport in a magnetic field

Monarkha, Sokolov, Hai, and Studart[61] considered the mobility of electrons in a quasi-one-dimensional electron system in the presence of a magnetic field parallel to the pressing electric field. Calculations done by the method of the dynamic structure factor showed that the effective mobility decreases with increasing magnetic field. It was found that the temperature dependence of the mobility in the pres-

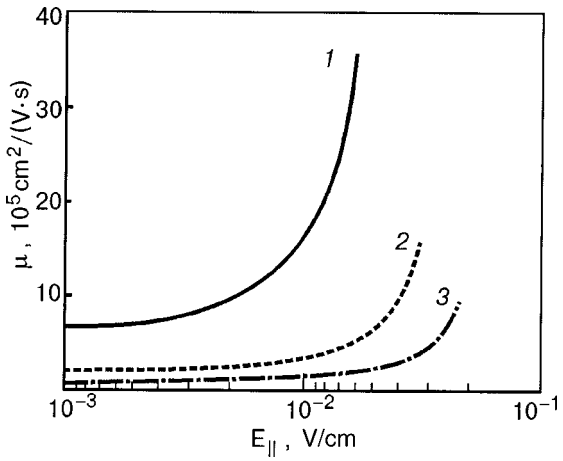

FIG. 11. Mobility of electrons in a quasi-one-dimensional system as a function of the driving electric field at $T=0.6$ K for $E_\perp$ [V/cm]: 1000 (*1*), 2000 (*2*), and 3000 (*3*).[60]

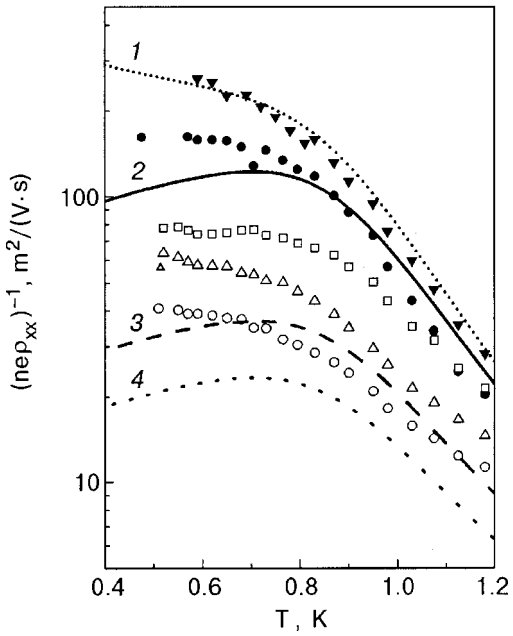

FIG. 12. Temperature dependence of $(ne\rho_{xx})^{-1}$ for electrons in quasi-one-dimensional channels: as-prepared substrate, $B=0$ (▼); substrate after several heating cycles for B [T]: 0 (●), 0.68 (□), 1.36 (△), 2.05 (○). Curve *1* is the calculation of Ref. 54, curves *2–4* are the calculations of Ref. 19 for a 2D system for $B=0.8$, 1.5, and 1.9 T, respectively.

ence of a small magnetic field is of a nonmonotonic character, just as in the absence of magnetic field (see Fig. 10).

The experimental curves of the temperature dependence of $(ne\rho_{xx})^{-1}$ for different magnetic fields B are shown in Fig. 12. The measurements were made using the experimental cell and technique described in Sec. 2.4. The substrate that was used contained defects, so that the electron mobility in zero magnetic field at 0.5 K was lower by approximately a factor of 1.5 than the maximum value of this quantity for a perfect substrate. Nevertheless, the data qualitatively reflect the influence of magnetic field on the character of the electron transport in a quasi-one-dimensional system. It is seen in Fig. 12 that the influence of magnetic field on the effective mobility is progressively greater the lower the temperature. When the magnetic field is increased to 2 T the effective mobility decreases by approximately a factor of 2 at 1.2 K and by approximately a factor of 5 at 0.5 K, falling to a value ~ 40 m^2/(V·s).

Figure 13 shows the magnetic-field dependence of the normalized mobility $\mu(B)/\mu_0$ [$\mu(B)$ is the mobility in a magnetic field, and μ_0 is the mobility at $B=0$] at a temperature of 0.5 K. The value of $\mu(B)$ decreases with increasing B; at low B the experimental data agree with the theoretical calculation[61] up to values $B\approx 0.03$ T.

A consistent calculation of the characteristics of quantum magnetotransport in a two-dimensional electron liquid was done in Ref. 19. The electron conductivity was written in terms of the dynamic structure factor. In that case the quantum electron transport is governed by the components of the conductivity tensor with a magnetic-field-dependent effective collision frequency $\nu_{\text{eff}}(B)$. Calculations using the results of Ref. 19 are shown by the dotted curves in Fig. 12. It is seen that for $T>0.8$ K the temperature dependence of the effective mobility is qualitatively close to the experimental

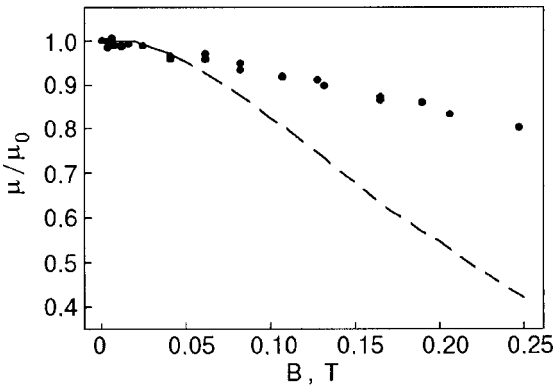

FIG. 13. Normalized electron mobility $\mu(B)/\mu_0$ in quasi-one-dimensional channels as a function of magnetic field. The dashed curve is the theory of Ref. 61.

dependence, but for $T<0.8$ K the theoretical temperature dependence decreases with with decreasing temperature, and that is not observed in the experiment. The difference between the theory and the experimental data may be due to the fact that the electrons in a quasi-one-dimensional channel are found in the potential well that forms the channel, and that can affect the features of the electron motion in a magnetic field.

The properties of the electron transport in a quasi-one-dimensional system in high magnetic fields was studied in Ref. 62. The mobility was calculated in the framework of the memory function formalism. The effective relaxation time, as in the case of a 2D electron system, was expressed in terms of the dynamic structure form factor, but with allowance for the presence of subbands in the quasi-one-dimensional system. The results of the calculation show a strong influence of magnetic field on the effective conductivity in both the gas scattering and ripplon scattering regions.

Dyugaev, Rozhavskiĭ, Vagner, and Wyder[63] considered the possibility of investigating the Aharonov–Bohm effect with the use of a ring of electrons on the liquid helium surface. At low magnetic field the electron spectrum is of the form

$$E_{l,n}^{(m)} = -\frac{\Delta}{l^2} + \left(n+\frac{1}{2}\right)\hbar\omega_0 + \frac{\hbar^2}{2mR_0^2}\left(m'+\frac{\Phi}{\Phi_0}\right)^2,$$

where R_0 is the radius of the electron ring, Φ_0 is the magnetic flux quantum, Φ is the magnetic flux through the ring, and $m'=0,\pm 1,\pm 2,\ldots$. The first two terms have the same form as in (13), while the third term describes the influence of magnetic field on the motion of the electrons in the ring. In spite of the fact that the corresponding studies require extremely low temperatures, experiments with such electron systems are interesting in that they make it possible to investigate the Aharonov–Bohm effect in ideal rings of Wigner crystals and Luttinger liquids.

2.6. Weak localization in quasi-one-dimensional electron systems on liquid helium

Localization effects in low-dimensional disordered electron systems have by now been rather widely studied both experimentally and theoretically.[64] Two localization regimes are distinguished: strong and weak. Strong localization arises

when the carrier mean free path l_0 associated with elastic scattering is small, and the condition $kl_0<1$ holds (k is the electron wave vector). In the weak localization regime the condition $kl_0>1$ holds. Weak localization arises as a result of the interference of the wave function of an electron when it is multiply scattered by impurities; this leads to appreciable corrections in the kinetic coefficients and, in particular, to a decrease in the conductivity. Inelastic scattering processes and a magnetic field will disrupt weak localization. Altshuller, Khmel'nitskii, Larkin, and Lee[65] showed that the conductivity of carriers increases in a magnetic field as a result of the suppression of localization; this negative magnetoresistance effect is one of the most characteristic signs of weak localization.

Until recently attention had been focused mainly on the study of weak localization effects in degenerate electron systems—in metals and semiconductors. Meanwhile, it is of great interest to study these effects in a nondegenerate electron gas, examples of which are electrons localized on the surface of liquid helium or of hydrogen and neon crystals. In nondegenerate systems, by changing the temperature one can controllably vary the electron wave vector $k \simeq k_T = \sqrt{2mT}/\hbar$ and hence the value of $k_T l_0$, which substantially determines the localization processes. In addition to changing k_T in the surface electron layer, there is also a possibility of changing the electron density n and the value of l_0 in a single experiment. This possibility can be important for studying subtle localization effects.

Weak localization effects in a two-dimensional system of electrons have been investigated by Adams and Paalanen[66] and by Adams[67] for a system on solid hydrogen in the presence of carrier scattering on surface roughness and on helium atoms and for a system on the surface of liquid helium in the presence of scattering on helium atoms in the vapor by Dahm and co-workers.[68] In those studies the magnetoconductivity of the electron layer was observed to increase with increasing magnetic field; this effect is due to the suppression of localization by the magnetic field.

Weak localization effects are most clearly manifested in quasi-one-dimensional and one-dimensional electron systems. Electron transport in quasi-one-dimensional and 1D systems under conditions of weak localization has been studied in various kinds of nanostructures: in metal films and semiconductors, in carbon nanotubes, and in other systems.

In Refs. 55–59, as a result of a study of the mobility of carriers on the surface of liquid helium in an electron system which was close to one-dimensional, it was found that localization of the carriers, leading to a substantial decrease in the effective mobility, occurs for $T<0.8$ K in the case when the substrate is contaminated by foreign impurities or has an accumulation of charge on it. However, because the experiments were done in zero magnetic field it is difficult to distinguish strong and weak localization processes.

Kovdrya, Nikolaenko, and Gladchenko measured the magnetoresistance in a close to one-dimensional electron system on liquid helium in the gas scattering region, in the temperature interval 1.3–2.0 K at a pressing electric field of 450 V/cm and a magnetic field of up to 2.5 T.[69] The results are presented in Fig. 14, which shows the values of the magnetoresistance $\rho_{xx}(B)$ divided by the resistance ρ_0 of the channels in zero magnetic field, for different values of the magnetic field B. It is seen that ρ_{xx}/ρ_0 initially decreases with increasing magnetic field and then, after passing through a minimum, begins to grow approximately as $\rho_{xx} \sim B^2$. It is natural to assume that the negative magnetoresistance observed in the experiments in low magnetic fields is due to weak carrier localization effects in a quasi-one-dimensional electron system. As we have said, a magnetic field suppresses localization and thereby leads to a decrease in ρ_{xx}. As the magnetic field is increased further, ρ_{xx} begins to grow as a result of a decrease of the effective relaxation time in connection with a transition to a quantum transport regime.

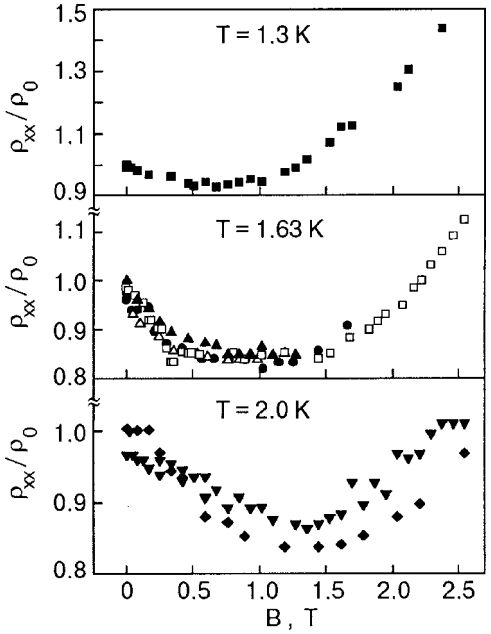

FIG. 14. Magnetic-field dependence of the channel resistance divided by the resistance in zero magnetic field[69] at different temperatures. The different symbols pertain to different experiments.

The data can be used to determine the value of the negative magnetoresistance $\Delta\rho_{xx}$ due to localization effects.

The characteristic length over which the coherence of the electronic states in the 2D system is disrupted is given by the expression

$$L_\varphi^{(2)} = \sqrt{\frac{1}{2} l_0 l_{\text{in}}}, \quad l_{\text{in}} = v_T \tau_\varphi, \tag{23}$$

where l_{in} is the mean free path in relation to inelastic processes, v_T is the thermal speed of the electron, and τ_φ is the time over which the coherence of the wave function of the localized state is disrupted. Stephen[70] has shown that for electron scattering by helium atoms

$$\tau_\varphi = (6\tau_0\tau_\lambda^2)^{1/3}, \quad \tau_\lambda = \frac{\hbar}{2k_B T}\left(\frac{M_4}{m}\right)^{1/2}, \tag{24}$$

where τ_0 is the relaxation time associated with inelastic processes, and M_4 is the mass of the ^{4}He atom. Table II shows the values of $L_\varphi^{(2)}$ calculated using Eqs. (23) and (24). We see that at relatively high temperatures $L_\varphi^{(2)}<y_n$, while for $T \leqslant 1.3$ K, on the contrary, $L_\varphi^{(2)}>y_n$. From a comparison of y_n

TABLE II. Characteristics of conducting channels.

T, K	τ_0, 10^{-11}s	l_0, 10^{-5} cm	$k_T l_0$	y_n, 10^{-5} cm	$L_\varphi^{(2)}$, 10^{-5} cm	ρ_0^0/ρ_0^l	$\Delta\sigma/n$, 10^{-3}cm^3/s
1.3	10.3	3.6	10.9	2.64	4.64	0.83	4.44
1.63	2.51	0.97	3.29	2.96	2.0	0.75	1.59
2.0	0.91	0.42	1.58	3.3	1.06	0.86	0.35

and $L_\varphi^{(2)}$ it follows that for the system under study the behavior due to localization effects is intermediate between 1D and 2D.

The value of $\rho_0^{(0)}/\rho_0^{(l)}$ for $B=0$ [$\rho_0^{(0)}$ and $\rho_0^{(l)}$ are the resistances of the channels in the absence and presence of localization, respectively], and also the values of l_0 and y_n are given in Table II. We see from the table that the effect of localization on the conductivity of the system in zero magnetic field amounts to $\sim 20\%$. The values given in the table for $\Delta\sigma/n$, which characterizes the decrease in conductivity per unit charge as a result of weak localization effects, are shown in Fig. 15 as a function of the density N_g of helium atoms in the vapor. It is seen that $\Delta\sigma/n$ increases with decreasing N_g.

The influence of weak localization on the magnetoconductivity of a nondegenerate electron gas was investigated in Ref. 70. The corresponding expression for σ_{xx} is analogous to that obtained in Ref. 65 and can be written in the form

$$\sigma_{xx}=\frac{2e^2}{m\tilde{d}}\int_{E_c}^{\infty}\frac{dE}{1+\mu^2B^2}\left(-\frac{\partial f}{\partial E}\right)\left[\nu_{\tilde{d}}^{\sim}E\tau_0-\frac{m\tilde{d}}{2\pi}J_{\tilde{d}}^{\sim}\right]. \quad (25)$$

Here E is the energy, f is the distribution function, $\nu_{\tilde{d}}^{\sim}$ is the density of states, E_c is the threshold energy below which localized electrons do not contribute to the conductivity, and $\tilde{d}$ is the dimensionality of the system. The quantity $J_{\tilde{d}}^{\sim}$ depends on the dimensionality of the system and for a two-dimensional electron gas is given by the expression

$$J_2=\frac{1}{4\pi}\left[\psi\left(\frac{1}{2}+\frac{\hbar m}{4eBE\tau_0^2}\right)-\psi\left(\frac{1}{2}+\frac{\hbar m}{4eBE\tau_0\tau_\varphi}\right)\right], \quad (26)$$

which for $B=0$ reduces to

$$J_2=\frac{1}{4\pi}\ln\frac{\tau_\varphi}{\tau_0}. \quad (27)$$

Here $\psi(x)$ is the digamma function. The decrease in conductivity of a two-dimensional electron system in zero magnetic field as a result of weak localization effects is given by the expression[70]

$$\Delta\sigma_2=-\frac{ne^2\hbar}{2\pi mk_BT}\ln\frac{\tau_\varphi}{\tau_0}. \quad (28)$$

In the derivation of (28) it was assumed that $E_c=0$, which is valid for electron scattering on helium atoms in the vapor, when the density N_g of helium atoms is low. The values of $\Delta\sigma_2/n$ calculated with the use of Eqs. (24) and (28) are presented in Fig. 15 (the dotted-and-dashed line). It is seen from Fig. 15 that relation (28) corresponds poorly to the experimental data.

With the use of Eq. (25), an expression describing the decrease in conductivity of a two-dimensional nondegenerate electron gas due to localization effects was calculated in Ref. 69. There it was assumed that for $\tilde{d}=1$ one obtains a value $J_{\tilde{d}}^{\sim}=a'(L_\varphi^{(1)}-l_0)$ (Ref. 64), where $L_\varphi^{(1)}$ is the characteristic distance over which the coherence of the wave function in the one-dimensional system is disrupted, and a' is a constant. The corresponding expression for $\Delta\sigma_1$ has the form

$$\Delta\sigma_1=-\left(\frac{2}{\pi}\right)^{1/2}\frac{ne^2}{m}\tau_0\left(\left(\frac{\tau_\varphi}{\tau_0}\right)^{1/2}-1\right). \quad (29)$$

In the derivation of (29) it was assumed that $a'=1$ and $L_\varphi^{(1)}=v_T(\tau_\varphi/\tau_0)^{1/2}$, where v_T is the thermal speed. Expression (29) gives a fair description of the experimental data if it one adopts a value $\tau_\varphi/\tau_0=1.44$ (the dashed curve in Fig. 15). The agreement of the calculated and experimental data apparently indicates that the system under study is close to one-dimensional in terms of the characteristics of weak localization processes in it at $T<2$ K.

It is interesting to note that the experimental values of τ_φ/τ_0 are less than the analogous quantities in Ref. 68. Apparently in the quasi-one-dimensional system under study, additional mechanisms that disrupt the coherence of the wave function appear, e.g., due to interlevel transitions.

It is known that a magnetic field will disrupt the localization when the magnetic length $\lambda_H \approx l_0$. However, this condition can scarcely be applicable to the system under study. As we mentioned in Sec. 2.1, the energy spectrum (13) of a one-dimensional electron system in a magnetic field is described by expression (15). An interesting feature in this

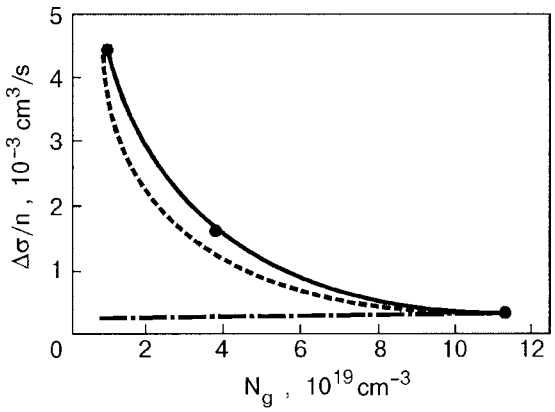

FIG. 15. Dependence of $\Delta\sigma/n$ on the density of helium atoms in the vapor.[69] The solid curve is experimental data, the dotted-and-dashed curve is the calculation of Ref. 70 for a 2D system, and the dashed curve is the calculation according to Eq. (29) for $\tau_\varphi/\tau_0=1.44$.

case is that, unlike a two-dimensional electron system, where an electron is localized by a magnetic field to a length of the order of λ_H, in the present study electron motion along the channel remains possible, since $k_x \neq 0$ in spectrum (15) in a magnetic field. It can be assumed that localization effects arising as a result of the interaction of electrons with scatterers are suppressed at substantially higher magnetic fields.

3. COLLECTIVE EFFECTS IN QUASI-ONE-DIMENSIONAL ELECTRON SYSTEMS

3.1. Plasma oscillations

The dispersion relation for plasma oscillations in a two-dimensional system of particles with the Coulomb interaction was first considered by Ritchie.[71] It was found that, in contrast to the three-dimensional case, the spectrum of plasma oscillations in a two-dimensional charge layer does not have a threshold frequency, and it can be written in the form

$$\omega(k)=\left(\frac{2\pi ne^2}{m}k\right)^{1/2}, \tag{30}$$

where k is the plasmon wave vector. The presence of metallic electrodes leads to partial screening of the Coulomb interaction, and spectrum (30) is altered. For thin films of helium, when the film thickness $d \ll a$ (a is the average distance between electrons), the spectrum of plasma oscillations in the long-wavelength limit, as was shown by Monarkha,[72] is of an acoustical character with a dispersion relation

$$\omega(k)=u_0 k, \quad u_0=\left(\frac{4\pi e^2 nd}{m}\right)^{1/2}. \tag{31}$$

The energy spectrum of plasma oscillations over bulk helium was first observed in Ref. 15.

The spectrum of plasma oscillations in a one-dimensional electron system was considered by Krasheninnikov and Chaplik in Ref. 73 and also by Chaplik in Ref. 38. It was found that to within a logarithmic factor the spectrum of the longitudinal plasmon branch is of an acoustical character and is given by the expression

$$\omega_{\parallel}(k)=c_{\parallel}k_x, \quad c_{\parallel}=e\sqrt{\frac{2}{ma}\ln\left(\frac{1}{k_x a}\right)}. \tag{32}$$

The dispersion relation for the collective modes in a one-dimensional chain of electrons found in a channel filled with liquid helium was investigated theoretically by Sokolov and Kirichek[74] over a wide interval of wave vectors k_x. The calculation was done for both zero and nonzero magnetic field. The results of the calculation are presented in Fig. 16: the dispersion relation for the longitudinal $\omega_{\parallel}$ and transverse $\omega_{\perp}$ modes of plasma oscillations for a single chain of electrons. We see that the transverse optical branch $\omega_{\perp}$, which starts at a threshold frequency ω_0 [see Eq. (11)], has the characteristic feature that $\omega_{\perp}(k_x)$ is a descending function from 0 to π/a. Calculations show that a magnetic field ''softens'' the longitudinal mode; in the limit $\omega_0 < \omega_c$ the lowest mode is determined by the expression $\omega_- \approx (\omega_0/\omega_c)\omega_{\parallel}$, i.e., $\omega_- < \omega_{\parallel}$.

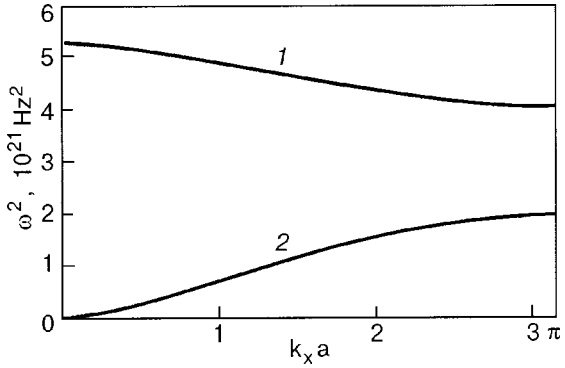

FIG. 16. Dispersion relation of collective modes $\omega_{\perp}$ (*1*) and $\omega_{\parallel}$ (*2*) for a one-dimensional chain of electrons for $r=5\times10^{-4}$ cm, $a=10^{-4}$ cm for $E_{\perp}=1500$ V/cm.[74]

The frequency of the plasma oscillations propagating in a system of parallel channels was calculated in Ref. 59. The plasmon dispersion relation was shown to have the form

$$\omega_p^2(k_x)=\frac{4\pi n_l e^2}{mb}k_x\frac{\Delta_{Dd}}{\Delta_{HD}}\sinh(k_x(H-d)),$$
$$k_x=\frac{\pi}{L_x}n, \quad n=1,2,3,\ldots . \tag{33}$$

The parameters Δ_{Dd} and Δ_{HD} are determined by the geometry of the cell:

$$\Delta_{Dd}=\varepsilon_d\cosh(k_x D)\sinh(k_x d)+\cosh(k_x d)\sinh(k_x D),$$
$$\Delta_{HD}=\varepsilon_d\cosh(k_x D)\sinh(k_x H)+\cosh(k_x H)\sinh(k_x D). \tag{34}$$

Here k_x is the wave vector of the oscillations, b is the distance between channels, D is the thickness of the dielectric substrate on which the channels are formed, d is the thickness of the helium layer in the channel, and H is the distance from the substrate to the upper electrode. In the analysis it was assumed that the electron density distribution transverse to the channel is δ-function-like.

The problem of plasma excitations in a nondegenerate quasi-one-dimensional electron system was considered in general form by Sokolov and Studart.[75] Employing a many-particle approach and using the random phase approximation, they calculated the response function of a quasi-one-dimensional system for arbitrary values of the wave vector k_x and subband number. In the limit of small wave vectors and low temperatures they obtained the spectra of plasmons propagating within a band and between bands. They showed that, in agreement with previous calculations,[74] the plasmon dispersion relation along the bands is of an acoustical character, while the plasma oscillations propagating transverse to the channels are optical.

Experiments on the direct measurement of the spectrum of plasma oscillations in one-dimensional and quasi-one-dimensional electron systems on liquid helium have not yet been done. In Refs. 55–59 the frequency of plasma oscillations was estimated using the corresponding expressions for the conductance of the experimental cell.[59] The values of $\tilde{\omega}_p$ found in the experiments turned out to be approximately three times larger than the theoretical values according to (33), (34). This difference was explained in Ref. 59 as being

the result of unavoidable slight imperfections of the profiled substrate on which the 1D system was realized, causing the channels to be divided into shorter segments, so that the average effective length of the liquid channels used in expressions (33), (34) should be smaller. This leads to an increase in k_x and, accordingly, in the frequency $\tilde{\omega}_p$. In Refs. 51 and 52 the characteristic frequencies of plasma oscillations were estimated from the data on the mobility of electrons under conditions of their strong localization. In both of those papers the results were of a qualitative nature that did not permit making a reliable comparison with the theory. We note that the plasma oscillations under the experimental conditions of Refs. 55–59 are strongly damped, so that one is actually talking about only some average frequencies characterizing the response time of the 1D system to a disturbance. Direct measurements of the spectrum of longitudinal plasma oscillations in a 1D system of electrons on liquid helium are possible only at low temperatures under conditions of high carrier mobility or at large values of the wave vector k_x, when the oscillation frequencies will be high.[75]

3.2. Transition to an ordered state

At sufficiently low temperatures and high particle densities a two-dimensional electron system undergoes a transition to a crystalline state. The transition occurs when the parameter Γ characterizing the ratio of the potential energy of the particles to their kinetic energy, $\Gamma = e^2\sqrt{\pi n}/k_BT$, reaches values $\Gamma_m = 127$.[25–27] The melting of the two-dimensional crystal is described by the Kosterlitz–Thouless theory,[76] which treats melting as the appearance of a large number of free dislocations, which had been bound to each other below the transition. It is shown in Ref. 76 that the melting temperature depends on the shear modulus of the two-dimensional crystal; an exact calculation of its value was done my Morf.[77] The value obtained there for Γ_m was in good agreement with the experimental data. The theory of dislocation melting, as has been established by Nelson and Halperin,[78] predicts the appearance of a hexatic phase above the melting temperature T_m, with the transition to an isotropic liquid occurring at higher temperatures.

In discussing the stability of a crystal, one considers the mean-square displacements of the particles at the lattice sites from their equilibrium positions. In the harmonic oscillation model these displacements can be written in the form[3]

$$\langle \Delta u^2 \rangle = \frac{\hbar}{2mN} \sum_{k,p} \frac{1}{\omega_p(k)} \coth \frac{\hbar \omega_p(k)}{2k_BT}, \quad p = l,t, \tag{35}$$

where N is the total number of particles in the system. For a three-dimensional crystal $\langle \Delta u^2 \rangle$ turns out to be a small quantity, while for a two-dimensional crystal it diverges as $\ln L$ (L is the size of the crystal). Nevertheless, in this case for a crystal of finite size the value of $\langle \Delta u^2 \rangle$ turns out to be finite at sufficiently low temperatures. For one-dimensional linear chains the situation is not so definite. Nevertheless, estimates show[38] that for a one-dimensional system of finite length the temperature of the transition to the ordered state is finite and approximately equal to

$$T_c \approx \frac{4\pi^2 a m c_\parallel^2}{k_B L}, \tag{36}$$

where $c_\parallel$ is taken from Eq. (32). Estimates shown that for typical dimensions of the conducting channels $L = 1$ cm and $a = 10^{-4}$ cm one would have $T_c \approx 1$ K. Thus for $T < T_c$ a one-dimensional electron system can be ordered.

In a two-dimensional crystal the electrons localized in the crystal lattice form a dimple on the liquid helium surface, and that leads to the appearance of coupled electron–ripplon modes,[25] which were studied in detail in Ref. 79. An analogous picture should be observed in a linear electron chain if it undergoes a transition to an ordered state. Sokolov and Studart[80] in a study of the properties of coupled electron–ripplon modes in an ordered linear chain showed that electron–ripplon coupling, as in the case of a 2D system, causes a dimple to form under the electrons, and in that case the effective masses $M_\parallel$ and $M_\perp$ for the longitudinal and transverse motions of the particles, respectively, will be different. Accordingly, the longitudinal plasma mode $\tilde{\omega}_l$ and the transverse frequency $\tilde{\omega}_0$ of electron oscillations in the channels assume the form

$$\tilde{\omega}_l = \omega_\parallel \left(\frac{m}{M_\parallel} \right)^{1/2}, \quad \tilde{\omega}_0 = \omega_0 \left(\frac{m}{M_\perp} \right)^{1/2}, \tag{37}$$

where $\omega_\parallel$ is taken from Eq. (32) and ω_0 from Eq. (11). Estimates show that for $a = 10^{-4}$ cm and $E_\perp = 3000$ V/cm the effective masses have the values $M_\parallel = 2.3 \times 10^4 m$ and $M_\perp = 10^{11} m$. These are much larger than the effective mass of an electron in the case of 2D ordering. The effects considered can be used to search for ordered phases in a 1D system of electrons on liquid helium.

The formation of a dimple in a 1D electron system on liquid helium with the corresponding increase in the effective mass should lead to a substantial decrease in mobility. Such an effect was observed for a two-dimensional electron crystal in Ref. 27. For a 1D electron system no mobility decrease due to the onset of ordering was noticed in Refs. 55–59 down to 0.5 K. Apparently the observation of this effect requires still lower temperatures.

A classical nondegenerate system of electrons in narrow channels (quasi-two-dimensional electron system) was studied by Bajaj and Mehrotra[81] by the molecular dynamics method. In a study of a layer containing up to 50 electrons along the channel and 8 electrons across the channel it was found that the critical value of the parameter Γ at which melting occurs is substantially larger than the analogous quantity for a 2D electron system. Figure 17 shows the dependence of the parameter Γ_m on the number of electrons along the channel, N_x. It is seen that up to $N_x = 20$ the parameter $\Gamma_m = 250–350$, and at larger N_x the value of Γ_m increases in a jump to $\Gamma_m = 550$. An interesting feature of the results obtained is that, as a calculation shows, in the liquid state the electrons are localized in the direction transverse to the channel and delocalized in the direction along the channel.

Experimentally the crystallization of electrons in a narrow channel was studied by Lea and co-workers.[82] They measured the electron conductivity along a channel 16 μm wide, 395 μm long, and 1.6 μm deep on a liquid helium surface. A schematic diagram of the electron microchannel is shown in Fig. 18. By applying suitable confining potentials to the electrodes, one can form an electron layer ~ 10 μm

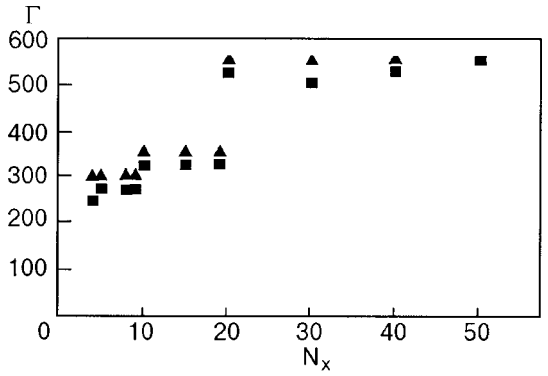

FIG. 17. Dependence of Γ on the number of electrons along the channel, N_x, for $N_y=8$: $\Gamma<\Gamma_m$ (■), $\Gamma>\Gamma_m$ (▲). The melting curve passes between the points denoted by different symbols.[81]

wide (in which case 30 electrons are found along the width of the channel) and measure the resistance of the channel by applying an ac voltage to the source and drain electrodes. The results are shown in Fig. 19 in the form of the temperature dependence of the resistance ρ of the channel. It is seen that for $T>0.8$ K the value of ρ decreases with decreasing T, and the dependence is well described by the theory. However, for $T<0.8$ K a significant growth of the channel resistance begins, and this growth gets stronger as the exciting signal acting on the electron layer is increased. This effect was attributed by the authors to a transition from an isotropic liquid at high temperatures to a spatially ordered phase near T_m. It was established that the value of the nonlinear effect depends on the electron velocity. Figure 20 shows the electric field acting on the electron layer for different velocities of the electron motion along the channel. At velocities $v<7$ m/s a linear regime is observed, while at $v_c=7.1$ m/s the moving electrons begin to emit ripplons with wave vector $q=G_1$ by a Cherenkov process (G_1 is the first reciprocal lattice vector of the crystal). For $v>v_c$ the electrons leave the dimples and move independently of them. Such a pattern has also been observed for a 2D crystal.[83] Since the electron

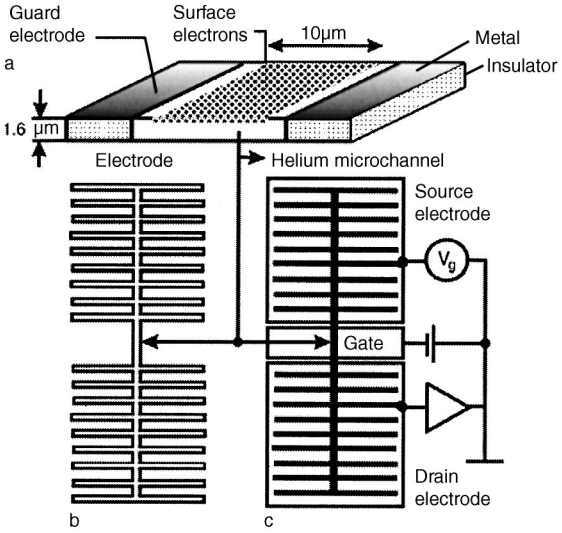

FIG. 18. Schematic diagram of an electron microchannel: cross-sectional view of the microchannel (a), photograph of a microchannel (b); connection of the measurement circuit to the microchannel (c).[82]

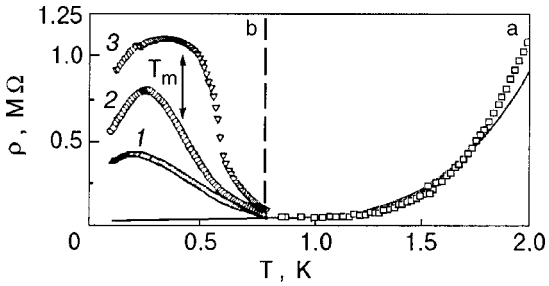

FIG. 19. Effective resistance of an electron layer in a microchannel: a—$\rho(T)$ for $T>0.8$ K for $n=5.1\times10^8$ cm^{-2}; the solid curve is the theoretical calculation; b—$\rho(T)$ for $T<0.8$ K for electron velocities of 16 (*1*), 31 (*2*), and 64 m/s (*3*) for $n=3.5\times10^8$ cm^{-2}. The arrow indicates the melting temperature of the crystal with the given electron density for a 2D layer.[82]

density is nonuniform over the width of the channel, electron streamlines appear, on some of which the electrons leave the dimples and in others the electron motion is due to motion of the dimples. This is due to the existence of a region in which v depends weakly on $E_\parallel$. The periodic oscillations of the maximum electric field realized in an electron channel are evidence of such dynamic ordering in a quasi-two-dimensional electron crystal.

4. ZERO-DIMENSIONAL ELECTRON SYSTEMS ON LIQUID HELIUM

A typical zero-dimensional system realized in liquid helium consists of an electron trapped in a bubble.[3] The characteristics of the bubble are determined by the pressure exerted by the trapped electron on the liquid and by the opposing surface tension and external pressure. The characteristic size of an electron bubble in liquid ^{4}He is ~25 Å, and the ground state energy is ~0.15 eV. The properties of electron bubbles in helium have been considered in many original papers and are discussed in reviews and monographs (see, e.g., Ref. 3).

Several types of zero-dimensional electronic states can be realized on the surface of liquid helium. Some of them will be examined in more detail. Electrons can also be localized in bubbles in dense gaseous helium; their properties were studied in detail in Ref. 84. Such bubbles can be localized near the liquid helium surface by an electric field, forming a peculiar zero-dimensional electron system at the interface between the liquid helium and the vapor. Aside from a study of the mobility of electron bubbles in the gas near the surface of the liquid,[10] there have been no experimental studies of the characteristics of such systems. In Ref. 85 a pecu-

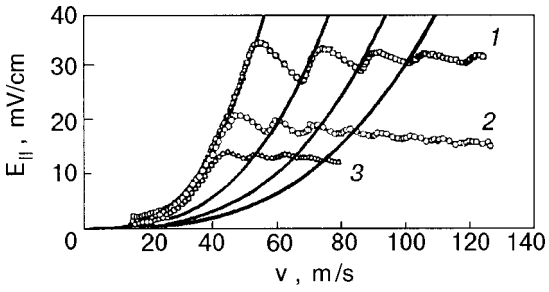

FIG. 20. Driving electric field-velocity characteristics of electrons for a pressing potential of 1.8 (*1*), 1.2 (*2*), and 0.8 V (*3*). The lines are drawn through the points where the features appear on the experimental curves.[82]

liar polaron state in which the electron is localized was predicted to exist in gaseous helium in a high magnetic field. We know of no experiments that have been done to observe and study the properties of this state, including near the liquid helium surface.

4.1. Polaron state of electrons on the liquid helium surface. Localization of electrons in polarons on the helium film

It was shown by Shikin[86] that in a sufficiently high pressing electric field an electron can be localized in the plane of the helium vapor–liquid interface. There appears on the liquid helium surface a sort of polaron—an electron plus a deformation of the surface of the liquid. Localization of the electron leads to an increase in the local pressure on the liquid helium surface, and the exertion of this pressure in turn causes deformation of the liquid surface, leading to the formation of a microscopic dimple. A self-consistent localization of the electron appears. It was shown by Shikin[86] and Shikin and Monarkha[87] that the energy of such a localized state of the electron can be written

$$W=-\frac{e^2E_\perp^2}{4\pi\alpha}\left[\ln\left(\frac{\sqrt{2}}{\kappa L\,\gamma_0^{1/2}}\right)-\frac{1}{2}\right],\quad \gamma_0=1.87, \tag{38}$$

where L is the characteristic size of the dimple, and $\kappa=\sqrt{\rho g/\alpha}$ is the capillary constant of liquid helium. The value of L is determined by the expression

$$L=\sqrt{\frac{4\pi\alpha}{m}}\,\frac{\hbar}{eE_\perp}. \tag{39}$$

It follows from Eq. (38) that W is negative if $\kappa L\ll 1$. For $E_\perp=3000$ V/cm one has $W=-0.1$ K and, hence, for $T<0.1$ K the formation of an electron polaron is energetically favorable. The volume of the dimple is determined by the relation

$$V_L=2\pi\int_0^\infty \xi(r)r\,dr=\frac{eE_\perp}{\alpha\kappa^2}, \tag{40}$$

where $\xi(r)$ is the deflection of the liquid surface. For $E_\perp=3000$ V/cm one has $V_L=10^{-6}$ cm^3, and, accordingly, the effective mass of the polaron can reach values of $10^2-10^3M_4$ (M_4 is the mass of the helium atom).

The electronic states in such a polaron can be regarded as zero-dimensional. They have characteristics—binding energy and localization length—peculiar to zero-dimensional systems, and also, if the potential well in which the electrons are localized is sufficiently deep, a set of energy levels.

A magnetic field normal to the surface of the liquid promotes the formation of an electron polaron. In the limit when the magnetic length $\lambda_H\ll L$, the binding energy of the polaron can be written in the form[3]

$$W=-\frac{e^2E_\perp^2}{4\pi\alpha}\ln\left(\frac{1.1}{\kappa\lambda_H}\right). \tag{41}$$

The characteristics of one-electron dimples on thin layers of liquid helium were considered by Monarkha.[33] As we have said, the presence of the substrate gives rise to an additional pressing electric field, and it is also necessary to take into account the renormalization of the capillary constant due to the van der Waals forces exerted by the substrate. The effective capillary constant of the film can be written in the form

$$\tilde{\kappa}^2=\frac{\rho}{\alpha}(g+\tilde{g}),\quad \tilde{g}=\frac{\partial\beta}{\partial d}, \tag{42}$$

$$\beta=-\frac{\beta_0}{d^3(1+d/d')},$$

where β_0 and d' are constants characterizing the substrate material. The binding energy of a polaron depends on the film thickness as d^{-4}. For thin films the value of W can reach several degrees, and the maximum deflection of the liquid in the dimple can reach several ångstroms.

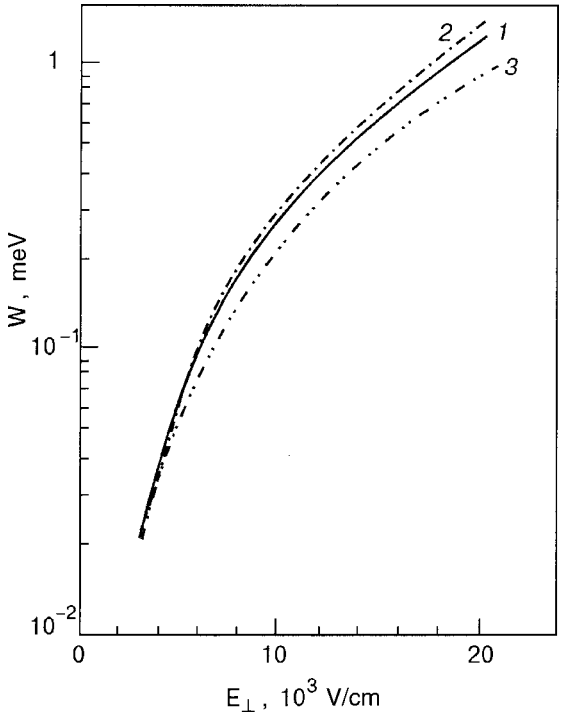

FIG. 21. Binding energy of an electron in a one-electron dimple as a function of the pressing electric field $E_\perp$: *1*—calculation of Ref. 88, *2*—calculation according to formula (38), *3*—calculation of Ref. 91.

Electron polarons on liquid helium are interesting because by changing the pressing electric field one can alter the value of the coupling of the particle with the medium. The binding energy and effective mass of an electron polaron were studied by Hippolito, Farias, and Studart[88] and by Jackson and Platzman[89,90] in the framework of the Feynman path-integral method. Figure 21 shows the calculated binding energy W of a polaron over bulk helium as a function of the pressing electric field. It is seen that the calculations done by different methods are in good agreement. Figure 22 gives the polaron effective mass M^* as a function of the thickness d of the helium film for different substrates.[92] The value of M^* increases sharply with decreasing d even for substrates with a weak van der Waals coupling, such as solid neon.

The hydrodynamic model of an electron polaron presupposes the absence of thermal ripplons on the liquid surface, i.e., strictly speaking, it is valid for $T=0$ K. The features of the formation of a polaron on a helium film at nonzero temperatures were considered in Refs. 89 and 90. The bind-

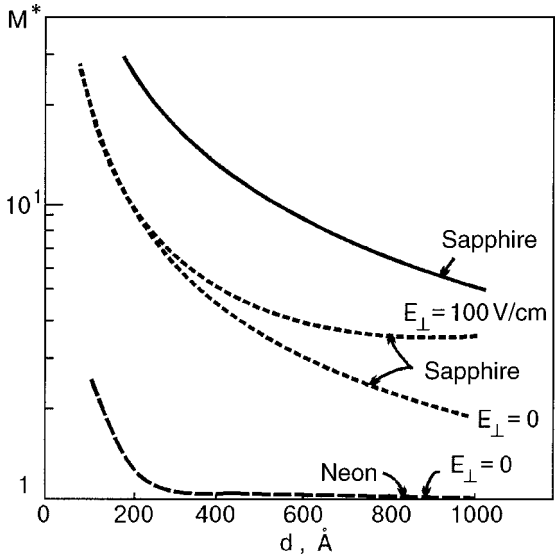

FIG. 22. Effective mass of a polaron versus the thickness of the helium film. The solid curve is a self-consistent calculation, and the dashed curves are the harmonic approximation.[88]

ing energy and effective mass of polarons for both thin films ($d=100$ Å) and for films of arbitrary thickness were calculated for various temperatures and for a coupling constant determined by the relations

$$\tilde{\alpha}=\frac{(eE_{\perp}^{*})^2}{8\pi\alpha E_c},\quad E_c=\frac{\hbar^2k_c^2}{2m}, \tag{43}$$

where k_c is taken equal to $\tilde{\kappa}$. It was found that the thermal ripplons destroy the polaron states, preventing the formation of a stable dimple, and the destruction of the localized state occurs at a rather small value of the ratio k_BT/W. Figure 23 shows the dependence of the polaron effective mass on α for different values of $x_0=E_c/k_BT$ (Ref. 89). It is seen that for small values of x_0 (high temperatures), polaron formation is difficult even at large values of the coupling constant.

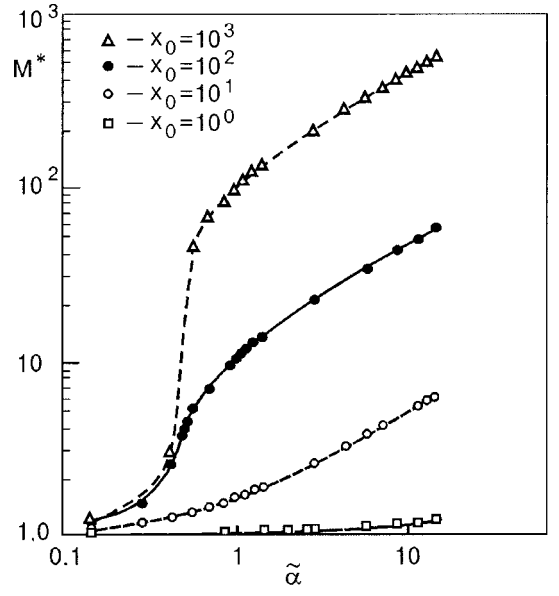

FIG. 23. Effective mass M^* of an electronic polaron as a function of the coupling constant $\tilde{\alpha}$ for various values of $x_0=E_c/k_BT$.[89]

A detailed analysis of the theoretical papers in which various characteristics of electron polarons on the surface of liquid helium have been calculated is given in the review by Studart and Sokolov (see p. 245 of Ref. 41).

Many papers have been devoted to the search for polaron states on the liquid helium surface. Although it is still too early to draw a final conclusion as to the detection of such states with a sufficiently high binding energy and stable dimple, it is nevertheless of interest to discuss the main results of the experiments that have been done and the directions of future searches.

The first information as to the possibility of formation of a magnetic polaron on liquid helium was obtained by Édel'man in cyclotron resonance (CR) experiments.[93] It was found that the CR lines are shifted to higher frequencies by an amount $\delta\omega_c$ that could be due in part to the formation of a magnetic polaron. According to the theoretical estimates[94–96]

$$\delta\omega_c=\frac{e^2E_{\perp}^2}{8\pi\alpha\hbar}. \tag{44}$$

The experimental value of $\delta\omega_c$ turns out to be approximately three times larger than the theoretical value, although the dependence of $\delta\omega_c$ on $E_{\perp}$ agrees qualitatively with Eq. (44).

The formation of a polaron should lead to a sharp change in the character of the electron motion along the liquid helium surface. If the mobility of free electrons is determined by their interaction with helium atoms in the vapor and with ripplons, then, since a polaron dimple on the helium surface has a characteristic size $L=10^{-5}$ cm, the mobility of an electron polaron should be determined by the viscosity of the liquid. In Ref. 87 it was shown that the mobility of a polaron on bulk helium can be written in the form

$$\mu=\frac{2\pi\hbar\alpha^{5/2}}{\eta m^{1/2}e^2E_{\perp}3}, \tag{45}$$

where η is the viscosity of liquid helium. The value of μ from (45) is much smaller than the mobility of free electrons. In addition, the temperature dependence of the mobility according to (45) is determined by the temperature dependence of α and η. Since for liquid ^{4}He at $T<1.3$ K the value of η increases with decreasing temperature, the value of μ should decrease accordingly. We also note that, unlike the case of free electrons, for which $\mu\sim E_{\perp}^{-2}$ at high pressing fields, for electron polarons one has $\mu\sim E_{\perp}^{-3}$. In Ref. 33 the following expression was obtained for the mobility of electron polarons on a helium film:

$$\mu=\frac{4\pi\alpha^2e(\tilde{\kappa}d)^2d}{3\eta(F^*)^2},\quad F^*=eE_{\perp}+F_d,\quad (\tilde{\kappa}d)^2<L/d, \tag{46}$$

where F_d is taken from Eq. (6).

Thus the formation of polarons on liquid helium is revealed most simply by the presence of features in the behavior of the mobility of electrons on liquid helium at high pressing electric fields and on thin helium films. This is the method that has mainly been used to register polaron states on liquid helium.

Even in the first experiments on the detection of surface electronic states on a helium film it was established that the

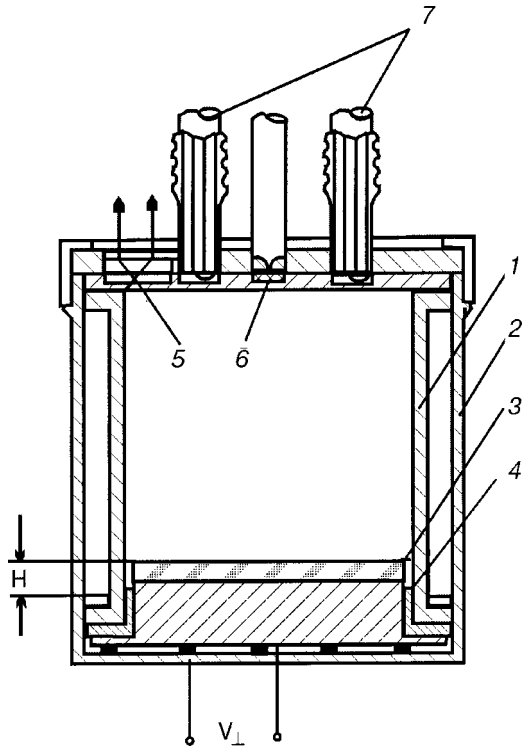

FIG. 24. Diagram of the experimental cell for investigating the high-frequency conductance of electrons on a helium film: *1*—cylindrical cavity, *2*—vacuum chamber, *3*—dielectric insert, *4*—bottom of cavity, *5*—heating filament, *6*—spark gap, *7*—coaxial cable.[34]

velocity of surface electrons on a film is very low. It remained unclear, however, whether this effect is due to a low electron mobility or to other mechanisms, e.g., a low rate of transition of electrons from the helium film to the bulk liquid, where they were registered. The first measurements of the mobility of surface electrons on a helium film with the use of microwave cavities[34] showed that, depending on the kind of substrate and the quality of its surface, the mobility of surface electrons for films 300 Å thick is 0.1–1.0 $m^2/(V \cdot s)$, which is much lower than the mobility of electrons on bulk helium.

The measurement cell used in Ref. 34 is shown in Fig. 24. A cylindrical cavity *1*, having a diameter and a height of 42 mm and with its walls covered by a layer of lead, was placed in a chamber *2*. The bottom of the cavity was electrically isolated from the walls. A dielectric insert *3*, with a thickness of 1 mm and a diameter of 41 mm, was placed on the bottom of the cavity. The electron source was either a rapidly switchable heating filament *5* or a discharge near a tungsten tip *6*. The microwave power was coupled in and out by coaxial lines *7*; their coupling coefficient with the cavity could be tuned by means of adjusting screws located on the outside of the cryostat. The H_{011} mode of electromagnetic oscillations of the cavity was used for the measurements. In that case the alternating electric field was directed parallel to the surface of the dielectric insert.

The Q of the cavity was determined from the damping decrement with with a relative error of $\sim 0.5\%$ with the aid of a precision Q meter.

The thickness of the film at a given value of H, which was determined from the shift in the frequency of the cavity when it was filled with helium to the necessary distance $d = k_0/H^{1/3}$ from the bottom, where k_0 was assumed equal to 3×10^{-6} $cm^{4/3}$. Measurements were made at a frequency of 9.4 GHz in the temperature range 1.65–2.15 and at electron densities of up to 6×10^9 cm^{-2}.

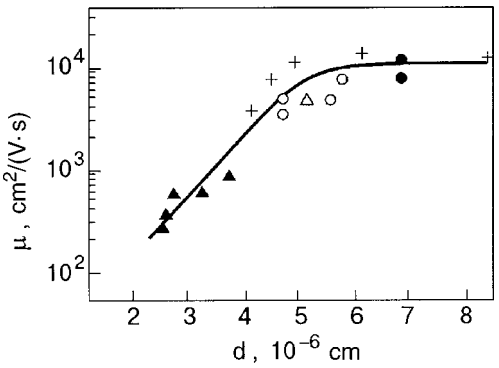

FIG. 25. Dependence of the effective high-frequency mobility of electrons on the thickness of a helium film on a Sitall substrate ($\varepsilon_d = 5.6$).[97]

The conductivity of the electron layer was determined from the shift in the Q of the cavity when the dielectric insert was charged with electrons. The relative error in determination of the Q was 5%.

The values obtained for the effective high-frequency mobility of the electrons for a film on the surface of a sapphire substrate was 0.1 $m^2/(V \cdot s)$ at 1.7 K. The electron mobility on a liquid helium layer on Sitall glass ($\varepsilon_d = 5.6$) as a function of the layer thickness d, obtained by Mende, Kovdrya, and Nikolaenko,[97] is shown in Fig. 25. It is seen that μ increases with increasing d, and at $d = 600$ Å the mobility μ reaches its value for surface electrons on bulk helium. It was found in that study that the electron mobility is approximately inversely proportional to the density of helium atoms in the vapor.

Low-frequency measurements of the mobility of electrons on a liquid helium film were first made in Ref. 35. The experimental cell used in that study had the feature that the liquid helium level relative to the substrate could be varied by means of a system of two coupled sylphons, into one of which helium was delivered under pressure. The helium level was measured by a capacitive sensor.

The results are presented in Fig. 26. It is seen that, starting at values $d = 800$ Å, the mobility falls sharply with decreasing thickness d of the helium film, reaching values of 10^{-4} $m^2/(V \cdot s)$, which are much lower than the mobility obtained in microwave measurements.

The low-frequency mobility of electrons on helium films on different substrates has been investigated in many studies. Wilen and Gianetta[98] measured the mobility of electrons on a helium film on a glass substrate in the temperature range 1.5–1.7 K. It was shown that at $d = 750$ Å the measured values of μ are close to those for the bulk liquid. With decreasing d the mobility falls and its value becomes irreproducible. Dahm and co-workers[99,100] made detailed and careful measurements of the mobility of surface electrons on films on smooth glass substrates (the substrate roughness was of the order of 20 Å) in the temperature region 1.2–1.9 K for film thicknesses of 220–250 Å. The electron density on the films was monitored by measuring the induction sig-

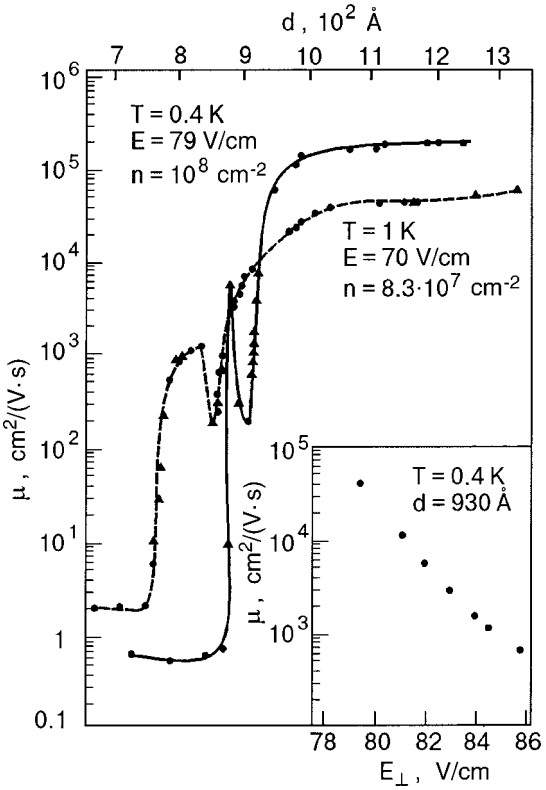

FIG. 26. Dependence of the low-frequency mobility μ on the film thickness for electrons on a helium film at two different temperatures.[35] The inset shows the dependence of μ on $E_\perp$ for a helium film 930 Å thick.

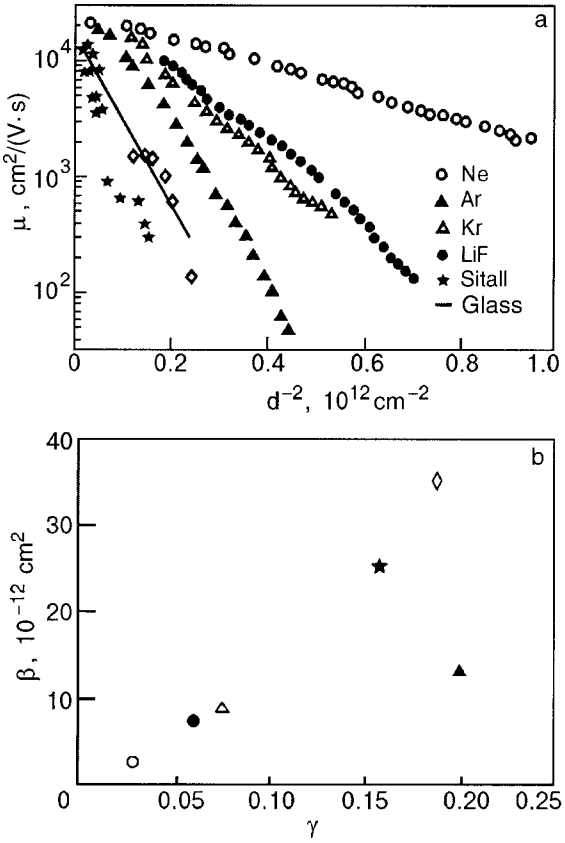

FIG. 27. Mobility of electrons on a helium film versus d^{-2} for different substrates (a) and the dependence of the parameter β on γ from Ref. 4 (b). The data of Ref. 105 for 1.5 K (○, ●, △, ▲); the data of Ref. 97 for $T=1.7$ K (★); the data of Ref. 106 for $T=1.6$ K (◇); the solid curve shows the data of Ref. 107 reduced by a factor of 10.

nal from the charge layer on a vibrating electrode. It was found that the experimental data differ from the results of theoretical calculations that take into account the scattering of electrons on helium atoms in the vapor[101] and also the one- and two-ripplon mechanisms of electron scattering.[102] It was established that the difference is practically independent of temperature, so that the additional scattering could be attributed to the interaction of electrons with defects of the substrate.

In measurements of the mobility of electrons on helium films on a solid substrate with weak van der Waals coupling (solid neon), Kajita and Sasaki[103] observed that for thin helium films (several monolayers) the relaxation time of the electrons is determined by the expression

$$\tau^{-1}=\tau_G^{-1}+\tau_S^{-1}, \tag{47}$$

where τ_G and τ_S are the relaxation times associated with the interaction of electrons with helium atoms in the vapor and with substrate roughness, respectively. In Ref. 104 the mobility of electrons on a helium film on a solid neon substrate was measured in a pressing field of up to 9000 V/cm. It was shown that μ depends weakly on the thickness of the helium film.

De Jeu and Platzman (see Ref. 105) measured the mobility of electrons on helium films covering substrates of solid Ne, Ar, Kr, and LiF in the temperature range 1.5–1.6 for film thicknesses up to $d\approx 800$ Å. They found that the mobility is inversely proportional to the density of helium atoms in the vapor and for $d\leqslant 550$ Å is described by the empirical formula $\mu\sim e^{-\beta/d^2}$, where β is a coefficient that depends on the substrate material. Dahm (p. 281 of Ref. 4) pointed out that this empirical dependence also gives a fair description of the data of Refs. 97, 106, and 107. The situation is illustrated by Fig. 27 (taken from Ref. 4), which shows plots of $\mu(d^{-2})$ and $\beta(\gamma)$, where $\gamma=(\varepsilon_d-1)/[4(\varepsilon_d+1)]$.

By analyzing the behavior of the mobility of electrons on a helium film from Ref. 97, Marquez and Studart[92] arrived at the conclusion that the motion of electrons on a film is of a polaronic character, involving the formation of a stable dimple, in which case the polaron mobility is given by an expression analogous to (46). This conclusion is in need of refinement, however. The problem is that the mobility of a polaronic dimple should be determined by the viscosity, while, according to the data of Ref. 97, the value of μ is approximately inversely proportional to the density N_g of helium atoms in the vapor. It was pointed out above that the mobility of electrons on a helium film in Ref. 105 is also inversely proportional to N_g, and the mobility measured in Refs. 99, 100, 106, and 107, except for the influence of surface roughness, is mainly determined by the scattering of electrons by helium atoms in the vapor.

In answering the question of whether the electron motion on a helium film is of the character proposed in Ref. 92 or is governed by some other mechanism, it is apparently necessary to take the roughness of the substrate into account in addition to the value of the effective pressing field $E_\perp^*=E_\perp+E_d$. It was established by an electron microscopic

analysis of the structure of the substrate surface[99] that the characteristic height of the substrate roughness is 20 Å, with an average distance between asperities of 10^{-4} cm. It was established in Ref. 34 that the characteristic roughness for a sapphire substrate consists of round protrusions 200–300 Å in height, with a density of $\sim 10^{10}$ cm^{-2}, and defects in the form of ''ridges'' with a height and width of 700 Å. The Sitall substrate used in Ref. 97 was smoother: the asperities on it had a characteristic height of 200 Å and a density of $\sim 10^{10}$ cm^{-2}. For a helium film 300 Å thick, roughness on such a scale should lead to rather large variations of the potential, although, because of the finite thickness of the helium film, they will be smoothed out in accordance with relation (14). We note that for the substrates used in Refs. 34 and 97 the density of potential wells was greater than the electron density.

One can propose the following picture of the motion of electrons on the surface of a helium film. By virtue of relation (14), the variations of the random potential owing to surface roughness are not very large, and the electrons are localized in the random potential not in a single potential well but in several of them, with a characteristic localization length (this is an analog of Anderson localization). The localized electron forms a polaron. The electron mobility is effected by jumps from one localized state to another, with the formation of a polaron in each localized state. This picture of the electron motion on a helium film was proposed by Jackson,[108] who found that the diffusion coefficient resulting from electron tunneling between localized states with a strong electron–ripplon interaction taken into account is given by

$$D = v_T^2 \tau \exp\left[-\frac{1}{4} k_c \frac{eE_\perp^*}{\pi \sqrt{2\alpha\nu}} \right], \tag{48}$$

where v_T is the thermal velocity of the electron, τ is the relaxation time, and ν is the density of states. The value of k_c is taken from Eqs. (42) and (43). Since $k_c \sim (d_0'/d)^2$, for $E_\perp > E_d$ one has $E_\perp^* = E_\perp$, and, accordingly, $\mu \sim \exp[-(d_0'/d)^2]$. In the opposite limiting case $E_\perp < E_d$, which is ordinarily realized in experiments, one has $\mu \sim \exp[-(d_0'/d)^4]$, in contradiction with the experimental results. In spite of the fact that the above expression was obtained for the condition $E_\perp < E_d$, one can assume that it remains approximately correct in a wider range of relationships between $E_\perp$ and E_d. It is not ruled out that the viscosity plays some role in the motion of electrons on a liquid helium film, as was noted in Ref. 92.

Wyder and co-workers[109] measured the mobility of electrons on a helium film covering a quartz substrate ($\varepsilon_d = 4.3$) in the region of film thicknesses 300–700 Å at a temperature of 1.3 K in magnetic fields up to 10 T at frequencies of 3–6 kHz. The characteristic height of the substrate roughness was less than 150 Å. The data obtained were explained by the authors in terms of the formation of stable electron polarons under the influence of the uniform external pressing electric field, which reached values of 8500 V/cm, and the field of the substrate. For thin films the polaron formation energy W was greater than $k_B T$, and the values obtained for the mobility agreed well with the theoretical predictions.[33] It was also shown that in a strong magnetic field the data on the longitudinal conductance can be explained in terms of an effective collision frequency of the magnetopolaronic dimple with helium atoms in the vapor.

A feature of the results is that no transition to free-electron mobility is observed for thick films, in spite of the fact that the value $W = 0.5$ K becomes less than the temperature of the experiment, and the polaron should not be stable.

Thus the experimental results on the electron mobility on helium films covering substrates that are not very smooth can be described in terms of polaron effects arising either as a result of a strong effective pressing electric field, as was proposed by the authors of Ref. 109, or as a result of substrate roughness, giving rise to a random potential in which electrons are localized with the subsequent formation of polaron states.

Coimbra, Sokolov, Rino, and Studart[110] calculated the mobility of electrons on a helium film with allowance for the scattering of electrons by substrate roughness and showed that under reasonable assumptions as to the average height of the asperities and the distance between them, the experimental data could be reconciled with the theoretical calculations in the case of thick films ($d > 350$ Å). For thinner films, however, the experimental values of the mobility are lower than the theoretical values by a factor of two to three. This may be evidence of electron localization in a random potential due to substrate roughness. Apparently this effect, as had been conjectured previously, is predominantly responsible for the character of the transport of carriers on thin films.

However, at present one cannot say with certainty that the polaron states predicted in Refs. 86 and 87 are in fact the peculiar zero-dimensional electronic formations on liquid helium which have been registered quite reliably in experiments. For reliable observation of polaron effects due to the presence of a uniform pressing electric field and the field of the substrate it will be necessary to investigate thin helium films on atomically smooth surfaces at ultralow temperatures.

The formation of polarons on the surface of liquid helium can also be detected from the resonance absorption of a microwave field in the transition of electrons localized in polarons from the ground energy level to excited levels. Lehndorff and Dransfeld[111] observed a peak in the absorption by electrons on thin helium films on a Mylar substrate at a temperature of 1.12 K and an electron density of 7×10^{10} cm^{-2}, which they interpreted as a transition to the first excited state of the polaron. However, it has been noted (p. 281 of Ref. 4) that at the given temperature and electron density it is possible for an electron crystal to form, and the absorption peak could thus be due to one of the modes of plasma oscillations of the crystal. The characteristics of polarons in one-dimensional and quasi-one-dimensional electron systems on liquid helium were examined in Ref. 112.

4.2. Bound states of an electron with a positive ion: diplons

As was shown by Monarkha and Kovdrya,[113] when a positive ion with charge q, which is coupled to the substrate, is present in the helium film, it can form peculiar bound states with an electron localized above it on the surface of the liquid helium (Fig. 28). Such a complex is called a diplon. The positive ion is attracted toward the solid sub-

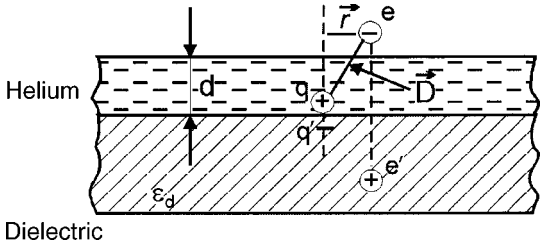

FIG. 28. Structure of a dipole complex (diplon).[113]

strate by image forces, and an image charge of negative sign, $e'=e(\varepsilon_d-\varepsilon)/(\varepsilon_d+\varepsilon)$, arises in the substrate. The total charge of the ion and its image is $Q=2|e|\varepsilon/(\varepsilon_d+\varepsilon)$. The potential energy of interaction of an electron on the liquid helium surface with the ion has the form

$$U=-\frac{Q|e|}{\varepsilon D}+\frac{Q|e'|}{\varepsilon_d D}=-\frac{2e^2(\varepsilon_d^2+\varepsilon^2)\varepsilon}{(\varepsilon_d+\varepsilon)^2\varepsilon_d\sqrt{(d+z)^2+r^2}}, \tag{49}$$

where $-Qe/\varepsilon D$ is the total interaction energy between the electron and the charge Q, $Qe'/\varepsilon_d D$ is the interaction energy of the charge Q with the image charge of the electron, D is the distance between the ion and the charges e and e', d is the thickness of the helium film, z is the distance between the electron and the surface of the liquid, and r is the deviation of the electron position from that corresponding to the minimum distance from the ion. Assuming that the displacements of the electron from the equilibrium position are small and expanding (49) in the parameters $r/(d+z)$ and z/d, we obtain

$$U\simeq-\frac{2e^2(\varepsilon_d^2+\varepsilon^2)\varepsilon}{(\varepsilon_d+\varepsilon)^2\varepsilon_d d}+eE_i z+\frac{1}{2}m\omega_d^2 r^2, \tag{50}$$

$$E_i=\frac{2|e|(\varepsilon_d^2+\varepsilon^2)\varepsilon}{(\varepsilon_d+\varepsilon)^2\varepsilon_d d^2},\quad \omega_d^2=\frac{2e^2(\varepsilon_d^2+\varepsilon^2)\varepsilon}{(\varepsilon_d+\varepsilon)^2\varepsilon_d m d^3}. \tag{51}$$

The spectrum and wave functions of an electron in the plane of the helium vapor–liquid interface are of an oscillatory nature with a characteristic frequency ω_d and a localization radius $L=(\hbar/m\omega_d)^{1/2}$. The distance between levels for a glass substrate ($\varepsilon_d=6$) and $d=300$ Å is ~ 13 K, and the corresponding localization length $L\approx 80$ Å. It was shown in Ref. 113 that for helium film thicknesses larger than 70 Å the diplons are stable formations both with respect to the penetration of electrons into the liquid phase under the influence of the electric field and also against small oscillations of the liquid surface. Estimates show that for a helium film 300 Å thick on a glass substrate the surface of the liquid is stable up to electron densities of $\sim 10^{10}$ cm^{-2}.

As we have said, a localized electron creates a local pressure on the liquid helium surface, and that can cause a dimple to form. A consistent treatment of the characteristics of diplons in such a case was given by Farias and Peeters,[114] who solved the Schrödinger equation for the electron jointly with the equation of mechanical equilibrium for the liquid surface with allowance for the influence of the external pressing electric field and an external magnetic field. They calculated the energies of the ground and first excited state of the electron in a diplon for various thicknesses of the helium film (Fig. 29) and also found the profile of the liquid surface over the positive ion (Fig. 30). For $d=300$ Å the binding energy was quite large, 170 K, and the maximum deflection of the liquid was ~ 2.5 Å. A magnetic field splits the level of the first excited state into two sublevels. At low fields B the distance ΔE between the ground and first excited level increases linearly with increasing B, while at high magnetic fields $\Delta E\sim B^2$.

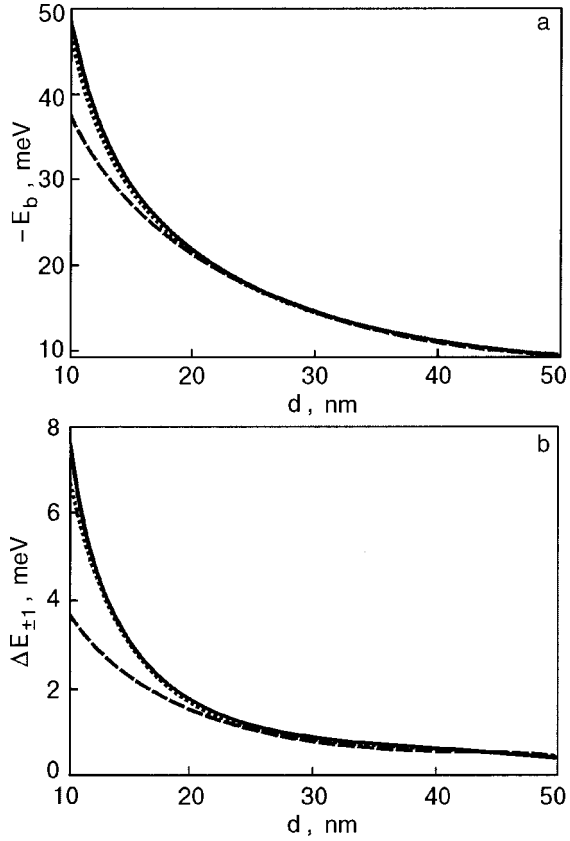

FIG. 29. Binding energy of an electron in a diplon (a) and the energy of the transition $1\rightarrow 2$ (b) as a function of the thickness of the helium film.[114] The dashed curve was calculated on the assumption of a smooth liquid surface, the dotted curve was calculated with the deformation of the surface taken into account as a perturbation, and the solid curve is an exact calculation.

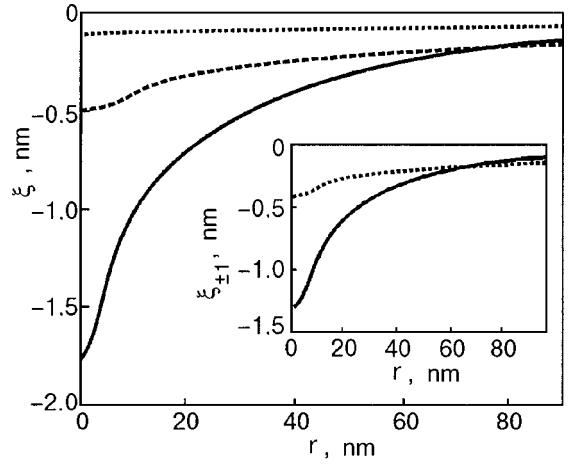

FIG. 30. Deformation of the liquid helium surface as a function of distance for an electron in the ground and excited (inset) states for different values of d [Å]: 100 (solid curve), 200 (dashed curve), 500 (dotted curve).[114]

An interesting question concerns the collective properties of such zero-dimensional systems as diplons, since a study of these properties will yield information about the characteristics of the diplons themselves. A positive ion in liquid helium presents as a sphere of solidified helium of radius 6 Å. The experiments of Maraviglia[115] have shown that ions in a helium film are mobile particles, with a mobility of $2.8\ \mathrm{cm}^2/(\mathrm{V}\cdot\mathrm{s})$ at $T=0.9$ K. Thus the ions localized near the substrate in a film will apparently form a rather uniform layer of charge. Monarkha[116] and also de Freitas, Rino, and Studart[117] considered the collective modes of a diplon liquid on the assumption that the positive ions are mobile particles. They showed that the plasma oscillations in such a system are of an acoustical character and are analogous to plasmons on a thin film covering a metallic surface:

$$\omega(k)=\left(\frac{4\pi n_i e^2 d}{M^*}\right)^{1/2} k, \tag{52}$$

where n_i is the density of diplons. We note that, according to Ref. 114, the effective mass of an electron, on account of the dimple it forms, can be very large, and the mass of a positive ion in helium is also quite large ($\sim 40M_4$).[118] Thus the total effective mass of a diplon will also be large and, hence, the frequency $\omega(k)$ will be small. The high-frequency electronic mode of a layer of diplons was calculated in Ref. 116, and it was noted that this mode has a threshold frequency ω_d.

Since the ions in a helium film on a solid substrate are relatively mobile, they can form an ion crystal. In that case a diplon crystal will form when the helium film is charged with electrons to a density $n=n_i$. The properties of the collective modes of a diplon crystal were studied in Ref. 116. It was shown that at a low frequency $\omega<\omega_r(G_1)$, where ($\omega_r(G_1)$ is the frequency of ripplons with a wave vector corresponding to a reciprocal lattice vector), a diplon crystal has two acoustic modes, longitudinal (l) and transverse (t), with velocities

$$c_{l,t}=b_{l,t}\left(\frac{\lambda e^2 d^2}{M^* a^3}\right)^{1/3}, \tag{53}$$

where $b_l=4.25$ and $b_t=1.43$; a is the distance between diplons. At a high frequency $\omega>\omega_r(G_1)$ the plasma oscillations acquire a threshold frequency

$$\omega_{l,t}^2=\tilde{\omega}_0^2+\omega_{l,t}^2,\quad \tilde{\omega}_0^2=\sum C_g\omega_r^2\ll\omega_d, \tag{54}$$

where C_g is the electron–ripplon coupling constant.

We note that the plasma modes obtained on the assumption that the positive ions are mobile should apparently be strongly damped by virtue of the low mobility of the ions.

The possibility of diplon formation in phase-separated ^{3}He–^{4}He solutions was analyzed by Monarkha.[119]

A system of diplons can be particularly interesting in the case $n<n_i$. Then the electrons can move from one positive ion to another, and, depending on the height and width of the barrier that an electron must overcome, its motion can be classical or quantum. If the ions form a crystal lattice, band motion of the electrons can arise. Dahm[120] considered the possibility that a Mott transition can occur as the overlap of the electron wave functions changes in response to variation of the thickness of the helium film.

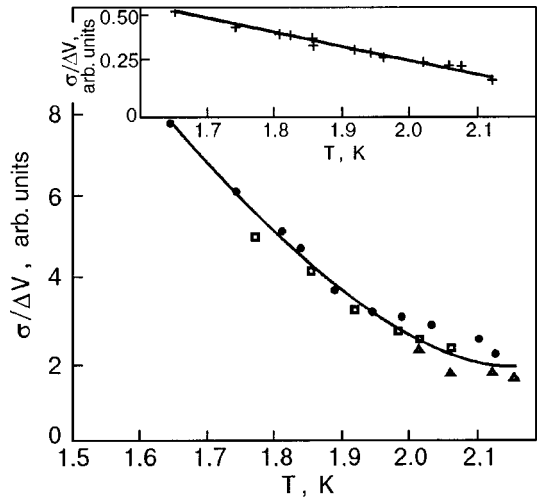

FIG. 31. Temperature dependence of the conductivity of an electron layer on a film of liquid helium, divided by the difference between the potentials V_1 at which the film was charged and V_2 at which the electrons were precipitated out onto the dielectric substrate:[34] $V_1=30$ V, $V_2=0$ (●); $V_1=150$ V, $V_2=75$ V (△); $V_1=200$ V, $V_2=150$ V (□). The inset shows the results for the case when the substrate was charged with positive ions at $V_1=-200$ V; the points (+) were obtained for $V_2=-25$ V.

The first experiments on the detection of diplons were done in Ref. 34 by measuring the microwave conductivity of electrons on a layer of positive ions coupled to a substrate covered with liquid helium. A film-coated substrate placed in a microwave cavity was charged with positive ions to a density $n_i=10^{10}\ \mathrm{cm}^{-2}$, and then an electronic charge was deposited on the liquid helium surface to an electron density $n=n_i$. Figure 31 shows the temperature dependence of $\sigma/\Delta V$ (σ is the conductivity of the electron layer, V is the pressing potential at which the film was charged with electrons) in the cases when the substrate did not contain ions and when it was charged with positive ions (inset). It is seen that if the substrate is charged with ions, the value of $\sigma/\Delta V$ is much less than the analogous value obtained in the absence of charge. Figure 32 shows how the effective mobility σ_{eff} of the electron layer in the case when the substrate was charged with positive ions depends on the thickness d of the helium film for an equal density of electrons and ions. At

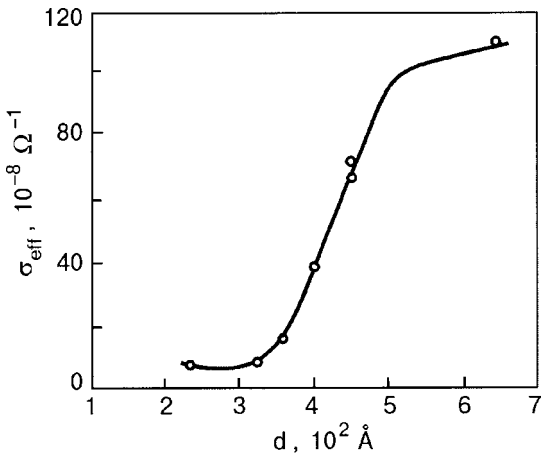

FIG. 32. Effective conductivity of an electron layer on a helium film as a function of the film thickness in the presence of positive ions on the substrate; $n=1.1\times10^{10}\ \mathrm{cm}^{-2}$ (Ref. 34).

first σ_{eff} varies weakly with increasing d, but, starting at $d \approx 400$ Å, it increases sharply, growing by more than an order of magnitude for $d \approx 500$ Å.

Thus the behavior of electrons on a helium film in the presence of positive ions on the substrate differs substantially from their behavior in the absence of positive charge. The effective mobility μ_{eff} of the electrons in the presence of positive ions on the substrate is $0.07\ \text{m}^2/(\text{V}\cdot\text{s})$ at 1.7 K, which is much less than the electron mobility in the absence of positive charge on the substrate. The temperature dependence is also noticeably different in the two cases. While for electrons over a substrate not containing positive charge the value of $\sigma/\Delta V$ is approximately inversely proportional to the density of helium atoms in the vapor, for electrons on a film in the case when positive ions are present on the substrate $\sigma/\Delta V$ is inversely proportional to the density of rotons. These results can be explained by the formation of dimples, with a large effective mass, beneath the electrons. According to estimates,[114] the effective mass of the dimples can reach values $M^* = (10^7 - 10^8)m$ (m is the electron mass). In this case, together with the optical mode characterized by the frequency ω_d from (51), there arises another optical mode with a lower threshold frequency

$$\tilde{\omega}_d \cong \omega_d \left(\frac{m}{M^*} \right)^{1/2}. \tag{55}$$

For a helium film of thickness $d = 300$ Å the frequency $\tilde{\omega}_d = 10^8 - 10^9\ \text{s}^{-1}$. At the frequency $\omega > \tilde{\omega}_d$ used in Ref. 114, the electrons will move together with the dimple under the influence of the microwave field. If the dimple is rather deep, as in the case of diplons, the dissipative losses will be determined by its interaction with thermal excitations of the bulk helium—rotons. With increasing thickness of the helium film the coupling of the electrons with the ions is weakened, and, accordingly, the high-frequency mobility increases. The experiments described are of a preliminary nature, and further study is required.

Lehndorff and co-authors[121] observed a narrow absorption peak at 9 GHz for electrons on a helium film in the presence of positive ions on the substrate, while in the absence of positive charge the absorption peak did not appear. The authors attributed the presence of the additional absorption peak to the formation of diplons in the helium film. It it possible that what was observed in Ref. 121 is a transition due to the presence of a threshold frequency $\tilde{\omega}_d$ in the plasma oscillations of electron–dimple complexes.

4.3. Electrons localized over nanostructures

An interesting example of a zero-dimensional electron system on liquid helium is a system of electrons localized over nanostructures. Such nanostructures might be either small helium clusters or thin layers of liquid helium covering a specially profiled substrate. Experiments in this area are now only beginning, but it is nevertheless appropriate to note the main trends and observations for this research.

Electronic states near a dielectric particle of spherical shape were first considered by Khaĭkin (for solid hydrogen).[122] It was found that stationary electronic levels exist which arise as a result of the attraction of a particle polarized by the field of the electron and the presence of a potential barrier preventing penetration of the electron into the medium. The spectrum of electronic surface levels on a spherical particle of solid hydrogen was found for particles of different radii, and it was shown that the frequency spectrum of the energy levels for particles of radius 1–10 μm extends from optical frequencies to 10^{11}–10^{12} Hz. It was conjectured that cosmic radiation from dust clouds might be due to the presence of such surface states on particles of solid hydrogen.

The analogous problem for helium clusters was considered by Rama Krishna and Whaley.[123] They solved the Schrödinger equation for clusters with a specified number of helium atoms and calculated the binding energy and also the position of the excited levels of an excess electron on the helium surface. It was shown that a liquid spherical cluster is stable against deformation. It was established as a result of the calculations that the binding energy of an electron with a helium cluster decreases with decreasing radius of the cluster. For example, for a cluster of radius 180 Å the binding energy is equal to 0.04–0.06 K, which is more than an order of magnitude smaller than the binding energy of an electron with bulk helium. The average distance of the electron from the liquid helium surface in such a cluster is $\langle z \rangle_1 = 200$ Å, as compared to 75 Å for bulk helium. As yet there have been no experimental studies of electronic states on helium clusters, although they are of interest, since they would allow one to determine various characteristics of the clusters, such as their size and temperature.

One of the ways of obtaining zero-dimensional electron systems on the surface of liquid helium, as in the case of one-dimensional and quasi-one-dimensional electron systems, is to use a specially profiled dielectric substrate covered by a thin layer of liquid helium. The profiled substrate has a system of identical recesses. If the liquid helium covering such a substrate is found at a certain height above the liquid level, it forms a system of dimples on the surface of the liquid. In the presence of a pressing electric field an electron can be localized in such a dimple. The characteristic frequency of oscillations of the electron and the localization length are determined by the same relations as for a one-dimensional system (see Sec. 2.1).

This way of realizing a quasi-zero-dimensional system was used by Sommerfeld and van der Heijden[124] and Valkering, Yayama, and van der Heijden.[125] The substrate used in Ref. 125 is shown schematically in Fig. 33. It contains a periodic array of prominances with a distance between them of 5 μm. The distance from the top of the prominances to the bottom of the recesses is 0.48 μm, and the distance from the saddle points to the bottom of the recesses is 0.4 μm. The substrate is positioned at a height of 5–8 mm above the helium level, and the deflection of the liquid $\Delta h = 0.06$ μm. The distance between energy levels in such a dimple at the pressing field $E_\perp = 500$ V/cm used in that study is ~ 0.1 K. The potential barrier for the transition of an electron from one dimple to the next is $U = eE\Delta h = 20$–40 K (in the limit of a low electron density). Obviously the electron–electron interaction will decrease U. By measuring the magnetoconductivity of the electrons in such a system, the authors established that the electron mobility is $0.26\ \text{m}^2/(\text{V}\cdot\text{s})$, approximately an order of magnitude lower than for

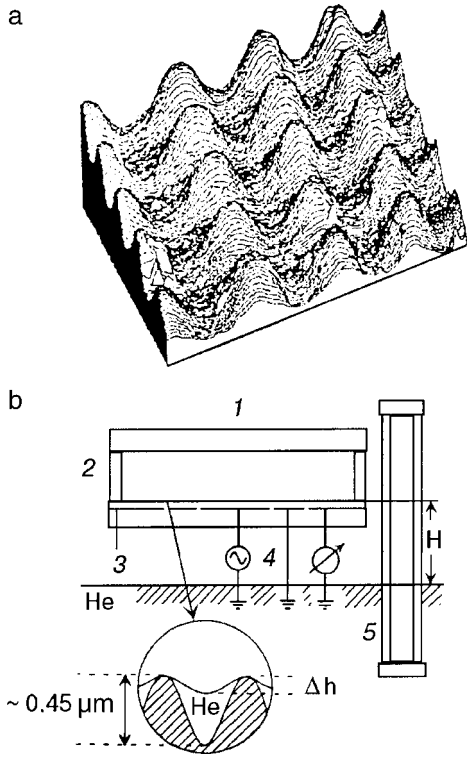

FIG. 33. Profiled dielectric substrate (a) and the experimental cell (b) for realizing a quasi-zero-dimensional electron system on liquid helium:[125] *1*—upper electrode, *2*—guard ring, *3*—profiled substrate and glass slab, *4*—electrodes, *5*—helium level gauge.

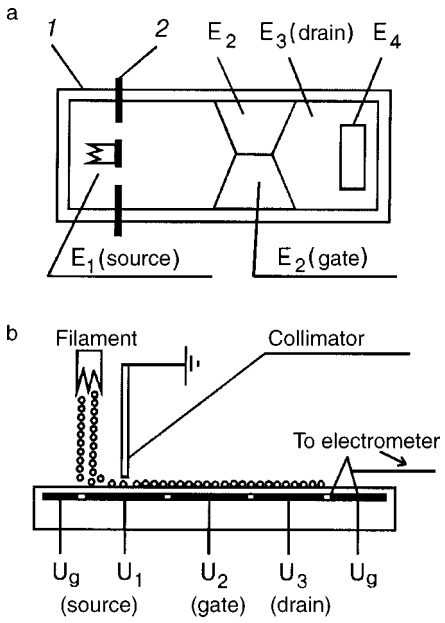

FIG. 34. A dc field-effect transistor utilizing surface electrons.[127] a: E_1 is the source electrode, E_2 is the gate, and E_3 and E_4 are drain electrodes; *1*—guard electrode; *2*—collimator. b—Side view of the device.

bulk helium. In spite of the fact that in the experiment $T > \Delta E/k_B$ and the system is not purely zero-dimensional, that study nevertheless demonstrated for the first time the possibility that zero-dimensional systems on liquid helium can be realized in such a way.

A similar system was realized by Leiderer and co-workers.[126] The substrate differed from that used in Ref. 125 only in that the distance between prominances was 0.6 μm and the average depth of the recesses of the substrate was 0.1 μm. Experiments were done for $H=1$ cm in the temperature range 0.2–1.4 K. It was found that below a certain temperature T_c the conductivity of the electrons decreases sharply, an effect which was attributed to localization of the electrons in the dimples formed on the liquid helium surface.

5. MICROELECTRONICS AND BITS FOR QUANTUM COMPUTERS WITH THE USE OF SURFACE ELECTRONS

A study of the properties of low-dimensional electron systems on liquid helium is not of only fundamental interest. In recently published studies, ideas for using surface electrons for practical applications have been proposed or implemented, viz., for the creation of microelectronic devices and bits for quantum computers.

Klier, Doicescu, and Leiderer[127] first made dc measurements in a quasi-two-dimensional electron system on a ^{4}He film covering a structured metallic surface. The device they created is an analog of a field-effect transistor utilizing surface electrons. The device is shown schematically in Fig. 34. It contains source and drain electrodes (E_1 and E_3, respectively) and a gate E_2, which is a narrow quasi-two-dimensional or one-dimensional channel 1 mm in length. A continuously heated tungsten filament emits electrons which pass through a collimator and enter a drift space. The electrons move from the source electrode E_1 to the drain E_3 through an electrode E_2 on which suitably chosen potentials are imposed so that it acts as a gate. The electrode E_4 is used for measuring the current that has passed through the device. The device is 10 mm long and 4 mm wide.

The current–voltage characteristics of the device were studied, and it was shown that such a device can be used to obtain and investigate a one-dimensional electron system—quantum wires, which are realized when the thermal de Broglie wavelength of the electron exceeds the width of the channel).

An analogous ac device created by Lea and co-workers[46] was considered in Sec. 4.3. The length of the device is 1 mm, and the length and width of a channel are 29 μm. This device was used to study the features of crystallization in a quasi-one-dimensional system on liquid helium.

The possibility of creating analog quantum computers and their working principles are widely discussed at present. Quantum computers can solve complex mathematical problems that cannot be solved on ordinary digital computers. A quantum computer contains N_q interacting quantum bits (qubits). Each qubit is a quantum system containing at least two levels, which, as for a classical bit, are assigned two values, $|0\rangle$ and $|1\rangle$. However, unlike classical bits, qubits can be found in a state corresponding to a linear superposition of the ground level and an excited level. This sharply increases the storage volume and the speed of quantum computers.

There is now an active search for systems that can be used in quantum computers. Systems that have been proposed for use as qubits include atoms in traps, electrodynamic cavities working in a quantum regime, nuclear spins of atoms, nuclei in complex molecules, electrons in potential wells, and Josephson structures (see Ref. 128). Among the

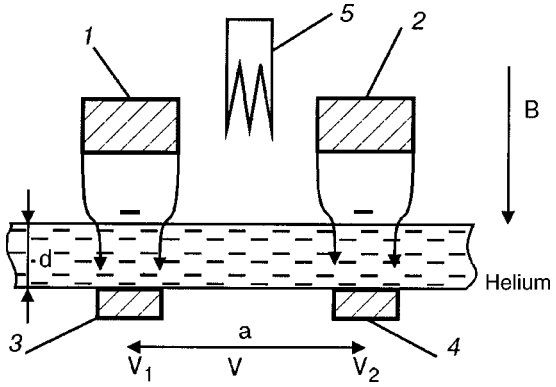

FIG. 35. Quantum bits (qubits) using surface electrons:[129] *1,2*—upper electrodes, *3,4*—lower electrodes, *5*—heating filament. V_1 and V_2 are the potentials on the electrodes. The arrow indicates the magnetic field direction.

quantum systems that could be used to construct quantum computers, a system of surface electrons on liquid helium is apparently one of the most promising. The idea of making quantum computers using surface electrons was proposed by Platzman and Dykman.[129] At sufficiently low temperatures ($T<0.1$ K) the vapor pressure over liquid helium is vanishingly small, and electrons localized on the surface of liquid helium are coupled to their surroundings only via ripplons. For $T=10$ mK the number of thermal ripplons is small, and the rms displacement of the surface of liquid helium is $\delta_T \approx (k_B T/\alpha)^{1/2}=2\times 10^{-9}$ cm.

For an electron found on the ground energy level, there exists a weak coupling with ripplons, limiting the mobility of the particles, which can reach values of 10^4 m^2/(V·s).[28] The interaction of an electron with ripplons having a characteristic wave vector $k=r_B^{-1}$ is determined by the relaxation time of an electron from the excited energy level to the ground level, which can be written as

$$T_1=\frac{\hbar}{R}\left(\frac{r_B}{\delta_T}\right)^2, \quad R=\frac{\Lambda^2 m}{2\hbar^2}. \tag{56}$$

Estimates show that $T_1\approx 10^{-5}$ s. Hence it follows that the two lowest electronic levels can be used for realization of a qubit. The state of the qubit can be changed using microwave radiation to transfer the electron from the ground to the excited level.

Figure 35 shows a schematic illustration of two coupled qubits based on surface electrons on liquid helium. The lower electrode, lying under a helium layer of thickness $d=0.5$ μm, is a system of metallic slabs at a positive potential (only two electrodes are shown in the figure). The size of the slabs and the distance between them are of the order of d. The upper electrode is also a set of analogous slabs placed opposite the lower slabs. One electron is localized on each slab on the liquid surface.

Unfortunately the lifetime according to Eq. (56) is short, and it would be desirable to increase it for more reliable operation of the quantum computer. This can be achieved by applying a magnetic field perpendicular to the liquid surface, which localizes an electron to the magnetic length $\lambda_H=(\hbar c/eB)^{1/2}$ (c is the speed of light). In a magnetic field the energy spectrum of the electrons acquires a discrete character, with a distance between levels of $\hbar\omega_c$. At sufficiently high magnetic fields the one-ripplon processes are suppressed, and the time T_2 for transition of the electrons from the excited to the ground level will be determined by two-ripplon processes, which are much less efficient:

$$T_2=\frac{\omega_{zB}^2\omega_l}{R^4}\left(\frac{r_B}{\delta_T}\right)^4\left(\frac{\lambda_H}{r_B}\right)^8, \quad \omega_{zB}=\frac{2\pi e^2}{d^3 m\omega_c}, \tag{57}$$

where ω_l is the frequency of the ripplon that is excited, with a wave vector $k_l\approx\lambda_H^{-1}$.

Estimates show that for $T=10$ mK this time has a value $T_2=10^{-4}$ s.

An important feature of qubits using electrons is the dipole–dipole interaction of two electrons localized over adjacent electrodes. It can be written as

$$V_{dd}\simeq\frac{e^2}{d^3}\langle z\rangle_1\langle z\rangle_2, \tag{58}$$

where $\langle z\rangle_1$ and $\langle z\rangle_2$ are the distances from the liquid surface for electrons in the ground and excited states, respectively. This interaction shifts the position of the electron levels by an amount that for $d=0.5$ μm is approximately equal to 10^{-2} K, and it leads to a coherent transfer of energy from one electron to another.

The qubits under discussion work as follows. By irradiating the electrons with a microwave field of a given frequency, one can, by choosing the pressing potentials V_1 and V_2 on the electrodes, transfer an electron in one of the qubits (e.g., the first) from the ground to the excited level. Then the value of V_2 is varied so that two levels pass through resonance. If the duration of this variation is suitably chosen, a superposition of the ground and excited states will arise for the second electron.

To determine the state of the wave function at time t after completion of the computations, it is proposed in Ref. 129 that the sign of the potentials V_1 and V_2 be changed to the opposite, so that the electrons localized near the surface of the liquid can tunnel to the vacuum and pass to the upper electrode, where they are registered. The values of the potentials V_1 and V_2 are chosen such that the lifetime of an electron on the excited level is short and the lifetime of an electron on the ground energy level is long. This allows one to obtain information about which state each qubit is found in at the end of the computations.

Surface electrons on liquid helium are an extremely promising system for implementing large analog quantum computers. The density of qubits in such a system can reach $N_q=10^8$ cm^{-2}. These qubits are easily controlled, it is comparatively easy to read out information from them, and they have an acceptable time for destruction of the coherent state.

We note that the diplons considered in Sec. 4.2 can be used as qubits. A system of such qubits will look like that shown in Fig. 35 except that the role of the lower electrodes will be played by the positive ions placed on the substrate surface. These qubits can be tuned by varying to voltage on the upper electrodes. The spectrum of an electron in a diplon, just as in the case of an electron in a magnetic field, is oscillatory, and an electron is localized around the atom within a localization length L, which in this case is analogous to the magnetic length. It can be assumed that one-ripplon pro-

cesses will also be suppressed in a diplon qubit, and that will increase the lifetime of an electron at the excited level.

The lifetimes $T_{1,2}$ of electrons at the excited level are related to the linewidth $\Delta\omega$ of the transition from level to level. The value of $\Delta\omega$ in the temperature range 1.3–2 K was measured by Grimes, Brown, Burns, and Zipfel.[6] It was shown that $\Delta\omega$ is determined by the interaction of the electrons with helium atoms in the vapor and at 1.3 K has a value of 10 GHz, which corresponds to $T_g = 10^{-10}$ s. Ando[130] calculated the values of $\Delta\omega$ both in the region of interaction of electrons with helium atoms in the vapor and in the ripplon region ($T < 0.8$ K). It was found that for $T < 0.7$ K the value of T_1 decreases as the pressing electric field $E_\perp$ is increased, and for $T = 0.5$ K it has a value of $10^{-7}-10^{-8}$ s for pressing fields in the range $E_\perp = 0-300$ V/cm.

The linewidth of the optical transitions in the ripplon scattering region was measured by Volodin and Édel'man,[131] who showed that, starting at $T = 0.6$ K, the linewidth of the transition $1 \rightarrow 2$ is independent of temperature and has a value of ~ 30 MHz, which is approximately 5.5 times larger than the theoretical values obtained for this linewidth with one-ripplon electron scattering processes taken into account. This difference was explained as being due to the possible influence of edge effects in the experimental cell, which lead to nonuniformity of the pressing electric field. Lea and co-workers[132] made measurements of $\Delta\omega$ up to temperatures of ~ 0.1 K and showed that the experimental results are in satisfactory agreement with the calculation of Ref. 130.

The author thanks V. N. Grigor'ev, Yu. P. Monarkha, and S. S. Sokolov for reading the manuscript and offering helpful suggestions.

*E-mail: kovdrya@ilt.kharkov.ua

[1]M. Cole and M. H. Cohen, Phys. Rev. Lett. **23**, 1238 (1969).
[2]V. B. Shikin, Zh. Éksp. Teor. Fiz. **58**, 748 1970 [Sov. Phys. JETP **31**, 936 (1970)].
[3]V. B. Shikin and Yu. P. Monarkha, *Two-Dimensional Charged Systems* [in Russian], Nauka, Moscow (1989).
[4]E. Andrei (ed.), *Two-Dimensional Electron Systems*, Kluwer, Dordrecht (1997).
[5]M. A. Woolf and G. W. Rayfield, Phys. Rev. Lett. **15**, 235 (1965).
[6]C. C. Grimes, T. R. Brown, M. L. Burns, and C. L. Zipfel, Phys. Rev. **13**, 140 (1976).
[7]A. M. Troyanovskiĭ, A. P. Volodin, and M. S. Khaĭkin, JETP Lett. **29**, 59 (1979).
[8]A. M. Troyanovskiĭ, A. P. Volodin, and M. S. Khaĭkin, JETP Lett. **29**, 382 (1979).
[9]V. B. Shikin, Yu. Z. Kovdrya, and A. S. Rybalko, Fizika Kondensirovannogo Sostoyaniya (FTINT, Kharkov), Vol. XV (1971), p. 99.
[10]W. T. Sommer and D. J. Tanner, Phys. Rev. Lett. **27**, 1345 (1971).
[11]C. C. Grimes and T. R. Brown, Phys. Rev. Lett. **32**, 280 (1974).
[12]D. K. Lambert and P. L. Richards, Phys. Rev. B **23**, 328 (1981).
[13]A. P. Volodin and V. S. Édel'man, JETP Lett. **30**, 633 (1979).
[14]A. S. Rybalko, Yu. Z. Kovdrya, and B. N. Esel'son, JETP Lett. **22**, 280 (1975).
[15]C. C. Grimes and G. Adams, Phys. Rev. Lett. **36**, 145 (1976).
[16]M. C. van der Sanden, R. W. van der Heijden, A. T. de Waele, and H. M. Gijsman, Jpn. J. Appl. Phys. **26**, 749 (1987).
[17]A. O. Stone, P. Fozooni, M. J. Lea, and M. Abdul-Gader, J. Phys.: Condens. Matter **1**, 2743 (1989).
[18]Yu. Z. Kovdrya, V. A. Nikolaenko, O. I. Kirichek, S. S. Sokolov, and V. N. Grigor'ev, J. Low Temp. Phys. **91**, 371 (1993).
[19]Yu. P. Monarkha, Shin-Ichiro Ito, K. Shirihama, and K. Kono, Phys. Rev. Lett. **78**, 2445 (1997).
[20]D. B. Mast, A. J. Dahm, and A. L. Fetter, Phys. Rev. Lett. **54**, 1706 (1985).
[21]D. C. Glattli, E. Y. Andrei, G. Deville, I. Poitrenaud, and F. I. B. Williams, Phys. Rev. Lett. **54**, 1710 (1985).
[22]S. S. Nazin and V. B. Shikin, Zh. Éksp. Teor. Fiz. **94**, 133 1988 [Sov. Phys. JETP **67**, 288 (1988)].
[23]O. I. Kirichek, P. K. H. Sommerfeld, Yu. P. Monarkha, P. J. H. Peters, Yu. Z. Kovdrya, P. P. Steijaert, R. W. van der Heijden, and A. T. A. M. de Waele, Phys. Rev. Lett. **74**, 1190 (1995).
[24]E. P. Wigner, Phys. Rev. **46**, 1002 (1934).
[25]C. C. Grimes and G. Adams, Phys. Rev. Lett. **42**, 795 (1979).
[26]A. S. Rybalko, B. N. Esel'son, and Yu. Z. Kovdrya, Fiz. Nizk. Temp. **5**, 947 (1979) [Sov. J. Low Temp. Phys. **5**, 450 (1979)].
[27]R. Mehrotra, C. J. Guo, V. Z. Ruan, D. B. Mast, and A. J. Dahm, Phys. Rev. B **29**, 5239 (1984).
[28]K. Shirihama, S. Ito, H. Suto, and K. Kono, J. Low Temp. Phys. **101**, 439 (1995); K. Shirihama, K. Kirichek, and K. Kono, Phys. Rev. Lett. **79**, 4218 (1997).
[29]V. B. Shikin and Yu. P. Monarkha, Fiz. Nizk. Temp. **1**, 957 (1975) [Sov. J. Low Temp. Phys. **1**, 459 (1975)].
[30]A. M. Gabovich, L. G. Il'chenko, and É. A. Pashitskiĭ, Zh. Éksp. Teor. Fiz. **81**, 2063 (1981) [Sov. Phys. JETP **54**, 1089 (1981)].
[31]A. S. Rybalko and Yu. Z. Kovdrya, Fiz. Nizk. Temp. **1**, 1037 (1975) [Sov. J. Low Temp. Phys. **1**, 498 (1975)].
[32]A. P. Volodin, M. S. Khaĭkin, and V. S. Édel'man, JETP Lett. **23**, 478 (1976).
[33]Yu. P. Monarkha, Fiz. Nizk. Temp. **1**, 526 (1975) [Sov. J. Low Temp. Phys. **1**, 258 (1975)].
[34]V. I. Karamushko, Yu. Z. Kovdrya, F. F. Mende, and V. A. Nikolaenko, Fiz. Nizk. Temp. **8**, 219 (1982) [Sov. J. Low Temp. Phys. **8**, 109 (1982)]; Yu. Z. Kovdrya, F. F. Mende, and V. A. Nikolaenko, Fiz. Nizk. Temp. **10**, 1129 (1984) [Sov. J. Low Temp. Phys. **10**, 589 (1984)].
[35]E. Y. Andrei, Phys. Rev. Lett. **52**, 1449 (1984).
[36]H. W. Jiang and H. J. Dahm, Jpn. J. Appl. Phys. **26**, 745 (1987).
[37]Vl. Ginzburg and Yu. P. Monarkha, Fiz. Nizk. Temp. **4**, 1236 (1978) [Sov. J. Low Temp. Phys. **4**, 580 (1978)].
[38]A. V. Chaplik, JETP Lett. **31**, 252 (1980).
[39]Yu. Z. Kovdrya and Yu. P. Monarkha, Fiz. Nizk. Temp. **12**, 1011 (1986) [Sov. J. Low Temp. Phys. **12**, 571 (1986)].
[40]S. S. Sokolov and N. Studart, Phys. Rev. B **51**, 2640 (1995).
[41]D. Marty, J. Phys. C: Solid State Phys. **19**, 6097 (1986).
[42]Yu. Z. Kovdrya and V. A. Nikolaenko, Fiz. Nizk. Temp. **18**, 1278 (1992) [Sov. J. Low Temp. Phys. **18**, 894 (1992)].
[43]Kh. Yayama and A. Tomokiyo, unpublished (1993); H. Yayama and A. Tomokiyo, Czech. J. Phys. **46**, Suppl. S1 353 (1996).
[44]O. I. Kirichek, Yu. P. Monarkha, Yu. Z. Kovdrya, and V. N. Grigor'ev, Fiz. Nizk. Temp. **19**, 458 (1993) [Low Temp. Phys. **19**, 323 (1993)].
[45]A. M. C. Valkering, P. K. H. Sommerfeld, P. J. Richardson, R. W. van der Heijden, and A. T. A. M. de Waele, Czech. J. Phys. **46**, Suppl. S1 321 (1996).
[46]P. Glasson, S. Efurt, G. Ensell, V. Dotsenko, W. Bailey, P. Fozooni, A. Kristensen, and M. J. Lea, Physica B **284**, 1916 (2000).
[47]Yu. Z. Kovdrya, V. A. Nikolaenko, and P. K. H. Sommerfeld, Czech. J. Phys. **46**, Suppl S1 347 (1996).
[48]X. L. Hu and A. J. Dahm, Cryogenics **32**, 681 (1992).
[49]A. M. C. Valkering, I. Klier, and P. Leiderer, Physica B **284**, 172 (2000).
[50]V. A. Nikolaenko, H. Yayama, Yu. Z. Kovdrya, and A. Tomokiyo, Fiz. Nizk. Temp. **23**, 642 (1997) [Low Temp. Phys. **23**, 482 (1997)].
[51]H. Yayama, A. Tomokiyo, O. I. Kirichek, I. B. Berkutov, and Yu. Z. Kovdrya, Fiz. Nizk. Temp. **23**, 1172 (1997) [Low Temp. Phys. **23**, 878 (1997)].
[52]Yu. Z. Kovdrya, V. A. Nikolaenko, H. Yayama, A. Tomokiyo, O. I. Kirichek, and I. B. Berkutov, J. Low Temp. Phys. **110**, 191 (1998).
[53]V. A. Buntar, V. N. Grigor'ev, O. I. Kirichek, Yu. Z. Kovdrya, Yu. P. Monarkha, and S. S. Sokolov, J. Low Temp. Phys. **79**, 323 (1990).
[54]S. S. Sokolov, Guo-Qiang Hai, and N. Studart, Phys. Rev. B **51**, 5977 (1995).
[55]Yu. Z. Kovdrya, V. A. Nikolaenko, S. P. Gladchenko, and S. S. Sokolov, Fiz. Nizk. Temp. **24**, 1113 (1998) [Low Temp. Phys. **24**, 837 (1998)].
[56]Yu. Z. Kovdrya, V. A. Nikolaenko, S. P. Gladchenko, and S. S. Sokolov, J. Low Temp. Phys. **113**, 1109 (1998).
[57]Yu. Z. Kovdrya, V. A. Nikolaenko, and S. P. Gladchenko, Physica B **284–288**, 168 (2000).
[58]S. P. Gladchenko, Yu. Z. Kovdrya, and V. A. Nikolaenko, Physica B **284–288**, 1958 (2000).
[59]S. P. Gladchenko, V. A. Nikolaenko, Yu. Z. Kovdrya, and S. S. Sokolov,

Fiz. Nizk. Temp. **27**, 3 (2001) [Low Temp. Phys. **27**, 1 (2001)].
[60]Yu. P. Monarkha, S. S. Sokolov, Guo-Qiang Hai, and N. Studart, Phys. Rev. B **52**, 15509 (1995).
[61]S. S. Sokolov, Guo-Qiang Hai, and N. Studart, Physica E **12**, 950 (2002).
[62]S. Nelson, Yu. P. Monarkha, S. S. Sokolov, and Guo-Qiang Hai, *International Symposium on Quantum Fluids and Solids. Abstracts*, Konstanz, Germany (2001), p. 18.
[63]A. M. Dyugaev, A. S. Rozhavskiĭ, I. D. Vagner, and P. Wyder, JETP Lett. **67**, 434 (1998).
[64]P. A. Lee and T. V. Ramakrishnan, Rev. Mod. Phys. **57**, 287 (1985).
[65]B. L. Altshuller, D. Khmelnitski, A. L. Larkin, and P. A. Lee, Phys. Rev. B **22**, 5142 (1980).
[66]P. W. Adams and M. A. Paalanen, Phys. Rev. Lett. **61**, 451 (1988).
[67]P. W. Adams, Phys. Rev. Lett. **65**, 3333 (1990).
[68]I. Karakurt, D. Herman, H. Mathur, and H. J. Dahm, Phys. Rev. Lett. **85**, 1072 (2000).
[69]Yu. Z. Kovdrya, V. A. Nikolaenko, and S. P. Gladchenko, JETP Lett. **73**, 465 (2001).
[70]M. J. Stephen, Phys. Rev. B **36**, 5663 (1987).
[71]R. H. Ritchie, Phys. Rev. **106**, 874 (1957).
[72]Yu. P. Monarkha, Fiz. Nizk. Temp. **3**, 1459 (1977) [Sov. J. Low Temp. Phys. **3**, 702 (1977)].
[73]M. V. Krasheninnikov and A. V. Chaplik, Fiz. Tverd. Tela (Leningrad) **21**, 2502 (1979) [Sov. Phys. Solid State **21**, 1444 (1979)].
[74]S. S. Sokolov and O. I. Kirichek, Fiz. Nizk. Temp. **20**, 764 (1994) [Low Temp. Phys. **20**, 599 (1994)].
[75]S. S. Sokolov and N. Studart, J. Low Temp. Phys. **126**, 499 (2002).
[76]I. M. Kosterlitz and D. J. Thouless, J. Phys. C **6**, 1131 (1973).
[77]R. H. Morf, Phys. Rev. Lett. **43**, 931 (1979).
[78]D. R. Nelson and B. I. Halperin, Phys. Rev. B **19**, 2457 (1979).
[79]V. E. Sivokon', V. V. Dotsenko, Yu. Z. Kovdrya, and V. N. Grigor'ev, Fiz. Nizk. Temp. **22**, 1107 (1996) [Low Temp. Phys. **22**, 845 (1996)]; V. V. Dotsenko, V. E. Sivokon', Yu. Z. Kovdrya, and V. N. Grigor'ev, Fiz. Nizk. Temp. **23**, 1028 (1997) [Low Temp. Phys. **23**, 772 (1997)].
[80]S. S. Sokolov and N. Studart, Phys. Rev. B **60**, 1556 (1999).
[81]K. M. S. Bajaj and R. Mehrotra, Physica B **194–196**, 1235 (1994).
[82]P. Glasson, V. Dotsenko, P. Fozooni, M. J. Lea, W. Bailey, G. Papageorgiou, S. E. Anderson, and A. Kristensen, Phys. Rev. Lett. **87**, 176802-1 (2001).
[83]A. Kristensen, K. Djerfi, P. Fozooni, M. J. Lea, P. J. Richardson, A. Santrich-Badal, A. Blackburn, and R. W. van der Heijden, Phys. Rev. Lett. **77**, 1350 (1996).
[84]A. G. Khrapak and N. T. Yakubov, *Electrons in Dense Gases and Plasma* [in Russian], Moscow, Nauka (1981).
[85]L. S. Kukushkin and V. B. Shikin, Zh. Éksp. Teor. Fiz. **63**, 1830 (1972) [Sov. Phys. JETP **36**, 969 (1973)].
[86]V. B. Shikin, Zh. Éksp. Teor. Fiz. **60**, 713 (1971) [Sov. Phys. JETP **33**, 387 (1971)].
[87]V. B. Shikin and Yu. P. Monarkha, Zh. Éksp. Teor. Fiz. **65**, 751 (1973) [Sov. Phys. JETP **38**, 373 (1974)].
[88]O. Hippolito, G. A. Farias, and N. Studart, Surf. Sci. **113**, 394 (1982).
[89]S. A. Jackson and P. M. Platzman, Phys. Rev. B **25**, 4886 (1982).
[90]S. A. Jackson and P. M. Platzman, Surf. Sci. **142**, 125 (1984).
[91]L. M. Sander, Phys. Rev. B **11**, 4350 (1975).
[92]G. E. Marques and N. Studart, Phys. Rev. B **39**, 4133 (1989).
[93]V. S. Édel'man, Zh. Éksp. Teor. Fiz. **77**, 673 (1979) [Sov. Phys. JETP **50**, 338 (1979)].
[94]V. B. Shikin, Zh. Éksp. Teor. Fiz. **77**, 717 (1979) [Sov. Phys. JETP **50**, 361 (1979)].
[95]A. Cheng and P. M. Platzman, Solid State Commun. **25**, 873 (1978).
[96]M. Saitoh, J. Phys. C **16**, 6983 (1983).
[97]F. F. Mende, Yu. Z. Kovdrya, and V. A. Nikolaenko, Fiz. Nizk. Temp. **11**, 646 (1985) [Sov. J. Low Temp. Phys. **11**, 355 (1985)].
[98]L. Wilen and L. Gianetta, in *Proceedings of the 17th International Conference on Low Temperature Physics*, Part I (1984), p. 221.
[99]H. W. Jiang and A. J. Dahm, Jpn. J. Appl. Phys. **26**, 745 (1987).
[100]H. W. Jiang, M. A. Stan, and A. J. Dahm, Surf. Sci. **196**, 1 (1988).
[101]M. Saitoh, J. Phys. Soc. Jpn. **42**, 201 (1977).
[102]V. B. Shikin and Yu. P. Monarkha, J. Low Temp. Phys. **16**, 193 (1974).
[103]K. Kajita and W. Sasaki, Surf. Sci. **113**, 419 (1982).
[104]K. Kajita, J. Phys. Soc. Jpn. **52**, 372 (1983); Surf. Sci. **142**, 86 (1984).
[105]P. M. Platzman, Surf. Sci. **170**, 55 (1986).
[106]H. W. Jiang and A. J. Dahm, Surf. Sci. **229**, 352 (1990).
[107]X. L. Hu, Y. Carmi, and A. J. Dahm, J. Low Temp. Phys. **89**, 625 (1992).
[108]S. A. Jackson, Surf. Sci. **170**, 65 (1986).
[109]O. Tres, Yu. P. Monarkha, F. C. Penning, H. Blayssen, and P. Wyder, Phys. Rev. Lett. **77**, 2511 (1996).
[110]D. Coimbra, S. S. Sokolov, J. P. Rino, and N. Studart, J. Low Temp. Phys. **126**, 505 (2002).
[111]B. Lehndorff and K. Dransfeld, J. Phys. (France) **50**, 2579 (1989).
[112]G. A. Farias, R. N. Costa Filho, F. M. Peeters, and N. Studart, *International Symposium on Quantum Fluids and Solids. Abstracts*, Konstanz, Germany (2001), p. 49.
[113]Yu. P. Monarkha and Yu. Z. Kovdrya, Fiz. Nizk. Temp. **8**, 215 (1982) [Sov. J. Low Temp. Phys. **8**, 107 (1982)].
[114]G. A. Farias and F. M. Peeters, Phys. Rev. B **55**, 3763 (1997).
[115]B. Maraviglia, Phys. Lett. A **25**, 991 (1969).
[116]Yu. P. Monarkha, Fiz. Nizk. Temp. **8**, 1133 (1982) [Sov. J. Low Temp. Phys. **8**, 571 (1982)].
[117]U. de Freitas, J. P. Rino, and N. Studart, *Lectures on Surface Science*, Springer-Verlag, New York (1987), p. 177.
[118]J. Poitrenaud and F. I. B. Wiliams, Phys. Rev. Lett. **29**, 1230 (1972).
[119]Yu. P. Monarkha, Fiz. Nizk. Temp. **5**, 940 (1979) [Sov. J. Low Temp. Phys. **5**, 447 (1979)].
[120]A. J. Dahm, Z. Phys. B: Condens. Matter **98**, 333 (1995).
[121]B. Lehndorff, C. Vossloh, T. Gunzler, and K. Dransfeld, Surf. Sci. **263**, 674 (1992).
[122]M. S. Khaĭkin, JETP Lett. **27**, 668 (1978).
[123]M. V. Rama Krishna and K. B. Whaley, Phys. Rev. B **38**, 11839 (1988).
[124]P. K. H. Sommerfeld and R. W. van der Heijden, J. Phys.: Condens. Matter **7**, 9731 (1995).
[125]A. M. C. Valkering, H. Yayama, and R. W. van der Heijden, J. Low Temp. Phys. **113**, 873 (1998).
[126]A. M. C. Valkering, I. Klier, and P. Leiderer, *International Symposium on Quantum Fluids and Solids. Abstracts*, Konstanz, Germany (2001), p. 50.
[127]J. Klier, I. Doicescu, and P. Leiderer, J. Low Temp. Phys. **121**, 603 (2000).
[128]S. Ya. Kilin, Usp. Fiz. Nauk **169**, 507 (1999).
[129]P. M. Platzman and M. I. Dykman, Science **284**, 1967 (1999).
[130]T. Ando, Phys. Soc. Jpn. **44**, 765 (1978).
[131]A. P. Volodin and V. S. Édel'man, Zh. Éksp. Teor. Fiz. **81** 368 (1981) [Sov. Phys. JETP **54**, 198 (1981)].
[132]P. G. Frayne, P. Fozooni, W. Baiey, P. Glasson, G. Papageorgiou, and M. J. Lea, *Europhysics Conference. Abstracts*, Vol. 26A (2002), p. 162.

Translated by Steve Torstveit